

https://dspace.org/

Search for new physics in events with missing transverse energy and the Higgs boson decaying to two photons with the ATLAS detector at CERN

Liao, Shell-may

2019

https://hdl.handle.net/10539/30456

Downloaded from a DSpace repository. https://dspace.org/

Search for new physics in events with missing transverse energy and the Higgs boson decaying to two photons with the ATLAS detector at CERN

By

SHELL-MAY LIAO

SUPERVISOR: PROFESSOR BRUCE MELLADO
CO-SUPERVISOR: DR. XIFENG RUAN



WITS
UNIVERSITY

Department of Physics
UNIVERSITY OF THE WITWATERSRAND

A dissertation submitted to the University of the Witwatersrand in accordance with the requirements of the degree of DOCTOR OF PHILOSOPHY in the Faculty of Science

MAY 2019

ABSTRACT

The discovery of the Higgs boson in 2012 by both the ATLAS and CMS experiments at the Large Hadron Collider (LHC) at CERN marked the beginning of a new age in particle physics. As the last missing piece in the Standard Model (SM), the Higgs boson plays a fundamental role in particle physics. Since its discovery, more emphasis has been placed on attempts to further understand its properties, opening up a new realm of beyond the Standard Model physics (BSM). A model was formulated based on various anomalies observed by both ATLAS and CMS in Run 1 of data taking. The model introduces a heavy scalar particle as well as an intermediate scalar, which can decay into both dark matter and SM particles. Initially, we hypothesize the heavy scalar decaying to the Higgs boson and two dark matter candidates ($H \to h\chi\chi$). A search is done in the diphoton channel and driven largely by missing transverse energy ($E_{\mathrm{T}}^{\mathrm{miss}}$) denoted $h(\to \gamma\gamma) + E_{\mathrm{T}}^{\mathrm{miss}}$. No significant excess over the expected background is observed in the dark matter search using data corresponding to an integrated luminosity of 36.1 fb^{-1}. As a result, the search was then redirected towards other final states. In November 2016, an excess was observed with a diphoton invariant mass around 248 GeV associated with moderate $E_{\mathrm{T}}^{\mathrm{miss}}$. In view of this result, we looked at the direct decay of H into $\gamma\gamma$, where $H(\to \gamma\gamma) + E_{\mathrm{T}}^{\mathrm{miss}}$. We looked for and found the same excess in Run 1 data. With the implementation of several $E_{\mathrm{T}}^{\mathrm{miss}}$ suppression techniques, the diphoton resonance search was performed using Run 2 data and extrapolated to the $Z\gamma$ final state. The analysis was redone following the migration from ATLAS Release 20 to Release 21 and was also documented. For the $\gamma\gamma$ channel most of the excess is found around approximately 246 GeV with a maximum local significance of 3 σ and a global significance of 2.5 σ (2015+2016+2017 data). In the $Z\gamma$ channel, the excess is found around 252 GeV with a maximum local significance of 4.14 σ and global of 3.41 σ (2015+2016+2017 data). This document also details the reconstruction and

performance of $\boldsymbol{E}_{\mathrm{T}}^{\mathrm{miss}}$ in these diphoton final state searches. The stability of the performance of $\boldsymbol{E}_{\mathrm{T}}^{\mathrm{miss}}$ is essential for all BSM searches at the LHC which adds a significant amount of value to this documentation. In an effort to aid in the 2019-2020 ATLAS detector upgrade, a comparative study was done to determine the most radiation hard brand of plastic scintillators in order to replace the gap and Minimum Bias Trigger scintillators of the Tile Calorimeter. The scintillators are exposed to harsh radiation environments within the detector, making them susceptible to damage. After experimenting on various scintillator grades, the EJ 200 polyvinyl toluene based scintillator was found to be the most suitable brand as it showed a fairly low decrease in light transmission, and a substantial amount of annealing after irradiation for intermediate to small doses.

DEDICATION AND ACKNOWLEDGEMENTS

First and foremost, I would like to express my humble gratitude to my supervisor Prof. Bruce Mellado who has played a continuous and fundamental role in the execution of this research. His patience, support, vast knowledge and guidance equipped me with the necessary tools that I needed to be able to take the bull by the horns throughout my research. The opportunities to travel to CERN and liaise with other experts in the field were at my disposal because of him and I am truly grateful. Thank you Prof, I could not have imagined having a better mentor for my research.

I would also like to extend my gratitude to my co-supervisor Dr. Xifeng Ruan who has also played a crucial role in my development as a scientist. The knowledge and skills that he so willingly imparted over the years helped me appreciate the significance and purpose of this research. His constant guidance was the driving force in assisting me to understanding the manifestations of this research in great depth. The dedication and enthusiasm that he has towards HEP is more than evident and is truly admirable. Thank you Xifeng for being such a great role model in this research field.

A special thanks to my colleagues and influential University of the Witwatersrand (Wits) Institute for Collider Particle Physics members: Prof. Alan Cornell, Prof. Elias Sideras-Haddad, Dr. Deepak Kar, Dr. Robert Reed, Dr. Mukesh Kumar, Dr. Debarati Roy, Yesenia Hernández, Harshna Jivan, Kehinde Tomiwa, Stefan von Buddenbroch, Laila Tribelhorn, Chad Pelwan, Tshidiso Molupe, Skhathisomusa Mthembu, Dingane Hlaluku, Humphrey Tlou, Abdualazem Mohammed and Joyful Mdluli. Thank you all for being incredibly supportive over the years and for the continued contribution towards us being a very effective team. Colleagues, I appreciate all of the fun times we shared both inside and outside the work environment. These are memories I will always treasure. An equally special thanks to Prof. Bertrand Laforge and

his students for working with us in part of the work documented in this thesis, your efforts and guidance are not taken for granted.

I would be thoughtless not to mention the support from my friends outside the academic environment. Thanks to Charmaine, Bulie, Melissa, Kelly, Ashton-Rae, Amanda, Lucille and Kaylene for all those ladies' lunches, dinners, and more that were very entertaining. Those events provided the balance that I needed to keep me sane throughout my research. I appreciate you all.

Last and most importantly, I would like to express my sincere gratitude to my wonderful family. A special thanks to my husband for being incredibly supportive and patient with me throughout my time away from him. The times I spent at CERN were the most difficult for us, and more so on some days. Thank you for keeping me motivated on those demanding days and for always reassuring me of the light at the end of the tunnel regardless of the distance between us. To my amazing dad, thank you for all the support and for being such an inspiration in my life. I am grateful to you for all those skype conversations which kept me motivated as well and gave me that extra push that I needed to get this done. Mei-ling and Edward, thank you for being amazing siblings. My dear mom in heaven, I miss you and dedicate this to you and all my loved ones.

The financial assistance from the National Research Foundation (NRF) towards this research is also acknowledged.

AUTHOR'S DECLARATION

I, Shell-may Liao, hereby declare that the work contained in this thesis is my own original work and that I have not previously in its entirety or in part submitted it at any university for a degree.

This dissertation has produced the following papers:

- Selection and performance for the $H \to \gamma\gamma$ and $H \to Z\gamma$ analyses. ATLAS internal note. **ATL-COM-PHYS-2015-1326** [1].
  Contributions: $E_{\mathrm{T}}^{\mathrm{miss}}$ validation.
- Measurement of Higgs Boson fiducial cross-section in the diphoton decay channel in pp collisions at centre-of-mass energy of 13 TeV with the ATLAS detector. ATLAS internal note. **ATL-COM-PHYS-2015-1388** [2].
  Contributions: $E_{\mathrm{T}}^{\mathrm{miss}}$ performance and validation.
- Search for a Higgs boson with the di-photon decay in association with missing energy in pp collisions at $\sqrt{s}$ = 13 TeV with the ATLAS detector. ATLAS internal note. **ATL-COM-PHYS-2015-1589** [3].
  Contributions: Optimization and categorization, theoretical uncertainties, $E_{\mathrm{T}}^{\mathrm{miss}}$ and photons, $E_{\mathrm{T}}^{\mathrm{miss}}$ validation.
- Selection and performance for the $H \to \gamma\gamma$ and $H \to Z\gamma$ analyses. ATLAS internal note. **ATL-COM-PHYS-2016-109** [4].
  Contributions: $E_{\mathrm{T}}^{\mathrm{miss}}$ validation.
- Search for a Higgs boson with the di-photon decay in association with missing energy in pp collisions at $\sqrt{s}$ =13 TeV with the ATLAS detector. ATLAS internal note. **ATL-COM-PHYS-2016-473** [5].
  Contributions: Kinematic distributions for different categories, $E_{\mathrm{T}}^{\mathrm{miss}}$ performance 2015/2016 data comparisons, $E_{\mathrm{T}}^{\mathrm{miss}}$ performance 2016 data md MC comparisons, Impact on $E_{\mathrm{T}}^{\mathrm{miss}}$ of choice of vertex for the soft component, Impact of $E_{\mathrm{T}}^{\mathrm{miss}}$ hardest vertex.
- Search for a Higgs boson with the di-photon decay in association with missing energy in pp collisions at $\sqrt{s}$ = 13 TeV with the ATLAS detector. ATLAS internal note. **ATL-COM-PHYS-2016-1732** [6].

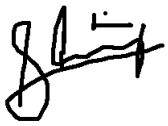
Contributions: Validation of $E_{\mathrm{T}}^{\mathrm{miss}}$ using diphoton vertex, $E_{\mathrm{T}}^{\mathrm{miss}}$ performance, editor of the supporting note.

- Search for dark matter in events with missing transverse momentum and a Higgs boson decaying to two photons in pp collisions at $\sqrt{s}$ = 13 TeV with the ATLAS detector. ATLAS internal note. **ATL-COM-PHYS-2016-708** [7].
  Contributions: Validation of $E_{\mathrm{T}}^{\mathrm{miss}}$ using diphoton vertex.
- Selection and performance for the $H \to \gamma\gamma$ and $H \to Z\gamma$ analyses. ATLAS internal note. **ATL-COM-PHYS-2016-862** [8].
  Contributions: $E_{\mathrm{T}}^{\mathrm{miss}}$ validation.
- An updated search for new phenomena in events with missing transverse momentum and a Higgs boson decaying to two photons in pp collisions at $\sqrt{s}$ = 13 TeV with the ATLAS detector. ATLAS internal note. **ATL-COM-PHYS-2016-911** [9]. **Contributions:** Analysis.
- Search for new phenomena in events with missing transverse momentum and a Higgs boson decaying to two photons in pp collisions at $\sqrt{s}$ = 13 TeV with the ATLAS detector. ATLAS Conference note. **ATLAS-COM-CONF-2016-078** [10].
  Contributions: Analysis.
- Search for dark matter in events with missing transverse momentum and a Higgs boson decaying to two photons in pp collisions at $\sqrt{s}$ = 13 TeV with the ATLAS detector using data in full years of 2015 and 2016. ATLAS internal note. **ATL-COM-PHYS-2016-1735** [11].
  Contributions: Validation of $E_{\mathrm{T}}^{\mathrm{miss}}$ using diphoton vertex, $E_{\mathrm{T}}^{\mathrm{miss}}$ performance, editor of the supporting note.
- Search for new phenomena in events with missing transverse momentum and a Higgs boson decaying to two photons in pp collisions at $\sqrt{s}$ = 13 TeV with the ATLAS detector. ATLAS Conference note. **ATLAS-CONF-2016-087** [12].
  Contributions: Analysis.
- Search for new phenomena in events with missing transverse momentum and a Higgs boson decaying to two photons in pp collisions at $\sqrt{s}$ = 13 TeV with the ATLAS detector. ATLAS Conference note. **ATLAS-CONF-2016-011** [13].
  Contributions: Analysis.
- Selection and performance for the $H \to \gamma\gamma$ and $H \to Z\gamma$ analyses. ATLAS internal note. **ATL-COM-PHYS-2017-357** [14].
  Contributions: $H \to \gamma\gamma$ analysis.
- Search for a resonance in the di-photon decay in association with missing energy in pp collisions at $\sqrt{s}$ = 13 TeV with the ATLAS detector. ATLAS internal note. **ATL-COM-PHYS-2017-1225** [15].
  Contributions: Validation of $E_{\mathrm{T}}^{\mathrm{miss}}$ performance, analyzer of the excess,

validating the data and MC, editor of the supporting note, version checks: h014 versus h015/h015d, pile-up dependency checks, shower shape checks.

- Search for a new resonance in the di-photon decay in association with missing transverse energy in pp collisions at $\sqrt{s}$ = 13 TeV with the ATLAS detector. ATLAS internal note. **ATL-COM-PHYS-2018-970** [16].
  Contributions: Validation of $E_{\mathrm{T}}^{\mathrm{miss}}$ performance, run I excess, validating the data and MC, event selection.
- Dark matter search in events with missing transverse energy and a Higgs boson decaying to two photons with the ATLAS detector. Kruger2018 conference. **ATL-COM-PHYS-2018-1641** [17]. **Contributions:** Analysis.
- A Search for dark matter in association with a Higgs boson decaying to two photons at $\sqrt{s}$ = 13 TeV with the ATLAS detector. Published in the Physics Review journal. doi: 10.1103/PhysRevD.96.112004. arXiv:1706.03948v3 [18]
  Contributions: Analysis.
- Proceedings: A comparative study of the radiation hardness of plastic scintillators for the upgrade of the Tile Calorimeter of the ATLAS detector. Published in the Workshop on High Energy Particle Physics (HEPPW2015) proceedings, doi:10.1088/1742-6596/645/1/012021 [19].
  Contributions: Analysis and documentation.
- Proceedings: Radiation hardness of plastic scintillators for the Tile Calorimeter of the ATLAS detector. Published in the Workshop on High Energy Particle Physics (HEPPW2015) proceedings, doi:10.1088/1742-6596/645/1/012023 [20].
  Contributions: Sample preparation, sample radiation, light transmission tests.
- Proceedings: Characterization of plastic scintillators using magnetic resonance techniques for the upgrade of the Tile Calorimeter in the ATLAS detector. Published in the Workshop on High Energy Particle Physics (HEPPW2015) proceedings, doi:10.1088/1742-6596/645/1/012023 [21].
  Contributions: Sample preparation, sample radiation, light transmission tests, student supervision.
- Proceedings: Neutron irradiation and light transmission assessment of plastic scintillators of the TileCal section of the ATLAS detector. Published in the Annual Conference of the South African Institute of Physics (SAIP2016) proceedings, ISBN: 978-0-620-77094-1 [22]
  Contributions: Sample preparation.
- Proceedings: Reconstruction of missing energy in events with two photons at the ATLAS detector in Large Hadron Collider. Published in the Annual Conference of the South African Institute of Physics (SAIP2017) proceedings, ISBN: 978-0-620-82077-6 [23]. **Contributions:** Validation of $E_{\mathrm{T}}^{\mathrm{miss}}$ performance.

- Proceedings: Reconstruction and performance of missing transverse energy at the ATLAS detector. Accepted for publication in the Workshop on High Energy Particle Physics (HEPPW2018) proceedings [24].
  Contributions: Analysis and documentation.
  Signed:



Date: 27 May 2019

TABLE OF CONTENTS

Page

List of Figures **xv**

List of Tables **xxiii**

1 Introduction and Theoretical Background **5**

1.1 Introduction 5

1.2 Standard Model of particle physics 6

1.2.1 The elementary particles 7

1.2.2 Quantum Chromodynamics 8

1.2.3 ElectroWeak Theory 10

1.3 The Higgs Boson 11

1.3.1 Production mechanisms 12

1.3.2 Decay mechanisms 14

1.3.3 History and discovery 15

1.4 The Madala Hypothesis 18

1.4.1 Testing the hypothesis in the diphoton channel 25

2 Experimental apparatus **29**

2.1 The Large Hadron Collider 29

2.2 The ATLAS detector 33

2.2.1 Magnetic system 35

2.2.2 Inner detector 35

2.2.3 The Calorimeter System 38
2.2.4 Muon Spectrometer 43
2.2.5 Trigger system 43

3 Investigating the radiation hardness of plastic scintillators for the upgrade of the ATLAS Tile Calorimeter 47
3.1 Introduction 48
3.2 The Scintillation Mechanism 49
3.3 Methods 53
3.3.1 Radiation environment modelling 53
3.3.2 Sample preparation 55
3.4 Experimental procedure 57
3.4.1 Radiation process 57
3.4.2 Transmission spectroscopy 58
3.5 Results and analysis 60
3.6 Conclusions 65

4 Object reconstruction at ATLAS 69
4.1 Track reconstruction 69
4.2 Vertex reconstruction 72
4.3 Photon reconstruction 73
4.3.1 Photon Identification and Isolation 74
4.4 Electron reconstruction 76
4.5 Muon reconstruction 77
4.6 Jet reconstruction 77
4.7 Missing transverse energy reconstruction 78
4.8 Conclusions 79

5 The $h \to \gamma\gamma$ decay channel 81
5.1 Diphoton Analysis Framework 81
5.2 Monte Carlo samples 83

5.2.1 Standard Model Higgs Monte Carlo samples 84
5.2.2 Background Monte Carlo samples 84
5.3 Object and event selection 86
5.3.1 Diphoton primary vertex 86
5.3.2 Diphoton event selection 86
5.4 Conclusion 87

6 Performance of $E_{\mathrm{T}}^{\mathrm{miss}}$ reconstruction for ATLAS with diphotons at $\sqrt{s}$ = 13 TeV 89
6.1 $E_{\mathrm{T}}^{\mathrm{miss}}$ reconstruction and calibration 90
6.1.1 $E_{\mathrm{T}}^{\mathrm{miss}}$ Soft Term reconstruction 91
6.1.2 $E_{\mathrm{T}}^{\mathrm{miss}}$ significance 93
6.1.3 Fake $E_{\mathrm{T}}^{\mathrm{miss}}$ 93
6.2 $E_{\mathrm{T}}^{\mathrm{miss}}$ reconstruction tools 94
6.2.1 $E_{\mathrm{T}}^{\mathrm{miss}}$ Handler 94
6.3 $E_{\mathrm{T}}^{\mathrm{miss}}$ Performance studies 96
6.3.1 $Z \rightarrow e^{+}e^{-}$ vertex reconstruction validation 96
6.3.2 The Same Vertex Method 99
6.3.3 Performance of 2015 data versus 2016 data 104
6.3.4 Impact on $E_{\mathrm{T}}^{\mathrm{miss}}$ of choice of vertex for the soft component 106
6.3.5 2016 data versus MC 113
6.3.6 2017 data versus MC 118
6.3.7 Pile-up dependency validations 121
6.4 Conclusions 122

7 Search for the Higgs boson in association with $E_{\mathrm{T}}^{\mathrm{miss}}$ in the diphoton channel 125
7.1 Introduction 126
7.2 Data and simulation samples 127
7.2.1 Signal samples 127
7.2.2 Background samples 128
7.3 Object and event selection 129

7.4 Event categorization . . . 129
7.4.1 The Madala framework . . . 130
7.4.2 Categorization results . . . 131
7.5 Signal and background parameterization . . . 131
7.5.1 Signal modelling . . . 134
7.5.2 Background modelling . . . 134
7.6 Systematic uncertainties . . . 136
7.6.1 Experimental uncertainties . . . 136
7.6.2 Theoretical uncertainties . . . 139
7.7 Statistical analysis . . . 140
7.8 Results . . . 141
7.9 Conclusions . . . 142

8 Search for a new resonance in the diphoton decay in association with $E_{\mathrm{T}}^{\mathrm{miss}}$ with Release 20 147

8.1 Introduction . . . 148
8.2 Data and simulation samples . . . 148
8.2.1 Signal samples . . . 148
8.2.2 Background samples . . . 149
8.3 The same vertex boundary tuning method . . . 150
8.4 Motivation for the resonance search . . . 152
8.4.1 The excess observed in data at $\sqrt{s}$ = 8 TeV . . . 152
8.4.2 The excess observed in data at $\sqrt{s}$ = 13 TeV . . . 154
8.5 Event selection and categorization . . . 158
8.5.1 Object and event selection . . . 158
8.5.2 Categorization . . . 159
8.6 Signal and background parameterization . . . 163
8.6.1 Signal modelling . . . 163
8.6.2 Spurious signal . . . 166
8.7 Statistical analysis . . . 168

8.8 Results . . . 169
8.9 Conclusions . . . 172

9 Search for a new resonance in the diphoton decay in association with $E_{\mathrm{T}}^{\mathrm{miss}}$ with Release 21 175

9.1 Introduction . . . 175
9.2 Data and simulation samples . . . 176
9.3 A Recap of analyses of 2015+2016 data in Release 20.7 and Release 21.2 . . . 176
9.4 Event optimization . . . 177
9.5 Signal and background parameterization . . . 182
9.5.1 Signal parametrization . . . 182
9.5.2 Background parametrization . . . 184
9.6 Results . . . 186
9.7 Conclusions . . . 189

10 Conclusions 195

A A comparative study of the radiation hardness of plastic scintillators for the upgrade of the Tile Calorimeter at ATLAS 199

A.1 . . . 199

B Performance of $E_{\mathrm{T}}^{\mathrm{miss}}$ reconstruction complementary material 201

B.1 . . . 201
B.2 . . . 201

C Search for the Higgs boson in association with $E_{\mathrm{T}}^{\mathrm{miss}}$ in the diphoton channel 205

C.1 . . . 205
C.2 . . . 205

D Search for a new resonance in the diphoton decay in association with $E_{\mathrm{T}}^{\mathrm{miss}}$ complementary material 213

D.1 . . . 213

D.2 213
D.3 214

Bibliography **225**

LIST OF FIGURES

FIGURE **Page**

1.1 Schematic diagram of the Standard Model particles 8
1.2 A simple illustration of quark color confinement 9
1.3 Graph of Goldstone's "Mexican hat" potential function V versus ϕ 12
1.4 Feynman diagrams showing bb fusion 13
1.5 Higgs boson branching ratios and their uncertainties 14
1.6 Feynman diagrams for the dominant Higgs production mechanisms at the LHC . 15
1.7 Higgs boson production cross sections 16
1.8 The observed local p_0 distribution as a function of m_h 17
1.9 The Feynman diagrams for the production and decay of the heavy scalar 19
1.10 Fits to the Run 1 ATLAS and CMS p_T spectra 21
1.11 A scan of minimized χ^2 values as a function of the the mass of H 22
1.12 Feynman diagrams of the Madala hypothesis 23
1.13 Distribution of the ATLAS data and SM background comparing to the BSM signal for the di-lepton invariant mass in events required to have two oppositely charged leptons ($e\mu$) with at least one b-tagged jet 24
1.14 The negative 2 times the logarithm of the profile likelihood ratios for each of the individual fit results 26

2.1 A diagram of the CERN accelerator complex 30
2.2 A cut-away view of the ATLAS detector 33
2.3 An illustration of the magnetic system at ATLAS 35
2.4 An illustration of the ATLAS Inner Detector and its sub-systems 37

2.5 A computer generated image of the ATLAS calorimeter 39
2.6 A section of the ATLAS electromagnetic calorimeter highlighting the accordion geometry 41
2.7 A schematic diagram of the tile calorimeter 42
2.8 A schematic diagram of the Muon system 44
2.9 A diagram showing the structure of the ATLAS trigger system 45

3.1 The location of the MBTS within the ATLAS detector. 49
3.2 Schematic diagram of the π-bond overlap. 50
3.3 The electronic energy levels of an organic molecule. 51
3.4 Schematic diagram of the scintillation 'ladder' 52
3.5 SRIM output interface 54
3.6 Images of the actual cutting and polishing of the samples 56
3.7 An image of EJ 200 scintillator after the cutting and polishing process 57
3.8 A schematic diagram of the tandem accelerator of iThemba LABS Gauteng . . . 58
3.9 An image of EJ 260 after irradiation using a high dose. 59
3.10 A photograph of the Varian Cary 500 spectrophotometer. 60
3.11 61
3.12 The % Transmission versus Wavelength distribution for EJ 200 for different doses. 62
3.13 The % Transmission versus Wavelength distribution for EJ 208 for different doses [19]. 63
3.14 The % Transmission versus Wavelength distribution for EJ 260 for different doses. 64
3.15 The % Transmission versus Wavelength distribution for EJ 200 corresponding to the intermediate dose (25 MGy) on different days. 65
3.16 The % Transmission versus Wavelength distribution for EJ 208 corresponding to the intermediate dose (25 MGy) on different days 66
3.17 The % Transmission versus Wavelength distribution for EJ 260 corresponding to the intermediate dose (25 MGy) on different days. 67

4.1 A segment along the transverse plane showing the trajectories of the various hard objects . . . 70
4.2 An illustration of the perigee parameters of a track . . . 71
4.3 An illustration of reconstructed vertices at ATLAS . . . 72
4.4 Distribution of JVT for pileup and hard-scatter jets with $20 < p_T < 30$ GeV . . . 78

5.1 An illustration of the ATLAS data flow into analysis . . . 83

6.1 A graphical illustration aiding in the explanation of $E_{\mathrm{T}}^{\mathrm{miss}}$ . . . 90
6.2 A graphical illustration of the constituents of the $E_{\mathrm{T}}^{\mathrm{miss}}$ . . . 92
6.3 A graphical illustration of the reconstruction of the different constituents of the $E_{\mathrm{T}}^{\mathrm{miss}}$ 95
6.4 The data and MC comparisons for the vertex reconstruction efficiency and reconstruction efficiency . . . 98
6.5 The direct comparison of the $E_{\mathrm{T}}^{\mathrm{miss}}$ between data and MC in the $Z \to e^+e^-$ control region . . . 99
6.6 The comparison in variation of $E_{\mathrm{T}}^{\mathrm{miss}}$ between data and MC in the $Z \to e^+e^-$ control region . . . 100
6.7 An illustration of real $E_{\mathrm{T}}^{\mathrm{miss}}$ and fake $E_{\mathrm{T}}^{\mathrm{miss}}$ . . . 101
6.8 Distributions showing the principle behind the same vertex method using the diphoton background, Zh signal and heavy scalar signal . . . 102
6.9 Distributions showing the same vertex fraction as a function of $E_{\mathrm{T}}^{\mathrm{miss}}$ and $E_{\mathrm{T}}^{\mathrm{miss}}$ significance . . . 103
6.10 $E_{\mathrm{T}}^{\mathrm{miss}}$ distributions comparing 2015 and 2016 data . . . 105
6.11 $E_{\mathrm{T}}^{\mathrm{miss}}$ resolution distributions showing the x and y components of the $E_{\mathrm{T}}^{\mathrm{miss}}$ as a function of μ, $\mathrm{N_{pv}}$ and $\sum E_{\mathrm{T}}$ . . . 107
6.12 $E_{\mathrm{T}}^{\mathrm{miss}}$ distributions for the $ggh125$ MC comparing $E_{\mathrm{T}}^{\mathrm{miss}}$ reconstructed using the diphoton vertex with that reconstructed with the hardest vertex . . . 109
6.13 $E_{\mathrm{T}}^{\mathrm{miss}}$ distributions for the $ggh125$ MC comparing $E_{\mathrm{T}}^{\mathrm{miss}}$ reconstructed using the diphoton vertex with that reconstructed with the hardest vertex . . . 110

6.14 $E_{\mathrm{T}}^{\mathrm{miss}}$ distributions for the $ggh125$ MC comparing $E_{\mathrm{T}}^{\mathrm{miss}}$ reconstructed using the diphoton vertex with that reconstructed with the hardest vertex for events within 50 GeV < Hardest vertex $E_{\mathrm{T}}^{\mathrm{miss}}$ < 100 GeV 111

6.15 $E_{\mathrm{T}}^{\mathrm{miss}}$ distributions for the $ggh125$ MC comparing $E_{\mathrm{T}}^{\mathrm{miss}}$ reconstructed using the diphoton vertex with that reconstructed with the hardest vertex for events with 50 GeV < Hardest vertex $E_{\mathrm{T}}^{\mathrm{miss}}$ < 100 GeV 112

6.16 $E_{\mathrm{T}}^{\mathrm{miss}}$ distributions comparing 2015+2016 data corresponding to 24.8 fb^{-1} and Sherpa $\gamma\gamma$ 113

6.17 $E_{\mathrm{T}}^{\mathrm{miss}}$ distributions comparing 2015+2016 data corresponding to 24.8 fb^{-1} and ggh MC 114

6.18 $E_{\mathrm{T}}^{\mathrm{miss}}$ distributions comparing 2015+2016 data corresponding to 24.8 fb^{-1} and Sherpa $\gamma\gamma$ 115

6.19 $E_{\mathrm{T}}^{\mathrm{miss}}$ resolution distributions showing the x and y components of the $E_{\mathrm{T}}^{\mathrm{miss}}$ as a function of μ, $\mathrm{N_{pv}}$ and $\sum E_{\mathrm{T}}$, 2015+2016 data corresponding to 24.8 fb^{-1} 116

6.20 $E_{\mathrm{T}}^{\mathrm{miss}}$ resolution distributions showing the x and y components of the $E_{\mathrm{T}}^{\mathrm{miss}}$ as a function of μ, $\mathrm{N_{pv}}$ and $\sum E_{\mathrm{T}}$, 2015+2016 data corresponding to 24.8 fb^{-1} 117

6.21 $E_{\mathrm{T}}^{\mathrm{miss}}$ resolution distributions showing the x and y components of the $E_{\mathrm{T}}^{\mathrm{miss}}$ as a function of μ, $\mathrm{N_{pv}}$ and $\sum E_{\mathrm{T}}$, 2017 data corresponding to 43.8 fb^{-1} 118

6.22 $E_{\mathrm{T}}^{\mathrm{miss}}$ resolution distributions showing the x and y components of the $E_{\mathrm{T}}^{\mathrm{miss}}$ as a function of μ, $\mathrm{N_{pv}}$ and $\sum E_{\mathrm{T}}$, 2017 data corresponding to 43.8 fb^{-1} 119

6.23 $E_{\mathrm{T}}^{\mathrm{miss}}$ resolution distributions showing the x and y components of the $E_{\mathrm{T}}^{\mathrm{miss}}$ as a function of μ, $\mathrm{N_{pv}}$ and $\sum E_{\mathrm{T}}$, 2017 data corresponding to 43.8 fb^{-1} 120

6.24 $E_{\mathrm{T}}^{\mathrm{miss}}$ resolution distributions showing the x and y components of the $E_{\mathrm{T}}^{\mathrm{miss}}$ as a function of μ, $\mathrm{N_{pv}}$ and $\sum E_{\mathrm{T}}$, 2017 data corresponding to 43.8 fb^{-1} 121

6.25 μ distributions comparing Sherpa $\gamma\gamma$ MC before and after re-weighting 122

6.26 $E_{\mathrm{T}}^{\mathrm{miss}}$ distributions comparing Sherpa $\gamma\gamma$ MC before and after re-weighting of μ . 123

7.1 Feynman diagrams for the production of DM (χ) in association with a SM Higgs boson (h) 127

7.2 The distribution of $S_{E_{\mathrm{T}}^{\mathrm{miss}}}$, $p_{\mathrm{T}}^{\gamma\gamma}$, and $p_{\mathrm{T}}^{\mathrm{hard}}$ after the selection of diphoton candidates in 120 GeV < $m_{\gamma\gamma}$ < 130 GeV and making the SV selection 132

7.3 An illustration of the double-sided Crystal Ball function and its parameters, for a signal mass $m_{\chi} = 600$ GeV 133

7.4 The diphoton invariant mass distributions for data and corresponding fitted signal and background in all the five categories 143

7.5 The expected and observed 95% CL exclusion upper limits: $m_{\chi} = 50$ GeV 144

7.6 The expected and observed 95% CL exclusion upper limits: $m_{\chi} = 60$ GeV 145

8.1 Schematic diagrams of the production and decay of the scalars in the simplified RSH and AZH models 149

8.2 $S_{E_{\mathrm{T}}^{\mathrm{miss}}}$ distributions for 2015+2016 data for different same vertex cuts 152

8.3 $S_{E_{\mathrm{T}}^{\mathrm{miss}}}$ distributions for the Wh sample for different same vertex cuts 153

8.4 $S_{E_{\mathrm{T}}^{\mathrm{miss}}}$ distributions for the heavy-scalar signal sample for different same vertex . 154

8.5 $S_{E_{\mathrm{T}}^{\mathrm{miss}}}$ distributions for the mono-Higgs signal sample for different same vertex cuts 155

8.6 Fit distributions corresponding to maximum significance 156

8.7 Fit distributions corresponding to maximum significance 159

8.8 Run 2 data $E_{\mathrm{T}}^{\mathrm{miss}}$ fit distributions 160

8.9 Run 2 data $E_{\mathrm{T}}^{\mathrm{miss}}$ fit distributions 161

8.10 Distributions showing significance as a function of $S_{E_{\mathrm{T}}^{\mathrm{miss}}}$ cut comparing Run 1 and Run 2 162

8.11 The distribution of $E_{\mathrm{T}}^{\mathrm{miss}}$, $S_{E_{\mathrm{T}}^{\mathrm{miss}}}$ and $p_{\mathrm{T}}^{\gamma\gamma}$ after the selection of diphoton candidates 164

8.12 The distribution of $E_{\mathrm{T}}^{\mathrm{miss}}$, $S_{E_{\mathrm{T}}^{\mathrm{miss}}}$ and $p_{\mathrm{T}}^{\gamma\gamma}$ after the selection of diphoton candidates 165

8.13 The results of simultaneous fits of DCSB parameters as a function of the invariant mass spectrum in data 166

8.14 Ratio of the fitted spurious signal yield to its uncertainty for the background models of as a function of the resonance mass 168

8.15 The individual fits at $m_X = 248$ GeV for each category 170

8.16 Comparison of local p_0 value scans for category 3 with two cuts on the missing energy significance, where (a) has a cut of 3.5 $\sqrt{\text{GeV}}$ and (b) has a cut of 3.2 $\sqrt{\text{GeV}}$. The largest significance from the background only hypothesis occurs at 248 GeV in the category with 2 central jets (category 3) with a slightly lower $S_{E_{\text{T}}^{\text{miss}}}$ and has a value of around 4.0 σ and a corresponding global significance of 2.8 σ [15]. . . 171

8.17 The fitted resonance mass with largest significance growing with luminosity, with full 2015 and 2016 data 173

8.18 The largest fitted significance growing with luminosity 173

9.1 The excess in the case of R21 for the non-EE, EEOS, EESS and merge categories 178

9.2 The variables used for the suppression of fake $E_{\text{T}}^{\text{miss}}$ in the 2017 pile-up conditions 181

9.3 The excess after the full event selection and merging 183

9.4 Results of individual fit of DCSB parameters 184

9.5 Re-weighting strategy from inclusive (nonEE 2 jet + EE 1 jet) Sherpa $\gamma\gamma$ MC events to signal region total background shape 185

9.6 Ratio of the fitted spurious signal yield to its uncertainty for the background models as a function of the resonance mass 186

9.7 Individual fit at $m_X = 248$ GeV for the merged category with 0 width assumption using 2015+2016 data 187

9.8 Local p_0 value scan as a function of mass for the merged category using 2015+2016 data 188

9.9 Global p_0 value scans as a function of mass for the merged category using 2015+2016 data 189

9.10 The individual fit at $m_X = 248$ GeV for the merged category with 0 width assumption using 2017 data 190

9.11 The local p_0 value scans and the global p_0 value scans 191

9.12 The local p_0 value scans and the global p_0 value scans 192

9.13 The individual fit at $m_X = 248$ GeV for the merged $ee + \mu\mu$ category using 2015+2016+2017 data 193

9.14 The local p_0 value scans as a function of mass for the various years of data taking (2015+2016+2017) for the $Z\gamma + E_{\mathrm{T}}^{\mathrm{miss}}$ analysis 193

A.1 Diagram of the internal components of the Varian Cary 500 spectrophotometer . . 200

B.1 The comparison of the photon pointing same vertex fraction of $E_{\mathrm{T}}^{\mathrm{miss}}$ between data and MC in the $Z \to e^+e^-$ control region 202

B.2 $E_{\mathrm{T}}^{\mathrm{miss}}$ and $E_{\mathrm{T}}^{\mathrm{miss}}$ significance distributions for 2017 data corresponding to 43.8 fb^{-1} versus Sherpa $\gamma\gamma$ 203

C.1 The results of a single fit of a DSCB function for a signal with m_h = 125 GeV . . 206

C.2 The spurious signal results of the direct fit method 207

D.1 $E_{\mathrm{T}}^{\mathrm{miss}}$ distributions for 2015+2016 data for different same vertex cuts 215

D.2 $E_{\mathrm{T}}^{\mathrm{miss}}$ distributions for the Wh sample for different same vertex cuts 216

D.3 $E_{\mathrm{T}}^{\mathrm{miss}}$ distributions for the heavy-scalar signal sample for different same vertex cuts 217

D.4 $E_{\mathrm{T}}^{\mathrm{miss}}$ distributions for the mono-Higgs signal sample for different same vertex cuts 218

D.5 Run 1 data $E_{\mathrm{T}}^{\mathrm{miss}}$ fit distributions for $S_{E_{\mathrm{T}}^{\mathrm{miss}}}$ 219

D.6 Run 1 data $E_{\mathrm{T}}^{\mathrm{miss}}$ fit distributions for $S_{E_{\mathrm{T}}^{\mathrm{miss}}}$ 220

D.7 Local p_0 value scans as a function of mass 221

D.8 Local p_0 value scans as a function of mass 222

D.9 The largest fitted significance 223

D.10 The excess in the case of R20 224

LIST OF TABLES

TABLE **Page**

1.1 A List of experimental results used to constrain the relevant parameters of the Madala hypothesis 18

1.2 A list of possible decay modes of the 2HDM scalars and S 23

1.3 A summary of the SM+BSM fit results 25

3.1 Table showing a log of the radiation dates, beam currents, beam times and radiation doses 59

3.2 Table showing the % transmission loss for all samples at a wavelength of 420 nm, considering all the different doses 63

3.3 Table showing the % transmission difference for different days over two doses . . 66

4.1 The discriminating variables used for loose and tight photon identification 75

5.1 MC samples for the different Higgs production modes used to study the signal shapes 85

5.2 Prompt diphoton background MC samples 85

5.3 Table showing the nominal diphoton selection cuts and their functions 88

6.1 Expected yields for the $ggh125$ MC in events with $E_{\mathrm{T}}^{\mathrm{miss}}$ calculated using the diphoton vertex and that calculated using the hardest vertex, respectively 108

7.1 A summary of all the background processes used in this $h(\rightarrow \gamma\gamma) + E_{\mathrm{T}}^{\mathrm{miss}}$ analysis 128

7.2 A summary of the set categories defined in a sequential manner 130

7.3 The event yields in the $m_{\gamma\gamma}$ window 122 GeV to 128 GeV 133

7.4 The analytic functions used to model the non-resonant $m_{\gamma\gamma}$ distribution, the uncertainty in the signal due to the non-resonant background modelling ($\Delta N_{bkg}^{non-res}$) and the relative uncertainties in the expected non-resonant background and signal for each category 135
7.5 A breakdown of the dominant systematic uncertainties in the range of 105 GeV < $m_{\gamma\gamma}$ < 160 GeV 137
7.6 Event yields for data, signal models, the SM Higgs boson background and non-Higgs boson backgrounds corresponding to 36.1 fb^{-1} 144
7.7 The 95% CL observed and expected limits: m_χ = 50 GeV 145
7.8 The 95% CL observed and expected limits: m_χ = 60 GeV 146

8.1 A list of the signal samples used for $H \to \gamma\gamma$ using the RSH and AZH models . 150
8.2 Significance and yield results for Run 1 data corresponding to 20.7 fb^{-1} 157
8.3 Significance and yield results for Run 2 data corresponding to 36.1 fb^{-1} 158
8.4 A summary of the set categories 162
8.5 The cutflow for data and MC including the statistical uncertainties 162
8.6 A summary of the parameterization of the fitted parameters from the simultaneous fit 167
8.7 Fitted spurious signal yield to its uncertainty, spurious signal yield and fit properties of tested function 167

9.1 The signal yields and the significance in different categories in R20.7 177
9.2 The signal yields and the significance in different categories in R21.2 177
9.3 The complete event selection including the fake $E_{\mathrm{T}}^{\mathrm{miss}}$ suppression variables . . . 180
9.4 The signal yields and the significance in different categories in different versions 182
9.5 Fitted spurious signal yield to its uncertainty, spurious signal yield and fit properties of tested functions 186

C.1 The experimental systematic terms derived from the MxAOD 208
C.2 The experimental systematic terms derived from the MxAOD 209
C.3 The experimental systematic terms derived from the MxAOD 210
C.4 The experimental systematic terms derived from the MxAOD 211

C.5 The experimental systematic terms derived from the MxAOD 212

D.1 Run 2 data significance and yield results for the scans of $S_{E_{\mathrm{T}}^{\mathrm{miss}}}$ 214

NOMENCLATURE

Abbreviations

2HDM Two-Higgs-Doublet Model

ALICE A Large Ion Collider experiment

ATLAS A Toroidal LHC Apparatus

bbh Higgs production through fusion of b quarks

BEH The Brout-Englert-Higgs mechanism

BSM Beyond the Standard Model

CERN European Organization for Nuclear Research

CMS Compact Muon Solenoid

CP Combined performance

CSC Cathode Strip Chambers

DM Dark Matter

DV Different Vertex

ECAL Electromagnetic Calorimeter

EF Event Filter

EM Electromagnetic

EW Electroweak

FullSim Full Simulation

GeV Giga Electronvolt

ggh Higgs production via gluon gluon fusion

ggF Higgs production via gluon gluon fusion

HCAL Hadronic Calorimeter

HEP High Energy Physics

HLT High-Level Trigger system

HV High Voltage

IBL Insertable B-layer

ID Inner detector

IP Interaction Point

IPEM Institute of Physics and Engineering in Medicine

ITER International Thermonuclear Experimental Reactor

LAr Liquid Argon

LEP Large Electron-Positron collider

LHC Large Hadron Collider

LO Leading Order

MBTS Minimum Bias Trigger Scintillators

MC Monte Carlo

MDT Monitored Drift Tubes

MET Missing Transverse Energy

MeV Mega Electron volt

MS Muon spectrometer

NLO Next-to-leading Order

NNLO Next-to-next-to-leading Order

N_{pv} Number of Primary Vertices

PDF Parton Distribution Function

PID Photon Identification

PIX Silicon Pixel detector

PMT Photo Multiplier Tube

pp Proton-proton

PS Proton Synchrotron

PV Primary vertex

QCD Quantum Chromodynamics

QED Quantum Electrodynamics

R20 Release 20

R21 Release 21

RMS Root-Mean-Square

ROD Read Out Driver

SCT Semiconductor Tracker

SM Standard Model

SPS Super Proton Synchrotron

SRIM Stopping and Range of Ions in Matter

SSB Spontaneous Symmetry Breaking

SV Same Vertex

m_h Higgs boson mass

m_H Heavy Scalar or Madala boson mass

TeV Tera Electronvolt

TRT Transition Radiation Tracker

tth Higgs production via top quark fusion

UV Ultraviolet

VBF Higgs production via vector boson fusion

Vh Higgs production via Wh or Zh

vev Vacuum expectation value

Wh Higgs production via W boson associated production

Wits University of the Witwatersrand

Zh Higgs production via Z boson associated production

Symbols

η Pseudorapidity

$\mathscr{L}$ Instantaneous Luminosity

σ Significance or cross-section

$\sqrt{s}$ Centre-of-mass energy

b Botton quark

c Charm quark

d Down quark

g Gluon

h Standard Model higgs Boson

H Heavy Scalar particle or Madala boson

q Quark

s Strange quark

S Inert Scalar

t Top quark

u Up quark

$W^{\pm}$ W bosons

Z Z boson

fb^{-1} Inverse femtobarns

χ Dark matter particle

$< \mu >$ Average interactions per bunch spacing

CHAPTER 1

INTRODUCTION AND THEORETICAL BACKGROUND

"Look up at the stars and not down at your feet. Try to make sense of what you see, and wonder about what makes the universe exist. Be curious" - Stephen Hawking

1.1 Introduction

Throughout history, scientists and philosophers have speculated about the origin of the universe. Any step closer to figuring out how the universe began is a step closer to us understanding ourselves better. Exploration has allowed us to discover new continents, find cures for diseases, advance in technology and means of communication and more. Correspondingly, exploring the origin of the universe equips us with the knowledge needed to better predict our future thus allowing us to shape our civilization. All in all, a better comprehension of our universe is part and parcel of human evolution. Our interest to address fundamental questions about the origin of the world has led us to build better technology to address the issue, technology that we have the privilege of utilizing today.

Human curiosity inspired high energy particle physics as a broad field of fundamental research dedicated to decipher the fundamental constituents of matter. The scrutiny of these constituents of matter is made possible through the development of powerful particle accel-

erators which have led to the discovery of new fundamental particles. In the 20^{th} century, a theoretical model called the Standard Model (SM) of particle physics was developed to understand these elementary particles and how they interact. The formulation of this elegant theory was based on a century's worth of gathered theoretical and experimental results. The discovery of the Higgs boson in 2012 triggered a rush of excitement throughout the high energy physics community as it constitutes a predominant part of this theory. The Higgs boson was the last missing piece of the SM and plays a crucial role as it couples to elementary particles and gives them mass.

In spite of its elegance and success, the SM has imperfections thus making it an incomplete theory. Some of the theory's shortcomings include the fact that it does not certain the description of gravity nor explain dark matter and dark energy. In addition, according to the SM, neutrinos are massless and matter-antimatter asymmetry cannot be explained. These limitations and others have emanated the existence of physics beyond the Standard Model (BSM), a new realm of physics which is an integral part of this documentation.

The remainder of the chapter is organized as follows: Section 1.2 gives a basic introduction to the SM of particle physics and the fundamental forces in the Universe. Section 1.3 describes the Higgs boson and its the role in the Standard Model. Section 1.4 describes the formulation of the Madala hypothesis used in the present search for dark matter particles.

1.2 Standard Model of particle physics

The Standard Model [25–28] is a successfully tested theory which provides a fundamental comprehension of the known phenomenology of particle physics. This physics model describes three of the four forces of nature: weak, strong and electromagnetic forces. It is the SM of particle physics which is at the helm of classifying the elementary particles of nature using a mathematical formalism referred to as quantum field theory [29, 30]. The interactions of such systems are governed by the SM Lagrangian which is invariant under space-time dependent continuous transformations of the gauge group $SU(3) \times SU(2) \times U(1)$. The SM Lagrangian and its constituents are shown in Equations 1.1-1.5 below.

$$\mathscr{L}_{\mathrm{SM}} = \mathscr{L}_{\mathrm{G}} + \mathscr{L}_{\mathrm{F}} + \mathscr{L}_{\mathrm{Y}} + \mathscr{L}_{\mathrm{H}}, \tag{1.1}$$

where the different components of this Lagrangian are defined as,

$$\mathscr{L}_{\mathrm{G}} = -\frac{1}{4} F_{\mu\nu} F^{\mu\nu} \tag{1.2}$$

$$\mathscr{L}_{\mathrm{F}} = i\bar{\psi}\not{D}\psi + h.c. \tag{1.3}$$

$$\mathscr{L}_{\mathrm{Y}} = \bar{\psi}_i y_i \psi_j \phi + h.c. \tag{1.4}$$

$$\mathscr{L}_{\mathrm{H}} = -|D_\mu \phi|^2 - V(\phi), \tag{1.5}$$

where $\mathscr{L}_{\mathrm{G}}$ represents couplings to gauge bosons, $\mathscr{L}_{\mathrm{F}}$ represents couplings to fermions, $\mathscr{L}_{\mathrm{Y}}$ represents Yukawa couplings and $\mathscr{L}_{\mathrm{H}}$ represents couplings to the Higgs boson. These terms also include the kinetic terms of various fields.

1.2.1 The elementary particles

All fundamental particles in nature are divided into two types: fermions and bosons [31]. Fermions possess half-integer spin whilst bosons possess integer spin. The SM comprises twelve spin $\frac{1}{2}$ fermions and their anti-particles which are classified according to how they interact. The spin 1 gauge bosons of the SM are defined as force carriers that mediate the strong, weak, and electromagnetic interactions. Figure 1.1 summarizes the SM particles.

Among the fermions are six quarks (up, down, charm, strange, top and bottom) and six leptons (electron, muon, tau, electron neutrino, muon neutrino and tau neutrino). Pairs from each class of fermions are grouped together to form the generations of matter which correspond to particles which exhibit similar physical behaviour except their mass. Among the bosons are gluons, photons, $W^{\pm}$ and Z bosons, as well as the Higgs boson. Gluons are massless and mediate the strong force between quarks, as well as interact with other gluons. Photons mediate the electromagnetic force and therefore couple with charged particles. $W^{\pm}$ and Z gauge bosons are massive and mediate the weak force between particles of different flavours. The photons, $W^{\pm}$ and Z gauge bosons collectively mediate the electroweak interaction which is

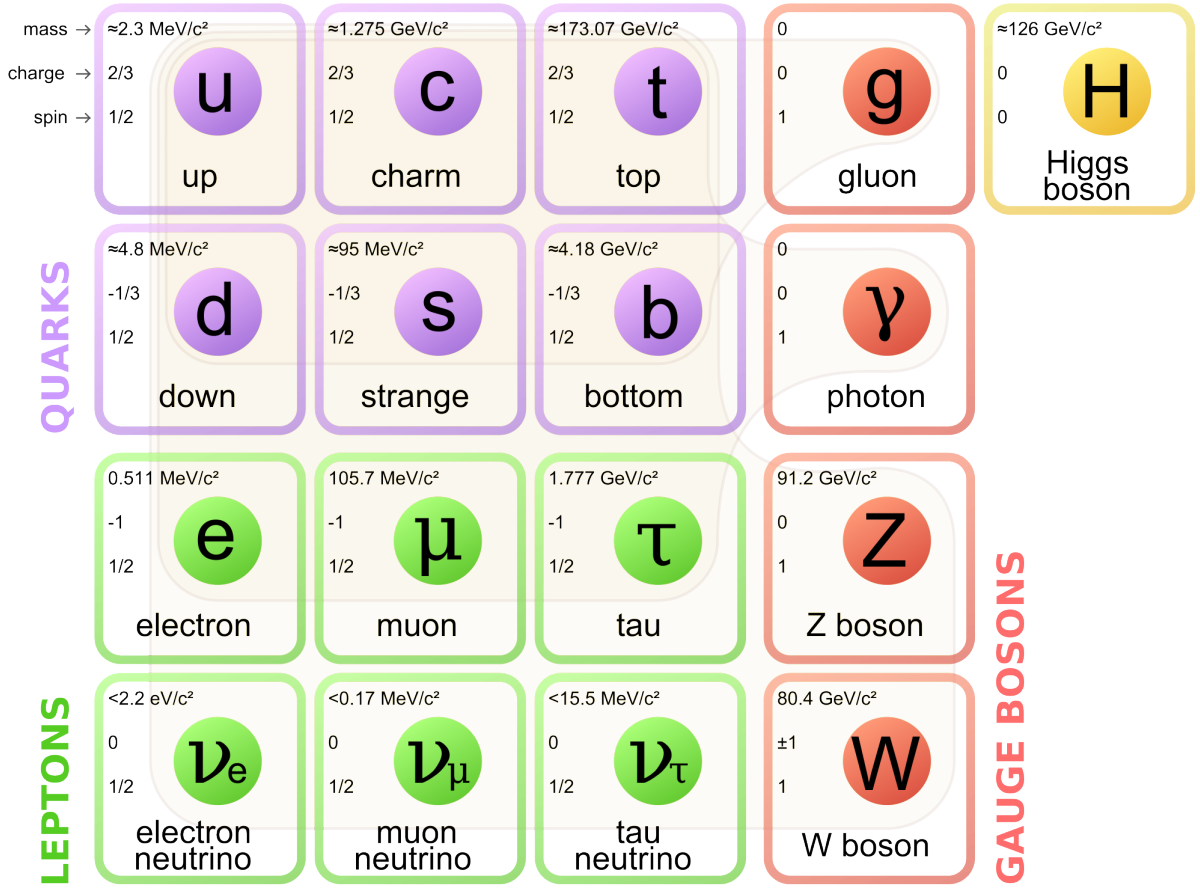


Figure 1.1: Schematic diagram of the Standard Model particles: The three generations of matter/fermions, gauge bosons and the Higgs boson.

a unification of the electromagnetic and weak forces of nature. Finally, the Higgs boson is a massive scalar spin 0 particle which explains why elementary particles acquire a mass through a dynamical process called the Higgs mechanism, allowing the electroweak theory to have a finite length of influence because the W, Z bosons have a mass. The Higgs boson model is discussed extensively in Section 1.3.

1.2.2 Quantum Chromodynamics

In the sixties, inelastic electron-proton scattering results showed that protons were made up of quarks and gluons [32]. Quantum chromodynamics (QCD) is the theory of the strong force which describes the interactions between these quarks and gluons. While this section describes

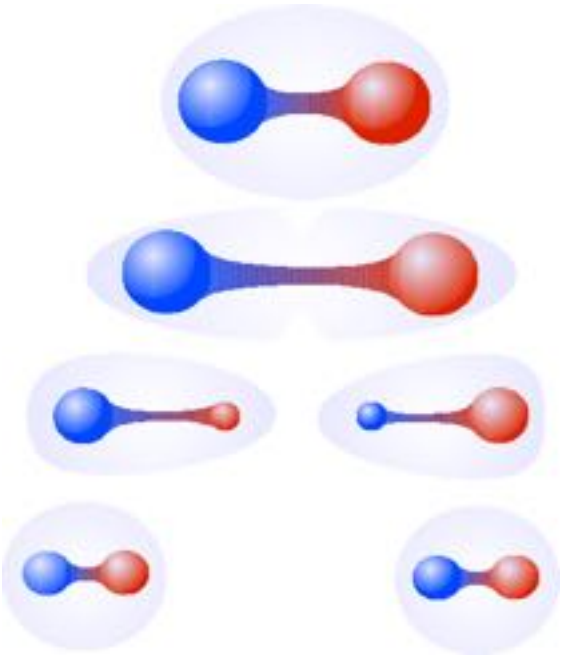


Figure 1.2: A simple illustration of quark color confinement.

the main attributes of QCD, [33] encompasses a more detailed description of the theory. The strong force can be formulated using the gauge group $SU(3)_C$, where C corresponds to color charge. The force carriers in this theory are the gluons which transmit the strong force between particles that carry color, namely quarks and other gluons. According to Reference [34], quarks occur in three different colors: red, green and blue.

Color charged particles cannot be isolated and therefore cannot be directly detected. This can be explained by one of the renowned properties of QCD known as confinement which occurs at low energies. According to the confinement phenomenon, the force between a quark pair does not diminish as they are separated. Instead, the strong force between the quark pair acts constantly whilst the potential energy grows linearly. As a result of this, the separation leads to the energy in the gluon field becoming large enough to create another quark pair and the quarks begin to form bound states called hadrons. Figure 1.2 shows a simple illustration of the quark confinement phenomenon. Hadrons have no color charge associated with them and can therefore be mesons or baryons. Mesons are comprised of one quark and one anti-quark, with a possible color configuration of red,anti-red. Baryons comprise three quarks, with a color configuration of red, green, blue. Another fundamental property of QCD is known as

asymptotic freedom which comes to play at high energies. In this regime, quarks and gluons interact very weakly, creating a quark-gluon plasma. Basically as the distance between quarks decreases, the strong force weakens until it reaches asymptotic freedom such that the particles no longer interact via the strong force.

1.2.3 ElectroWeak Theory

The electroweak theory is a unified description of the electromagnetic and weak forces of nature. The electroweak interaction can be formulated as a quantum field theory whose Lagrangian is symmetric under the $SU(2)_L \times U(1)_Y$ gauge group, where L denotes the left-handed fields and Y denotes the hypercharge. β-decay studies revealed that only left-handed fermions take part in charged current weak interaction [35]. The hypercharge is introduced in order to combine the weak and electromagnetic forces and is given by

$$Y = 2(Q - T_3) \tag{1.6}$$

where Q is the electric charge and T_3 is the third component of weak isospin of the particle. Introducing the massive mediators destroys on a general basis gauge invariance. The gauge symmetry then basically forbids the inclusion of a mass term for the gauge bosons such that the $SU(2)_L \times U(1)_Y$ Lagrangian equations only contain massless fields. Therefore, electroweak symmetry must be broken to allow for the incorporation of the massive gauge bosons ($W\pm, Z$) together with the massless photon into the SM Lagrangian.

1.2.3.1 The BEH mechanism and Spontaneous symmetry breaking

The Brout-Englert-Higgs (BEH) mechanism provides the means by which the fermions and gauge bosons acquire mass in the process of spontaneous symmetry breaking (SSB) [36–40]. SSB describes systems where the Lagrangian obeys certain symmetries, but the corresponding lowest-energy vacuum solutions manifest a restricted group of symmetries. In other words, under BEH mechanism a solution of a problem does not necessarily have the same symmetry as the problem. Figure 1.3 shows the “Mexican hat" potential which illustrates that phenomenon. One can consider a scalar field, ϕ, in a simple potential V whereby the Lagrangian is given by

$$\mathscr{L} = \frac{1}{2}\partial_\mu\phi\partial^\mu\phi - V(\phi) \tag{1.7}$$

where the potential is given by

$$V(\phi) = \frac{1}{2}\mu^2\phi^2 + \frac{1}{4}\lambda\phi^4. \tag{1.8}$$

In the case where the mass term is chosen to be positive ($\mu^2 > 0$), the minimum of the potential will be at 0. On the other hand, if the mass term is chosen to be negative ($\mu^2 < 0$), then the minimum is no longer 0, but instead lies within a circle of radius $v = \sqrt{-\mu^2/\lambda}$. One can conclude that the symmetry has been broken spontaneously as encapsulated in Figure 1.3, where the field develops a non-zero value referred to as the vacuum expectation value (vev). This vev couples with fermion (with the addition of extra Yukawa terms) and gauge fields in such a way that mass terms are incorporated while maintaining gauge invariance. This allows fermions and gauge bosons to appear massive, consistent with experimental observation.

In many body systems SSB is a common occurrence, but within the SM an intriguing consequence of SSB is the prediction of a massive scalar particle known as the Higgs boson. A neutral massive spin-0 particle which is given mass by the generated vev and is discussed in detail in Section 1.3.

1.3 The Higgs Boson

The SM predicts the existence of the Higgs boson as shown in Section 1.2.1 which has a mass denoted m_h. In order for the Higgs mechanism to explain the non-zero masses of the $W^\pm$ and Z bosons, m_h must also be non-zero. The Higgs mass is a free parameter in the SM and the preferred production and decay modes of the Higgs boson are strongly dependent on it as seen in Figures 1.5 and 1.7, respectively. The mass of the Higgs boson itself is given by:

$$m_h = \sqrt{2\lambda v^2}, \tag{1.9}$$

where λ is a free parameter, hence why one cannot predict the mass of the Higgs boson mass in the SM, it can only be measured through observation.

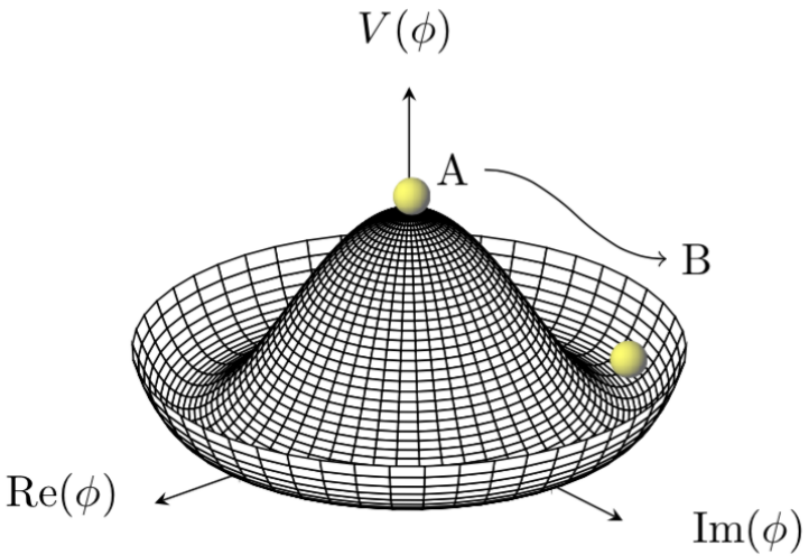
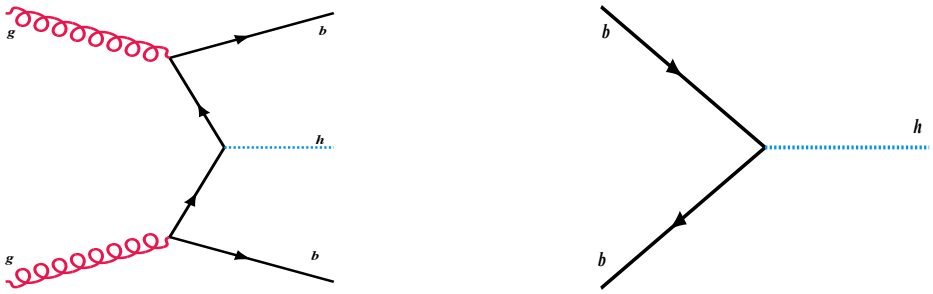


Figure 1.3: Graph of Goldstone's "Mexican hat" potential function V versus ϕ.

The BEH in the SM includes an extension of the simple model discussed with spinor complex scalar fields that give the $m = 0$ state of the massive $W^{\pm}$ and Z bosons. Three fields are absorbed by the massive bosons as degrees of freedom and the remaining state in scalar field is the Higgs boson.

1.3.1 Production mechanisms

The Higgs mechanism is characterized by the generation of masses for the $W^{\pm}$ and Z weak gauge bosons through electroweak symmetry breaking [41]. The BEH mechanism discussed in Section 1.2.3.1 allows fermions and the massive gauge bosons to aqcuire mass by interacting with the Higgs field which permeates all space. At the Large Hadron Collider (LHC) at CERN, Higgs boson production is possible through five main production processes, namely, gluon-gluon fusion (ggF), vector boson fusion (VBF), associated Vh production or Higgs Strahlung (Wh and ZH), Top fusion ($t\bar{t}h$ and th) and bb fusion (bbh). [42]. The figures to follow show the leading order (LO) Feynman diagrams representing the different Higgs production mechanisms. The cross sections for the different production processes as a function of the



(a) (b)

Figure 1.4:

Higgs boson mass are shown in Figure 1.7.

The most dominant production process at $\sqrt{s} = 13$ TeV is the gluon-gluon fusion (ggF) process in which two gluons fuse and produce a Higgs boson via a loop of virtual heavy quarks (top and bottom quarks), shown in Figure 1.6a. Another common process is the vector boson fusion (VBF) process which is initiated by two quarks or two anti-quarks colliding and exchanging a virtual W or Z boson which emits a Higgs boson as demonstrated in Figure 1.6b. Figure 1.6c shows the case whereby a Higgs boson is emitted by a W boson through a process referred to as Higgs strahlung (Vh). In this process a quark and anti-quark collide resulting in a W or Z boson which can emit a Higgs boson if it carries a sufficient amount of energy. The least common process is the top fusion ($t\bar{t}h$ and th) process in which a Higgs boson is produced in association with a heavy quark and anti-quark pair and $t\bar{t}h$ production is shown in Figure 1.6d.

In $b\bar{b}h$ production, a Higgs boson is produced in association with b-quarks as shown in Figure 1.4. This $b\bar{b}h$ mechanism is suppressed by the size of the Yukawa coupling, however, in a supersymmetric conjecture, the b-quark Yukawa coupling can be enhanced, which can result in this mechanism being the most dominant one.

The contributions from NLO in QCD corrections were calculated in the References [43–54] and the next-to-next-to-Leading order (NNLO) corrections were calculated in the references [55–60].

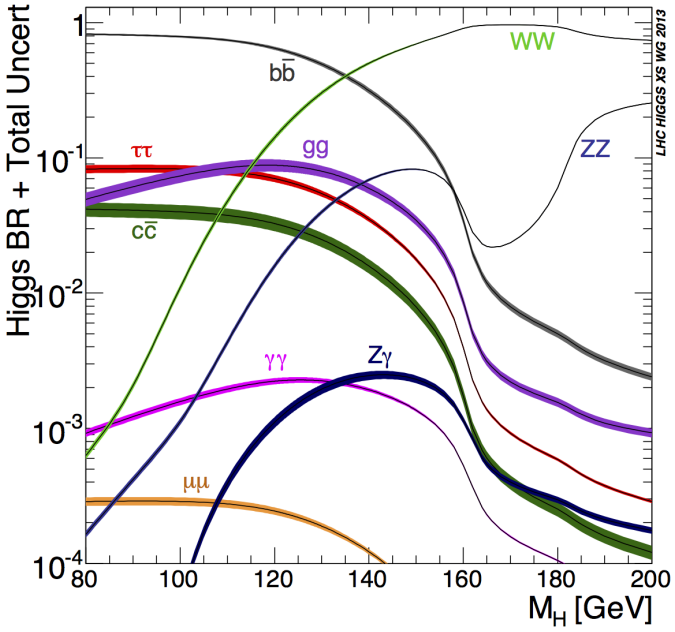


Figure 1.5: Higgs boson branching ratios and their uncertainties for the mass range around 125 GeV [61].

1.3.2 Decay mechanisms

The Higgs boson decays into lighter particles and does so through many processes, each with its own probability expressed as a branching ratio. Figure 1.5 shows the branching ratios as a function of m_h for the various Higgs decay modes.

For the lower mass Higgs boson, the most dominant decay mode is the $b\bar{b}$ due to the heavy mass of the b-quark and occurs approximately 56.1% of the time [62] at $m_h = 125\,\text{GeV}$. Another low mass decay mode is the $\tau\bar{\tau}$ pair which occurs approximately 6% of the time. The Higgs boson can also decay into massless gauge bosons via a loop of virtual heavy quarks, that is, the gg and $\gamma\gamma$ decay modes which happen about 8.5% of the time. The $\gamma\gamma$ decay mode is very rare and is mediated by a loop of W bosons or heavy quarks with a branching ratio of 0.2% at $m_h = 125\,\text{GeV}$. In the case of the higher mass Higgs bosons, the WW and ZZ decay modes are dominant and WW decays occur 23.1% of the time at $m_h = 115\,\text{GeV}$ whilst ZZ decays occur 2.9% of the time at $m_h = 125\,\text{GeV}$. However, the $\gamma\gamma$ decay is very useful because the energy and momentum of the photons can be measured very precisely thus giving accurate reconstruction of the invariant mass of the decaying products, allowing to fight against the large

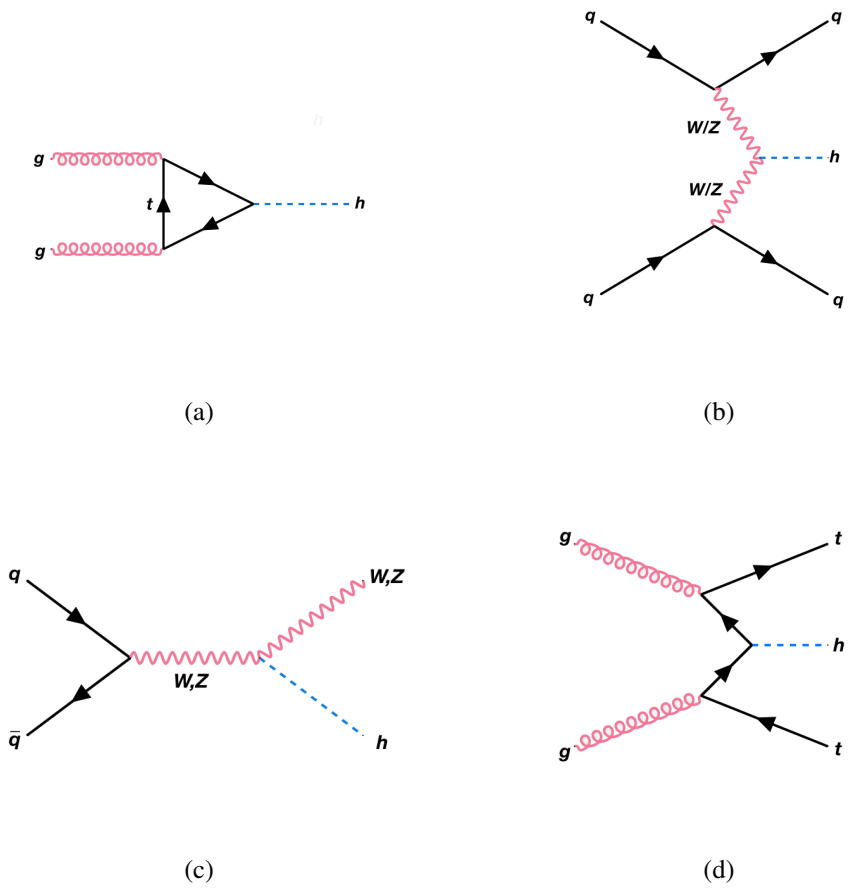


Figure 1.6: Feynman diagrams for the dominant Higgs production mechanisms at the LHC: (a) Gluon-gluon fusion, (b) vector boson fusion, (c) Higgs strahlung, (d) top associated production.

QCD background. This document focuses on searching for the Higgs Boson in the $\gamma\gamma$ decay mode.

1.3.3 History and discovery

At CERN, searches for the last missing piece of the SM began around the 80's. The expedition was facilitated by the Large Electron-Positron (LEP) collider, the largest electron-positron collider ever built, covering a 27 km circumference. The collisions produced by the LEP were explored by 4 large detectors (ALEPH, DELPHI, L3 and OPAL). The LEP operated at 100 GeV for several years and this energy doubled after modifications and upgrades, producing double the amount of particles. Unfortunately, the Higgs boson was not observed during this

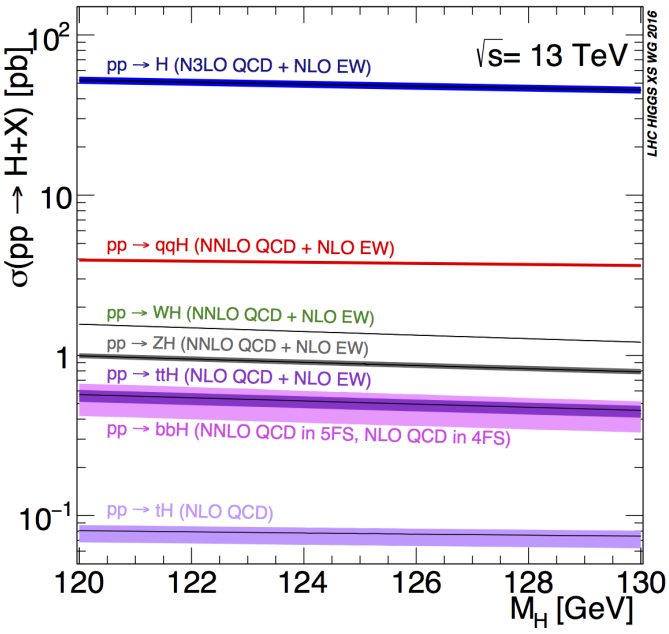
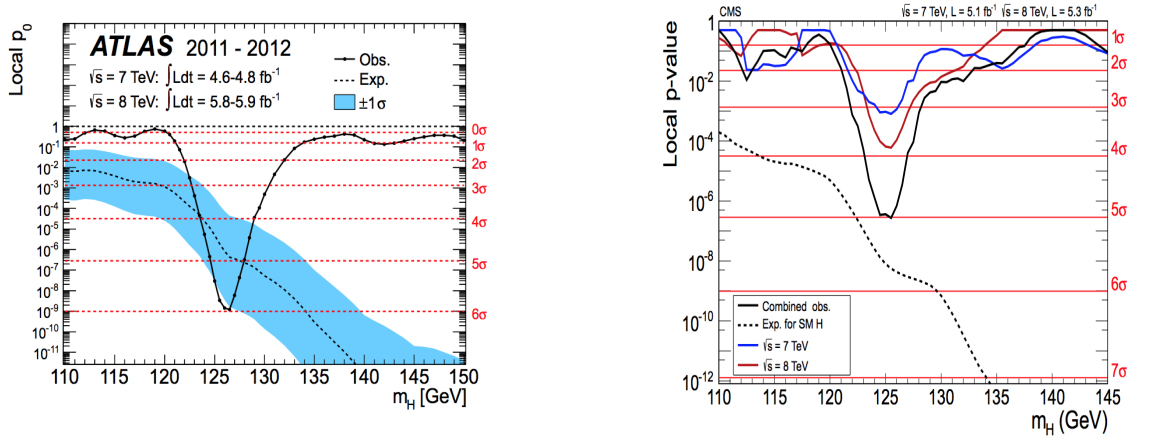


Figure 1.7: Higgs boson production cross sections [61].

era, on the bright side, detailed studies of the electroweak interactions were made possible by this experiment before it ended at the dawn of the 3^{rd} millennium.

Following shut down, the LEP was replaced by the Large Hadron Collider (LHC) whose infrastructure is explored in detail in Section 2.1. The LHC began operation in 2008 and enticing hints of the Higgs boson were observed in 2011. At the time, the consensus was that if the Higgs does in fact exist, its mass must be constrained within the range 116-130 GeV (ATLAS) and 115-127 GeV (CMS). Regrettably, these hints were not strong enough to claim a discovery. The search continued at Fermilab in the United States, where the Tevatron (the collider that discovered the top quark), had been upgraded for this purpose. The Tevatron was only able to exclude further ranges for the Higgs mass, and the final analysis of the data excluded the possibility of a Higgs boson with a mass between 147-180 GeV. In addition, there was a small excess of events possibly indicating a Higgs boson with a mass between 115-140 GeV [63].

In 2012, the observation of a Higgs boson with a mass of approximately 125 GeV was disclosed by both the ATLAS and CMS collaborations [64, 65]. This was one of the greatest achievements of the LHC program at the European Organization for Nuclear Research (CERN)



(a) (b)

Figure 1.8: The observed local p_0 distribution as a function of m_h for (a) ATLAS and (b) CMS for 7 TeV and 8 TeV data [64, 65].

and denotes a historic moment. The Higgs boson particle was discovered through the detection of its decay products with both the ATLAS and CMS experiments operating at $\sqrt{s} = 7$ TeV and $\sqrt{s} = 8$ TeV in 2011 and 2012 respectively. The observed local p_0 values obtained from the combination of the channels $h \to ZZ$, $h \to \gamma\gamma$ and $h \to WW$ are shown as a function of m_h in Figure 1.8 for ATLAS and CMS, respectively. Both experiments measured a significance of $\geq 5\,\sigma$, a clear-cut discovery marking a momentous time in particle physics.

The discovery of the Higgs boson marked the beginning of exploration for particle physicists worldwide. At disposal was the opportunity to better comprehend the properties of this Higgs boson particle through theory and experimentation. With the discovery of the Higgs boson the SM is now complete, yet unanswered questions still prevail. The SM cannot account for the nature and origin of dark matter, nor does it address the hierarchy problem between the electroweak and Planck scales. Solving the issues at hand would entail the introduction of new models, which allow us to probe new realms of physics that today constitute what is known as Beyond the Standard Model (BSM) physics.

Table 1.1: A List of experimental results used to constrain the relevant parameters of the Madala hypothesis [66].

Results	**Publication**	
Differential Higgs boson p_T spectra	ATLAS	Fiducial cross section measurements on $h \to \gamma\gamma$ [68] and $h \to ZZ^* \to 4l$ [69]
	CMS	Fiducial cross section measurements on $h \to \gamma\gamma$ [70] and $h \to ZZ^* \to 4l$ [71]
Di-Higgs boson resonance searches	ATLAS	Limits on $H \to hh \to b\bar{b}\tau\tau$, $\gamma\gamma WW^*$, $\gamma\gamma b\bar{b}$ and $b\bar{b}b\bar{b}$ [72]
	CMS	Limits on $H \to hh \to \gamma\gamma b\bar{b}$ [73], $b\bar{b}\tau\tau$ [74] and multi-lepton [75]
Top associated Higgs boson production	ATLAS	Limits on $h \to \gamma\gamma$ [76], Measurements on multi-lepton decay channels [77] and $h \to b\bar{b}$ [78]
	CMS	Limits on $h \to \gamma\gamma$ and $h \to b\bar{b}$ [79]
$H \to VV$ decays	ATLAS	Limits on $H \to WW$ [80] and $H \to ZZ$ [81]
	CMS	Limits on $H \to WW$ and $H \to ZZ$[82]

1.4 The Madala Hypothesis

In an effort to unravel the possible connection among a number of anomalies in the data, the Wits Institute for Collider Particle Physics together with colleagues from India developed the Madala hypothesis. As forerunners of this hypothesis, the institute took the initiative to name the model "Madala" which means "old one" in the South African Zulu language. In South African culture the term "Madala" is used as a form of respectful address towards elderly men, a naming convention considered fitting for the hypothesized heavy scalar particle, H, the Madala boson.

The Madala hypothesis is described in detail in the references [66, 67] and was formulated based on inconsistencies in Run 1 data measured by ATLAS and CMS. Table 1.1 highlights measurements made by ATLAS and CMS which were considered in the design of the Madala hypothesis. Results from the Higgs boson $p_{T,h}$ spectra, di-Higgs boson searches, top associated Higgs production and VV decays were used to assist in constraining the relevant parameters of the hypothesis.

Run I data reflected an excess in the Higgs boson $p_{T,h}$ spectrum which reflected an inconsistency with the SM prediction, encouraging speculation of BSM physics. In other words,

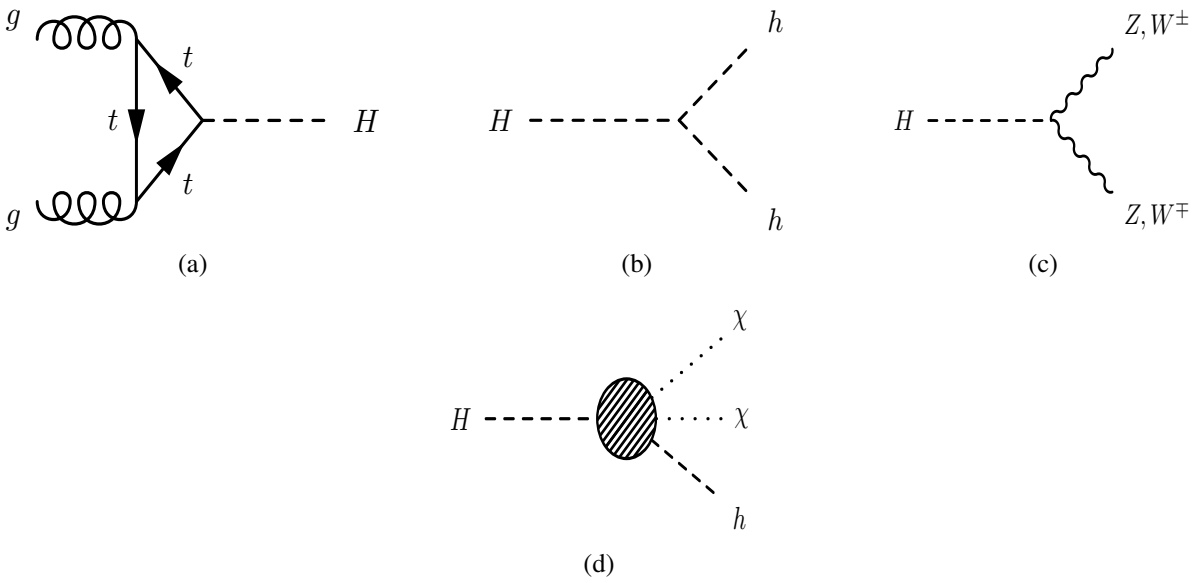


Figure 1.9: The Feynman diagrams for the production (a) and decay (b,c,d) of the hypothetical heavy scalar.

the distortion of the Higgs boson $p_{T,h}$ spectrum can be seen as a possible indication of Higgs production in association with missing energy thus inferring new physics. In fact, the Madala model describes the excess in the $p_{T,h}$ spectrum quite well, as observed later in this section, the Higgs $p_{T,h}$ continues to be distorted [83] and the rate of the Higgs boson continues to be elevated [84]. It is worth mentioning that the Higgs boson $p_{T,h}$ on its own can never be a smoking gun, it was merely an indication that something at the EW scale may be at hand.

In an attempt to describe the Higgs $p_{T,h}$ spectrum, a heavy scalar H which can decay to at least one Higgs boson is initially introduced. That is, $H \rightarrow hh, h\chi\chi$, where χ is a dark matter (DM) candidate. The production and decay modes of H are shown schematically in Figure 1.9.

In order to explain the excesses in data, a BSM extension to the SM is required:

$$\mathscr{L} = \mathscr{L}_{\mathrm{SM}} + \mathscr{L}_{\mathrm{BSM}}, \tag{1.10}$$

where all new interactions and states are encompassed in $\mathscr{L}_{\mathrm{BSM}}$ which constitutes:

$$\mathscr{L}_{\mathrm{BSM}} = \mathscr{L}_{\mathrm{H}} + \mathscr{L}_{\mathrm{Y}} + \mathscr{L}_{\mathrm{T}} + \mathscr{L}_{\mathrm{Q}}. \tag{1.11}$$

The different sectors of this Lagrangian are defined as:

$$\mathscr{L}_H = -\frac{1}{4}\,\beta_g \kappa^{\mathrm{SM}}_{hgg}\, G_{\mu\nu}G^{\mu\nu}H + \beta_V \kappa^{\mathrm{SM}}_{hVV}\, V_\mu V^\mu H, \tag{1.12}$$

$$\mathscr{L}_{\mathrm{Y}} = -\frac{1}{\sqrt{2}}\,\Big[y_{ttH}\bar{t}tH + y_{bbH}\bar{b}bH\Big], \tag{1.13}$$

$$\mathscr{L}_{\mathrm{T}} = -\frac{1}{2}\,v\Big[\lambda_{Hhh}Hhh + \lambda_{h\chi\chi}h\chi\chi + \lambda_{H\chi\chi}H\chi\chi\Big], \tag{1.14}$$

$$\begin{aligned}\mathscr{L}_{\mathrm{Q}} = &-\frac{1}{2}\lambda_{Hh\chi\chi}Hh\chi\chi - \frac{1}{4}\lambda_{HHhh}HHhh \\ &-\frac{1}{4}\lambda_{hh\chi\chi}hh\chi\chi - \frac{1}{4}\lambda_{HH\chi\chi}HH\chi\chi,\end{aligned} \tag{1.15}$$

where the terms $\mathscr{L}_{\mathrm{Y}}$, $\mathscr{L}_{\mathrm{T}}$ and $\mathscr{L}_{\mathrm{Q}}$ are the Yukawa, trilinear, and quartic interactions pertinent to this formulation, respectively. H, χ and v denote the heavy scalar, dark matter candidate and vacuum expectation value ($v = vev = 246$ GeV), respectively.

The effective coupling of gluons to H is represented by the first term in Equation 1.12, where $\kappa^{\mathrm{SM}}_{hgg}$ is the SM coupling and is defined as $\alpha_s/(3\pi v)$. The parameter β_g is dimensionless and controls the rate at which H is produced via ggF. The product $\beta_g\kappa^{\mathrm{SM}}_{hgg}$ is regarded as the effective coupling strength of gluons to H. Similarly, in the second term of Equation 1.12, $\kappa^{\mathrm{SM}}_{hVV} = m_V^2/v$ represents the coupling of H to weak vector bosons and β_v is there to control the branching ratio of $H \to VV$.

The Yukawa couplings between H and the heaviest quarks are given in Equation 1.13 and are considered to be SM-like Yukawa couplings multiplied by the factor β_g. This term allows for $H \to b\bar{b}$ decay, but is considered negligible due to its subdued branching ratio.

The possible trilinear and quartic couplings between h, H and the DM candidate χ are encapsulated in Equations 1.14 and 1.15, where χ is assumed to be scalar for simplicity. The trilinear coupling in Equation 1.14 allows for $H \to hh$ decays on account of the excesses observed in the resonant di-Higgs production results. The quartic couplings in Equation 1.15 ($\lambda_{Hh\chi\chi}$) allow for Higgs boson decays in association with missing transverse energy ($E_{\mathrm{T}}^{\mathrm{miss}}$ or MET).

The proposed model was fit against the four classes of constraints featured in Table 1.1 and both the ATLAS and CMS results were used for impartiality. A simultaneous fit was done in terms of calculating and minimizing a combined χ^2 value while varying β_g as a function of the

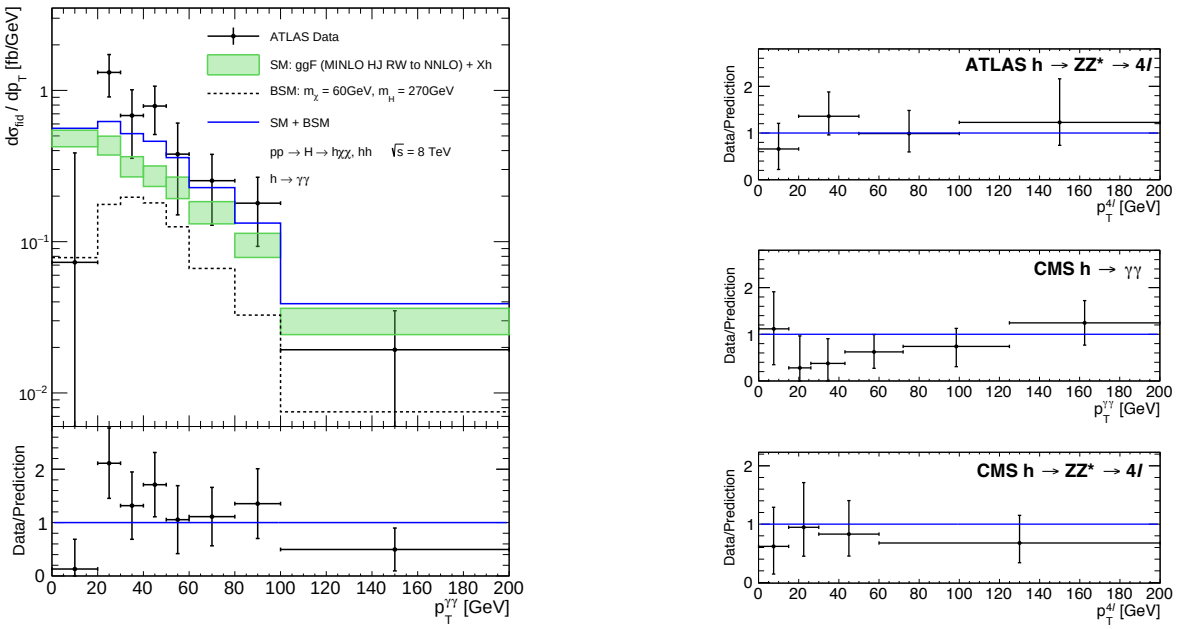


Figure 1.10: Fits to the Run 1 ATLAS and CMS p_T spectra. The ATLAS $H \to \gamma\gamma$ [68] result has been shown with a decomposition of the SM prediction and the SM+BSM prediction (left), while the ATLAS $H \to ZZ$ result [69] and CMS results are shown only as ratio plots of data and SM+BSM predictions [70, 85].

mass of H (m_H). It was observed that the lower values of m_H fit the experimental data better than the higher ones and the masspoint m_H = 270 GeV minimized χ^2 the most. Figure 1.10 shows the examples of fits at the minimized χ^2. In addition, an interpolation between mass points yields the smallest combined minimized χ^2 at m_H = 272 GeV, with upper and lower errors being 12 GeV and 9 GeV, respectively. This best fit is shown in Figure 1.11.

In equation 1.15 the decay $H \to h\chi\chi$ is treated through an effective quartic interaction. However, the DM candidates can originate from an inert scalar (S) [67, 86]. S is assumed to have a mass $m_h \leq m_S \leq m_H - m_h$, allowing for new processes associated to the decays of H. In Figure 1.12, S is assumed to mediate the $H \to h\chi\chi$ interaction by decaying into a pair of DM particles. This implies 100% branching ratio of $S \to \chi\chi$, which may not necessarily be the case. As a result, this $S \to \chi\chi$ possibility allows for new prospective searches such as $H \to SS$ and $H \to Sh$ which produce events that include photons, jets, leptons and $E_{\mathrm{T}}^{\mathrm{miss}}$. The introduction of the two scalars S and χ into the 2HDM model generates five new scalars and

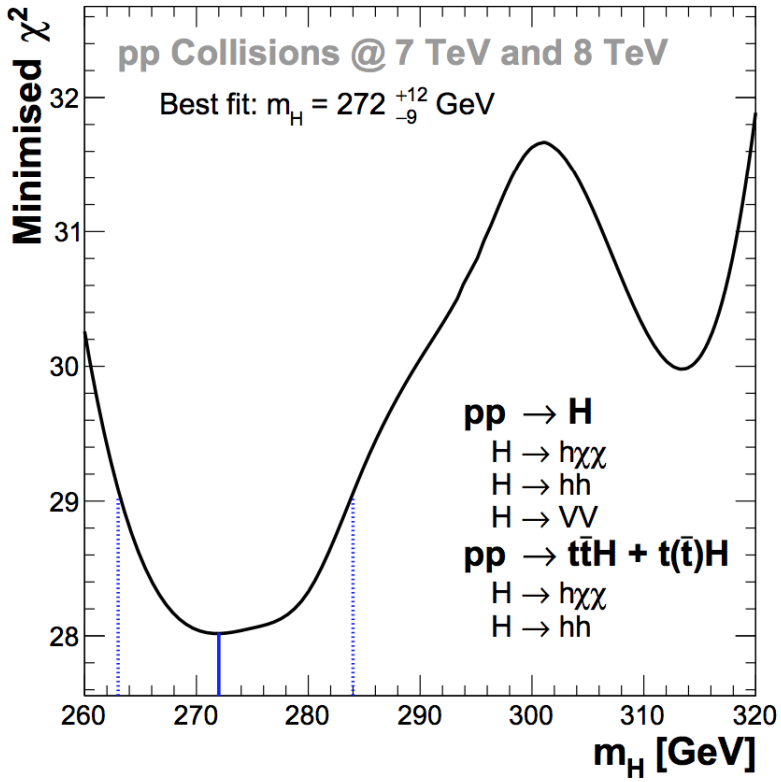
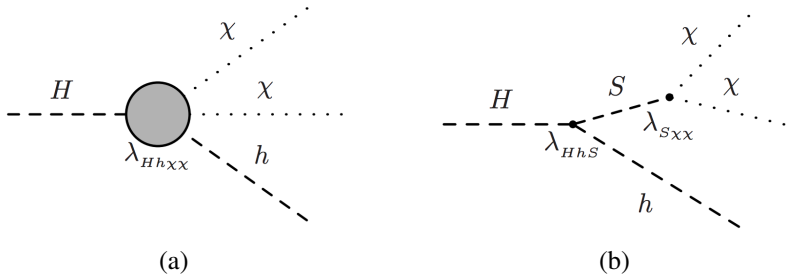


Figure 1.11: A scan of minimized χ^2 values as a function of the the mass of H.

several new decay possibilities summarized in Table 1.2. Taking the existence of S into account could prove to be advantageous as it would broaden the scope of searches associated to the Madala boson. If S is assumed to exhibit Higgs-like behaviour, one would expect it to decay predominantly to vector bosons. References [67, 87] also discusses the prospects of embedding the Madala hypothesis into a Two-Higgs-Doublet model plus scalar singlet (2HDM+S).

As a result of the work in this thesis, it is established that a big excess is not observed in the search for DM particles, indicating that S does not in fact decay 100% to DM as previously speculated. Since then, members of the institute have focused on other final states, in particular multi-lepton final states.

Within the context of new possibilities, the Madala hypothesis can be used to scrutinize the various ATLAS and CMS di-lepton invariant mass spectra. An excess in events containing two leptons plus jets and $E_{\mathrm{T}}^{\mathrm{miss}}$ was predicted in Reference [66]. In an effort to understand this



(a) (b)

Figure 1.12: Feynman diagrams of the Madala hypothesis: (a) the decay of a heavy scalar, H, through the effective quartic $\lambda hH\chi\chi$ vertex and (b) due to the additional scalar S under a λHhS $\lambda S\chi\chi$ replacement [67].

Table 1.2: A list of possible decay modes of the 2HDM scalars and S based on the explicit mass choices as described in the text in Reference [67].

S. No.	**Scalars**	**Decay modes**
D.1	h	$b\bar{b}$, $\tau^+\tau^-$, $\mu^+\mu^-$, $s\bar{s}$, $c\bar{c}$, gg, $\gamma\gamma$, $Z\gamma$, W^+W^-, ZZ
D.2	H	D.1, hh, SS, Sh
D.3	A	D.1, $t\bar{t}$, Zh, ZH, ZS, $W\pm H\mp$
D.4	$H\pm$	$W\pm h$, $W\pm H$, $W\pm S$
D.5	S	D.1, $\chi\chi$

excess, a study focused on the decay of S to di-lepton final states was set in motion [88]. The BSM di-lepton signal was compared to the ATLAS and CMS data and the best event yield was calculated by varying the BSM normalization and fitting the SM+BSM prediction to the data using several measurements discussed in Reference [88]. Figure 1.13 shows the distribution of the ATLAS data and SM background compared to the BSM signal for the di-lepton invariant mass in events with leptons and at least one b-tagged jet. The extension to the SM that introduces a Higgs-like S describes the data quite well for higher masses, however, visible discrepancies in the lower mass range are observed. This, together with several other anomalies is indicative of the fact that multi-lepton final states are not well understood at the moment. In a continued effort to try and comprehend the anomalies in multi-lepton final states while testing the Madala hypothesis, we consider the same simplified model where $H \to Sh$ and S is Higgs-like and only consider one parameter [84]. The masses are fixed to $m_H = 270$ GeV and $m_S = 160$ GeV, respectively. The idea is to try and figure out how compatible these discrepancies in data are.

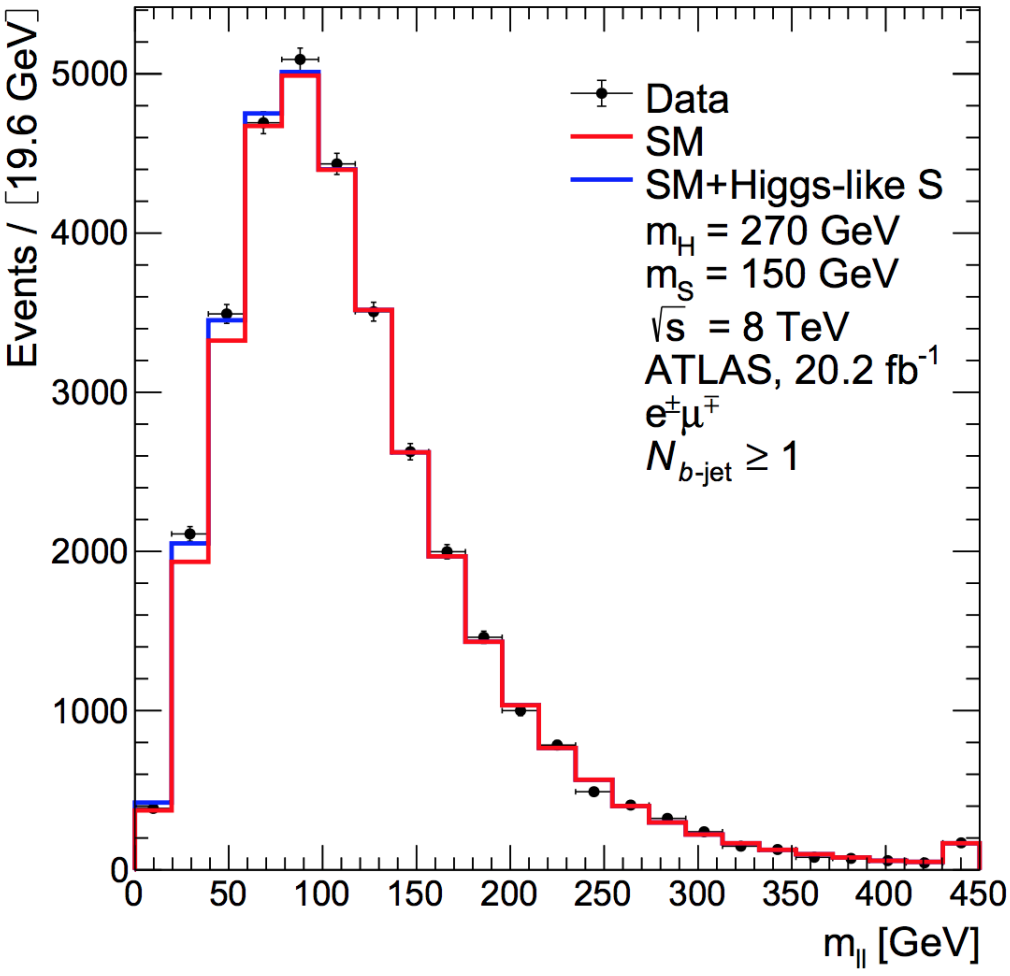


Figure 1.13: Distribution of the ATLAS data and SM background comparing to the BSM signal for the di-lepton invariant mass in events required to have two oppositely charged leptons ($e\mu$) with at least one b-tagged jet. The data used here is from pp collision collected by the ATLAS experiment at $\sqrt{s} = 8$ TeV with an integrated luminosity of 20.2 fb^{-1} [88].

Simultaneous fits for all the measurements in Table 1.3 are done and the profile likelihood ratio for each individual result and their combination is shown in Figure 1.14. The best fit is $\beta_g^2 = 2.92 \pm 0.35$ which corresponds to a significance of 8.04 σ. This is a clear measure of the inability of the current tools to describe multiple-lepton data and how our simplified model is able to capture the effect with just one parameter. The concept of embedding of the Madala hypothesis into a 2HDM+S model is actually now in good shape to be tested by experiments to further explore these discrepancies in multi-lepton final states.

Table 1.3: A summary of the SM+BSM fit results for each measurement considered, along with the result of their combination [84].

Selection	**Best-fit β_g^2**	**Significance (σ)**
ATLAS Run 1 SS ll and $lll+$ b-jets	6.51 ± 2.99	2.37
ATLAS Run 1 OS $e\mu$+b-jets	4.09 ± 1.37	2.99
CMS Run 2 SS $e\mu$ $\mu\mu$ $lll+$ b-jets	1.41 ± 0.80	1.75
CMS Run 2 OS $e\mu$	2.79 ± 0.52	5.45
CMS Run 2 $lll + E_{\mathrm{T}}^{\mathrm{miss}}$ (WZ)	9.70 ± 3.88	2.36
ATLAS Run 2 SS ll and $lll+$ b-jets	2.22 ± 1.19	2.01
ATLAS Run 2 OS $e\mu$+b-jets	5.42 ± 1.28	4.06
ATLAS Run 2 $lll + E_{\mathrm{T}}^{\mathrm{miss}}$ (WZ)	9.05 ± 3.35	2.52
Combination	2.92 ± 0.35	8.04

Last but not least, we continue to test the Madala hypothesis by looking at direct H productions into $\gamma\gamma$ and $Z\gamma$, which has been documented in detail in this thesis. It goes without saying that this thesis covers years of work efforts towards comprehending the Madala Hypothesis and therefore concludes what the Madala Hypothesis is at present.

1.4.1 Testing the hypothesis in the diphoton channel

This discovery of the Higgs boson opened up new possibilities for BSM physics. The diphoton channel is important for BSM physics searches as new high-mass states decaying to two photons are predicted in many sectors of the extensions of the SM. The Madala hypothesis discussed in Section 1.4 is one such extension in search for new physics phenomena. As highlighted in Section 1.3.2 the diphoton final state provides a clean experimental signature, with a commendable invariant mass resolution, making it an ideal channel for BSM searches.

DM matter makes up approximately 25% of the entire universe, raising some of the biggest questions in the study of space and physics. Questions such as what is this DM? What is the source of all the out there in the universe? The presence of dark matter is suggested in several astrophysical observations through gravitational effects. When adding up all the constituents of the universe, things just do not add up to give the total gravity that governs our universe. Knowledge about a DM puzzle dates back to the 1930s and is the longest standing unsolved problem in modern physics. In an effort to unravel the mysteries of DM, we perform DM

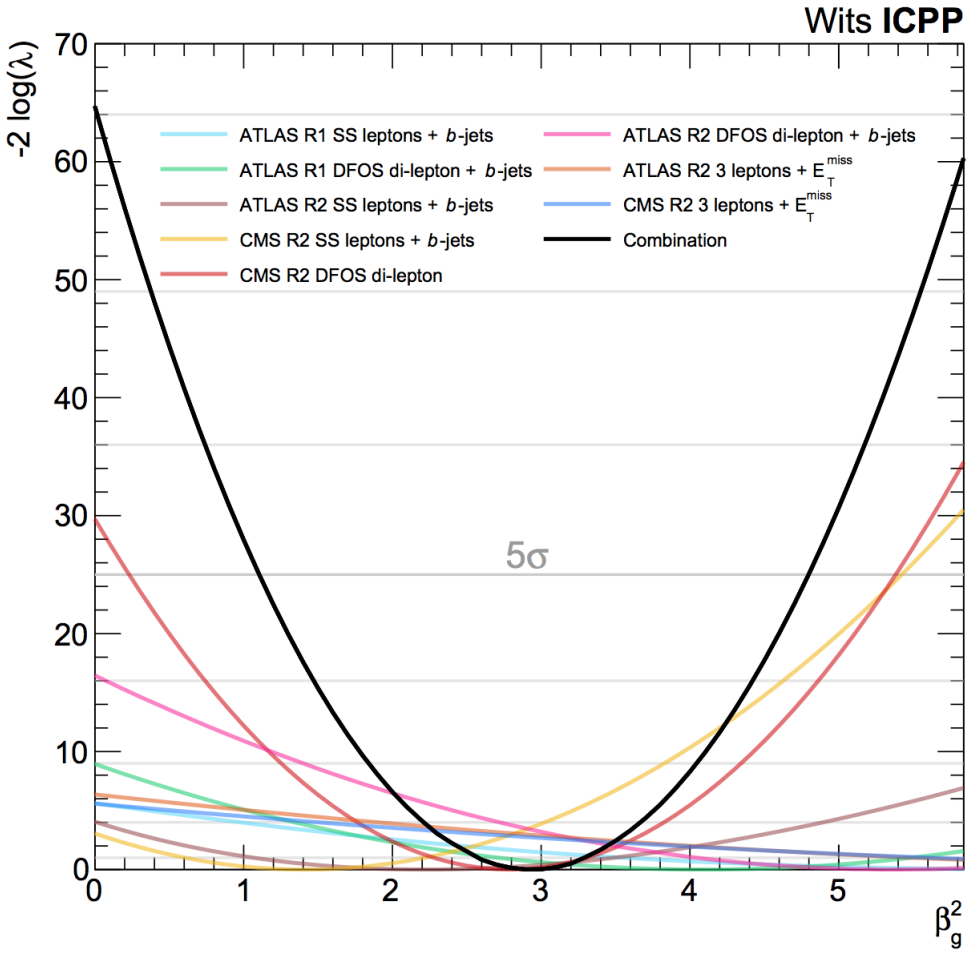


Figure 1.14: The negative 2 times the logarithm of the profile likelihood ratios for each of the individual fit results considered in Reference [84], overlaid with that of their combination. The significance of a result is calculated as the square root of the point which intersects the y-axis (that is, the SM-only hypothesis where ($\beta_g = 0$)).

searches at the LHC. The existence of DM particles is undeniably evident in astrophysics [89], but DM particles produced in SM collisions have a very minute interaction probability. DM searches at the LHC are therefore driven primarily by $E_{\mathrm{T}}^{\mathrm{miss}}$ signatures produced with detectable particles ($X + E_{\mathrm{T}}^{\mathrm{miss}}$). This possibility allows us to test the Madala hypothesis by searching for DM particles in events with $E_{\mathrm{T}}^{\mathrm{miss}}$ and a Higgs boson decaying to two photons ($h(\rightarrow \gamma\gamma) + E_{\mathrm{T}}^{\mathrm{miss}}$), which is documented in this thesis. This documentation plays a major role in the understanding of the Madala hypothesis as well as the direction to take going forward. In addition, as highlighted, this thesis details direct decay of H into $\gamma\gamma$ where $H(\rightarrow \gamma\gamma) + E_{\mathrm{T}}^{\mathrm{miss}}$.

The search is extrapolated to the $Z\gamma$ channel and the results of this extrapolation are also documented. Due to the importance of the $\boldsymbol{E}_{\mathrm{T}}^{\mathrm{miss}}$ signature in these analyses, the performance of $\boldsymbol{E}_{\mathrm{T}}^{\mathrm{miss}}$ reconstruction is also detailed in this documentation. This thesis essentially concludes what the Madala hypothesis is after several years of work.

CHAPTER 2

EXPERIMENTAL APPARATUS

In the scientific method, experimentation is a requisite procedure for supporting or refuting a hypothesis. In High Energy Physics (HEP), hypotheses are formulated on the basis of trying to unravel the mysteries of the universe thus paving the way for exploration through experimentation. Consequently, the apparatus used to drive experiments are of great importance in the testing of these hypotheses such as our Madala hypothesis. This chapter provides a laconic introduction to the experimental apparatus used in facilitating this research and is organized as follows: Section 2.1 provides an overview of the Large Hadron Collider (LHC) and Section 2.2 gives a description of the A Toroidal LHC ApparatuS (ATLAS) detector.

2.1 The Large Hadron Collider

The LHC is the largest and most powerful particle accelerator and collider in the world. A More detailed description of the design, construction and overall operation of the LHC can be found in the References [90–92]. The LHC lies in a 27 km circumference tunnel, approximately 175 m beneath the France-Switzerland boarder near Geneva at CERN. This marvel was designed back in the 80's during the time when the LEP collider was being constructed. After several years of work on its blueprint, the CERN council approved the building of the LHC in 1994. The LHC was finally built between 1998 and 2008 in collaboration with scientists and engineers

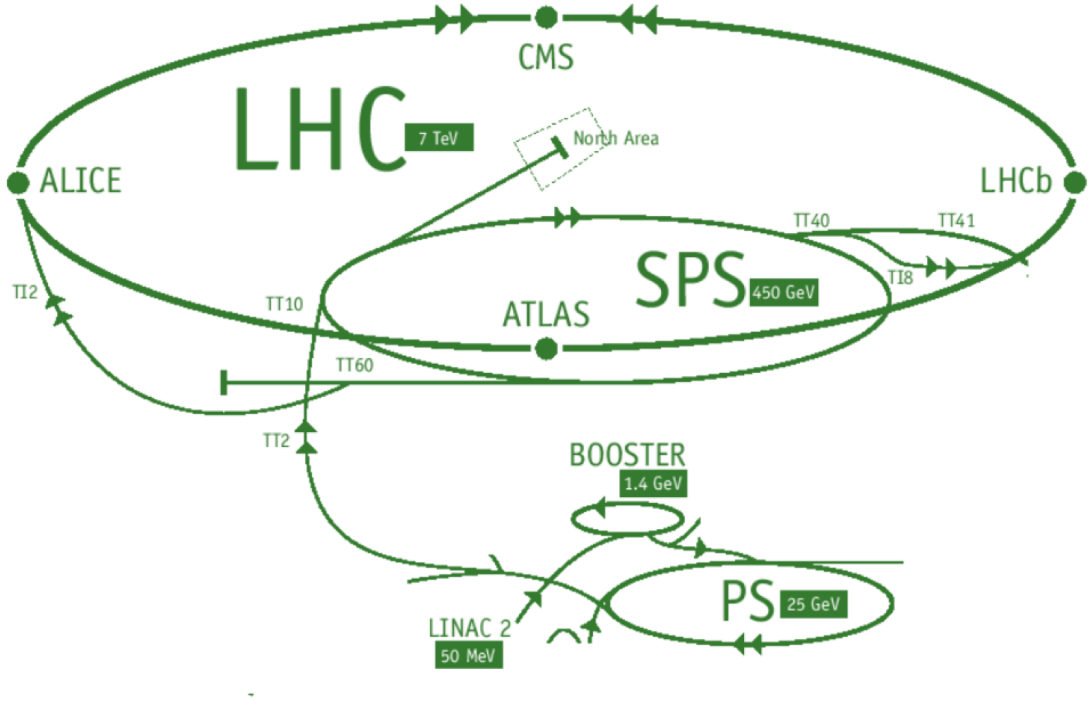


Figure 2.1: A diagram of the CERN accelerator complex.

from all over the world. The content of this thesis relates to LHC operations as a proton-proton collider, however, it is worth mentioning that the LHC can also use beams of ions (Proton-lead and lead-lead) to study the extreme state of nuclear matter such as quark-gluon plasma.

The LHC ring comprises of two parallel beam pipes which house the beams of particles travelling in opposite directions around the ring. However, before the beam is injected into the LHC it is accelerated by several pre-accelerators. Each accelerator boosts the energy of the beam of particles as it passes through. The proton source is Hydrogen gas whose atoms are ionized by an applied high frequency electric field. The protons are passed into the linear accelerator *Linac2* which accelerates them up to 50 MeV before feeding them into the Proton Synchrotron booster (PSB). The PSB boosts the proton beam up to an energy of 1.4 GeV before passing it into the synchrotron accelerators. The Proton Synchrotron (PS) accelerates

the beam up to 26 GeV followed by further acceleration up to 450 GeV by the Super Proton Synchrotron (SPS) before injection into the LHC ring. Figure 2.1 shows an illustration of the CERN accelerator complex, including the pre-accelerators used to prepare beam for injection into the 2 beam pipes of the LHC.

The LHC is designed to produce proton-proton (pp) collisions at a centre-of-mass energy of 14 TeV. The LHC rings consist of accelerating structures and a large magnetic system surrounding the beam pipes. After filling the LHC ring, each beam of protons is accelerated to the maximum energy of 7 TeV (energies that will be reached in Run 3 in 2021) and these beams are kept in a circular trajectory by the magnetic system. Each proton beam circulates the ring in bunches and under normal working conditions each beam contains 2808 bunches producing several pp collisions. Collisions commence once the beams are declared stable and can continue for up to 24 hours, depending on when the luminosity drops to 50%. Luminosity refers to the number of collisions that can be produced per area per second and is expressed as follows:

$$\mathscr{L} = \frac{N_b^2 n_b f_{rev} \gamma_r}{4\pi \epsilon_n \beta^*} F, \tag{2.1}$$

where:

- N_b is the number of particles per bunch,
- n_b is the number of bunches per beam,
- f_{rev} is the revolution frequency,
- γ_r is the relativistic gamma factor,
- ϵ_n is the normalized transverse beam emittance,
- β^* is the beta function at the collision point given by:

$$\beta^* = \frac{\sigma^2 \gamma_r}{\epsilon_n}, \tag{2.2}$$

where σ is the beam size and

- F is the geometric luminosity reduction factor which is given by:

$$F = \frac{1}{\sqrt{1 + (\frac{\theta_c \sigma_z}{2\sigma^*})^2}}, \tag{2.3}$$

  where θ_c is the crossing angle of the beams, σ_z is the RMS bunch length and σ^* is the RMS transverse beam size at the interaction point.

Such that the observed number of events produced by a phenomena with cross-section is:

$$N = \sigma_{process} \mathscr{L}, \tag{2.4}$$

where $\sigma_{process}$ describes the probability of two particles interacting.

The LHC operation is divided into Runs which last several years and are separated by long shutdowns which are essential for maintenance, overhauls and upgrades. The first beam was circulated through the LHC in September 2008, however, due to a quench incident the rest of that year and most of 2009 was spent on repairs caused by the predicament. The first official operational Run, referred to as Run 1, began in November 2009 and was anticipated to progress till the end of 2012. In 2010 the LHC collected 5.08 fb^{-1} of data at 7 TeV and 21.3 fb^{-1} at 8 TeV in 2012. Run 1 of data taking was a monumental Run as it saw the discovery of the Higgs boson and in light of such an event, Run 1 ended up advancing into early 2013 to allow for more data collection. Following this, the LHC shutdown for a 2 year upgrade with the ambition to achieve higher luminosities. In April 2015, the LHC restarted and Run 2 began allowing for 6.5 TeV per beam (13 TeV in total), which is the operating energy to date. Luminosities have increased over the years in this Run, reaching up to 46.9 fb^{-1} in 2017. Achieving 14 TeV collisions is the goal for Run 3 with anticipated luminosities of ?.

The pp collisions occur at four main points around the LHC ring and the debris from these collisions is collected and analyzed as data by four main experiments located at these beam intersection points. These experiments include:

- A Toroidal LHC ApparatuS (ATLAS) [93].
- Compact Muon Solenoid (CMS) [94].

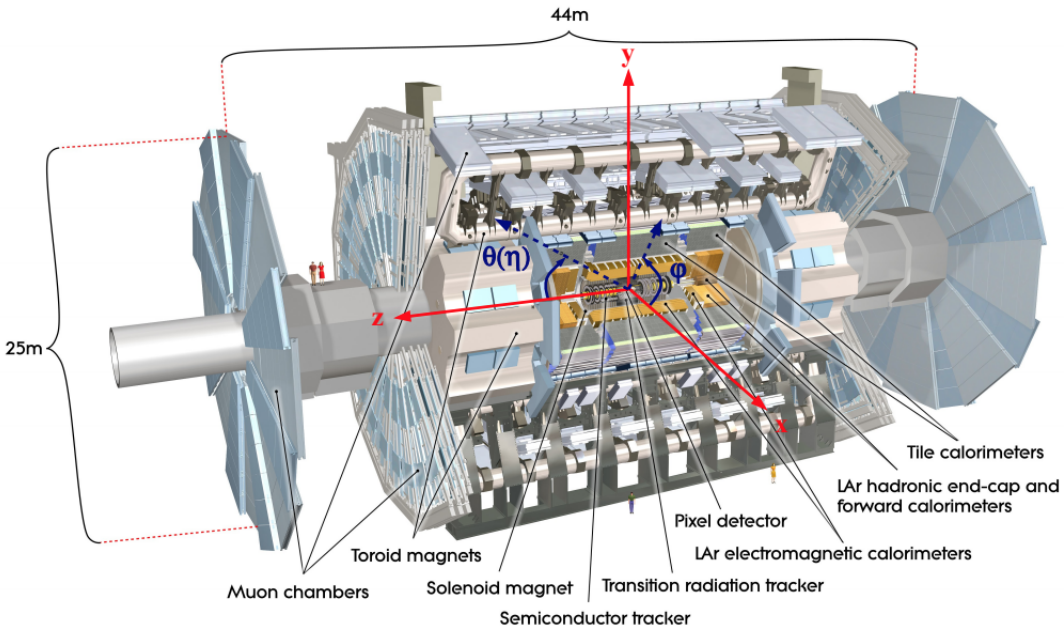


Figure 2.2: A cut-away view of the ATLAS detector [93].

- A Large Ion Collider Experiment (ALICE) [95].
- Large Hadron Collider beauty (LHCb) [96].

ATLAS and CMS are the largest experiments at the LHC and are used to investigate a wide range of physics including searching for the Higgs boson, extra dimensions and particles that make up dark matter. The goal of the ALICE experiment is to characterize the physical properties of quark-gluon plasma and that of the LHCb experiment is to record the decay of particles containing b mesons. The dataset used in this thesis was recorded with the ATLAS detector which is described in detail in the next section.

2.2 The ATLAS detector

The ATLAS experiment is a particle physics experiment conducted at the LHC in the search for new physics through head on collisions of high energy protons. The detector itself is located in its experimental cavern at point 1 of CERN's Meyrin site. ATLAS is the largest general

purpose detector in the world, weighing approximately 7000 tonnes and having a cylindrical geometry covering a length of 44 m and height of 25 m. The existence of such apparatus makes it possible to study an unprecedented scope of physics which may lead to discoveries that go beyond the SM thus equipping us with the tools we need to understand the world around us.

The ATLAS detector comprises several coaxially cylindrical layers, where each layer is a sub-detector. Each sub-detector is sensitive to the different types of particles produced in the collisions. Figure 2.2 shows a schematic diagram of the ATLAS detector and its different sub-detector systems. Closest to the interaction point is the Inner Detector (ID) [97–99] which comprises of the Pixel Detector (PIX), Semiconductor Tracker (SCT) and the Transition Radiation Tracker (TRT). Surrounding the ID cavity is a thin superconducting solenoid and the ID itself is immersed in this 2 Tesla solenoid magnetic field. The ID is surrounded by the calorimeter system [100] which comprises of the Liquid Argon Electromagnetic calorimeter, Tile Calorimeter, Hadronic EndCap Calorimeter and Forward Calorimeter. Surrounding the calorimeters is the muon spectrometer (MS) [101, 102] which is made up of muon chambers operating in a toroidal magnetic field.

ATLAS uses a right-handed coordinate system with the origin at the interaction point (IP) in the centre of the detector. The z-axis is along the beam pipe, the x-axis points from the IP to the centre of the LHC ring and the y-axis points upwards towards the earth's surface as shown in Figure 2.2. In the transverse plane, cylindrical (r,ϕ) coordinates are used, where r is a radial dimension measuring the distance from the beam line and ϕ is the azimuthal angle around the beam pipe. The polar angle θ is the angle measured from the beam axis as illustrated in Figure 2.2 and the pseudorapidity is defined in terms of this angle as η = -ln[tan(θ/2)]. The pseudorapidity is used as an angular coordinate in place of θ and the angular separation between objects is defined as $\Delta R = \sqrt{\Delta\eta^2 + \Delta\phi^2}$. Both $\Delta\eta$ and $\Delta\phi$ are invariant with boost along the z-axis, precisely the nature of of the boost of a pair of colliding partons at the LHC with respect to the lab frame. The transverse momentum, transverse energy and missing transverse momentum are all defined in the x-y plane.

The remainder of this chapter discusses the ATLAS detector sub-systems whose functions form the essence of the research in this thesis.

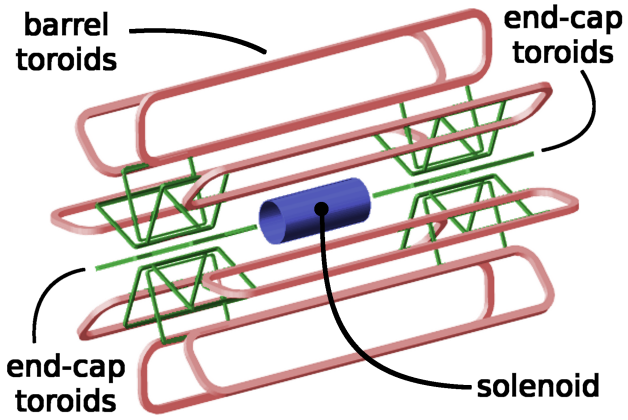


Figure 2.3: An illustration of the magnetic system at ATLAS.

2.2.1 Magnetic system

There are two magnetic systems at ATLAS whose sole purpose is to bend charged particles in the ID and muon spectrometer, respectively [97, 103], to allow two independent measurements of their momenta if they cross both systems. The first magnetic system is housed between the ID and EM calorimeter and provides a 2 Tesla solenoidal magnetic field parallel to the beam axis. The second magnetic system is a toroidal system which provides a magnetic field of up to 4 Tesla and is orthogonal to the muon trajectories. A large barrel toroid magnet provides the magnetic deflection of muon tracks within $\eta < 1.4$ and in the $1.6 < \eta < 2.7$ range, the bending is provided by small endcap magnets. Over the $1.4 < \eta < 1.6$ range, the bending is done by a combination of these barrel and endcap fields. The magnetic systems are cooled using liquid helium and operate at a temperature of 4.5 K. Figure 2.3 shows an illustration of the magnetic field system at ATLAS.

2.2.2 Inner detector

The ID provides precision tracking of charged particles as they navigate the detector. The system measures the positions of charged particles along their path and within $\eta < 2.5$. The ID is also designed to determine the primary and secondary vertices as well as the impact parameter of a trajectory w.r.t. a vertex and also facilitate the identification of electrons and positrons. This detector is immersed in a 2 Tesla magnetic field provided by a solenoid which

allows the deflection and bending of charged particles, facilitating accurate measurement of their momenta. Charged particles with transverse momentum below 500 MeV do not reach the LAr calorimeter therefore pnly those with a momentum above this threshold are reconstructed in the ID. Usually only tracks with $p_{\mathrm{T}} > 1\,\mathrm{GeV}$ are used in the analyses.

Figure 2.4a illustrates the 3 independent sub-systems that make up the ID. The sub-systems are discussed in the sub-sections that follow.

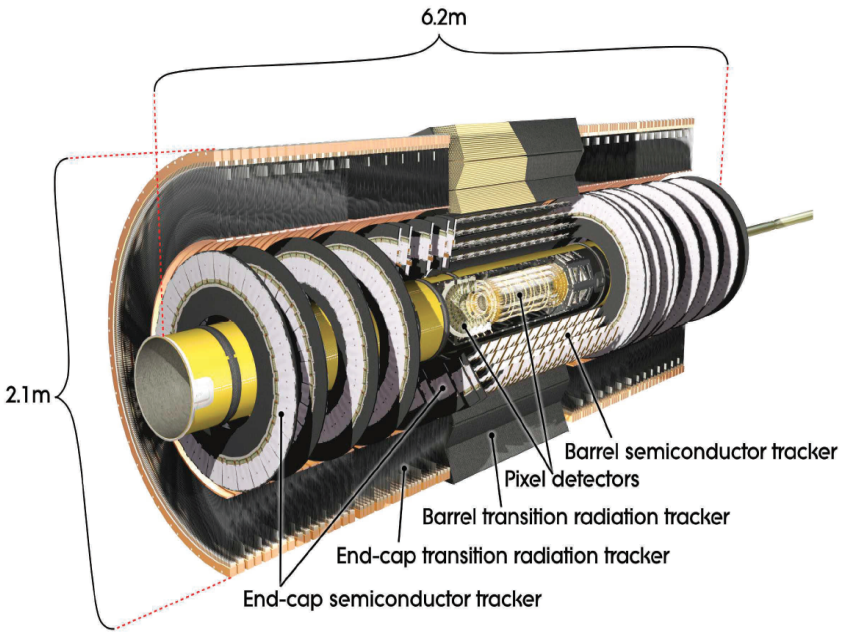
2.2.2.1 Silicon pixel detector

The silicon pixel (PIX) detector is closest to the beam pipe and comprises of three concentrically arranged silicon-pixel layers at various distances from the beam pipe [97–99]. Figure 2.4b shows the silicon-pixel layers and their distances from the beam axis. The layers are segmented in r-ϕ and z, where the r-ϕ plane is defined with r as the transverse radial distance from the centre of the detector. The PIX detector features 80 million read-out channels and provides on average three measurements per charged particle and has a position resolution of 10 μm in the r-ϕ plane and 115 μm along z covering $|\eta| < 2.5$.

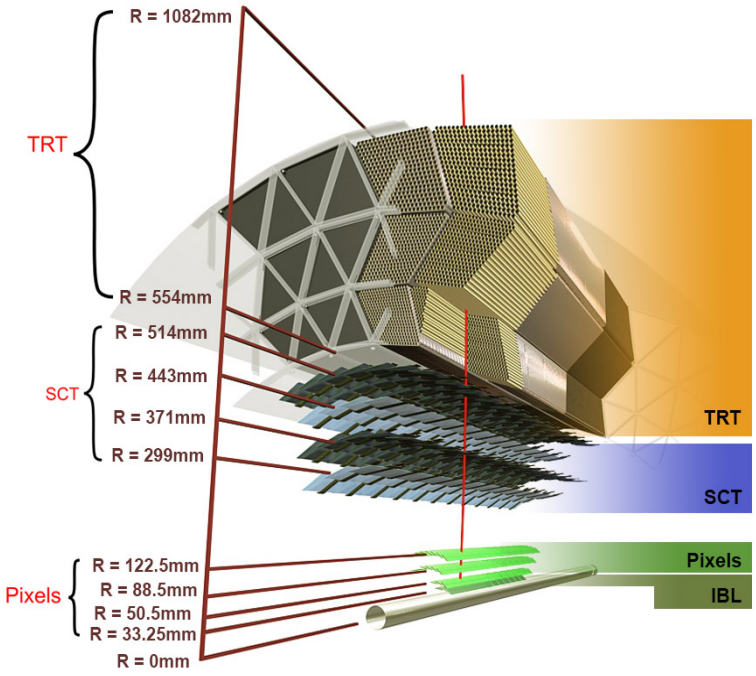
A new detector referred to as the Insertable B-layer (IBL) was installed during the 2013-2014 upgrade between the existing pixel detector and a new, smaller radius beam pipe at the radius of 3.3 cm. The IBL was built to cope with high radiation and occupancy, and is the first large scale application of 3D sensors and CMOS 130 nm technology. The IBL consists of 14 tilted staves (64 cm long 2 cm wide and tilted in ϕ of 14°) equipped with 32 front-end chips per stave and sensors facing the beam pipe. The operation of the IBL began in 2015 and has since improved the ATLAS tracking performance.

2.2.2.2 Semiconductor Tracker

Surrounding the pixel detector is the semiconductor tracker (SCT) [97–99] which is made up of four silicon micro-strip layers in the barrel region and nine disks in the end-cap region. Each silicon detector in the SCT barrel has dimensions 6.36 mm X 6.40 mm and consists of 768 read-out strips of width 80 μm. In each barrel layer, one set of strips is aligned parallel to the beam direction and the other at a small 40 mrad angle to allow measurement of the z position.



(a)



(b)

Figure 2.4: (a) An illustration of the ATLAS Inner Detector and its sub-systems and (b) A cut-away view of the central region barrel of the ATLAS Inner Detector showing the Pixel layer, SCT and TRT. The distances of concentric layers from the beam axis are drawn to scale and labelled [104].

On the other hand, the end-cap SCT disks contain double-layer strips which are aligned with a small angle as well to allow for the measurement of r. The disks use sensors which have constant azimuthal angle coverage along their length and an average pitch of approximately 80 mm. The SCT sensors cover an area of 61 m^2 with approximately 6.2 million readout channels. The SCT provides a position resolution of 16 μm in the r-ϕ plane and 580 μm along z with a $|\eta| < 2.5$ coverage. Figure 2.4b shows the SCT layers and their varying distances from the beam axis.

2.2.2.3 Transition Radiation Tracker

The Transition Radiation Tracker (TRT) forms the outermost layer of the ID and is the largest sub-detector in the ID [97–99]. It consists of approximately 280 000 straw drifts tubes which are 4 mm in diameter and whose centres contain a 31 μm anode made out of gold plated tungsten supported by end-plugs. The tubes are filled with a Xe-based gas mixture which facilitates the measurement of transition radiation as charged particles traverse through the TRT. Within the barrel region, the straws are positioned in 73 layers aligned parallel to the beam direction which then split into two halves at $|\eta| = 0$. Moreover, the endcaps of the TRT contain 160 layers of long tubes which are positioned radially around the beam axis. The TRT provides a position resolution with an accuracy of approximately 130 μm in ϕ with a coverage of up to $|\eta| = 2.0$. Aside from tracking, the TRT also provides particle identification through the detection of the transition radiation, which allows the discrimination of electrons from other charged hadrons.

2.2.3 The Calorimeter System

The calorimeter system is designed to provide a precise measurement of the energy of all the particles that leave the ID and enter the calorimeters, except for muons and neutrinos [100]. The calorimeters cover the full pseudorapidity range of $|\eta| < 4.9$ and are segmented into towers in both η and ϕ, pointing towards the centre of the detector. The fractional calorimeter resolution as a function of energy is expressed as:

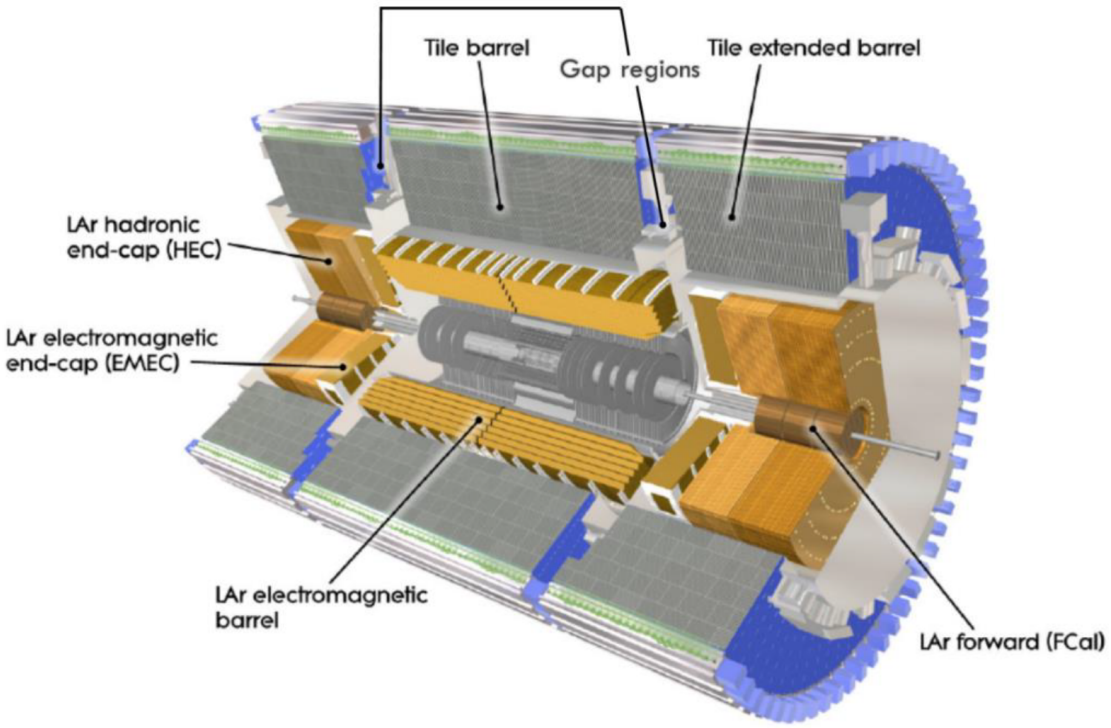


Figure 2.5: A computer generated image of the ATLAS calorimeter [105].

$$\frac{\sigma_E}{E} = \frac{N}{E} \oplus \frac{S}{\sqrt{E}} \oplus C, \tag{2.5}$$

where:

- N represents the noise due to background and electronics
- S refers to the stochastic uncertainty caused by the random sampling nature
- C is the constant term which reflects the non-uniformities in the detector structure

Figure 2.5 shows a schematic view of the ATLAS calorimetric system. The two main systems that make up to calorimeter are the Electromagnetic Calorimeter (ECAL) and the Hadronic Calorimeter (HCAL) discussed in the upcoming sub-sections.

2.2.3.1 Electromagnetic Calorimeter

The Electromagnetic (EM) Calorimeter is a sampling calorimeter [106, 107] surrounding the ID and solenoid system. It is designed mainly to measure the energy of particles that interact electromagnetically and is therefore used to distinguish between electrons and photons alongside the ID. The EM calorimeter is made up of layers of dense absorber material made of lead as well as an active Liquid-argon (LAr) medium. The lead plates possess an accordion shape which enables a constant distance between the absorber layers within the detector allowing uniform ϕ coverage and fast read-out, while avoiding dead zones usually used to extract the signal. This so-called accordion geometry can be seen in Figure 2.6 which shows a section of the EM calorimeter. When charged particles interact in this calorimeter, an electromagnetic shower develops resulting in the build up of numerous charged particles which ionize the argon. Electrodes which are kept at high voltage are located within the LAr and the dense absorber material is connected to ground, producing a high intensity electric field within the detector of about 2000 V/mm Under the influence of this electric field, the ionized argon and electrons coast towards the electrodes, inducing an electrical signal which is processed by the read-out electronics. The EM calorimeters cover a pseudorapidity range of $|\eta| < 3.2$ with a gap between $1.37\ |\eta| < 1.52$ where the barrel components end and the endcap begins ("crack" region). In the region $|\eta| < 2.4$, the EM calorimeter is divided into three sampling layers that are longitudinal in shower depth and vary in granularity in the η direction. The first layer is referred to as the strip layer and is segmented with strips along the η direction providing high granularity. This provides discrimination between showers initiated by photons or electrons and those initiated by isolated neutral hadrons. The middle layer contains projective cells which collect most of the energy deposited by photon and electron showers and has a fine segmentation in both η and ϕ. The rear layer is coarser than the previous and corrects for leakage of high-energy showers beyond the EM calorimeter.

2.2.3.2 Hadronic Calorimeter

The hadronic calorimeters surround the EM calorimeters and measure the remaining part of the energy of hadron showers within $|\eta| < 3.2$. The hadronic calorimeters are divided into three

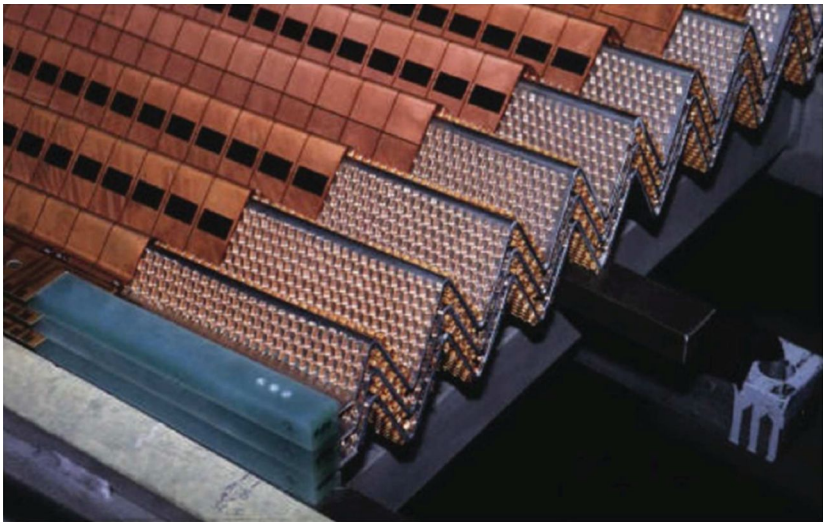


Figure 2.6: A section of the ATLAS electromagnetic calorimeter highlighting the accordion geometry [105].

parts: Tile Calorimeter (TileCal), LAr Hadronic End-cap Calorimeter (HEC) and LAr Forward Calorimeter (FCal).

The TileCal [107, 108] is located within $|\eta| < 1.7$ just outside the LAr calorimeters and consists of plastic scintillator tiles with steel absorbers. This detector extends from an inner radius of 2.28 m to an outer radius of 4.25 m. The TileCal is made up of a central barrel which covers $|\eta| < 1.0$ as well as two extended barrels, one on either side, covering $0.8 < |\eta| < 1.7$ as shown in Figure 2.7. These barrels are segmented into 64 wedge-shaped modules arranged in ϕ around the beam line and contain the scintillators, steel absorbers and read-out electronics. There are wavelength shifting fibres which are attached to the sides of the scintillator plates and are read-out by photomultiplier tubes (PMT) at the edge of each tile module. When hadrons pass through the detector they produce a shower of hadrons (jets) which interact with the plastic scintillators producing light which is guided by the wavelength shifting fibres and read-out through the PMT tubes.

The energy resolution of the TileCal is given by:

$$\frac{\sigma_E}{E} = \frac{50\%}{\sqrt{E}} \oplus 3\%, \tag{2.6}$$

where the first term on the right-hand-side of Equation 2.6 is the stochastic term and the

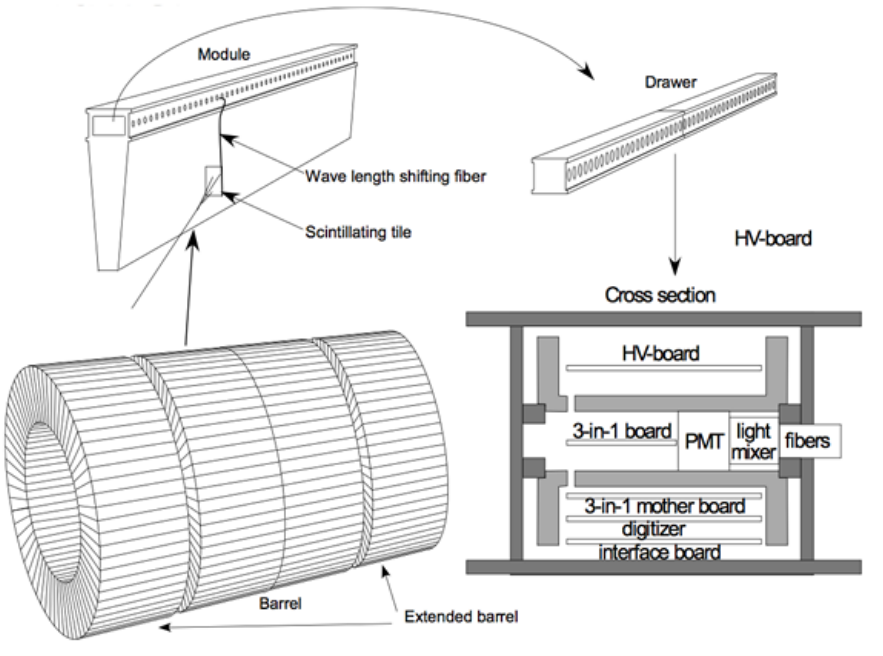


Figure 2.7: A schematic diagram of the tile calorimeter [105].

second term is the constant term.

The HEC has a coverage of $1.5 < |\eta| < 3.2$ and uses LAr as an active medium and copper as a passive absorber material. The HEC comprises of two wheels at each endcap and each wheel is divided into 32 modules.

The energy resolution of the HEC is given by:

$$\frac{\sigma_E}{E} = \frac{71\%}{\sqrt{E}} \oplus 1.5\%. \tag{2.7}$$

The FCal [109] covers up to $|\eta| = 4.9$ and just like the ECal and HEC the active medium in FCal is LAr. The FCal is made up of three layers and the first layer uses copper as the absorber material whilst the other two use tungsten. The first layer is dedicated to electromagnetic measurements whilst the other two are devoted to hadronic measurements.

The energy resolution of the FCal is given by:

$$\frac{\sigma_E}{E} = \frac{94\%}{\sqrt{E}} \oplus 7.5\%. \tag{2.8}$$

2.2.4 Muon Spectrometer

The Muon spectrometer (MS) [102] forms the outermost part of the ATLAS detector covering the region $|\eta| < 2.7$. This detector is designed to measure the position and momenta of muons that pass through the ID and calorimeters. Three large air-core toroids deflect the muons as they reach the MS, allowing for accurate measurement of their momenta. Figure 2.8 shows the different components of the MS. Two main precision chambers are used in the MS: the monitored drift tubes (MDT) [101] and the cathode strip chambers (CSC) [110]. The MDT covers most of the range $|\eta| < 2.7$ except in between $2.0 < |\eta| < 2.7$ which consists of the CSC. The MDT chambers consist of eight layers of drift tubes which operate at an absolute pressure of 3 bars and achieve a position resolution of 80 μm per tube and 35 μm per chamber. The MDT drift tubes contain a gaseous mixture of 93% argon and 7% carbon dioxide as well as a central tungsten-rhenium wire which acts as the anode and collects ionized electrons from the gas. The CSC is made up of multiwire proportional chambers arranged into two disks each with eight chambers with orthogonal planar cathodes arranged. They have a higher radiation tolerance than the MDT and are therefore placed in the forward region to handle higher particle fluxes. While the calorimeter σ_E/E decreases with energy, the tracking resolution σ_{p_T}/p_T is increasing with p_T since the larger the p_T, the straighter the tracks. The design resolution of the MS is given by 10% for a track p_T of 1 TeV.

2.2.5 Trigger system

The high luminosity of the LHC results in $\sim 10^3$ - 10^{10} interactions per second, most of which do not carry useful information for physics analyses. In addition, only a small fraction of these interactions can be recorded due to limitations in data storage and rates. A trigger system is employed to perform a run-time selection which classifies events and selects only the interesting ones for physics analyses. The ATLAS trigger system comprises of the hardware-based Level 1 trigger (L1) and events which pass the L1 trigger move on to the High-Level trigger system (HLT) [111]. The HLT is made up of the Level 2 trigger (L2) and the Event Filter (EF).

The L1 trigger has a maximum acceptance rate of approximately 75 kHz and decisions

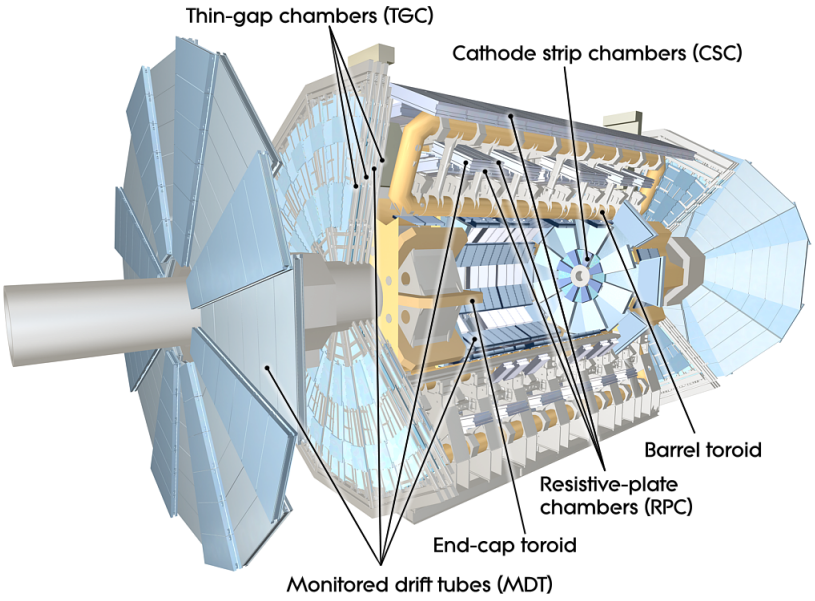


Figure 2.8: A schematic diagram of the Muon system [105].

must reach the front-end electronics within a time period of 2.5 μs. This trigger has access to information from the calorimeters and MS and selects events with high p_{T} objects (muons, electrons, photons, jets, taus decaying into hadrons and also large transverse missing energies).

The HLT follows the L1 trigger and operates at 1 kHz. The L2 trigger performs measurements with a finer granularity than the L1 trigger and includes information from the ID. The L2 trigger reduces the event rate to a maximum of approximately 3.5 kHz with an average processing time of 40 ms. At the L2 trigger the number of steps are performed sequentially, that is, at each step only the data required to make the decision at that step is acquired and analyzed. This helps to reduce bandwidth requirements by allowing some events to be rejected before reading the full event set. The EF does the full reconstruction of the event by applying reconstruction algorithms using the ATLAS Athena control framework, which is based on the GAUDI framework [112]. The acceptance event rate is reduced further at this level to approximately 1 kHz. The events passing this level are written to the main analysis stream and data is periodically reprocessed. The recorded events are checked for data quality and those recorded during malfunctions are flagged for removal from the analysis. Figure 2.9 shows the structure of the ATLAS trigger system.

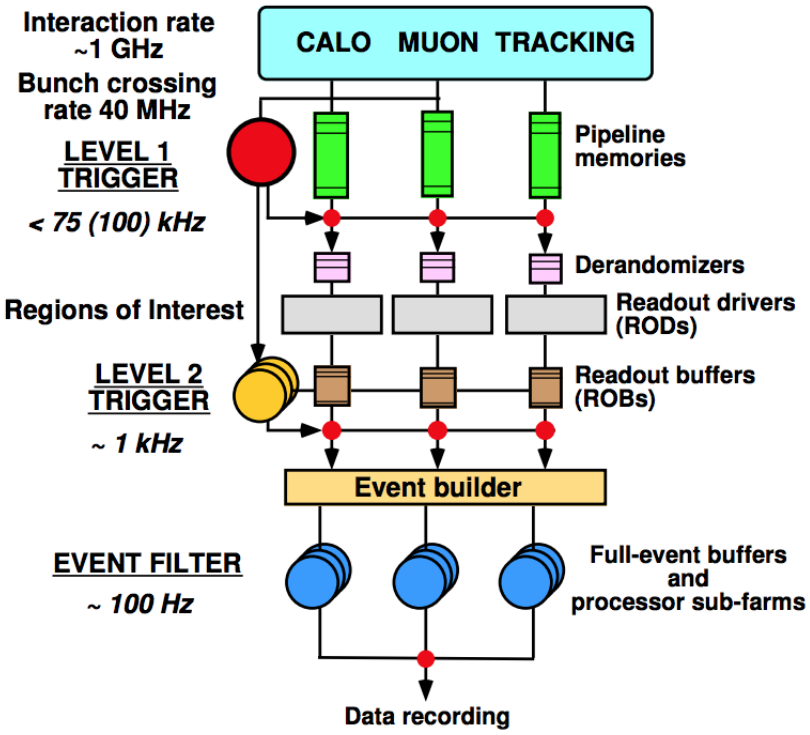


Figure 2.9: A diagram showing the structure of the ATLAS trigger system [105].

CHAPTER 3

INVESTIGATING THE RADIATION HARDNESS OF PLASTIC SCINTILLATORS FOR THE UPGRADE OF THE ATLAS TILE CALORIMETER

A comparative study of the radiation hardness of plastic scintillators is reported here. This study was done in an effort to replace the gap scintillators as well as the minimum bias trigger scintillators (MBTS) with more radiation hard ones during the upgrade of the TileCal of the ATLAS detector. In the detector, plastic scintillators are exposed to a harsh radiation environment, and are therefore susceptible to radiation damage. The highest dose currently expected within the TileCal over the next several years is approximately 10 kGy. The influence of radiation on the light transmittance of various types of plastic scintillators was investigated. Plastic scintillators display high optical transmittance, an essential property for the effective functioning of TileCal. The samples were irradiated using a 6 MeV proton beam at various doses and the transmission spectra corresponding to the irradiated and unirradiated samples were obtained and analyzed. It is worth mentioning that this work has been cited by individuals from the Institute of Physics and Engineering in Medicine (IPEM) [113] in the United Kingdom, CMS [114], the International Thermonuclear Experimental Reactor (ITER) [115] in France, the University of Surrey also in the United Kingdom [116] and individuals affiliated to various intitutes in Istanbul, Turkey [117].

Sections 3.1 gives an introduction to the overall experiment. Section 3.2 gives a description of the scintillation mechanism. The methods used are discussed in Section 3.3 and the experimental procedure is summarized in Section 3.4. The results are documented in Section 3.5 and summarized in Section 3.6.

3.1 Introduction

Plastic scintillators exhibit the property of luminescence when excited by ionizing radiation. This, paired with their high optical transmission property makes them suitable for use within large particle detectors, such as ATLAS. The plastic scintillators of interest are the gap scintillators and the MBTS located within the Tile Calorimeter of the ATLAS detector, which is situated within the hadronic calorimeter discussed in detail in Section 2.2.3.2 of this document.

Gap scintillators are located in the region between the central and extended Tile barrels which were also discussed in Section 2.2.3.2. They cover the $1.0 < \eta < 1.2$ region. The gap houses services to the ID systems, read-out electronic crates and the LAr cryostat flange, which result in "dead material" , where reconstructed energy signals may be lost. The additional plastic scintillator plates in this region correct for the energy loss. The scintillators are coupled to fibres which lead to the PMT's and the signals are read-out using the electronics used in the Tile barrels.

The MBTS are located within the gap and are mounted on the inner face plate of the electromagnetic endcap calorimeters as illustrated in Figure 3.1. They are situated at a smaller radius from the beam pipe and cover the $2.08 < \eta < 3.75$ region. These scintillators form part of the first level hardware trigger system and provide a trigger signal for events with potential physics of interest.

With the anticipated increase in beam energy, one would expect that the amount of radiation that the scintillator tiles are exposed to would also increase. As a result of this, the implementation of more radiation hard plastic scintillators is paramount in the upcoming upgrade of the Tile Calorimeter.

The plastic scintillators under scrutiny are EJ-200, EJ-208 and EJ-260, which were provided

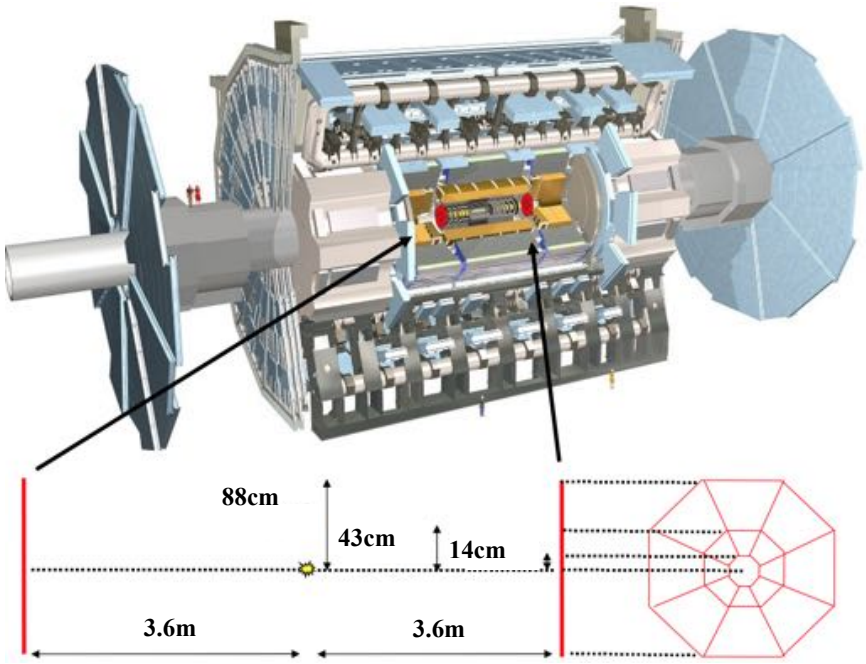


Figure 3.1: The location of the MBTS within the ATLAS detector.

to us by ELJEN technologies and are renowned for their commendable properties. These are polyvinyl toluene (PVT) based polymers which are scintillators that are doped with a certain amount of organic fluors. An additional PVT based scintillator and two polystyrene (PS) based scintillators were also investigated, namely, Bicron, Dubna and Protvino, respectively. In an effort to mimic the environment within the Tile Calorimeter, the different plastic scintillators are exposed to various radiation doses. The samples are then analyzed and the scintillator whose light transmittance is least affected by the radiation damage is considered as a potential suitable brand for the upgrade.

3.2 The Scintillation Mechanism

Plastic scintillators are described as materials that exhibit scintillation when excited by ionizing radiation. When scintillators are struck by incoming particles they absorb the energy and re-emit the absorbed energy in the form of light. The light that is created by the scintillators is proportional to the energy deposited by the incoming particles. There are many types of scintillators, ranging from organic to inorganic, and solids to liquids. The PVT based polymers

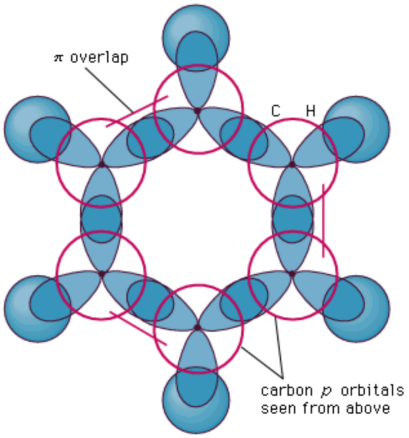


Figure 3.2: Schematic diagram of the π-bond overlap.

under investigation in this study are organic solid scintillators. PVT is a synthetic polymer which can be doped with anthracene to produce a plastic scintillator [118]. Anthracene is an organic semi-conductor which is a solid polycyclic aromatic hydrocarbon consisting of fixed benzene rings [119]. However, it is not known exactly what dopants are used on the plastic scintillators under scrutiny. The fast response and low cost production of organic scintillators such as the PVT based makes them a rational choice for use in large detectors. Such organic scintillators are made up of long chain vinyl toluene molecules. The Vinyl toluene is produced using ethyl benzene via a zinc-oxide catalyzed dehydrogenation reaction, and then polymerized to polyvinyl toluene [119]. Toluene is a benzene ring which is bonded to a methyl (CH_3) and a vinyl group (CH_2-CH-) [119]. On the other hand, polystyrene is a chain hydrocarbon chain with alternating carbon centers attached to phenyl groups, also a derivative of benzene.

The benzene ring is a common feature in plastic scintillators and is characterized by the delocalization of 3 π-bonds [120]. The chemical bonds that are present in a benzene ring include σ-bonds which are in the plane and π-bonds which are out of the plane and overlap. The π-bonds are responsible for the cloud of electrons above and below the molecular plane and these π electrons are completely delocalized. Figure 3.2 shows the overlap of the π-bonds which give rise to the delocalized electrons. It is these delocalized electrons that are prone to excitation by radiation, an essential integrant in the scintillation process. In actual fact, it is the de-excitation of these delocalized π electrons which results in luminescence. Figure 3.3 shows

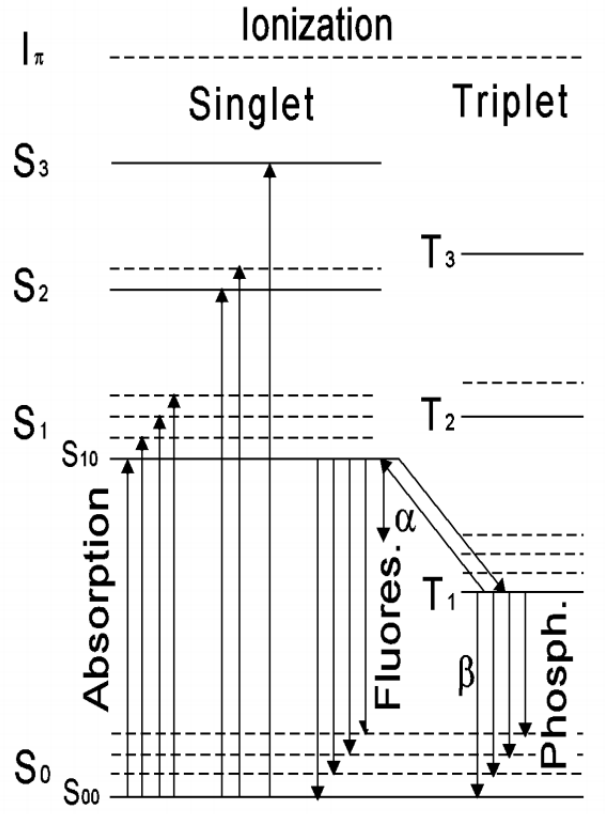


Figure 3.3: The electronic energy levels of an organic molecule.

the π-electronic energy levels of an organic molecule. In Figure 3.3, S_0 represents the ground state, S_1, S_2, and S_3 represent the excited singlet states and T_1, T_2 and T_3 represent the excited triplet states. S_{00}, S_{01}, S_{10}, and so on are all vibrational sub-levels. When particles strike the surface of the scintillator, the radiation is absorbed and results in a molecular excitation to the S_1 state. This is almost instantaneously followed by de-excitation back to the ground state (S_0), which is referred to as fluorescence. As shown in Figure 3.3, the fluorescence emission spectrum is roughly a "mirror image" of the absorption spectrum. The absorbed energy can also be emitted through two other processes: Phosphorescence and delayed fluorescence. Phosphorescence emits at longer wavelengths with exponential decay, whilst delayed fluorescence has the same spectrum as fluorescence but has no exponential decay and has a longer decay period.

It is worth mentioning that plastic scintillator bases have a very low fluorescent yield. They are not very transparent to their own scintillation light. This attribute elicits the need to

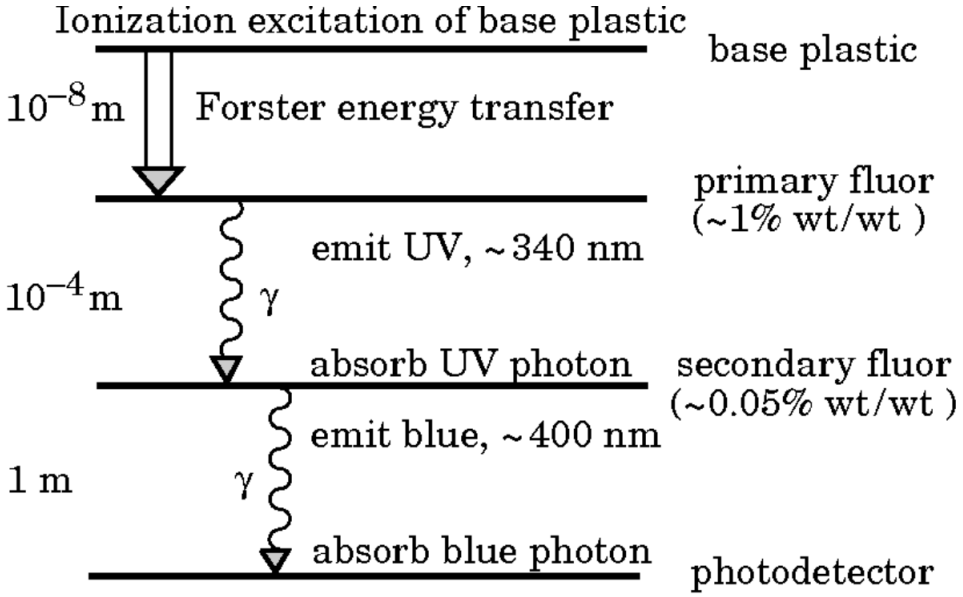


Figure 3.4: Schematic diagram of the scintillation 'ladder' depicting the operating mechanism of plastic scintillator.

incorporate additional fluors to the base in order to obtain a realistic and useful scintillator. Useful plastic scintillators are usually doped with organic fluors. These fluors are compounds, which absorb the base scintillation and re-emit it at longer wavelengths, which can be read-out by the PMTs. The schematic diagram in Figure 3.4 illustrates the different fluors under discussion. The plastic scintillator base absorbs energy from the incoming particles and emits it in the form of Ultraviolet (UV) radiation. The plastic scintillators are doped with a primary fluor which converts this UV radiation into visible light which is easier to propagate. For PS and PVT based scintillators, a primary fluor with a high quantum yield is added such that the absorption band overlaps the emission spectrum of the base [121]. Typical wavelength outputs are 340-360 nm, which is below that which can be read by the PMTs. A second fluor which further absorbs this visible light and emits it at even longer wavelengths, (typically in the blue) in order to allow this light to propagate to the edge of the scintillator with reasonably low loss of intensity due to attenuation. Typical output peaks are 400-410 nm as illustrated in the scintillation 'ladder' in Figure 3.4. Taking everything into account, the fluors are there to ensure that the wavelength of light leaving the scintillator is suitable for detection by the optical fibres which lead to the PMT tubes.

3.3 Methods

3.3.1 Radiation environment modelling

Inside the TileCal, the incoming particle showers carry high energy and interact with the plastic scintillators by imparting this energy through ionization. This ionization process is essential in understanding the damage mechanism within the target. In order to obtain useful results, a method to model the radiation environment prior to the actual radiation process is necessary. This modelling is done using a program called SRIM which stands for Stopping and Range of Ions in Matter. The SRIM program comprises of two parts: Stopping/Range tables and TRIM calculations, where TRIM stands for the Transport of Ions in Matter. The SRIM program takes into account the screened coulomb collisions between ions and target atoms. In addition, it also considers the exchange and correlation interactions between the overlapping electron shells. As a result of all this, SRIM gives detailed information about the interactions of the ions with the target atoms thus yielding meticulous predictions about the interactions that one ought to expect.

During the ionization process, the ions propagate straight through the material without stopping, hence the need to ensure that the beam of ions that will be used during radiation also pass straight through the scintillators without stopping. SRIM simulations were done to find the stopping range of 6 MeV protons as well as their energy deposited within the scintillator material. As shown in Figure 3.5, SRIM simulation results reflected that a 6 MeV proton beam would stop at a distance of 474.17 μm. This meant that the prepared samples would have to be $<$ 474.17 μm thick. We decided to prepare 350 μm thick samples.

The TRIM software is used to establish collisions between the ions and target atoms and thus gives information about the energy lost by the protons during ionization. From the simulations, the average energy of the transmitted protons through a 350 μm thick PVT target was found to be approximately 2.8 MeV, which implies that the energy lost by the 6 MeV protons is given by:

$$6 \text{ MeV} - 2.8 \text{ MeV} = 3.2 \text{ MeV} \tag{3.1}$$

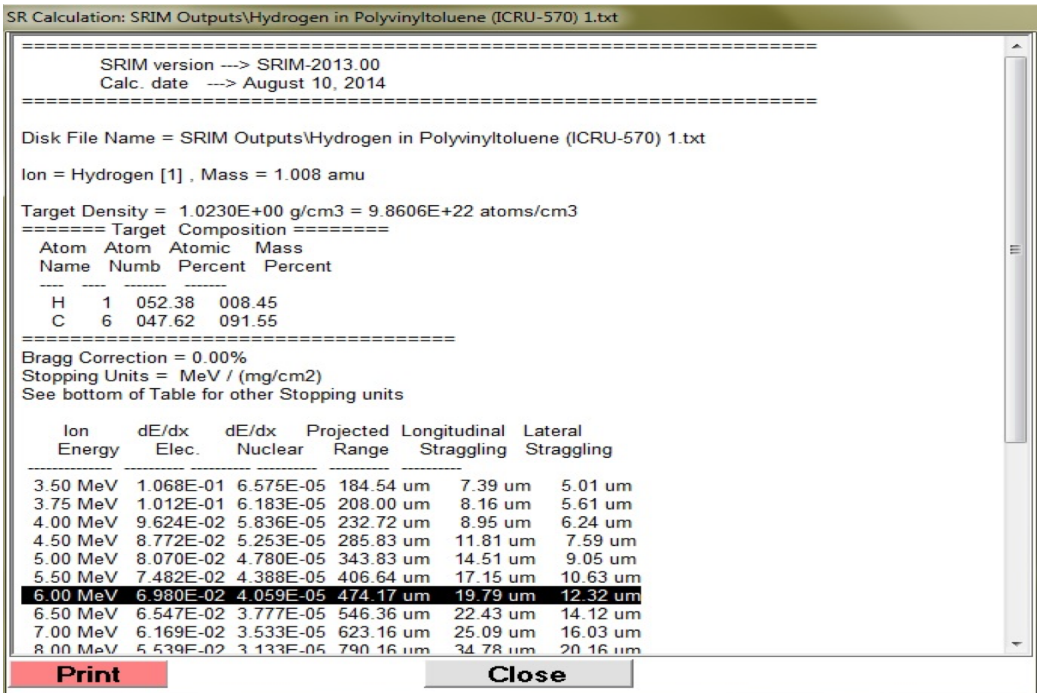


Figure 3.5: SRIM output interface showing the stopping range of protons in PVT based scintillator.

From this, one is able to plan the beam time and beam currents needed to achieve the anticipated radiation doses using the following relation:

$$R = \frac{N_p \times E_{lost}}{m}, \tag{3.2}$$

where:

- N_p is the number of protons impinging the sample,
- E_{lost} is the energy lost by protons (eV),
- m is the mass of the irradiated sample (kg),

such that:

$$N_p = \frac{i \times t}{q}, \tag{3.3}$$

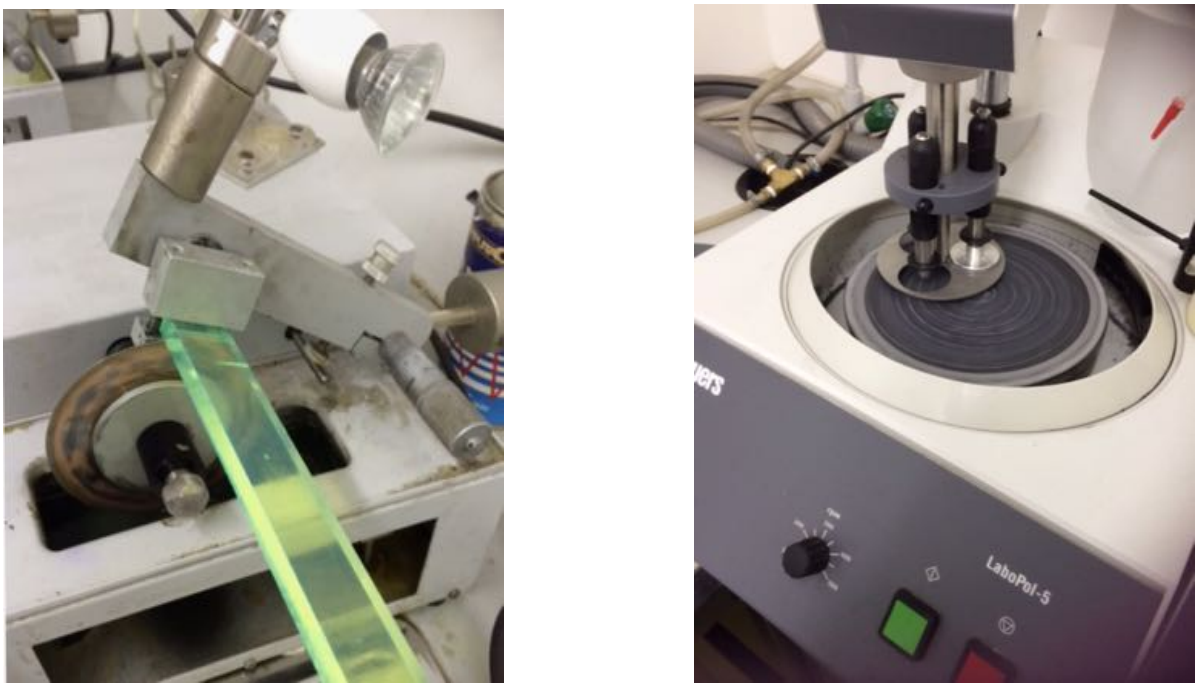
where:

- i is the beam current (A),
- t is the beam time or irradiation time (s),
- q is the proton charge (eV),

3.3.2 Sample preparation

Sample preparation is a crucial part of scientific research, that is, the accuracy at which samples are prepared for experimentation procedures affects the outcome of the research. Consequently, the sample preparation is a very delicate process and ought to be carried out carefully especially in the case of the very thin plastic scintillators samples. The sample preparation process was carried out at the 'Materials Preparation Lab' of the Physics building at the University of the Witwatersrand. The 'Metallographic Technique' was employed for this process, a technique which comprises of book-keeping, sectioning and cutting, mounting, rough polishing, final polishing and hardness testing.

During the book-keeping, one has to document the initial specimen condition in order to maintain quality control. Initially, the plastic scintillator samples were of dimensions of approximately 200 mm × 25 mm × 10 mm in length, width and thickness, respectively. After documentating the initial dimensions, the samples need to be sectioned and cut into the dimensions of interest. The target dimensions are 5 mm × 5 mm × 0.35 mm in length, width and thickness, respectively. A Buehler Isomet low speed cut off machine was used to cut the samples to the dimensions of interest. The machine uses a diamond coated blade with cutting fluid and uses relatively low speeds of between 0-300 rpm. The speed can be adjusted accordingly depending on the samples being cut. Higher speeds can be used for larger samples while lower speeds can be used for smaller ones as they are more fragile. Also, a force can be applied to the blade depending again on the sample sizes. All the loads available were used when cutting the larger samples, whilst a few loads were applied when cutting the smaller ones. The samples were cut into an area of 5 mm × 5 mm and thicknesses ranging between 0.4-0.7 mm. These samples were then prepared for polishing in order to attain the thickness of interest. Figure 3.6a shows the initial cutting of the EJ 260 sample.



(a) (b)

Figure 3.6: (a) An image of the actual sample cutting process using the Buehler Isomet low speed cut off machine. (b) An image of the actual sample polishing process using the Struers Metallographic Polishing Machine.

For the purpose of polishing, Figure 3.6b illustrates the polishing process, which required the samples to be mounted onto aluminum holders in order to be polished down. They were subjected to medium polishing as well as final polishing. During the medium polishing, the samples were polished using a 6 μm diamond suspension on Struers MD-Dac polishing cloth (acetate cloth) at a speed of 120 rpm in 5 minute intervals. The final polishing was done using a 1 μm diamond suspension on Struers MD-Nap cloth (synthetic cloth) at a speed of 150 rpm again in 5 minute intervals. After polishing, the sample thicknesses were measured using a micrometer screw gauge and were found to range between 300 μm and 380 μm. In order to ensure accurate beam time planning, simulations were also done for these various samples. The final samples after the preparation process are shown in Figure 3.7.



Figure 3.7: An image of EJ 200 scintillator after the cutting and polishing process and being mounted onto the sample holder.

3.4 Experimental procedure

3.4.1 Radiation process

The plastic scintillators were exposed to radiation using a Tandem accelerator situated at iThemba LABS Gauteng. Figure 3.8 shows a schematic diagram of the tandem accelerator. The tandem accelerator is a 2-stage accelerator which is run using a generator that acts as a high voltage source. For the first part of the accelerator, the ion source at the terminal produces a beam of positively charged ions which is accelerated to a low energy by the high voltage supply. The beam then passes through a region containing a gas at low pressure where some of the protons are converted to negative hydrogen ions by addition of two electrons. As the mixture of charged particles passes through the magnetic field, the positively charged ones are defected away and the negatively charged ones are deflected into the accelerator tube. The beam of negative ions are accelerated to 3 MeV towards a positive high voltage terminal. Within the terminal, the particles pass through thin carbon foil that strips off two electrons thus converting many of the negative ions back into positive particles. The protons are repelled by the terminal and further accelerated to an additional 3 MeV through the second part of the tube. At the output end of the accelerator, the protons are magnetically separated from other particles in the beam through the extraction line and the extracted beam is then directed to the target of interest using quadrupole magnets.

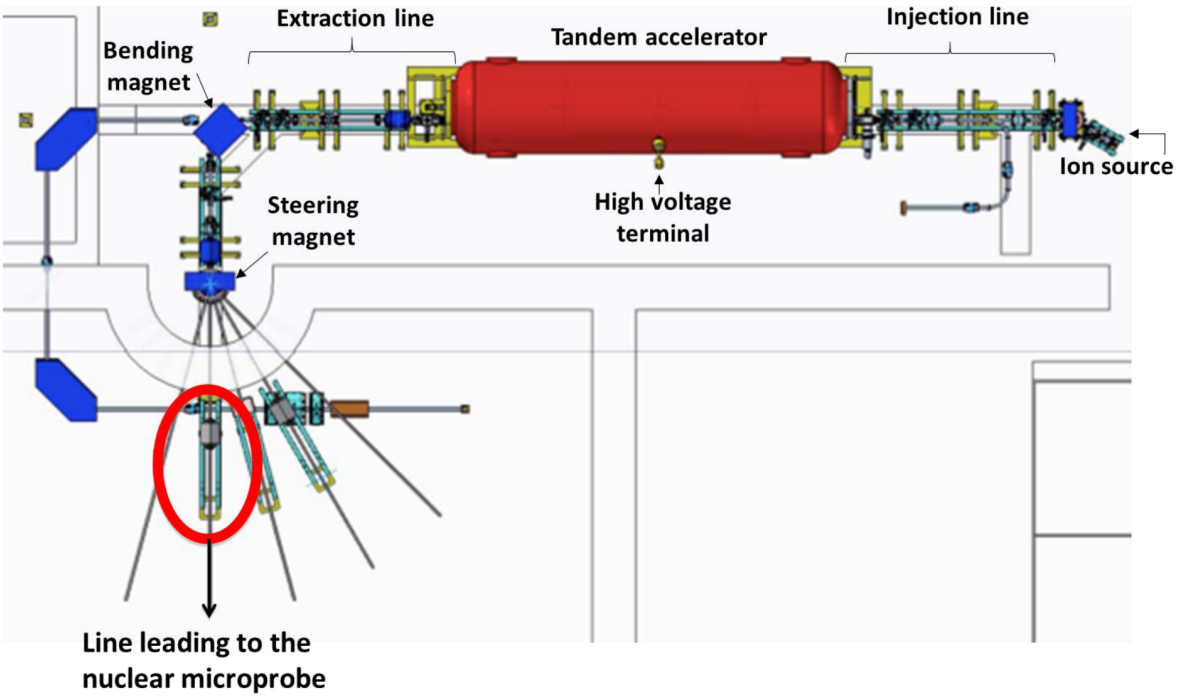


Figure 3.8: A schematic diagram of the tandem accelerator of iThemba LABS Gauteng.

The samples were mounted onto holders and then carefully placed inside a carousel located inside a microprobe chamber which was then mechanically lowered into a nitrogen vacuum chamber. They were irradiated using a 6 MeV proton beam at a high dose of 80 MGy, an intermediate dose of 25 MGy, a medium dose of 8 MGy and a low dose of 0.8 MGy. Table 3.4.1 summarizes the log of the radiation dates, beam currents, beam times and radiation doses for the PVT scintillators provided by ELJEN technologies. Figure 3.9 shows the EJ 260 sample after the irradiation process.

3.4.2 Transmission spectroscopy

After irradiation the samples were subject to transmission spectroscopy. Light transmittance data corresponding to the PVT based plastic scintillators was collected. The data was collected using the Varian Cary 500 spectrophotometer which is also available within the physics building of the University of the Witwatersrand. Figure 3.10 shows an image of the spectrophotometer using in this analysis. A detailed diagram of the internal components of the Varian Cary 500

Table 3.1: Table showing a log of the radiation dates, beam currents, beam times and radiation doses for the various PVT based scintillators.

Radiation date	Sample	Number	Thickness	Energy lost (MeV)	Current (nA)	Time (min)	Dose (MGy)
17/08/14	EJ 200	13	365	3.4	13-16	35	85.58
	EJ 208	11	320	2.83	16-18	30	80.78
28/08/14	EJ 260	13	360	3.33	10-12	45	82
18/09/14	EJ 208	12	300	2.71	1.2-1.4	45	8.8
19/09/14	EJ 260	15	360	3.33	2.2	23	8.5
	EJ 200	11	340	3.07	1.3	39	8.3
29/09/14	EJ 260	18	330	2.95	0.45-0.55	11	0.88
30/09/14	EJ 200	14	385	3.68	0.4	12	0.831
	EJ 208	13	300	2.71	0.45-0.50	12	0.858
06/10/14	EJ 208	15	350	3.2	2.5	60	24.8
	EJ 200	16	330	2.95	3.5	45	25.4
07/10/14	EJ 260	19	350	3.2	3	52	25.8



Figure 3.9: An image of EJ 260 after irradiation using a high dose.

spectrophotometer can be seen in Appendix A.

The Varian Cary 500 is a dual beam spectrometer, which has a very stable internal light source. It uses a tungsten lamp and deuterium lamp to probe both the visible light and ultra-violet light spectrum, respectively. Prior to the transmission process, the machine is turned on to warm up for approximately 30 minutes in order to allow the internal components and the thermoelectrically cooled Pbs detector to achieve thermal equilibrium. In addition, the spectrometer was calibrated prior to taking the transmission measurements. The Varian Cary contains two ports available for the transmission measurements. Sample holders specific to the machine as well as unique to our PVT based scintillators were manufactured for us within the physics building for this process. Both holders were placed into the sample port and reference port respectively in the absence of the samples being measured. A baseline as well as zeroing



Figure 3.10: A photograph of the Varian Cary 500 spectrophotometer.

calibration were performed on the machine prior to each days testing.

3.5 Results and analysis

Following data collection, distributions of percentage transmission against the wavelength of light were plotted. This was done in order to observe the effects of radiation on the light transmission of plastic scintillators. Data corresponding to % light transmission at various wavelengths, between 300 nm and 800 nm was collected and analyzed.

Figure 3.11 shows the % light transmission versus the wavelength for the unirradiated EJ 200, EJ 208 and EJ 260. From the literature [122], it is mentioned that PVT scintillators typically absorb radiation in the UV region hence why one can see a decline in transmission around 400 nm in the distributions. For the EJ 260, there is an absorption dip between 370 nm and 470 nm, which is accounted to the base being doped with fluors that absorb light in that region. From reading off the data for the % transmission of each sample at approximately 480 nm, it is observed that EJ 200 possesses 85.7% transmission, EJ 208 possesses 83.2%

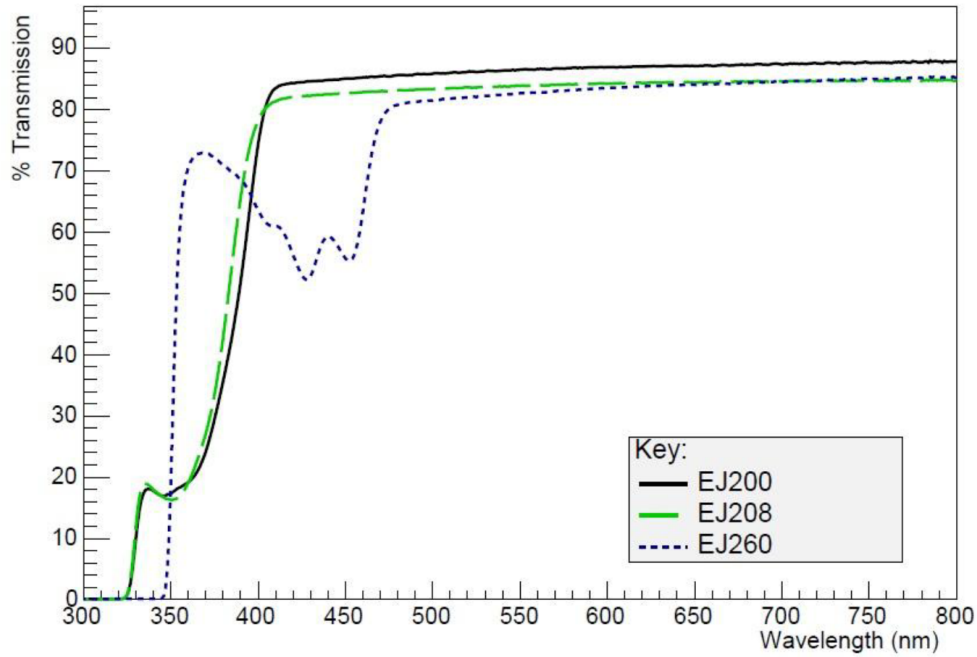


Figure 3.11: The % Transmission versus Wavelength distribution for the unirradiated EJ 200, EJ 208 and EJ 260 samples.

transmission and EJ 260 possesses 80.8% transmission. From this distribution it is clear that EJ 200 possesses the highest light transmission properties prior to radiation exposure.

According to [122], exposing PVT based polymers to a significant amount of radiation results in the breaking of their chemical bonds, which affects their properties. Free radicals are formed at the breaking points of the carbon and hydrogen bonds, resulting in hydrogen degassing, which in turn results in a carbon enriched sample. The formation of free radicals is bound to affect the scintillating mechanism of the plastic scintillators as they tend to absorb fluorescent light thus limiting their light yield capacity.

The transmission data for all the samples was collected one day after they were exposed to radiation. Distributions of % light transmission against the wavelength for each scintillator grade at various doses were also considered. Figures 3.12, 3.13 and 3.14 show the distributions corresponding to the EJ 200, EJ 208 and EJ 260, respectively, at various doses: 80 MGy, 25 MGy, 8 MGy and 0.8 MGy. For each distribution, the irradiated samples are compared to their unirradiated. From the Figures one can observe that the irradiated samples form absorption

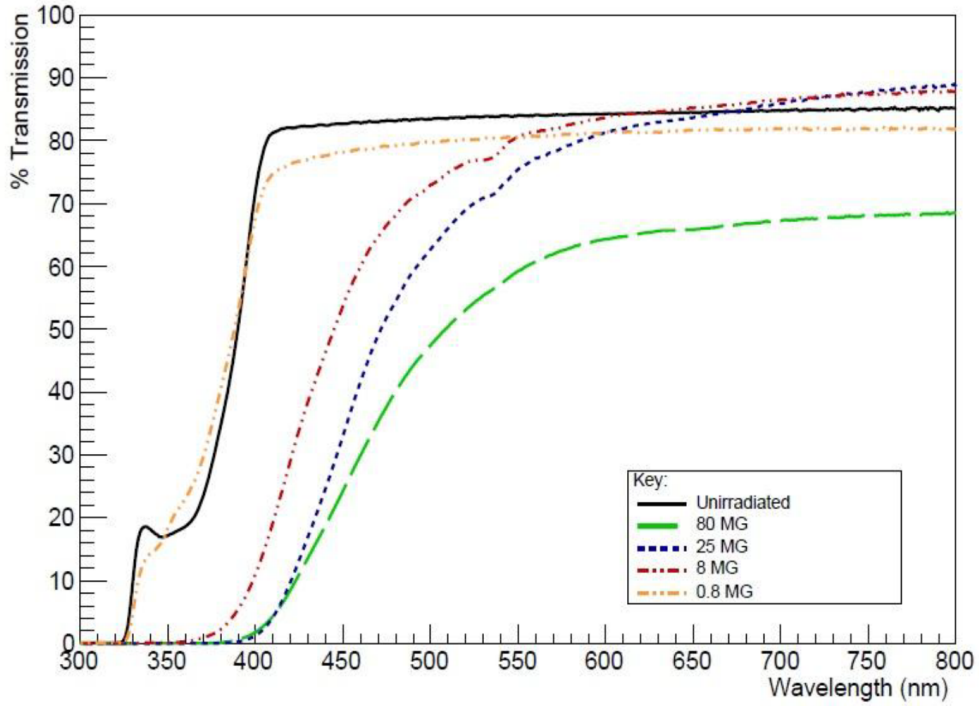


Figure 3.12: The % Transmission versus Wavelength distribution for EJ 200 for different doses.

centres which tend to shift to longer wavelengths as the dose is increased. The PVT and PS based plastic scintillators typically emit light in the blue end of the spectrum, approximately between 400-495 nm, hence why calculations to compare transmission decrease was done within that range of wavelengths.

Calculations to compare transmission decrease were done at a wavelength of 420 nm, the wavelength that is read out by the optical fibres of the TileCal, using the following relation:

$$\%\ \text{transmission loss} = \%\ \text{transmission of unirradiated} - \%\ \text{transmission of irradiated.} \quad (3.4)$$

The % transmission loss results are summarized in Table 3.2 and loss calculations were done at a wavelength of 420 nm, within the read-out range. Transmission data corresponding to the Protvino, Dubna and Bicron samples was previously collected by my colleague and was used to compare. It is observed that the PS based plastic scintillators, that is, Protvino and Dubna undergo a high decrease in transmission for most of the doses. The exception being Protvino, which has a low decrease in transmission for the intermediate (25 MGy) and low

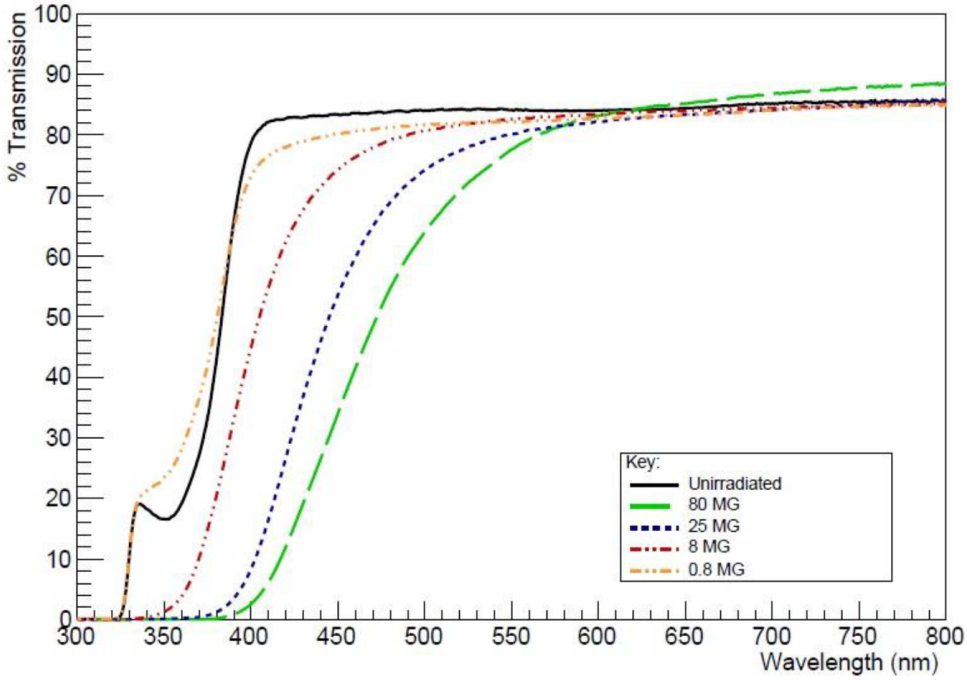


Figure 3.13: The % Transmission versus Wavelength distribution for EJ 208 for different doses [19].

Table 3.2: Table showing the % transmission loss for all samples at a wavelength of 420 nm, considering all the different doses: 80 MGy, 25 MGy, 8 MGy and 0.8 MGy [19].

Sample	**Dose (MGy)**	**% Trans. loss**	**Sample**	**Dose (MGy)**	**% Trans. loss**
EJ 200	80	42.9	Protvino	80	60.8
	25	28.6		25	34.8
	8	14		8	7.4
	0.8	3.9		0.8	3.3
EJ 208	80	29.1	Dubna	80	51.3
	25	14.9		25	35.1
	8	4.7		8	26.6
	0.8	2.5		0.8	5.5
EJ 260	80	44.8	Bicron	80	45.5
	25	15.5		25	39.5
	8	14.3		8	11.5
	0.8	6.6		0.8	8.7

doses (0.8 MGy). The Protvino type was manufactured for TileCal so a better replacement would be ideal. The PVT based scintillators provided by ELJEN technologies show overall

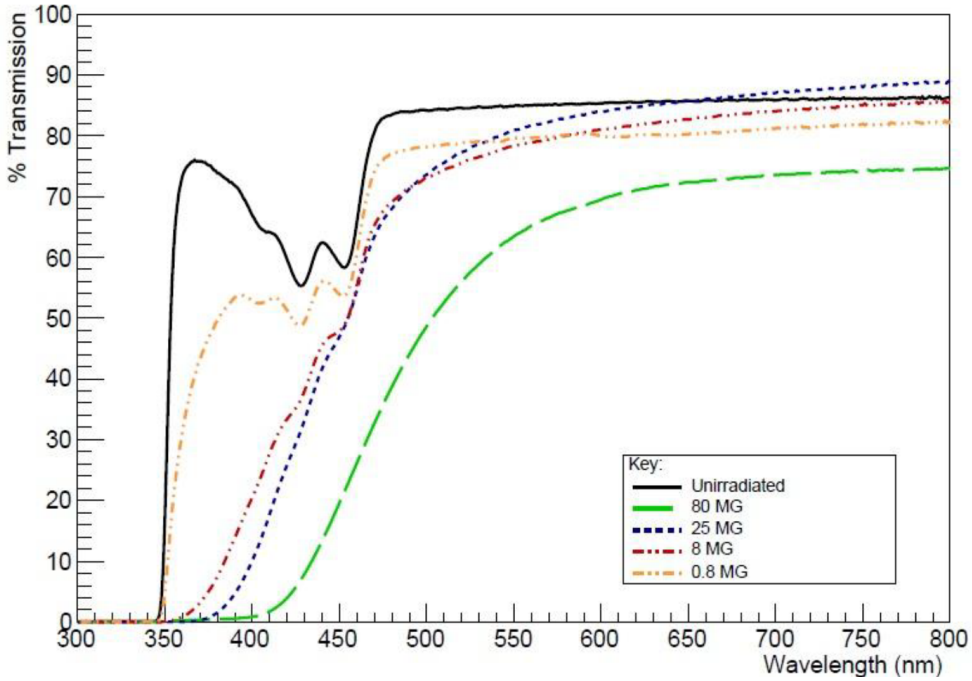


Figure 3.14: The % Transmission versus Wavelength distribution for EJ 260 for different doses.

reasonable amount of decline in percentage transmission for all the doses in comparison to all the other grades. In fact, for the high dose (80 MGy), intermediate dose (25 MGy) and low dose (0.8 MGy), EJ 260 has the highest decrease in % transmission. EJ 200 has the highest decrease in the intermediate dose case (25 MGy) while EJ 260 shows the highest decrease in transmission for all four doses. Among the ELJENs, EJ 208 and EJ 200 are more suitable replacement candidates since they show the least amount of decrease in transmission for the lowest dose which is closer to that of the detector environment. However, other additional experiments are performed in order to isolate the most suitable candidate among these two.

In an effort to evaluate recovery or annealing after the radiation process, graphs of % transmission versus wavelength for each grade for transmission taken on different days were also compared. Figures 3.15, 3.16 and 3.17 show the % transmission versus wavelength distributions for EJ 200, EJ 208 and EJ 260, respectively, corresponding to the intermediate dose (25 MGy) on different days. From the distributions, it is observed that on the day of irradiation the absorption centre had shifted away from the unirradiated to approximately between 400 nm and 500 nm. Two or 3 days after irradiation, the absorption dip shifted more

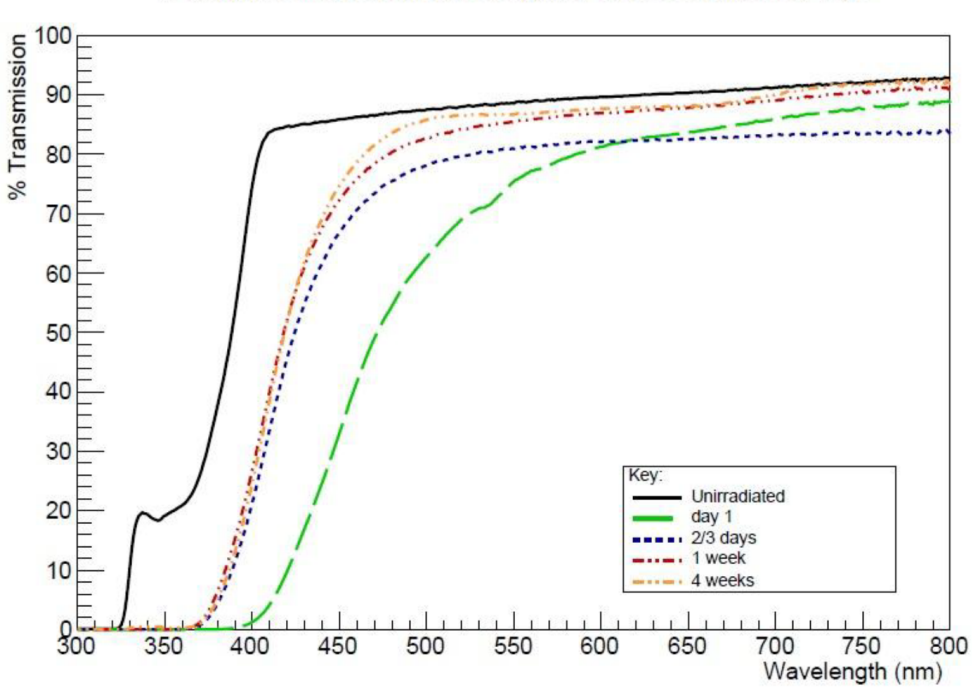


Figure 3.15: The % Transmission versus Wavelength distribution for EJ 200 corresponding to the intermediate dose (25 MGy) on different days.

towards lower wavelengths towards the unirradiated graph. After one week, again there was a slight shift in the absorption dip, towards the unirradiated distribution. This is a clear indication of the annealing process undergone by the samples. In fact, the yellowing that was observed on the samples after irradiation began to fade after even just a day after irradiation. Table 3.3 shows the difference in % transmission between two different days that transmission data was taken at a wavelength of 480 nm. This is shown for all the EJ 200, EJ 208 and EJ 260 for only two specific doses: 25 MGy and 8 MGy. For the higher dose EJ 208 showed the most amount of healing as a large difference in transmission is seen. For the smaller dose, EJ 200 reflected the most amount of healing in comparison to the others.

3.6 Conclusions

Plastic scintillators generally possess commendable properties, however, their vulnerability when exposed to high doses of radiation is a major issue. All types of scintillators are affected

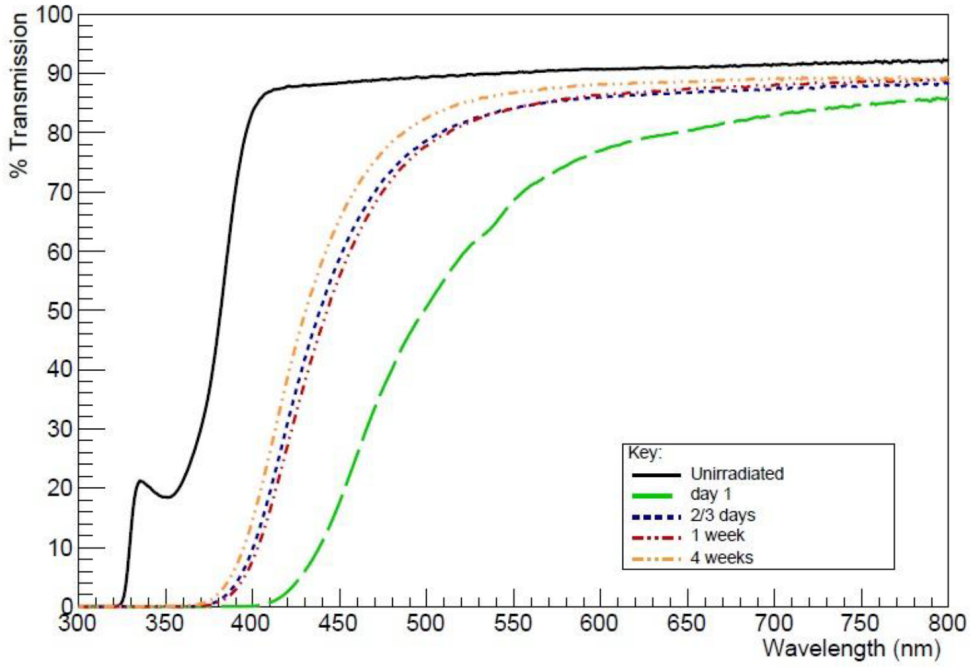


Figure 3.16: The % Transmission versus Wavelength distribution for EJ 208 corresponding to the intermediate dose (25 MGy) on different days [19].

Table 3.3: Table showing the % transmission difference for different days over two doses: intermediate dose (25 MGy) and medium dose (8 MGy) [19].

Sample	**Dose (MGy)**	**%Trans. diff. (Day1 - 1 Week)**
EJ 200	25	30.38
EJ 208	25	37.06
EJ 260	25	6.45
		%Trans. diff. (Day 1 - 4 Weeks)
EJ 200	8	15.05
EJ 208	8	5.92
EJ 260	8	2.22

by radiation exposure. Studies show that when polymer based scintillators are exposed to high radiation doses, their chemical bonds are broken and their polymer properties are changed. At the breaking points of the hydrogen and carbon bonds, free radicals are formed resulting in hydrogen degassing which leaves a carbon enriched material. This formation of free radicals affects the scintillating mechanism of the plastic scintillators.

The transmission results obtained in the present study reflect that indeed an increase in

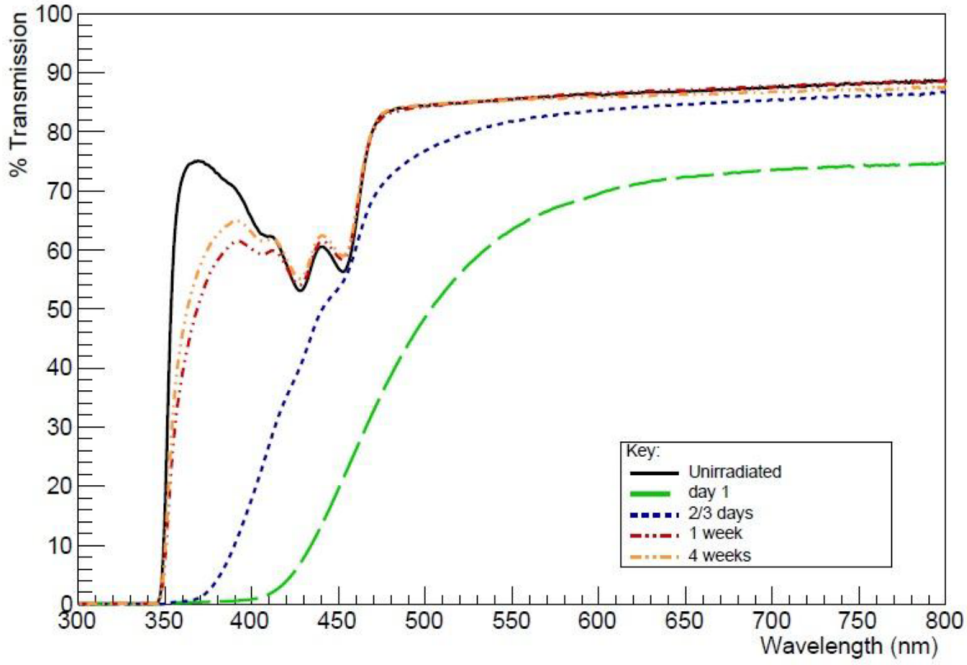


Figure 3.17: The % Transmission versus Wavelength distribution for EJ 260 corresponding to the intermediate dose (25 MGy) on different days.

radiation results in a decline in light transmission for all of the various grades of plastic scintillators considered. This behaviour could also be associated to the dopants absorbing the base scintillation rather than emitting it. When comparing the transmission spectra of each dose with its unirradiated in the wavelength range that is read out by the optical fibres of the ATLAS detector, we found that the PVT based scintillators provided by ELJEN technologies showed the least amount of decline in percentage transmission in comparison to the other brands.

Data corresponding to the Protvino, Dubna and Bicron samples was collected and compared. It was observed that the PS based plastic scintillators (Protvino and Dubna) undergo a high decrease in transmission for most of the doses. Even though Protvino showed a low decrease in transmission for the intermediate (25 MGy) and low doses (0.8 MGy), it was not as low as the case of EJ 208. It was observed that EJ 208 showed the least amount of decline in percentage transmission for most of the doses. By contrast, EJ 260 showed the highest amount of decline in percentage transmission in comparison to the other two ELJEN brands.

To add on, the annealing of a sample after irradiation plays an important role in establishing

whether a material is radiation hard or not. From the transmission data collected on different days, it was observed that the plastic scintillators do indeed undergo some healing after radiation. From comparing the annealing associated with both doses, it was found that EJ 208 and EJ 200 both experienced a substantial amount of annealing in comparison to EJ 260. Also, it was also noted that for all the ELJEN grades, the most amount of healing occurred within the first few days after irradiation in comparison to weeks later. Moreover, from these results and observations, it is clear that even though EJ 200 showed the best transmission properties at the start, after irradiation, EJ 208 possessed the better transmission properties, with EJ 200 following. This is supported by the fact that these samples showed the least amount of decrease in percentage light transmission for most the doses. The general conclusion would be that among the PVT based scintillators provided by ELJEN technologies the EJ 200 and EJ 208 are generally more radiation hard than the EJ 260, with EJ 200 showing the most amount of annealing in comparison to the others. All the scintillators maintained their structural properties, the damage could therefore be correlated to a bleaching related effect of the fluors. The bleaching could be as a result of oxygen reacting with the free radicals which are formed during the breaking of the atomic bonds.

Light yield studies were also later conducted [20] to further aid in the recommendation of the best plastic scintillator grade to use during the upgrade of the Tile Calorimeter of ATLAS. Since it also remains fairly transparent to its light output as well at a dose of 0.8 MGy, it is rendered the most suitable candidate to use for the upgrade. Since the highest dose currently expected within the TileCal over the next several years is approximately 10 kGy, EJ 200 may be considered a potential candidate for replacement of the gap and MBTS scintillators in 2019-2020 since it shows the most amount of annealing at 0.8 MGy.

CHAPTER 4

OBJECT RECONSTRUCTION AT ATLAS

The accurate reconstruction of physics objects in the ATLAS detector is crucial for physics analyses. The search for a Higgs boson decaying to two photons in association with missing transverse energy requires the precise reconstruction and identification of photons, jets, electrons, muons and missing transverse energy. This chapter describes the reconstruction of particle tracks, vertices and particle energies from the signals of these objects in the ATLAS detector described in the previous chapter.

Sections 4.1 and 4.2 highlight the reconstruction of charged particle tracks and vertices. Sections 4.3, 4.6, 4.4 and 4.5 detail the reconstruction, identification and isolation of photons, electrons, muons and jets respectively. Section 4.7 gives a brief introduction to missing transverse energy which is discussed in detail in a separate chapter as it forms a predominant aspect of the research documented in this thesis.

4.1 Track reconstruction

The precise track reconstruction is critical for physics analyses at ATLAS. From a reconstructed track, one can determine the origin, direction and momentum of a particle. As charged particles traverse the detector they deposit energy along their path, leaving signals in various sensors. Figure 4.1 shows the trajectories of various hard objects as they move through the detector.

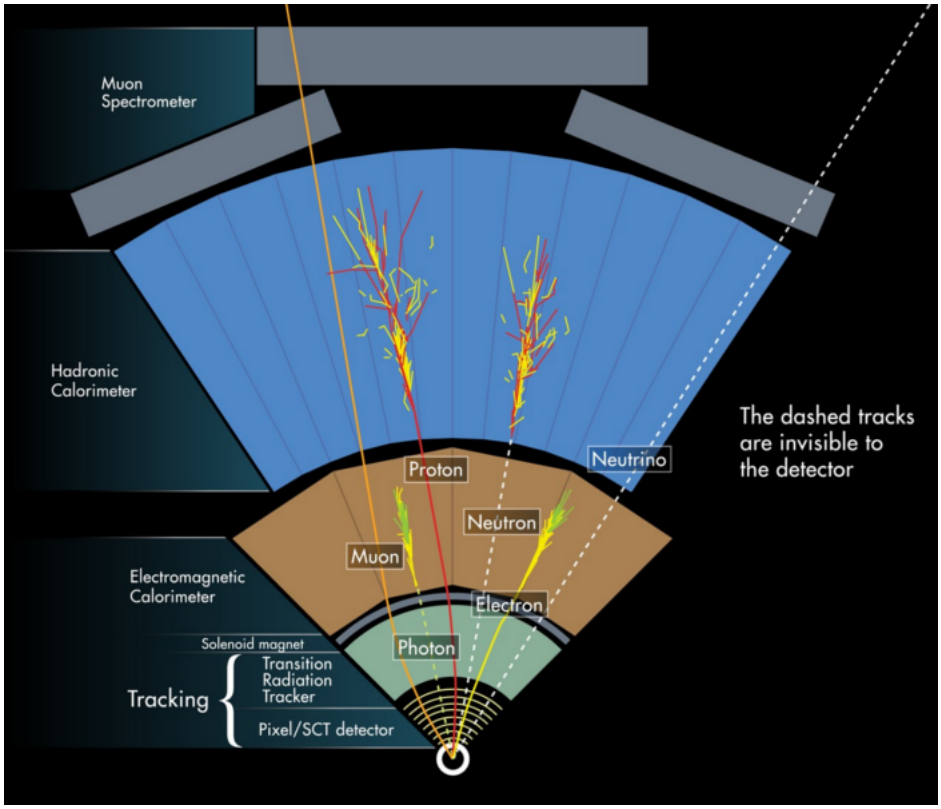


Figure 4.1: A segment along the transverse plane showing the trajectories of the various hard objects as they traverse the detector.

The collection of these sensor measurements are referred to as "hits" and track reconstruction associates these hits to individual particles and maps out their trajectories.

At ATLAS, tracks are reconstructed in the ID using a sequence of algorithms. Details of these can be found in Reference [123]. The first stage of tracking operates an *inside-out* tracking algorithm, which begins with seeds in the silicon detector and performs a first track reconstruction, which is extended to the TRT [124]. Seeds are produced from three-dimensional space points corresponding to the locations of the hits and provide sufficient directional information to predict regions with further hits corresponding to a particular track. A track fitting Kalman filter algorithm [125] beginning from the seeds is done each time hits are added to tracks. The tracks reconstructed by this algorithm are required to have $p_{\mathrm{T}} > 400$ MeV and after a sequence of quality selections, the selected tracks are then extended into the TRT.

In the second stage the track search begins from the segments reconstructed in the TRT

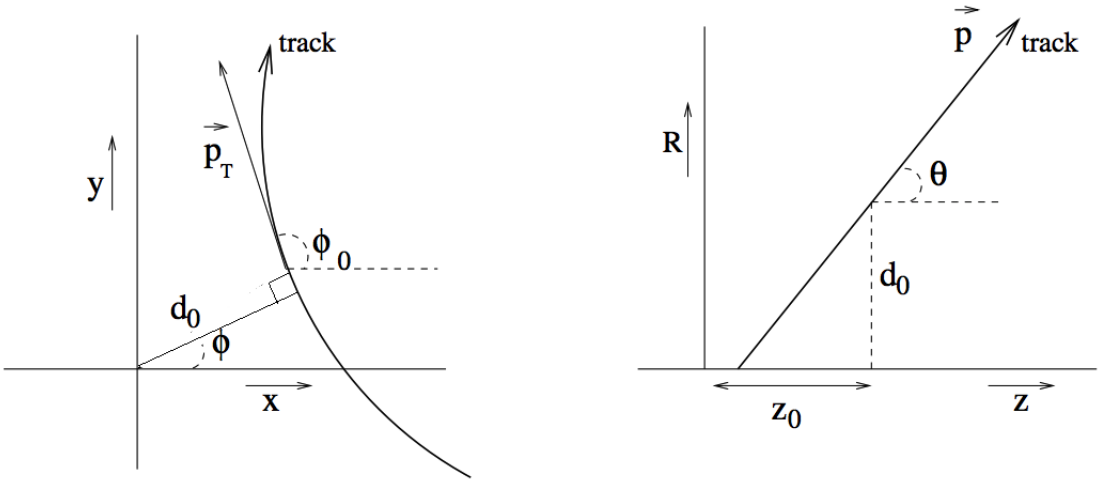


Figure 4.2: An illustration of the perigee parameters of a track in the $x-y$ plane (left) and $r-z$ plane (right), as described in the global ATLAS tracking frame.

and extends inwards by adding silicon hits. This is referred to as the *outside-in* sequence or back-tracking. This is designed to reconstruct secondary charged particles which are produced in the interactions of primary ones as well as take into account all the hits that were not selected by the previous sequence. When further hits are found the tracks are then refined using the same Kalman filter algorithm.

A track is parametrized using 5 perigee parameters as shown in Figure 4.2:

- $\frac{q}{p}$: the particle charge divided by its momentum
- ϕ_0: the angle with the x-axis in the $x-y$ plane at the perigee point (azimuthal angle)
- θ_0: the angle with the z-axis in the $r-z$ plane (polar angle)
- d_0: the track impact parameter in the transverse plane. The signed distance to the z-axis
- z_0: the track impact parameter in the longitudinal plane. The z-coordinate of the track at the point of closest approach to the global z-axis

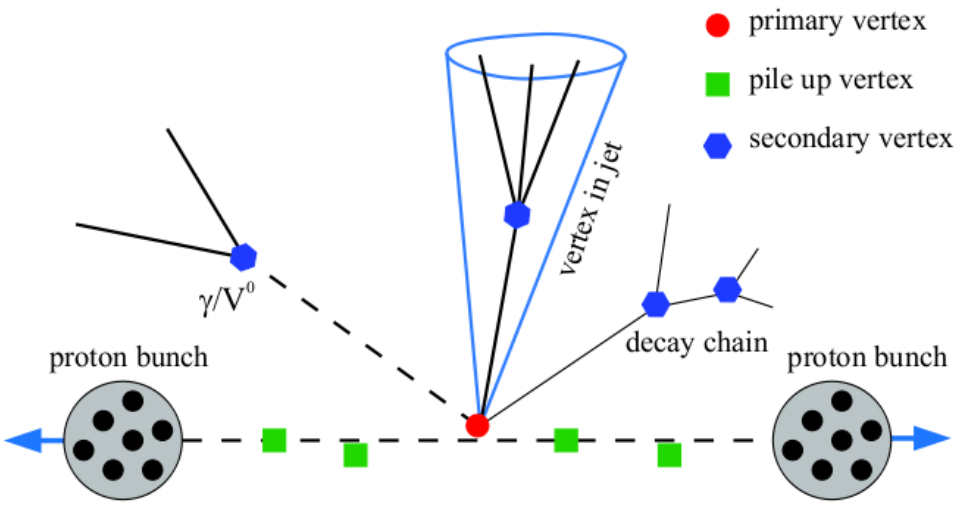


Figure 4.3: An illustration of reconstructed vertices at ATLAS.

4.2 Vertex reconstruction

After the tracks are established, the vertices from which they emanate are then reconstructed. A Primary Vertex (PV) is a pp collision point from which most of the reconstructed tracks originate. PVs are reconstructed from a combination of tracks using an adaptive vertex fitting algorithm [126] which comprises of two steps: A PV finding algorithm and a vertex fitting algorithm. The PV finding algorithm associates reconstructed tracks to the vertices and the latter estimates the vertex position and corresponding uncertainties.

Vertex seeds are obtained from the z-position of the beamline of the reconstructed tracks and an iterative χ^2 fit is made using the seed and nearby tracks. Tracks that are displaced by more than 7σ from the vertex are used to seed a new vertex and the process is repeated until there are no longer any vertices. During vertex reconstruction, the vertices are required to have at least 2 tracks with $p_{\mathrm{T}} > 400$ MeV associated with them in order to enhance the resolution of the vertex spatial position.

However, the presence of pile-up increases the number reconstructed vertices in the event. This is due to the fact that the high pile-up environment enhances the number of fake tracks thus increasing the probability of reconstructing a fake vertex. To deal with this predicament

the vertex with the highest sum of the squared track p_{T} is considered to correspond to the hardest pp interaction. This is defined as the main vertex or primary vertex [127] and the rest of the PVs are assumed to be as a result of pile-up interactions. In addition, the vertices which are inharmonious with the beam collision region are considered to be secondary PVs. Figure 4.3 shows an illustration of reconstructed vertices at ATLAS. It is worth mentioning that a different method of identifying the PV is employed in the $h \rightarrow \gamma\gamma$ analysis described in Chapter 5 of this thesis. This method is used to identify the exact location of the diphoton vertex and is employed in an effort to achieve a precise measurement of the diphoton invariant mass, $m_{\gamma\gamma}$, as well as a precise computation of track-based quantities.

4.3 Photon reconstruction

Photons form the basis of the main analysis in this documentation and will therefore be discussed in detail. When a photon is produced at an interaction point it first passes through the tracker then enters the EM calorimeter and loses all its energy through EM showering which can be spread over a wide range. The photon can exhibit two different behaviours: remain unconverted and traverse through the tracker without interacting or convert into an electron-positron pair before entering the EM calorimeter. As a result, in order to ensure the inclusion of all the energy deposits, photons are reconstructed by clustering the energy deposits in the EM calorimeter and using track information to match the clusters accordingly.

Photon candidates are reconstructed from the clusters of energy deposits in the EM calorimeter and are required to have $E_{\mathrm{T}} > 2.5$ GeV [128, 129]. The reconstruction of photons starts with the search for energy clusters in the calorimeters. The calorimeter is divided into a grid of towers each sized $\Delta\eta \times \Delta\phi = 0.075 \times 0.025$ and the total tower energy is equivalent to the sum of energy deposits from all the layers of the calorimeter. A sliding window algorithm of size $\eta \times \phi = 3 \times 5$ towers selects the cluster seeds with a total $E_{\mathrm{T}} > 2.5$ GeV or more. An additional duplicate removal algorithm is employed whereby several cluster seeds within any 2×2 tower region are selected and only the one with the largest transverse energy is selected. The information from tracks is then used to classify the cluster seeds as either electrons or

photons in order to construct the appropriate type of cluster. The reconstruction algorithm looks for matches between energy clusters and tracks that are reconstructed in the ID and extrapolated to the calorimeter. Clusters without matching tracks are classified as unconverted photon candidates and those matched to pairs of tracks consistent with a $\gamma \rightarrow e^+e^-$ conversion process are known as converted photon candidates. Due to the uncertainty that comes with discriminating between electron and photon signatures, clusters may be reconstructed with both in consideration in order to maximize the reconstruction efficiency for both candidates. In fact, clusters matched to single tracks without hits in the pixel layer active region closest to the beam pipe are considered both as converted photons as well as electrons. The efficiency to correctly reconstruct photons from these clusters and tracks is 96% with the remaining 4% corresponding to those that are incorrectly reconstructed as electrons. Generally, the energy measurement is done by summing all the deposits in the EM calorimeter cells corresponding to the candidate clusters. This energy has to be corrected for energy losses, energy deposits outside the cluster area as well as the variation of energy response as a function of impact point on the calorimeter. A detailed discussion on the calibration can be found in Reference [130]. The calibration factors for the energy scale are obtained from $Z \rightarrow e^+e^-$ events. This is done using a data-driven method whereby by the width of the Z boson resonance is matched to the one that is observed in data resulting in an additional contribution to the electron energy resolution.

4.3.1 Photon Identification and Isolation

Attentive photon identification (PID) is essential at ATLAS in order to segregate photons which arise from hadronic decays. Algorithms for PID at ATLAS rely on the shower shape variables. Shower shape variables are determined from rectangular cuts on calorimeter variables which describe how the energy deposited in the EM shower is deposited. These variables can be broadly categorized into measuring hadronic leakage, energy distributions in the middle-layer and strip layer of the calorimeter system. These are briefly described in Table 4.1 and a more detailed description can be found in References [131, 132]. The shapes of the showers induced by photons, electrons and jets vary. Photons tend to have narrow showers in comparison to jets

Table 4.1: The discriminating variables used for loose and tight photon identification with indication of which cuts are used in loose and tight photon identification.

Category	**Description**	**Name**	***loose***	***tight***
Acceptance	$\|\eta\| < 2.37$, with $1.37 < \|\eta\| < 1.52$ excluded	-	✓	✓
Hadronic leakage	Ratio of E_{T} in the first sampling layer of the HCal to E_{T} of the EM cluster (used over the range $\|\eta\| < 0.8$ or $\|\eta\| > 1.37$)	R_{had_1}	✓	✓
	Ratio of E_{T} in all layers of the hadronic calorimeter to the E_{T} of the EM cluster (used over the range $0.8 < \|\eta\| < 1.37$)	R_{had}	✓	✓
EM middle layer	Ratio between the sum $E^{s_2}_{3\times7}$ of the cell energies in a 3×7 rectangle (measured in cell units in $\eta \times \phi$), and a sum $E^{s_2}_{7\times7}$ of the cell energies in a 7×7 rectangle, both centered around the cluster seed	R_{η}	✓	✓
	Lateral width of the shower in the η direction	w_{η_2}	✓	✓
	Ratio between the sum $E^{s_2}_{3\times3}$ of the cell energies in a 3×3 rectangle (measured in cell units in $\eta \times \phi$), and a sum $E^{s_2}_{3\times7}$ of the cell energies in a 3×7 rectangle, both centered around the cluster seed	R_{ϕ}		✓
EM strip layer	Lateral shower width for maximum strip and two neighbours	w_{s_3}		✓
	Total lateral shower width	$w_{s_{tot}}$		✓
	Fraction of energy outside core of three central strips but within seven strips	F_{side}		✓
	Difference between the energy of the strip associated with the second maximum in the strip layer, and the energy reconstructed in the strip with the minimal value found between the first and second maxima	ΔE_s		✓
	Ratio of the energy difference associated with the largest and second largest deposits over the sum of these energies	E_{ratio}		✓

and jets deposit most of their energy in the hadronic calorimeter. As seen in Table 4.1, the *loose* PID applies cuts only on the shower shapes R_η, w_{η_2}, and either R_{had} or R_{had_1}, depending on the pseudorapidity range of the photon candidate. The *tight* PID applies stricter cuts on these mentioned shower shapes and applies additional cuts to other shower shapes, mainly in the first layer of the EM calorimeter. This selection is designed to have a high background rejection rate while retaining a high signal yield. The *loose* selection applies the same cuts to both converted and unconverted photons whilst the *tight* selection is optimized separately for the two cases. The PID efficiency of the unconverted (converted) photons range from 95% to 98% (85% to 95%) between 25 GeV and 200 GeV. In order to account for small discrepancies between data and MC, small corrections are applied to the photon shower shapes.

In the effort to further segregate photons from jets, two complimentary isolation variables are employed. The first is defined as the sum of the transverse energy of the topological clusters with positive energy [133] reconstructed in the calorimeter around each photon candidate in a cone of radius $\Delta R = 0.4$. This follows after the subtraction of the contributions from the photon itself and correcting for the leakage in photon energy. The second isolation variable is the scalar sum of transverse momenta of all tracks with $p_T > 1$ GeV and within a cone of size $\Delta R = \sqrt{(\Delta\eta)^2 + (\Delta\phi)^2} = 0.2$ around each photon candidate. For $h \to \gamma\gamma$ final states only tracks consistent with originating from the diphoton production vertex discussed in Section 5 are used and the tracks associated to converted photon candidates are excluded.

4.4 Electron reconstruction

Leptons are a primary signature for electro-weak processes and are used in a wide range of physics analyses including precision standard model measurements and searching for new physics. Electrons are reconstructed from energy clusters in the EM calorimeter associated with tracks in the ID. The determination of the electron candidate energy is performed using the same methods described for photons in Section 4.3. The candidates are required to have $p_{\mathrm{T}} > 7$ GeV and be within a region defined by $|\eta| < 2.47$ and those within the transition or "crack" region defined by $1.37 < |\eta| < 1.52$ are not considered. The electrons are required to

satisfy a loose PID criterion based on the electron shower shapes in the EM calorimeter as well as its leakage into the TileCal [134]. Finally, the electron candidates must satisfy both the calorimetric isolation and track-based criteria relative to the p_{T} of the candidate. The calorimeter isolation energy within $\Delta R < 0.4$ is required to be less than 20% of the candidate's p_{T}. In the case of the track isolation, the sum of track p_{T} within $\Delta R < 0.2$ around the track of the electron candidate is required to be less than 15% of the electron candidate's p_{T}.

4.5 Muon reconstruction

Muons are reconstructed from tracks in the ID and MS. Muon candidates are built based on the available information from these sub-detectors. The main algorithm combines tracks that are reconstructed separately by the ID and MS. The muon candidates are required to to have $p_{\mathrm{T}} > 7\,\mathrm{GeV}$ within a region defined by $|\eta| < 2.47$ as well as pass a "medium" identification criteria. For events containing muons, the $|d_0|$ with respect to the PV in the event must be less than 1 mm and the $|z_0|$ with respect to the primary vertex in the event must be less than 10 mm. The muon candidates are also required to be isolated with algorithms that are consistent with those discussed in the case of electrons.

4.6 Jet reconstruction

Jets are reconstructed using topological clusters [136] within the EM and hadronic calorimeters using the anti-kt algorithm [137] with a distance parameter of $R = 0.4$. All jets are required to be within a region defined by $|\eta| < 4.5$ and depending on the location of the jet, different p_{T} requirements are applied. All central jets within $|\eta| < 2.4$ are required to have $p_{\mathrm{T}} > 25$ GeV while those outside this region are required to have $p_{\mathrm{T}} > 30$ GeV. Data-driven corrections are applied to reduce energy dependence on pile-up which in turn refine the jet calibration. Jets produced from pile-up interactions are diminished by ensuring that the jets originate from the diphoton vertex. This is achieved using a Jet-Vertex-Tagger (JVT) algorithm [135, 138, 139] which has replaced the Run 1 Jet-Vertex-Fraction (JVF) algorithm [139]. The JVT technique

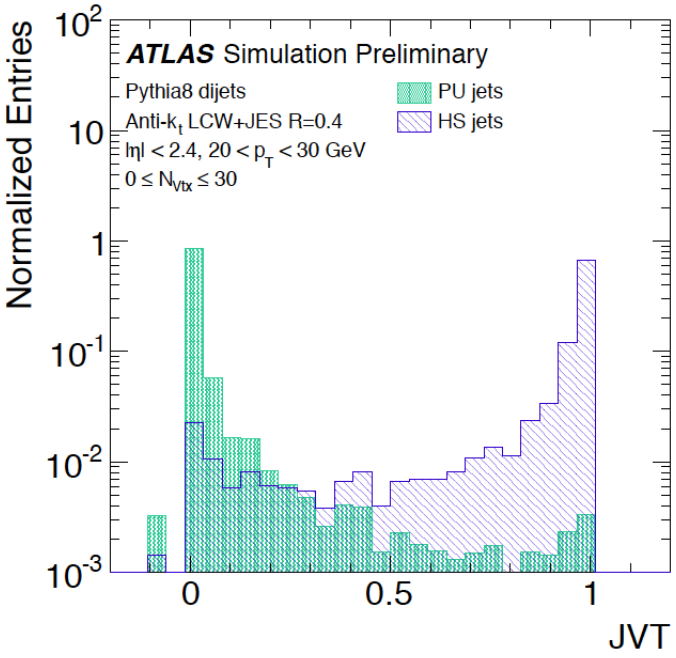


Figure 4.4: Distribution of JVT for pileup and hard-scatter jets with $20 < p_T < 30$ GeV [135].

essentially discriminates hard scatter jets from pile-up jets in the central region of the detector. Figure 4.4 shows the distribution of JVT for pileup and hard-scatter jets with $20 < p_T < 30$ GeV, where the values of JVT range between 0 (probably a pile-up jet) to 1 (probably a hard-scatter jet). Jets used in the $h \to \gamma\gamma$ final state analysis are required to have a JVT score greater than 0.59. Jets within $|\eta| < 2.4$ with $p_{\mathrm{T}} < 60$ GeV and JVT cut of less than 0.59 are rejected. Jets are an integral part of the reconstruction of $E_{\mathrm{T}}^{\mathrm{miss}}$ and also form one of the components of $E_{\mathrm{T}}^{\mathrm{miss}}$. The raw jets container without any applied selection are used in the reconstruction of the $E_{\mathrm{T}}^{\mathrm{miss}}$ and only the central jets within $|\eta| < 2.5$ are used in the jet binning. Jet binning refers to making a requirement on the “number of jets" selection, for instance, exactly one jet or at least one jet.

4.7 Missing transverse energy reconstruction

Missing transverse energy, denoted $E_{\mathrm{T}}^{\mathrm{miss}}$, will be discussed in detail later on since it is a key aspect of the main analysis in this thesis and forms a predominant part of my work. $E_{\mathrm{T}}^{\mathrm{miss}}$ is a

key part of numerous analyses at the LHC, including Higgs boson measurements and BSM physics searches. $\boldsymbol{E}_{\mathrm{T}}^{\mathrm{miss}}$ is described as the transverse energy which is not detected in a particle detector but is expected to be due to the laws of conservation of momentum. In pp collisions most of the SM particles leave tracks inside the detector, however, undetectable particles such as SM neutrinos and other possible BSM particles escape without leaving a trace. Strictly speaking, no direct evidence of such particles can be measured in any general purpose detector. Nevertheless, the total momenta of the colliding protons is almost zero in the transverse plane such that the presence of undetectable particles can be inferred by the resultant momentum imbalance in this plane. This momentum imbalance in the plane transverse to the beam axis, compelled by momentum conservation describes $\boldsymbol{E}_{\mathrm{T}}^{\mathrm{miss}}$. It is a z-axis boost invariant quantity, which if measured in the lab frame is also very easy to interpret in the parton-parton hard scattering centre-of-mass frame.

4.8 Conclusions

The reconstructed and identified objects representing the observed characteristics of the particles originating from the pp collisions are the starting point of all ATLAS physics analyses. The algorithms developed to reconstruct and identify these physics objects are constantly improved to keep up with the changing energies and pile-up conditions at the LHC. A good understanding of these reconstructed objects is a prerequisite for all measurements, searches or discoveries at the LHC. Before the diphoton event selection, an overlap removal between the reconstructed objects is applied in order to avoid duplications. This overlap removal procedure is discussed in detail in the next chapter. The content that has been presented in this chapter forms an integral part of the discussions in all the chapters that follow. More importantly, a very detailed discussion on the reconstruction and performance of $\boldsymbol{E}_{\mathrm{T}}^{\mathrm{miss}}$ is documented in Chapter 6 and constitutes the bulk of the contribution of this thesis to the overall BSM searches.

CHAPTER 5

THE $h \to \gamma\gamma$ DECAY CHANNEL

This chapter introduces the diphoton channel as it forms the basis for the chapters to follow in this thesis. In Run 1 the $h \to \gamma\gamma$ channel played an important role in the discovery of the Higgs boson [128] and now in Run 2 this channel remains one of the most useful in performing precise characterization of Higgs properties [140]. This is because despite this channels' small branching ratio for a Higgs boson of mass 125 GeV, the $h \to \gamma\gamma$ decay channel provides a very clean final-state topology with an invariant mass peak that is reconstructed with great precision, allowing an efficient fight against QCD and other non-resonant backgrounds.

Section 5.1 briefly touches on the software tools used in the diphoton analysis framework. Section 5.2 discusses the Monte Carlo simulation samples produced centrally for this channel. Lastly, Section 5.3 describes the object and event selection in the diphoton decay channel, which is in fact an extension of the content discussed in Chapter 4.

5.1 Diphoton Analysis Framework

A common and robust analysis framework is paramount in dealing with the huge amount of data produced by ATLAS. ATLAS uses a standard framework called ATHENA for simulations, reconstructions and analyses. ATHENA is implemented based on the GAUDI framework [141]

which essentially facilitates the development of data processing. The ATHENA framework comprises several components which take care of different tasks in the simulation, reconstruction and analysis chain. The framework does so by handling the configuration and execution of numerous algorithms built in C++ packages.

The various data formats handled by the ATLAS Event Data Model (EDM) in Run 2 are shown in Figure 5.1 and are discussed briefly below.

- **RAWdata**: Contains the detector output produced by either real or simulated events after the HLT and the size of each event is approximately 1.6 MB.
- **Event Summary Data (ESD)**: Contains the detailed output of the reconstructed process and adopts an object-oriented format. The approximate event size is usually several MBs.
- **xAOD**: Introduced in Run 2 and replacing Run 1's AODs and D3PDs. This is a sub-set of the ESD and contains the physical objects used in analyses as well as reduced detector level information and can be read either from ROOT [142] or ATHENA. The event size is approximately 500 KB.
- **DxAOD**: Contains a sub-set derived from the xAOD specific to an analysis or performance group. Several derivations are produced and the data is reduced by selecting specific objects and specific information about those objects. The final event size varies depending on the derivation process.

The RAW detector data and simulated detector output (RDO) data are reconstructed into our xAOD format which is the Run 2 analysis EDM. From these xAOD events, several derived formats (DxAODs) are made.

The diphoton analysis framework, referred to as the `HGamAnalysisFramework`, is built in ROOT which is an object oriented data analysis framework. This framework is intended to provide a final mini xAOD (MxAOD) with all the calibrated objects and user-level variables. Analyzers are provided a skeleton code along with example codes which they run in order to make selections specific to their analyses thus reducing the DxAODs into xAODs and even further into MxAODs. These MxOADs are produced centrally in the diphoton channel analysis

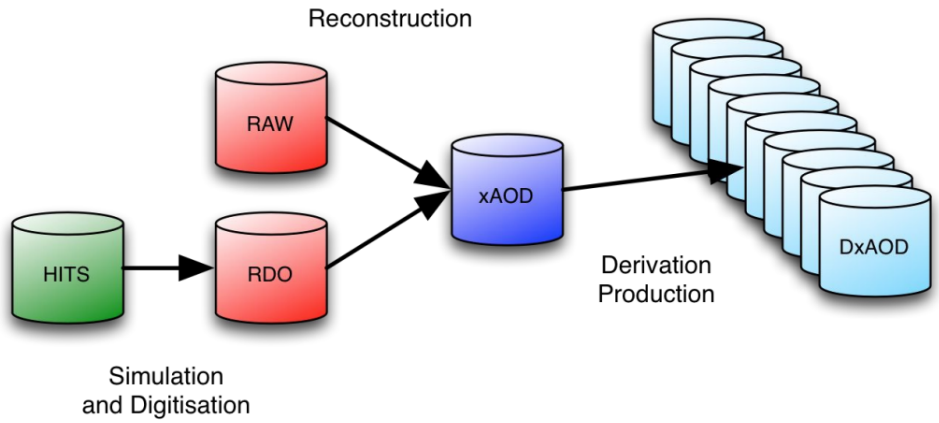


Figure 5.1: An illustration of the ATLAS data flow into analysis.

group using this framework and contain information after the nominal diphoton selection discussed in Section 5.3.2.2. The flexibility of the framework also allows the incorporation of additional C++ scripts which inherit from the main HGamAnalysisFramework and further reduce MxAODs to small ntuples. Both MxAODs and small ntuples are small enough to be run locally which is more convenient for analyzers.

The HGamAnalysisFramework is made up of several object handlers which made up the HGam components, namely: Electron handler, Photon handler, jet handler, muon handler, overlap removal handler, $\boldsymbol{E}_{\mathrm{T}}^{\mathrm{miss}}$ handler, event handler, truth handler and var handler. Each handler contains a set of code with functions that manage the various objects. The work done in the context of this thesis contributed in managing the $\boldsymbol{E}_{\mathrm{T}}^{\mathrm{miss}}$ handler as its precise reconstruction is essential for the studies documented in this thesis.

5.2 Monte Carlo samples

Monte Carlo (MC) simulations of the studied physics processes are crucial for all analyses at the LHC. This section describes the MC samples of the signal and background processes in the diphoton final state channel. In this case, the simulated samples are used to determine the shape of the diphoton mass spectra for signal and background processes. Several MCs are used

to simulate the Higgs boson production and decay modes which were discussed in Section 1.3.

5.2.1 Standard Model Higgs Monte Carlo samples

The Higgs boson signal MC samples are produced for the production modes shown in Table 5.1. The signal samples produced via ggF and VBF are generated with POWHEG [143, 144] and passed to PYTHIA8 [145] for parton showering. The ggF samples are normalized to calculations at NNLO in QCD [55–57], with NLO electroweak corrections [43–47] also applied. On the other hand, the VBF samples are normalized to cross-sections calculated with NLO electroweak corrections as well as NLO QCD corrections with an additional NNLO QCD correction [48, 59].

The associated Higgs production with W and Z bosons are generated with PYTHIA8 and $t\bar{t}h$ samples are generated with MADGRAPH5 aMC@NLO [146]. The Wh and Zh samples are normalized to cross sections calculated at NLO [49, 50, 60] and at NNLO with NLO electroweak radiative corrections applied. For the $t\bar{t}h$ normalization, full NLO QCD corrections have been calculated in References [51–54].

After the showering and hadronization processes, stable particles are defined as those with lifetimes longer than 10 ps and these are passed through GEANT4 [147, 148]. GEANT4 simulates the detector response and the events from the signal samples passed through it are reconstructed using the same analysis software that is used for real data. This is referred to as Full Simulation (FullSim) or Atlfast-II fast simulation [149]. The pile-up interactions are also taken into account and added to the events. These are minimum bias events which are generated with PYTHIA8 and are reweighted to accurately reproduce the pile-up distribution observed in data.

5.2.2 Background Monte Carlo samples

The SM backgrounds for prompt diphoton events are simulated using the SHERPA version 2.1 event generator [150] with up to two additional partons in the final state with the CT10 PDF. SHERPA is also used to generate $V\gamma$ and $V\gamma\gamma$ backgrounds which are also contributors in the diphoton channel. The events are filtered by requiring the presence of two photons with

Table 5.1: MC samples for the different Higgs production modes used to study the signal shapes, with the available simulated mass values and corresponding statistics.

Process	**Generator**	**Mass [GeV]**	N_{events} ($\times 10^3$)
ggF	POWHEG+PYTHIA8	200-400-750-800 1000-1200-1600-2000-2400	30
VBF	POWHEG+PYTHIA8	200-300-400-500-600 800-1000-1500-2000	30
Wh	PYTHIA8	200-300-400-500-600 800-1000-1500-2000	30
Zh	PYTHIA8	200-300-400-500-600 800-1000-1500-2000	30
$t\bar{t}h$	MADGRAPH5 aMC@NLO	200-300-400-500-600 800-1000-1500-2000	30

Table 5.2: Prompt diphoton background MC samples.

Generator	**Samples**	**Simulation**	**N Events**	**Remarks**
SHERPA	$\gamma\gamma$+0, 1, 2 jets	Full	1M	Slicing $m_{\gamma\gamma}$ 0, 55, 100, 160 GeV
SHERPA	$\gamma\gamma$+0, 1, 2 jets	Full	500k	Slicing $m_{\gamma\gamma}$ 160, 250, 400, 650, 1000 GeV
SHERPA	$\gamma\gamma$+0, 1, 2 jets	Full	500k	Slicing $m_{\gamma\gamma}$ 1000~ 2500 every 500 GeV
SHERPA	$\gamma\gamma$+0, 1, 2 jets	Full	100k	Slicing $m_{\gamma\gamma}$ 2500~ 5000+ every 500 GeV
SHERPA	$\gamma\gamma$+0, 1, 2, 3 jets	Full	5M	Slicing $m_{\gamma\gamma}$ 100-160 GeV
SHERPA	$\gamma\gamma$+0, 1, 2, 3 jets	AF2	100M	Slicing $m_{\gamma\gamma}$ 100-165 GeV
SHERPA	γ jet+0, 1, 2 jets	Full	20M	Slicing p_γ^T 35, 70 GeV, b, c/b, $/c/b$ filter
SHERPA	γ jet+0, 1, 2 jets	Full	2M	Slicing p_γ^T 70, 140 GeV, b, c/b, $/c/b$ filter
SHERPA	γ jet+0, 1, 2 jets	Full	10M	Slicing p_γ^T 140, 280 GeV, b, c/b, $/c/b$ filter
SHERPA	γ jet+0, 1, 2 jets	Full	1M	Slicing p_γ^T 280, 500 GeV, b, c/b, $/c/b$ filter
SHERPA	γ jet+0, 1, 2 jets	Full	200k	Slicing p_γ^T 500, 1000 GeV, b, c/b, $/c/b$ filter
SHERPA	γ jet+0, 1, 2 jets	Full	100k	Slicing p_γ^T 1000, 2000 GeV, b, c/b, $/c/b$ filter
PYTHIA	jet jet	Full	2M	JZNW, N=0 ~ 8
PYTHIA	jet jet	Full	500k	JZNW, N=9 ~ 12

a transverse energy larger then 20 GeV in the final state. In order to maximize the available statistics over the mass range of interest, the simulation is separately performed in exclusive slices of the diphoton invariant mass $m_{\gamma\gamma}$. Table 5.2 lists the properties of these prompt diphoton samples, including the corresponding number of events and $m_{\gamma\gamma}$ slices. All background and signal samples undergo FullSim except for the case of the huge diphoton plus three jets sample which goes through Fast Simulation (AF2) [149].

5.3 Object and event selection

5.3.1 Diphoton primary vertex

As already highlighted in the previous chapter, in order to achieve a precise measurement of the diphoton invariant mass, $m_{\gamma\gamma}$, as well as a precise computation of track-based quantities, the exact location of the diphoton vertex is necessary. This diphoton vertex determination process uses the *photon-pointing* capability of the EM calorimeter that allows the use of showers in longitudinal layers to extrapolate the photon track to the beam axis. The two hardest photons are used to identify the diphoton vertex. For converted photons, the position of the conversion vertex is also used if the conversion tracks have hits in the silicon detectors. The diphoton vertex is discriminated among other vertices using a Neural Network algorithm which uses photon information from the ID and EM calorimeter. The expected efficiency of finding a primary vertex within 0.3 mm of the true one is on average better than 80% [151]. The evaluation is done using $Z \to e^+e^-$ from both data and MC and is found to be acceptable.

5.3.2 Diphoton event selection

The object selection in the diphoton channel inherits from the main object reconstruction procedure at ATLAS already discussed in Chapter 4. All the reconstructed objects: photons, electrons, muons, jets and $E_{\mathrm{T}}^{\mathrm{miss}}$ enter the diphoton analysis framework in order for the nominal $h \to \gamma\gamma$ final state selections to be performed.

5.3.2.1 Overlap removal

Before the actual diphoton event selection, an overlap removal selection between objects is performed in order to avoid unnecessary duplications. During reconstruction particles can be reconstructed as various objects, that is, a photon can be reconstructed as a jet or electron. As a result, it is of utmost importance to apply an overlap removal in favour of the selected photons in the event for the final state of interest in this analysis to maximise signal efficiency. The selections are done in the following manner:

- Electrons within $\Delta R = 0.4$ of selected photons are removed.
- Jets within $\Delta R = 0.4$ of selected photons are removed.
- Jets within $\Delta R = 0.2$ of selected electrons are removed.
- Muons within $\Delta R = 0.4$ of selected photons or jets are removed.
- Electrons within $\Delta R = 0.4$ of selected jets are removed.

5.3.2.2 Event selection

The $h \to \gamma\gamma$ final state requires the selection of at least two centrally located photon candidates which pass the *loose* trigger where the leading photon has $p_{\mathrm{T}} > 35$ GeV and the sub-leading has $p_{\mathrm{T}} > 25$ GeV. In order to maintain data quality control, a Good Runs List (GRL) selection is applied to filter out any corrupted data collected in the data taking process and the selected events pass a selection which checks the data quality. The selected two hardest photon candidates are the ones used to identify the diphoton vertex. For the precise measurement of $m_{\gamma\gamma}$, the precise location of the diphoton vertex is essential. In addition, according to the discussion in the previous chapter, the photon candidates must satisfy *tight* PID criteria based on the EM showers shapes as well as pass the isolation requirements. Also, the photons must satisfy relative p_{T} cuts: leading must satisfy $p_{\mathrm{T}_{\gamma 1}}/m_{\gamma\gamma} > 0.35$ and sub-leading must satisfy $p_{\mathrm{T}_{\gamma 2}}/m_{\gamma\gamma} > 0.25$. The events are required to have 105 GeV $< m_{\gamma\gamma} <$ 160 GeV where the diphoton mass is calculated assuming that the photons originate from the diphoton primary vertex. Table 5.3 summarizes the nominal diphoton event selection stratagem.

5.4 Conclusion

In Run 2 of data taking, all physics analyses at the LHC are performed using xAODs or DxAODs and in the diphoton analysis case, even MxAODs. Lightweight data formats referred to as TAGs are used to facilitate efficient event selection. I developed the very first framework TAG for the $h \to \gamma\gamma$+$\boldsymbol{E}_{\mathrm{T}}^{\mathrm{miss}}$ final state inherited from the central HGAMANALYSISFRAMEWORK which was used in the beginning of the main analysis documented in this thesis. The work

Table 5.3: Table showing the nominal diphoton selection cuts as well as their functions.

Selection	**Function**
No duplicates	Removes duplicated events in the sample
Pass Trigger	Selects events that pass the g35_loose_g25 *loose* trigger
GRL	Data is rid of corrupt datasets by passing this selection
Detector DQ	Quality of data is checked
Has PV	The diphoton objects should satisfy the reconstructed vertex
Two *loose* photons	Events should contain two *loose* identified photons
$e\gamma$ ambiguity	Selection rejects events with ambivalent photons
Trigger match Identification	Selection matches the trigger to the g35_loose_g25 *loose* trigger Two photons should pass the *tight* PID
Isolation	Two photons should pass the isolation requirements
Relative p_{T}	γ_1 and γ_2 required to have $p_{\mathrm{T}_{\gamma 1}}/m_{\gamma\gamma} > 0.35$ and $p_{\mathrm{T}_{\gamma 2}}/m_{\gamma\gamma} > 0.25$, respectively
Mass window	Events required to pass 160 GeV $< m_{\gamma\gamma} <$ 400 GeV

done in the context of the present PhD provided a contribution to the initial development and maintenance of the $\boldsymbol{E}_{\mathrm{T}}^{\mathrm{miss}}$ handler tool which is discussed in detail in the next chapter. All in all, Chapters 4 and 5 have established the foundations for the studies in the chapters to follow.

CHAPTER 6

PERFORMANCE OF $E_{\mathrm{T}}^{\mathrm{MISS}}$ RECONSTRUCTION FOR ATLAS WITH DIPHOTONS AT $\sqrt{s}$ = 13 TEV

The role played by $\boldsymbol{E}_{\mathrm{T}}^{\mathrm{miss}}$ in BSM physics searches is of utmost importance. For instance, $\boldsymbol{E}_{\mathrm{T}}^{\mathrm{miss}}$ signatures play an important role is searches for supersymmetry [152, 153] and DM [154, 155] at the LHC. The information obtained from the reconstruction of this $\boldsymbol{E}_{\mathrm{T}}^{\mathrm{miss}}$ sheds light on new discovery possibilities, where long-lived non-interacting particles are produced in pp collisions, bringing us closer to tackling the unanswered questions about our world. This chapter not only scrutinizes the reconstruction of $\boldsymbol{E}_{\mathrm{T}}^{\mathrm{miss}}$, but also displays the performance of this $\boldsymbol{E}_{\mathrm{T}}^{\mathrm{miss}}$ which validates its precise reconstruction. The studies in this section are evaluated based on data collected with the ATLAS detector, corresponding to various luminosities of pp collisions at the LHC at a center-of-mass energy of 13 TeV collected in 2015, 2016 and 2017. This study is part of the subsequent BSM physics searches driven by $\boldsymbol{E}_{\mathrm{T}}^{\mathrm{miss}}$.

Section 6.1 details how the $\boldsymbol{E}_{\mathrm{T}}^{\mathrm{miss}}$ is reconstructed and calibrated at ATLAS. Section 6.2.1 reviews the infrastructure of the $\boldsymbol{E}_{\mathrm{T}}^{\mathrm{miss}}$ handler as well as how it operates within the main $h \to \gamma\gamma$ framework. Finally, Section 6.3 presents all the $\boldsymbol{E}_{\mathrm{T}}^{\mathrm{miss}}$ performance studies based on data and MC.

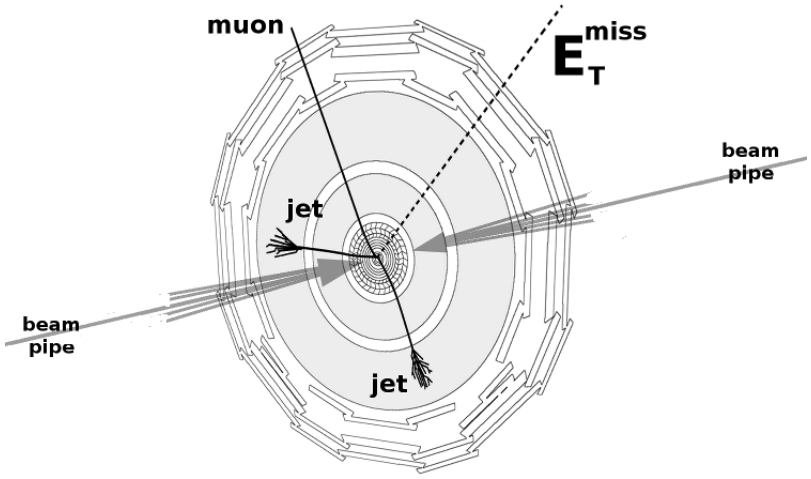


Figure 6.1: A graphical illustration aiding in the explanation of $E_{\mathrm{T}}^{\mathrm{miss}}$.

6.1 $E_{\mathrm{T}}^{\mathrm{miss}}$ reconstruction and calibration

$E_{\mathrm{T}}^{\mathrm{miss}}$ has been introduced in Chapter 4 as being the transverse energy which is undetected in particle detectors but is expected due to laws of conservation. The transverse momentum of the colliding protons is very small and only given by the fermi notation of partons inside the proton. This transverse momentum is approximately equivalent to the mass of a proton. Missing energy is carried by particles that do not interact with the various components of the detector as they traverse it, making it a key signature for BSM physics. Figure 6.1 shows a shifted transverse view of the detector explaining the concept of $E_{\mathrm{T}}^{\mathrm{miss}}$.

The $E_{\mathrm{T}}^{\mathrm{miss}}$ is reconstructed from the negative vector sum of the transverse momenta of all the particles detected. The reconstruction process uses energy deposits from reconstructed and calibrated physics objects to estimate the amount of $E_{\mathrm{T}}^{\mathrm{miss}}$ in the detector. These objects include electrons, photons, hadronically decaying τ-leptons, jets and muons [156, 157], most of which were discussed previously in Chapter 4. In addition, deposits that are not associated to any of these hard physics objects are also taken into account in the $E_{\mathrm{T}}^{\mathrm{miss}}$ calculation and make up what is referred to as the "Soft Term". The $E_{\mathrm{T}}^{\mathrm{miss}}$ is calculated as follows:

$$E_{\mathrm{x(y)}}^{\mathrm{miss}} = E_{\mathrm{x(y)}}^{\mathrm{miss,e}} + E_{\mathrm{x(y)}}^{\mathrm{miss},\gamma} + E_{\mathrm{x(y)}}^{\mathrm{miss},\tau} + E_{\mathrm{x(y)}}^{\mathrm{miss,jets}} + E_{\mathrm{x(y)}}^{\mathrm{miss},\mu} + E_{\mathrm{x(y)}}^{\mathrm{miss,Soft\ Term}}, \tag{6.1}$$

where each term is calculated as the negative vectorial sum of the calibrated reconstructed objects, projected onto the x and y directions. Each term in Equation 6.1 is calculated as follows:

$$E_{\mathrm{x}}^{\mathrm{miss,term}} = -\sum_{i=1}^{N_{cell}^{term}} E_i sin\theta_i cos\phi_i, \tag{6.2}$$

$$E_{\mathrm{y}}^{\mathrm{miss,term}} = -\sum_{i=1}^{N_{cell}^{term}} E_i sin\theta_i sin\phi_i, \tag{6.3}$$

where the summations are over all cells in the range $|\eta| < 4.5$. Beyond well identified objects (e, τ, γ, μ), the jets and the soft part only use cells belonging to 3D topological clusters are used in order to suppress noise and limit the number of cells used by focusing on those that contain a significant signal.

The magnitude of the $E_{\mathrm{T}}^{\mathrm{miss}}$ and its azimuthal coordinate ϕ^{miss} are given respectively by:

$$E_{\mathrm{T}}^{\mathrm{miss}} = \sqrt{(E_{\mathrm{x}}^{\mathrm{miss}})^2 + (E_{\mathrm{y}}^{\mathrm{miss}})^2}, \tag{6.4}$$

$$\phi^{\mathrm{miss}} = \arctan(E_{\mathrm{y}}^{\mathrm{miss}}/E_{\mathrm{x}}^{\mathrm{miss}}). \tag{6.5}$$

The total transverse energy ($\sum E_{\mathrm{T}}$) in the calorimeters is an important quantity to parameterize and understand the $E_{\mathrm{T}}^{\mathrm{miss}}$ performance. $\sum E_{\mathrm{T}}$ is defined as the scalar sum of the transverse energy of all the reconstructed and calibrated objects that go into the $E_{\mathrm{T}}^{\mathrm{miss}}$ calculation, including the Soft Term. That is,

$$\sum E_{\mathrm{T}} = \sum E_{\mathrm{T}}^{e} + \sum E_{\mathrm{T}}^{\gamma} + \sum E_{\mathrm{T}}^{\mu} + \sum E_{\mathrm{T}}^{\tau} + \sum E_{\mathrm{T}}^{\mathrm{jets}} + \sum E_{\mathrm{T}}^{\mathrm{SoftTerm}}. \tag{6.6}$$

6.1.1 $E_{\mathrm{T}}^{\mathrm{miss}}$ Soft Term reconstruction

The Soft Term comprises part of the hard scatter signals, the underlying event activity as well as pile-up interaction contributions thus making it an essential attribute of the $E_{\mathrm{T}}^{\mathrm{miss}}$. Several algorithms have been developed at ATLAS to ensure precise measurement of the $E_{\mathrm{T}}^{\mathrm{miss}}$ Soft Term. These methods aid in reducing the effects of pile-up interactions by making use of track

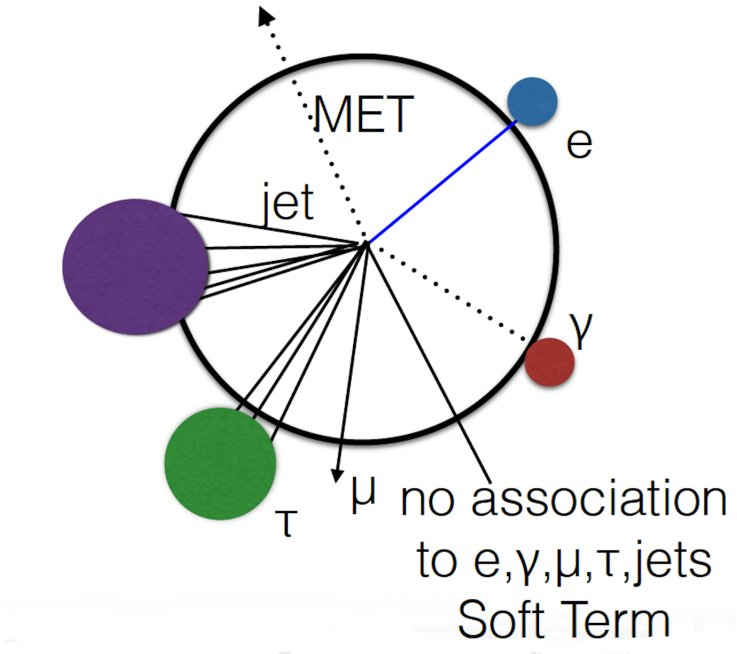


Figure 6.2: A graphical illustration of the constituents of the $E_{\mathrm{T}}^{\mathrm{miss}}$ including the Soft Term.

information since ID tracks can be reliably matched to the PV corresponding to the hard scatter process [158]. All the $E_{\mathrm{T}}^{\mathrm{miss}}$ terms in Equation 6.1 are affected by pile-up, but the most affected are the jet and soft terms due to the fact that their constituents are spread over larger regions of the calorimeters in comparison to the others. Substantial degradation in the $E_{\mathrm{T}}^{\mathrm{miss}}$ resolution is accounted to the increase in these pile-up interactions. It is therefore imperative to incorporate methods of pile-up suppression in the reconstruction of $E_{\mathrm{T}}^{\mathrm{miss}}$. The pile-up suppression Soft Term used in the $E_{\mathrm{T}}^{\mathrm{miss}}$ calculation is referred to as the Track Soft term.

6.1.1.1 Track Soft Term (TST)

The TST term is constructed from tracks which pass the selections outlined in Sections 4.1 and 4.2 but not matching the hard physics objects. Only tracks associated to the PV through requirements on the longitudinal and transverse impact parameters are included. In addition, the TST incorporates overlap removals between tracks and calorimeter clusters associated to the high-p_{T} objects. These are summarized as follows:

- Tracks within ΔR (track, electron/photon cluster) < 0.05 are removed.

- Tracks within ΔR (track, τ-lepton) < 0.2 are removed.
- ID tracks associated to combined or segment-tagged muons are replaced with the combined ID+MS fit.
- Tracks associated with jets using the ghost-association technique [159, 160] are removed.
- Isolated tracks of $p_{\mathrm{T}} \geq 120\,\mathrm{GeV}$ ($\geq 200\,\mathrm{GeV}$ for $|\eta| < 1.5$) with momentum uncertainties larger than 40% or with no matching calorimeter deposit are removed.

In addition, tracks associated to jets which do not pass the JVT score described in Section 4.6 enter the Soft Term. However, the Soft Term does not include contributions from soft neutral particles and from forward regions described by $|\eta| > 2.5$.

6.1.2 $E_{\mathrm{T}}^{\mathrm{miss}}$ significance

The $E_{\mathrm{T}}^{\mathrm{miss}}$ significance is a very important quantity because it can be used as an estimator of $E_{\mathrm{T}}^{\mathrm{miss}}$ with a higher pile-up resilience. The high luminosities of Run 2 result in the degradation of the resolution of $E_{\mathrm{T}}^{\mathrm{miss}}$ since it goes the square root of the total energy in the calorimeter as shown in Equation 6.6. $E_{\mathrm{T}}^{\mathrm{miss}}$ significance is described by the following ratio:

$$E_{\mathrm{T}}^{\mathrm{miss}}\text{significance} = \frac{E_{\mathrm{T}}^{\mathrm{miss}}}{\sqrt{\sum E_{\mathrm{T}}^{\mathrm{miss}}}}, \tag{6.7}$$

which is basically the ratio of the $E_{\mathrm{T}}^{\mathrm{miss}}$ and the resolution of $E_{\mathrm{T}}^{\mathrm{miss}}$. As the amount of pile-up interactions increase, the total transverse energy (scalar sum) also increases, and according to Equation 6.7, this results in a smaller pile-up dependence.

6.1.3 Fake $E_{\mathrm{T}}^{\mathrm{miss}}$

In the measurement of $E_{\mathrm{T}}^{\mathrm{miss}}$, maximizing the detector coverage is an important requirement. However, this stretch can result in $E_{\mathrm{T}}^{\mathrm{miss}}$ mismeasurement or what is renowned as "fake" $E_{\mathrm{T}}^{\mathrm{miss}}$. Instrumental contributions to this fake $E_{\mathrm{T}}^{\mathrm{miss}}$ include: cosmic-rays and beam-halo muons crossing the detector, various sources of noise as well as the presence of dead regions within

the detector. With the LHC's increasing luminosities, contributions to fake $E_{\mathrm{T}}^{\mathrm{miss}}$ also escalate. Several fake $E_{\mathrm{T}}^{\mathrm{miss}}$ suppression methods are developed at ATLAS, one such method is discussed in Section 6.3.2.

6.2 $E_{\mathrm{T}}^{\mathrm{miss}}$ reconstruction tools

$E_{\mathrm{T}}^{\mathrm{miss}}$ reconstruction for the LHC Run 2 of data taking inherits the basic strategies originally developed for Run 1, but with completely redesigned software. The Run 2 software uses the xAOD-based data model and provides support for the MET reconstruction within the ATHENA framework and in a ROOT-based environment. This section discusses the Run 2 software used in the reconstruction of $E_{\mathrm{T}}^{\mathrm{miss}}$.

6.2.1 $E_{\mathrm{T}}^{\mathrm{miss}}$ Handler

The $E_{\mathrm{T}}^{\mathrm{miss}}$ handler "ETmissHandler" is a package within the HGamAnalysisFramework which handles the reconstruction of $E_{\mathrm{T}}^{\mathrm{miss}}$. The author of this thesis contributed to the initial development of the handler. The handler contains code written in C++ which retrieves calibrated physics objects from their respective handlers and feeds them into the METUtilities tool which rebuilds the $E_{\mathrm{T}}^{\mathrm{miss}}$. METUtilities is a tool that allows users to rebuild the $E_{\mathrm{T}}^{\mathrm{miss}}$ incorporating scaling, smearing as well as systematics in a manner consistent to the $E_{\mathrm{T}}^{\mathrm{miss}}$ algorithms.

The METUtilities package is made up of a METMaker tool and a METSystematics tool. The METMaker uses an association map called 'MissingETAssociationMap' which essentially maps the objects to their corresponding topoclusters or tracks. The particle containers which contain the selected objects are passed to this tool since it does not actually apply the standard selection cuts. However, in the case of jets, the full containers are passed into this tool since the jets used in the reconstruction need to satisfy the $p_{\mathrm{T}} > 20\,\mathrm{GeV}$ criteria which is not the case in the nominal selection. In addition, a JVT cut is also incorporated into the METMaker in order to rebuild the TST term since jets that do not pass this selection are considered in this term. The hardest vertex as well as the diphoton vertex are also taken into consideration at this stage, and are incorporated into the METMaker to compute the soft Term. The hardest vertex is also

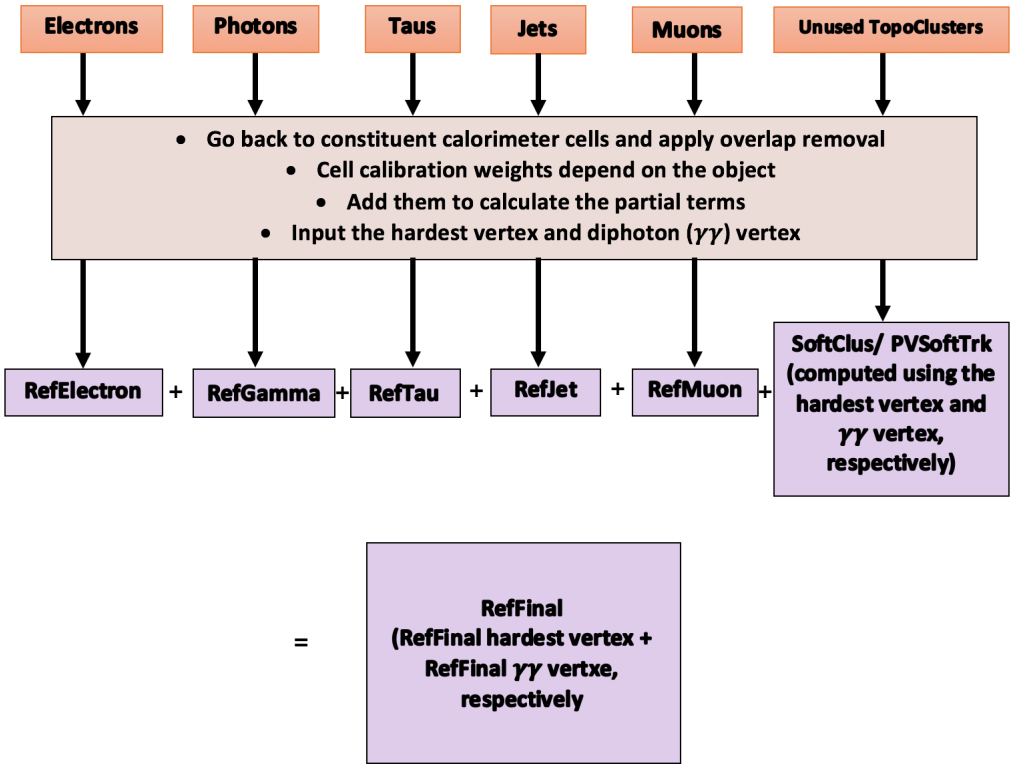


Figure 6.3: A graphical illustration of the reconstruction of the different constituents of the $E_{\mathrm{T}}^{\mathrm{miss}}$.

taken into account in order to perform validation studies. The METSystematics tool provides uncertainties for the $E_{\mathrm{T}}^{\mathrm{miss}}$ soft terms while those for the hard physics objects are propagated via the the METMaker. Once this tool is loaded with the physics objects and is configured, the output provides the user with the different components of the $E_{\mathrm{T}}^{\mathrm{miss}}$ referred to as the $E_{\mathrm{T}}^{\mathrm{miss}}$ Ref Terms. Figure 6.3 summarizes the tools' $E_{\mathrm{T}}^{\mathrm{miss}}$ reconstruction sequence. Each Ref term is calculated from the negative sum of calibrated cell energies corresponding to the various objects.

The METMaker performs some overlap removals in order to avoid double counting of any sort. The reconstruction sequence plays a crucial role in this. The METMaker keeps track of the calorimeter clusters that have already been assigned to specific objects. If a calorimeter cluster has already been used, the additional object linked to it is rejected. For instance, in the case where the RefEle term has already been calculated and a photon is being considered for

the calculation of the RefGamma term, if this photon happens to point to the same topocluster that an electron pointed to previously, the photon is removed from the $E_{\mathrm{T}}^{\mathrm{miss}}$ calculation. In the case where this problematic object is a jet, only a fraction of its kinematics are added to the $E_{\mathrm{T}}^{\mathrm{miss}}$ calculation, provided that this fraction is above a certain threshold. Additionally, if this fraction does not meet the threshold requirements, it is then introduced into the soft term. The performance of this $E_{\mathrm{T}}^{\mathrm{miss}}$ reconstruction is presented in Section 6.3 of this chapter.

6.3 $E_{\mathrm{T}}^{\mathrm{miss}}$ Performance studies

In this section, the behaviour of the reconstructed $E_{\mathrm{T}}^{\mathrm{miss}}$ is examined in data and MC for various studies involving $E_{\mathrm{T}}^{\mathrm{miss}}$. The content in this section encompasses fake $E_{\mathrm{T}}^{\mathrm{miss}}$ suppression methods, vertex selection effects on $E_{\mathrm{T}}^{\mathrm{miss}}$ as well as general evaluation of the performance of $E_{\mathrm{T}}^{\mathrm{miss}}$.

6.3.1 $Z \rightarrow e^+e^-$ vertex reconstruction validation

The reconstruction of $E_{\mathrm{T}}^{\mathrm{miss}}$ is sensitive to the vertex finding algorithm. As a result, the validation of the photon pointing vertex finding algorithm using data and MC is of great importance. The downside of such a validation is that it is not possible to know the truth vertex reconstruction efficiency in the data diphoton events. A solution to this problem is the use of $Z \rightarrow e^+e^-$ events and hence the Z mass control window to do the data and MC validation. The $Z \rightarrow e^+e^-$ events are very similar to diphoton events since the electrons can mimic the photons if the two tracks that are attached to the electrons are removed. Also, the $Z \rightarrow e^+e^-$ hardest vertex is almost 100% equal to the truth vertex making these events very beneficial in this check. Also, the effect of choosing the wrong vertex on the $E_{\mathrm{T}}^{\mathrm{miss}}$ can also be evaluated in the data.

By comparing the variation of the discrepancies in data and MC when changing from the hardest vertex to photon pointing vertex, the systematic uncertainty can be evaluated. This systematic uncertainty is obtained only from the photon pointing method. The selection structure for this validation is as follows:

- Events with two tight electrons in the $Z \rightarrow e^{+}e^{-}$ mass window m_{ll} in [85,95] GeV are selected.

- Two sets of vertices are selected:

  - One set by the largest $\sum p_{\mathrm{T}}^{2}$

  - One set by removing tracks attached to the two selected electrons

- The JVT value is set for both vertices

- The TST $E_{\mathrm{T}}^{\mathrm{miss}}$ is reconstructed for both vertices.

- The photon pointing vertex finding efficiency is compared between data and MC.

- For $E_{\mathrm{T}}^{\mathrm{miss}}$ cut of 50 GeV (intermediate $E_{\mathrm{T}}^{\mathrm{miss}}$ boundary) or 100 GeV (high $E_{\mathrm{T}}^{\mathrm{miss}}$ boundary) the difference in the event yield variation is derived, where the relative uncertainty is given by:

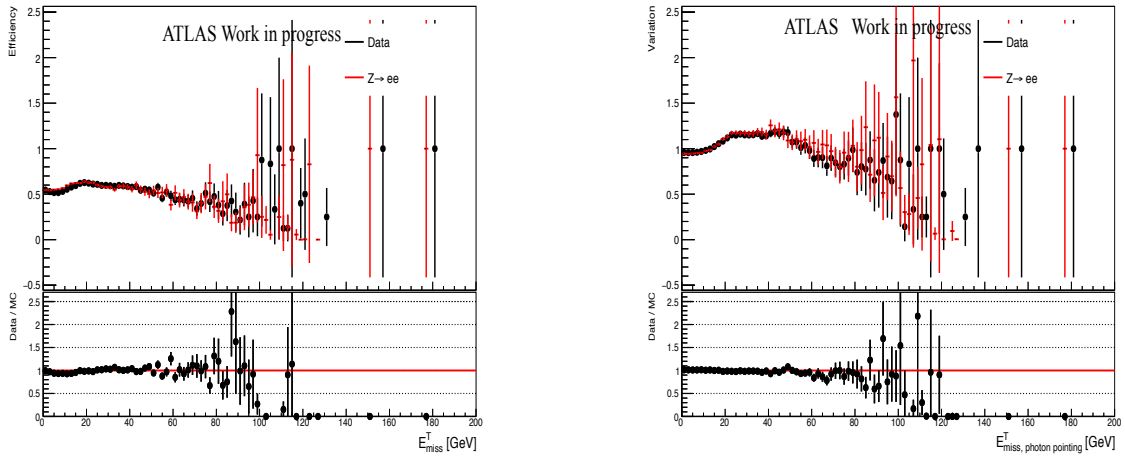
$$\frac{Data_{hardestPV}/MC_{hardestPV}}{Data_{photonpointingPV}/MC_{photonpointingPV}}, \tag{6.8}$$

where $Data_{hardestPV}$ and $MC_{hardestPV}$ refer to data and MC, respectively, under the hardest vertex finding algorithm. $Data_{photonpointingPV}$ and $MC_{photonpointingPV}$ refer to data and MC, respectively, under the photon pointing vertex finding algorithm previously discussed in Section 5.3.1.

Figure 6.4a shows the photon pointing vertex finding algorithm efficiency distribution as a function of $E_{\mathrm{T}}^{\mathrm{miss}}$ and Figure 6.4b shows the variation by changing from the hardest vertex to the photon pointing method. Efficiency and variation are defined as follows:

- **Efficiency**: the number of events in which the two vertex finding methods point the same vertex over the total number of events in each bin.

- **Variation**: the photon pointing $E_{\mathrm{T}}^{\mathrm{miss}}$ shape divided by the hardest vertex $E_{\mathrm{T}}^{\mathrm{miss}}$ shape.

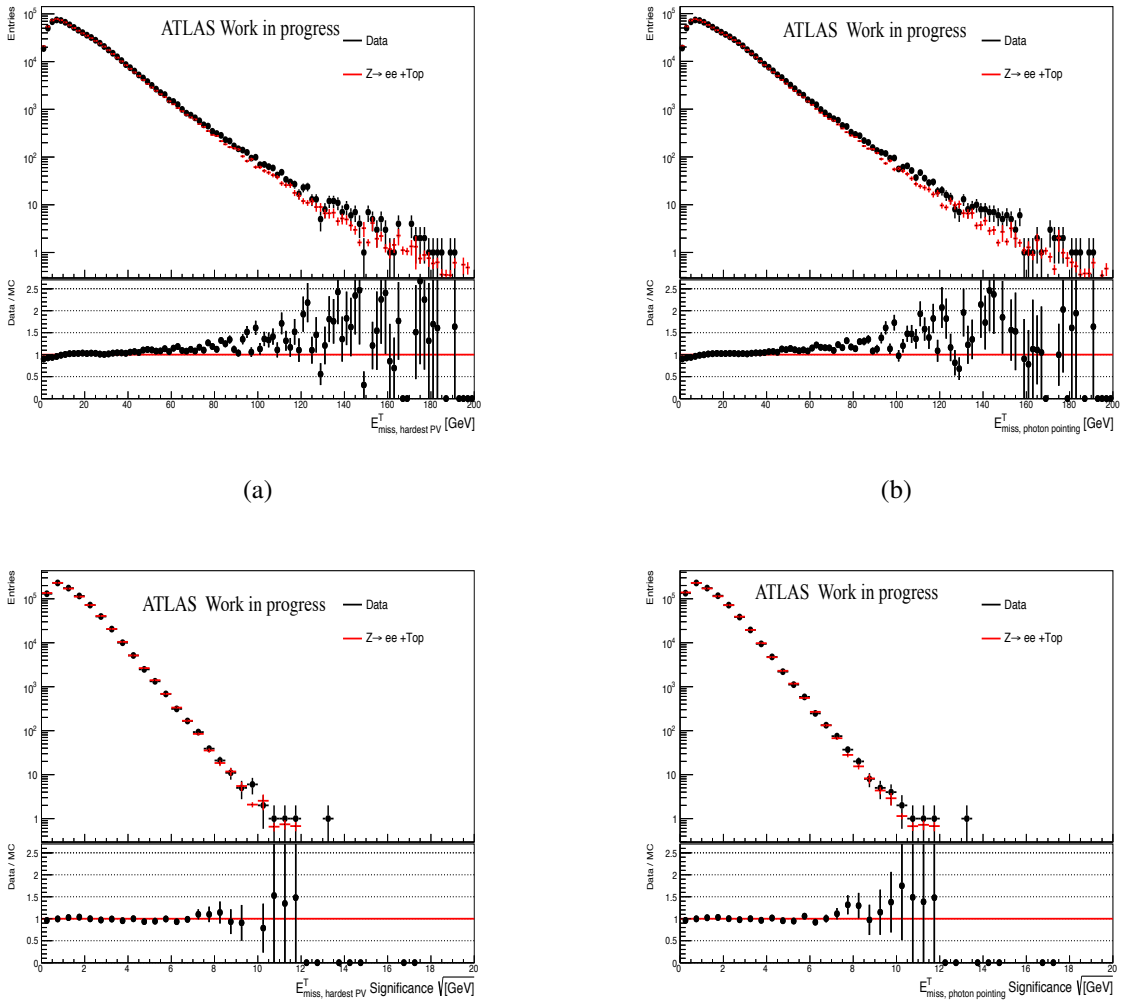


(a) (b)

Figure 6.4: The data and MC comparisons for the (a) vertex reconstruction efficiency for the photon pointing method and (b) variation of changing from the hardest vertex to the photon pointing vertex [3].

The data and MC comparisons in both distributions in Figure 6.4 show reasonable agreement with small discrepancies. The systematic uncertainties evaluated are 3.8% and 20% for the intermediate $E_{\mathrm{T}}^{\mathrm{miss}}$ and high $E_{\mathrm{T}}^{\mathrm{miss}}$ regions, respectively. This $Z \rightarrow e^{+}e^{-}$ study basically shows that the $E_{\mathrm{T}}^{\mathrm{miss}}$ shape for the photon pointing method is consistent in both data and MC. This validation also verifies that in $Z \rightarrow e^{+}e^{-}$ data, the photon pointing method gives the correct vertices 50-60% of the time. This study was introduced in our 2016 Moriond note [3].

This study was repeated using the 2016 reconstructed $E_{\mathrm{T}}^{\mathrm{miss}}$ in order to further validate the photon pointing method. Figure 6.5 shows the direct comparisons in $E_{\mathrm{T}}^{\mathrm{miss}}$ and $E_{\mathrm{T}}^{\mathrm{miss}}$ significance between data and MC for the different vertices. Figure 6.6 shows the variation by using the photon pointing method. All figures show good agreement between data and MC meaning the diphoton vertex is validated once more. Additional figures that supplement this study are shown in Appendix B.



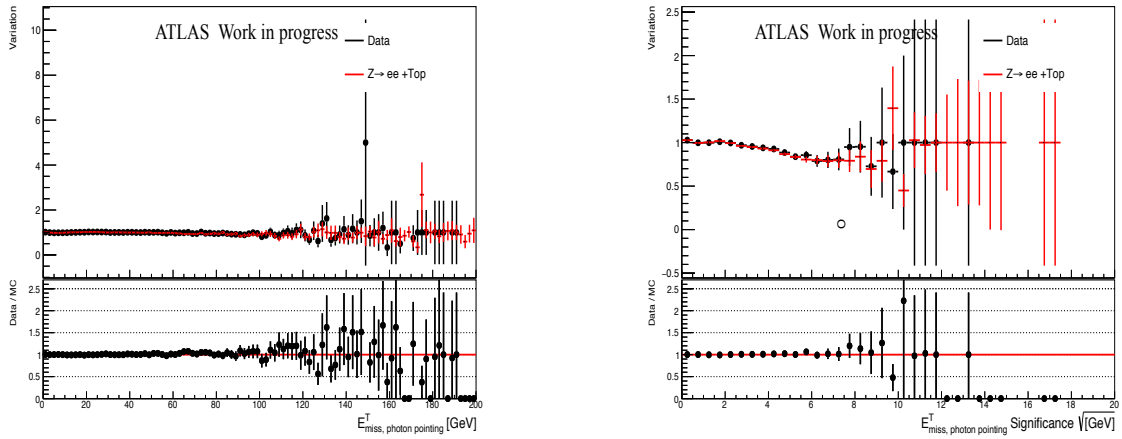
(a) (b)

(c) (d)

Figure 6.5: The direct comparison of the $E_{\mathrm{T}}^{\mathrm{miss}}$ between data and MC in the $Z \to e^{+}e^{-}$ control region. The distributions on the left represent the hardest vertex case and the distributions on the right represent the photon pointing case. The top distributions represent $E_{\mathrm{T}}^{\mathrm{miss}}$ and the bottom $E_{\mathrm{T}}^{\mathrm{miss}}$ significance. Good agreement between data and MC is observed [6].

6.3.2 The Same Vertex Method

The high pile-up conditions in Run 2 at the LHC tend to result in higher fake $E_{\mathrm{T}}^{\mathrm{miss}}$, an alarming attribute in BSM searches. Several methods have been developed at ATLAS to mitigate the effects of pile-up on $E_{\mathrm{T}}^{\mathrm{miss}}$ as discussed previously in this chapter, but these are not sufficient. In fact, following our two analyses in the diphoton channel with $E_{\mathrm{T}}^{\mathrm{miss}}$, we realized that further



(a) (b)

Figure 6.6: The comparison in variation of $E_{\mathrm{T}}^{\mathrm{miss}}$ between data and MC in the $Z \rightarrow e^{+}e^{-}$ control region. The variation from hardest vertex to photon pointing vertex is shown for (a) $E_{\mathrm{T}}^{\mathrm{miss}}$ and (b) $E_{\mathrm{T}}^{\mathrm{miss}}$ significance. Good agreement between data and MC is observed [6].

methods to suppress fake $E_{\mathrm{T}}^{\mathrm{miss}}$ were essential in order to ensure improved BSM physics discovery sensitivity for all searches associated with $E_{\mathrm{T}}^{\mathrm{miss}}$. The WITS institute therefore developed what is now referred to as the "Same Vertex Method" in this effort, a method that has been accepted by ATLAS.

When comparing the consistency of the two types of vertices, that is, photon pointing and the hardest vertex, it was observed that they vary in signal and background. This was essentially the starting point or rather the motivation for this method. This observed feature preceded the potential development of an additional fake $E_{\mathrm{T}}^{\mathrm{miss}}$ suppression method. Figure 6.7 illustrates the difference in vertices between signal and background.

The left of Figure 6.7 shows a signal process resulting in real $E_{\mathrm{T}}^{\mathrm{miss}}$ whereby there is only one physics vertex with a real $E_{\mathrm{T}}^{\mathrm{miss}}$ component. On the other hand, the diagram on the right shows a diphoton background process which includes a secondary pile-up vertex whereby the physics vertex contains no real $E_{\mathrm{T}}^{\mathrm{miss}}$. The study shows that when the $E_{\mathrm{T}}^{\mathrm{miss}}$ is large, the events with fake $E_{\mathrm{T}}^{\mathrm{miss}}$ (diphoton continuous background or SM ggh events) tend to contain large p_{T} pile-up jets. These hard pile-up jets are contained in events which are not fully rejected by the JVT criteria and cause an imbalance in the $E_{\mathrm{T}}^{\mathrm{miss}}$. The JVT cuts are only applied to jets with

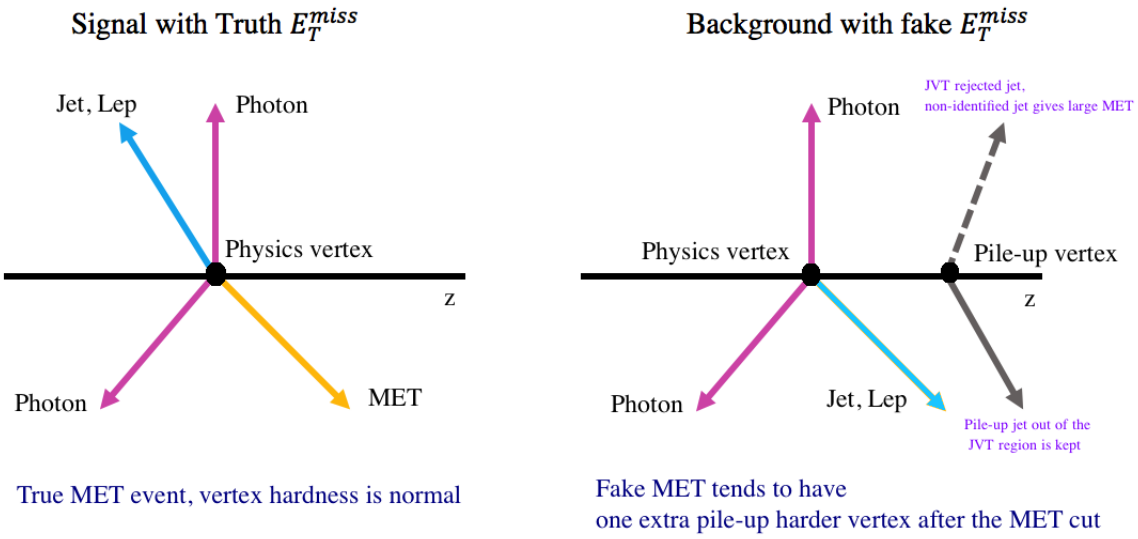


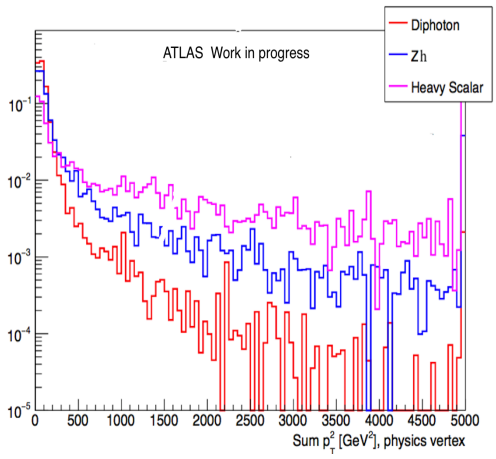
Figure 6.7: An illustration of real $E_{\mathrm{T}}^{\mathrm{miss}}$ with a physics vertex (left) and fake $E_{\mathrm{T}}^{\mathrm{miss}}$ caused by an additional pileup vertex.

$p_{\mathrm{T}} < 60$ GeV, resulting in a fake component to the $H(\rightarrow \gamma\gamma) + E_{\mathrm{T}}^{\mathrm{miss}}$ analysis.

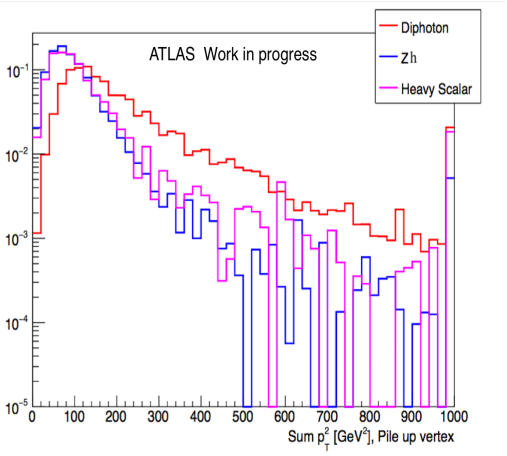
The limited performance of this JVT selection in the high jet p_{T} region or the forward region results in a lot of contamination in the high $E_{\mathrm{T}}^{\mathrm{miss}}$ region which has worked to our advantage. When there is a hard pile-up jet, there is a corresponding hard pile-up vertex which is identified by the hardest $\sum p_{\mathrm{T}}^2$ of the tracks. In the diphoton channel, there is no hard track attached to the physics vertex as the physics vertex is selected through the photon pointing method. This implies that in the high $E_{\mathrm{T}}^{\mathrm{miss}}$ case, events that come from fake $E_{\mathrm{T}}^{\mathrm{miss}}$ are inferred by the pile-up vertex being harder than the photon pointing one. As a result, in order to reject these fake $E_{\mathrm{T}}^{\mathrm{miss}}$ events, one would have to require the diphoton vertex to be the same as the hardest vertex.

The MC samples used in this study include:

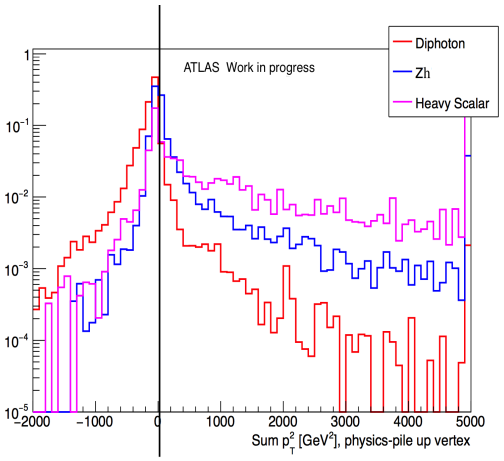
- Diphoton `SHERPA` background.
- SM $Zh(\nu\nu)$ which contains truth $E_{\mathrm{T}}^{\mathrm{miss}}$ but not many radiated jets.
- The heavy scalar sample which contains moderate truth $E_{\mathrm{T}}^{\mathrm{miss}}$ and radiated jet from the gluon gluon fusion. This sample is specific to the main analysis in the next chapter and is



(a)



(b)



(c)

Figure 6.8: Distributions showing the principle behind the same vertex method using the diphoton background, Zh signal and heavy scalar signal. (a) Shows the $\sum p_{\mathrm{T}}^2$ physics vertex distribution, (b) shows the $\sum p_{\mathrm{T}}^2$ pile-up vertex and (c) shows the difference between the $\sum p_{\mathrm{T}}^2$ of the two vertices [6].

discussed in detail there.

Figure 6.8 illustrates the principle of the same vertex method. Figure 6.8a compares the three physics processes with respect to the $\sum p_{\mathrm{T}}^2$ physics vertex, Figure 6.8b compares them with respect to the $\sum p_{\mathrm{T}}^2$ pile-up vertex and Figure 6.8c compares with respect to the difference $\sum p_{\mathrm{T}}^2$ physics vertex - $\sum p_{\mathrm{T}}^2$ pile-up vertex. The diphoton background process has the softest $\sum p_{\mathrm{T}}^2$ physics vertex while having the hardest $\sum p_{\mathrm{T}}^2$ pile-up vertex. On the contrary, the two signals exhibit a more continuous behaviour in the $\sum p_{\mathrm{T}}^2$ physics vertex case and a plummeting one in

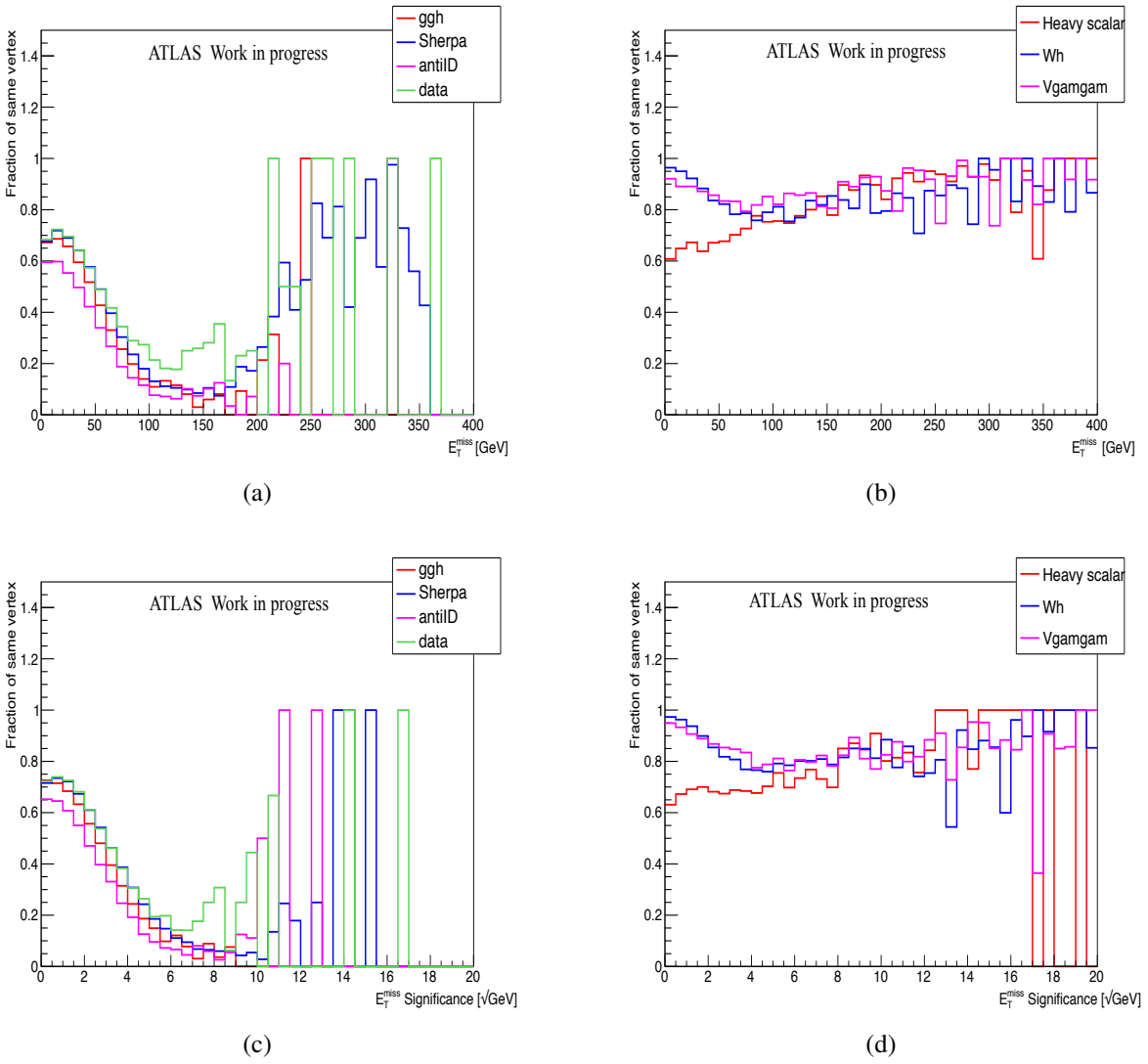


Figure 6.9: Distributions showing the same vertex fraction as a function of $E_{\mathrm{T}}^{\mathrm{miss}}$ (Top) and $E_{\mathrm{T}}^{\mathrm{miss}}$ significance (bottom) for various samples with true and fake $E_{\mathrm{T}}^{\mathrm{miss}}$, respectively. Data corresponds to 2015+2016 data (36.1 fb^{-1}) [6].

the other. Figure 8.2c shows that a large fraction of the diphoton background is concentrated on the negative side of the distribution, indicating that the $\sum p_{\mathrm{T}}^2$ pile-up vertex is generally larger than the $\sum p_{\mathrm{T}}^2$ physics vertex on account of the events with fake $E_{\mathrm{T}}^{\mathrm{miss}}$. So, in order to reject background events, one can require the diphoton pointing vertex to be the same as the hardest vertex.

The same vertex method selection is therefore given by:

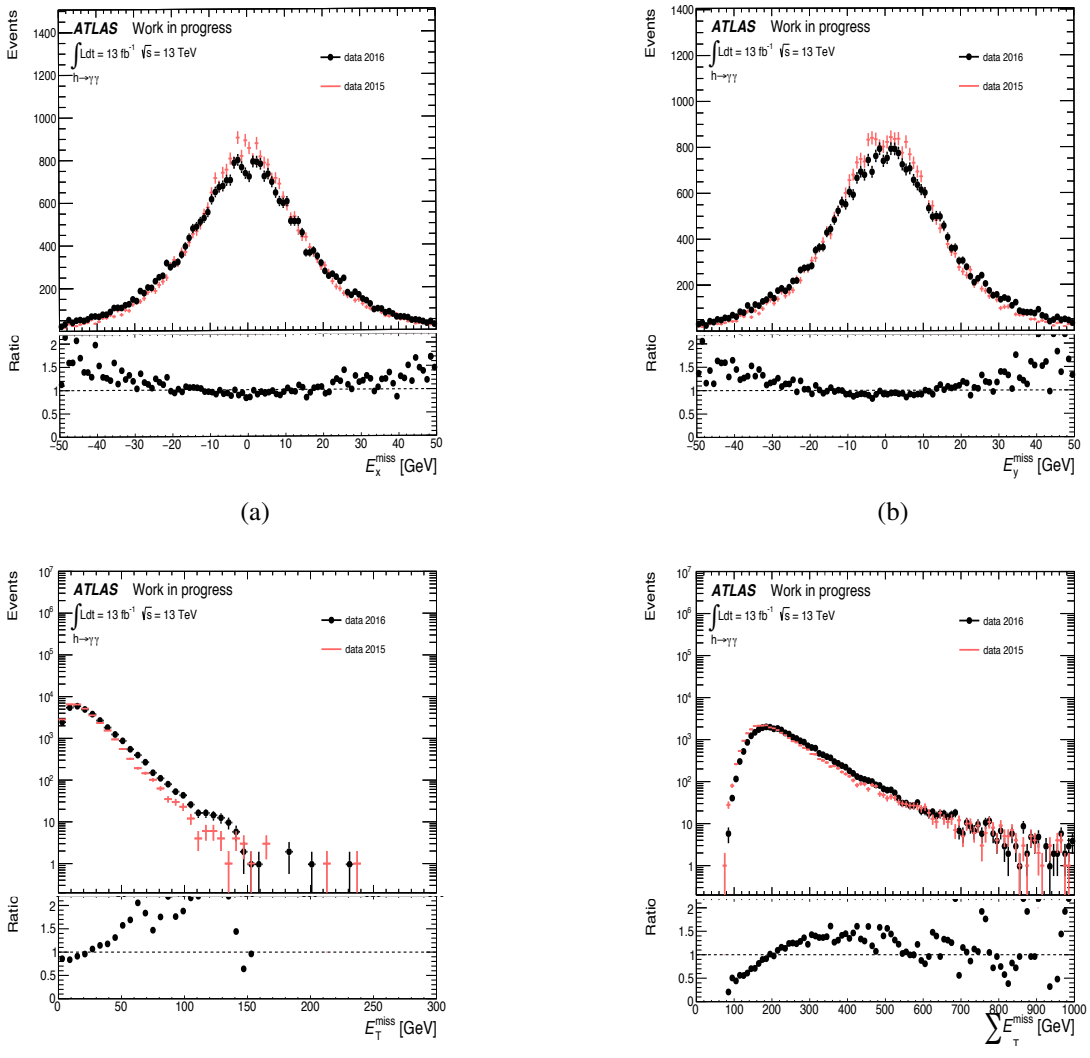
- $\sum p_{\mathrm{T}}^2$ physics - $\sum p_{\mathrm{T}}^2$ pileup ≥ 0.

Figure 6.9 shows the same vertex fraction as a function of $E_{\mathrm{T}}^{\mathrm{miss}}$ and $E_{\mathrm{T}}^{\mathrm{miss}}$ significance, respectively, for various samples. The fake $E_{\mathrm{T}}^{\mathrm{miss}}$ samples tend to always have a different vertex in the high $E_{\mathrm{T}}^{\mathrm{miss}}$ regions while those with truth $E_{\mathrm{T}}^{\mathrm{miss}}$ events have the same vertex fraction varying from 50% to 100%. This variation is dependent on the amount of additional hard tracks attached to the diphoton vertex. The heavy scalar and Wh samples have the same vertex fraction varying from 85% to 100% attributed to the additional jets or leptons attached to the vertex.

The same vertex method essentially suppresses fake $E_{\mathrm{T}}^{\mathrm{miss}}$ significantly especially in the high $E_{\mathrm{T}}^{\mathrm{miss}}$ region, paving the way for BSM physics discoveries. The versatility of this method allows it to be used across the diphoton, ll, $Z\gamma$, $4l$ and even jet channels. The same vertex method was approved by the ATLAS $E_{\mathrm{T}}^{\mathrm{miss}}$ analysis group (JETmiss group) and is documented in the supporting note found in Reference [6]. The note also discusses the derived data driven systematics of splitting the vertex in signal and background. The systematics for this method are derived from the $Z \rightarrow e^+e^-$ method described in the previous section.

6.3.3 Performance of 2015 data versus 2016 data

In this section the $E_{\mathrm{T}}^{\mathrm{miss}}$ performance comparisons between 2015 and 2016 data are shown. Such studies are essential in ensuring that there are no unexpected discrepancies between the datasets which can be caused by incorrect reconstruction or calibration. Studies are performed inclusively and the amount of 2016 data corresponds to 13.3 fb^{-1} of integrated luminosity and the diphoton mass range considered is 105 GeV $< m_{\gamma\gamma} <$ 160 GeV. The 2015 data corresponding to 3.2 fb^{-1} of integrated luminosity has been normalized to the number of events in the inclusive sample of the 2016 dataset. Figures 6.10a and 6.10b show the x and y components of $E_{\mathrm{T}}^{\mathrm{miss}}$, respectively. A significant degradation of the $E_{\mathrm{T}}^{\mathrm{miss}}$ is observed when going from 2015 and 2016, which is expected due to the high pile-up conditions. Figures 6.10c and 6.10d show the $E_{\mathrm{T}}^{\mathrm{miss}}$ and $\sum E_{\mathrm{T}}$ distributions, respectively. Good agreement between both sets of data is observed up to $E_{\mathrm{T}}^{\mathrm{miss}}$ around 50 GeV where the 2016 data has a significantly large number of events also accounted to the new pile-up conditions.



(a) (b)

(c) (d)

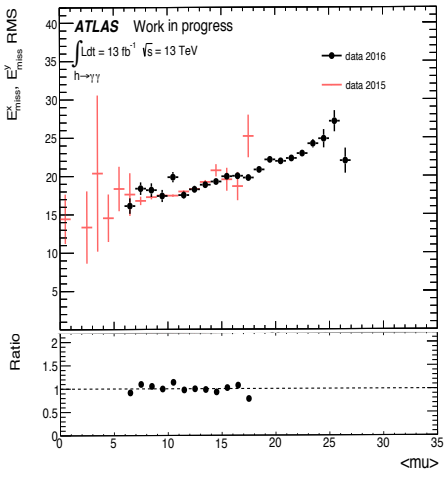
Figure 6.10: $E_{\mathrm{T}}^{\mathrm{miss}}$ distributions comparing 2015 and 2016 data, where (a) and (b) are the x and y components of $E_{\mathrm{T}}^{\mathrm{miss}}$, (c) is the $E_{\mathrm{T}}^{\mathrm{miss}}$ and (d) is the $\sum E_{\mathrm{T}}$. The 2016 data corresponds to 13.3 fb^{-1} of integrated luminosity and 2015 data corresponds to 3.2 fb^{-1} of integrated luminosity. The 2015 data has been normalized to the number of events in the inclusive sample of the 2016 data set. Significant degradation of the $E_{\mathrm{T}}^{\mathrm{miss}}$ is observed when going from 2015 and 2016 accounted to the additional pile-up interactions. Good agreement between both sets of data is observed up to $E_{\mathrm{T}}^{\mathrm{miss}} > 50$ GeV where the 2016 data has a significantly large number of events due to the new pile-up conditions [5].

In order to scrutinize the degradation of the $E_{\mathrm{T}}^{\mathrm{miss}}$ performance in 2016 in comparison to 2015, the $E_{\mathrm{T}}^{\mathrm{miss}}$ resolution distributions come into play. Figures 6.11 show the $E_{\mathrm{T}}^{\mathrm{miss}}$ resolution distributions as a function of average interactions per bunch crossing ($< \mu >$), number of primary vertices ($\mathrm{N_{pv}}$) and $\sum E_{\mathrm{T}}$. The root-mean-square (RMS) of the superimposed x and y components of the $E_{\mathrm{T}}^{\mathrm{miss}}$ is used to estimate the resolution. The RMS tends to be more reliable than the width of Gaussian fits due to the non-Gaussian tails of the $E_{\mathrm{T}}^{\mathrm{miss}}$. Also, Gaussian fits are less reliable because they are altered as the fit range changes. To add on, Gaussian fits are inclined to miss the important information about the $E_{\mathrm{T}}^{\mathrm{miss}}$ tails because their restricted range only allows them to extract the core of the distribution. Similar resolution versus $< \mu >$ and $\mathrm{N_{pv}}$ is observed between the two sets of data. Some discrepancies are observed when binning in $\sum E_{\mathrm{T}}$ due to the fact that in Run 2 the $\sum E_{\mathrm{T}}$ has two components with different pile-up dependencies. That is, the $\sum E_{\mathrm{T}}$ is made of a track-based component as well as a calorimeter-based one, each with a different dependency on the pile-up.

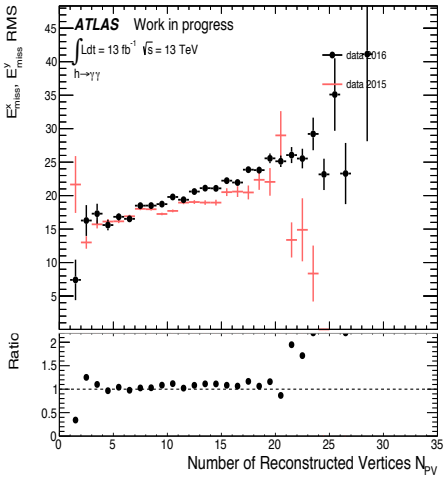
6.3.4 Impact on $E_{\mathrm{T}}^{\mathrm{miss}}$ of choice of vertex for the soft component

In the beginning of 2016, the diphoton vertex was used to compute the $E_{\mathrm{T}}^{\mathrm{miss}}$ jet component and the hardest vertex was used to compute the soft component. Later that year, the computation of the soft term was also then computed using the diphoton vertex. Checking the performance of $E_{\mathrm{T}}^{\mathrm{miss}}$ under the two reconstructions was of great importance in order to ensure that reconstructing both components using the diphoton vertex would improve the $E_{\mathrm{T}}^{\mathrm{miss}}$ performance. The checks are done using $ggh125$ MC and Table 6.1 shows the expected yield for the $ggh125$ MC in events with $E_{\mathrm{T}}^{\mathrm{miss}}$ calculated using the diphoton vertex and that calculated using the hardest vertex, respectively. The yields are are the same in both cases up to the analysis categorization which is detailed in Section 7.4 of the next chapter. HMHP refers to the High-$E_{\mathrm{T}}^{\mathrm{miss}}$ High-$p_{\mathrm{T}}^{\gamma\gamma}$ category, HMLP refers to the High-$E_{\mathrm{T}}^{\mathrm{miss}}$ Low-$p_{\mathrm{T}}^{\gamma\gamma}$ category, IntMET refers to the Intermediate-$E_{\mathrm{T}}^{\mathrm{miss}}$ category and Rest is the rest category. One can observe small differences which give a slightly higher yield in the diphoton vertex selection case.

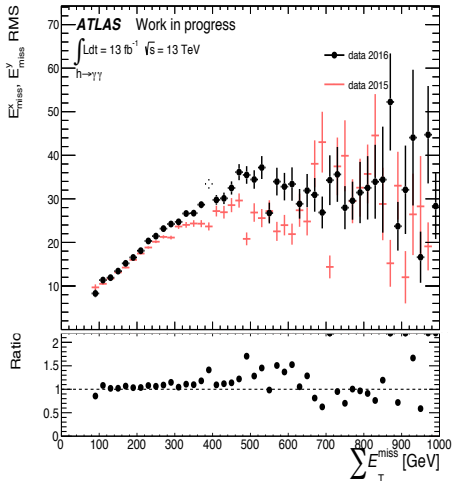
Figures 6.12 and 6.13 show the $E_{\mathrm{T}}^{\mathrm{miss}}$ distributions, including various Ref terms and $\sum E_{\mathrm{T}}$ for the $ggh125$ MC. These are shown for events within a $E_{\mathrm{T}}^{\mathrm{miss}}$ hardest vertex > 100 GeV.



(a)



(b)



(c)

Figure 6.11: $E_{\mathrm{T}}^{\mathrm{miss}}$ resolution distributions showing the x and y components of the $E_{\mathrm{T}}^{\mathrm{miss}}$ as a function of (a) μ, (b) $\mathrm{N_{pv}}$ and (c) $\sum E_{\mathrm{T}}$. The comparisons are between the 2015 full data and 2016 data corresponding to 3.2 fb^{-1} and 13.3 fb^{-1} of integrated luminosity, respectively. Similar resolution versus $<\mu>$ and $\mathrm{N_{pv}}$ is observed between data 2015 and data 2016. Discrepancies observed when binning in $\sum E_{\mathrm{T}}$ are due to the Run 2 $\sum E_{\mathrm{T}}$ having components with different pile-up dependencies [5].

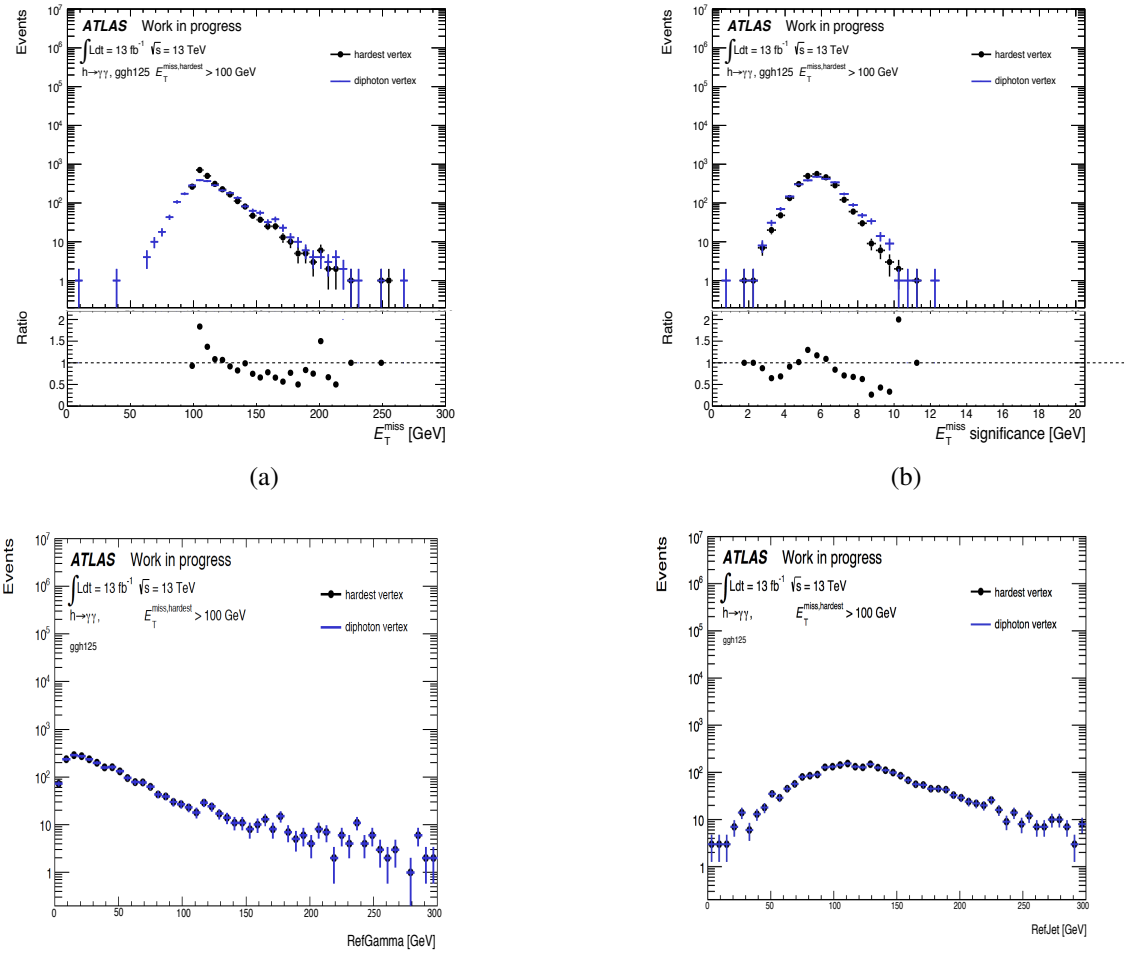
Figures 6.14 and 6.15 show the same $E_{\mathrm{T}}^{\mathrm{miss}}$ distributions for the $ggh125$ MC. These are now shown for events within 50 GeV < Hardest vertex $E_{\mathrm{T}}^{\mathrm{miss}}$ < 100 GeV.

Following several validation checks, it was observed that the diphoton vertex $E_{\mathrm{T}}^{\mathrm{miss}}$ performs better at low and intermediate $E_{\mathrm{T}}^{\mathrm{miss}}$ values than the hardest vertex $E_{\mathrm{T}}^{\mathrm{miss}}$. However, the diphoton

Table 6.1: Expected yields for the $ggh125$ MC in events with $E_{\mathrm{T}}^{\mathrm{miss}}$ calculated using the diphoton vertex and that calculated using the hardest vertex, respectively. The selections follow the nominal diphoton event selection detailed in Section 5.3.2.2.

$ggh125$	Diphoton vertex		Hardest vertex	
	Events	**Stat. error**	**Events**	**Stat. error**
No Duplicates	357.51	0.46	357.51	0.46
Trigger	220.64	0.36	220.64	0.36
GRL	220.64	0.36	220.64	0.36
DQ	220.64	0.36	220.64	0.36
Vertex	220.64	0.36	220.64	0.36
Loose PID	188.97	0.33	188.97	0.33
Ambiguity	188.97	0.33	188.97	0.33
Trig Match	188.97	0.33	188.97	0.33
Tight PID	166.84	0.32	166.84	0.32
Iso	151.90	0.30	151.90	0.30
Rel. p_T Cuts	139.84	0.29	139.84	0.29
$m_{\gamma\gamma}$ Window	139.81	0.29	139.81	0.29
HMHP	0.06	0.01	0.05	0.01
HMLP	0.29	0.01	0.23	0.01
IntMET	5.89	0.05	5.94	0.05
Rest	103.89	0.25	103.85	0.25

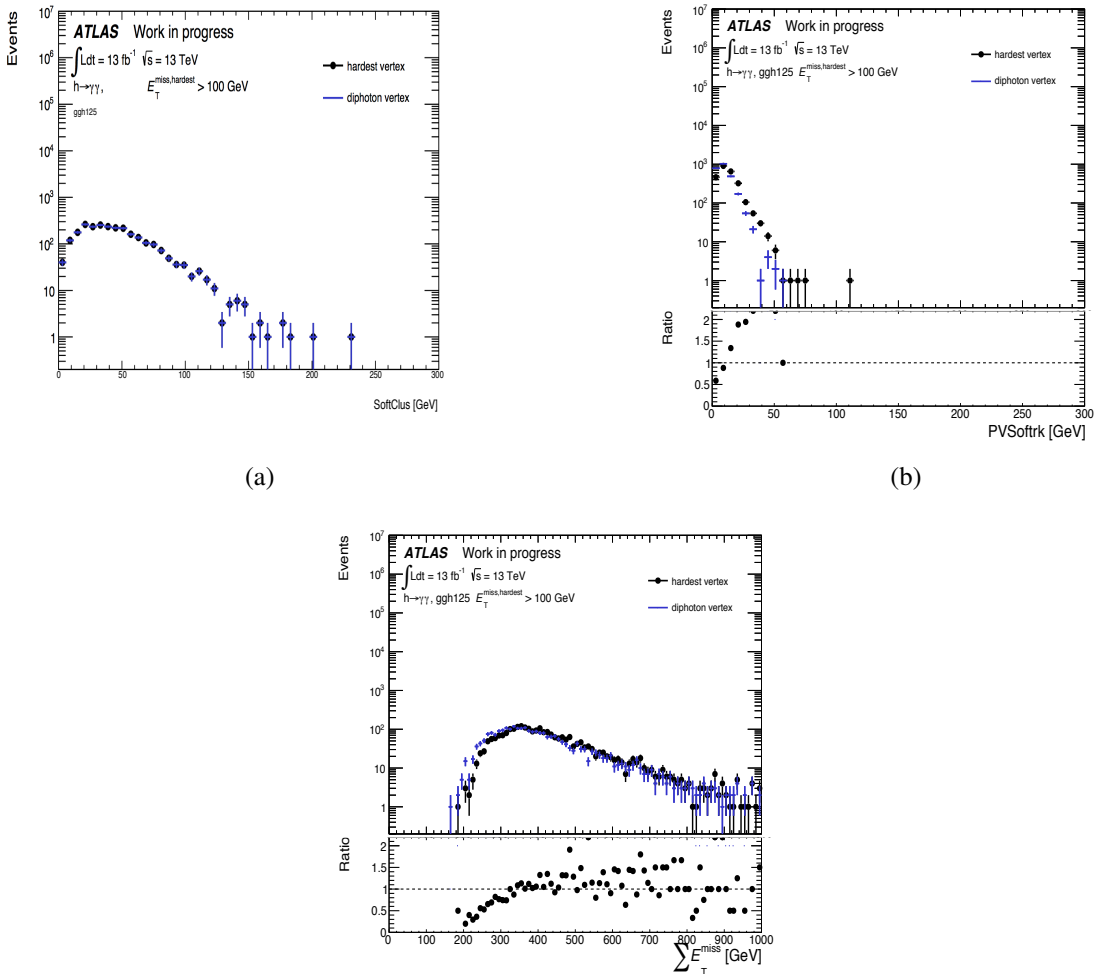
vertex tends to possess larger tails. At this point, the $E_{\mathrm{T}}^{\mathrm{miss}}$ validations needs to be studied further due to the $E_{\mathrm{T}}^{\mathrm{miss}}$ tails in our regions of interest. The distributions presented highlight that the tails are dominated by events with jets implying that some effort in incorporating additional cuts on events with jets would be ideal in resolving this issue.



(a) (b)

(c) (d)

Figure 6.12: $E_{\mathrm{T}}^{\mathrm{miss}}$ distributions for the $ggh125$ MC comparing $E_{\mathrm{T}}^{\mathrm{miss}}$ reconstructed using the diphoton vertex with that reconstructed with the hardest vertex. This is for events with Hardest vertex $E_{\mathrm{T}}^{\mathrm{miss}} > 100$ GeV. Distributions are as follows: (a) $E_{\mathrm{T}}^{\mathrm{miss}}$, (b) $E_{\mathrm{T}}^{\mathrm{miss}}$ significance, (c) RefGamma term and (d) RefJet term [5].

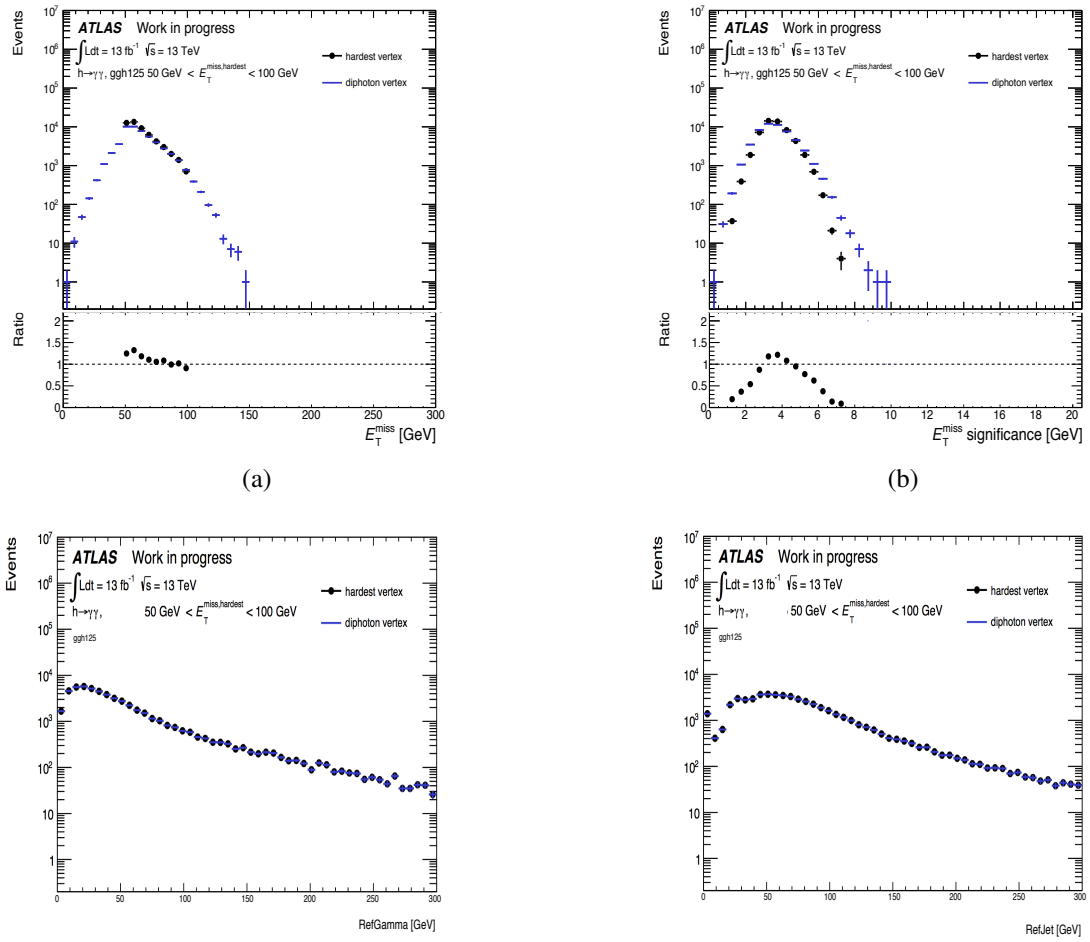


(a)

(b)

(c)

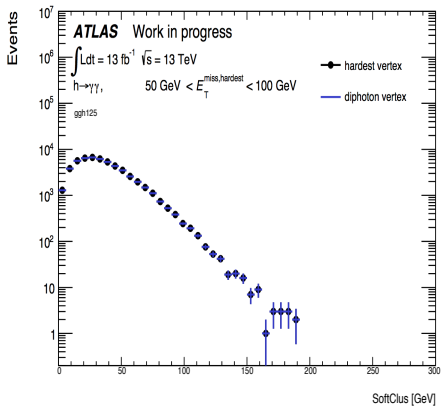
Figure 6.13: $E_{\mathrm{T}}^{\mathrm{miss}}$ distributions for the $ggh125$ MC comparing $E_{\mathrm{T}}^{\mathrm{miss}}$ reconstructed using the diphoton vertex with that reconstructed with the hardest vertex. This is for events with Hardest vertex $E_{\mathrm{T}}^{\mathrm{miss}} > 100\,\mathrm{GeV}$. Distributions are as follows: (a) SoftClus term, (b) Softrack term and (c) $\sum E_{\mathrm{T}}$ [5].



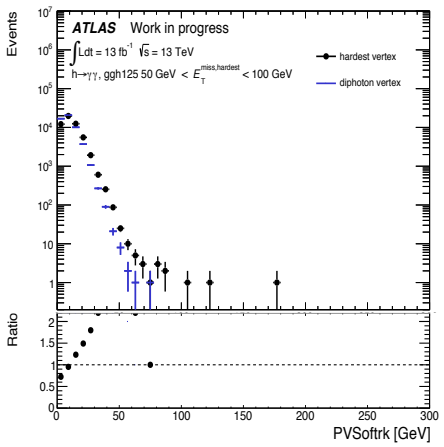
(a) (b)

(c) (d)

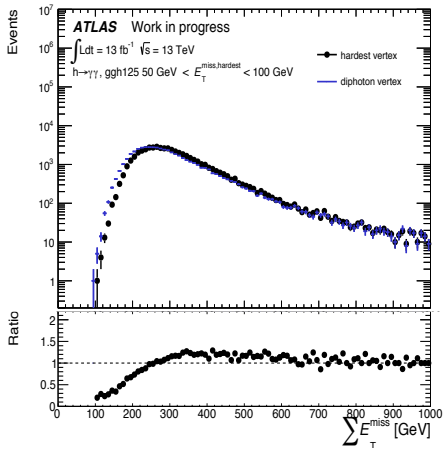
Figure 6.14: $E_{\mathrm{T}}^{\mathrm{miss}}$ distributions for the $ggh125$ MC comparing $E_{\mathrm{T}}^{\mathrm{miss}}$ reconstructed using the diphoton vertex with that reconstructed with the hardest vertex. This is for events within 50 GeV < Hardest vertex $E_{\mathrm{T}}^{\mathrm{miss}}$ < 100 GeV. Distributions are as follows: (a) $E_{\mathrm{T}}^{\mathrm{miss}}$, (b) $E_{\mathrm{T}}^{\mathrm{miss}}$ significance, (c) RefGamma term and (d) RefJet term [5].



(a)

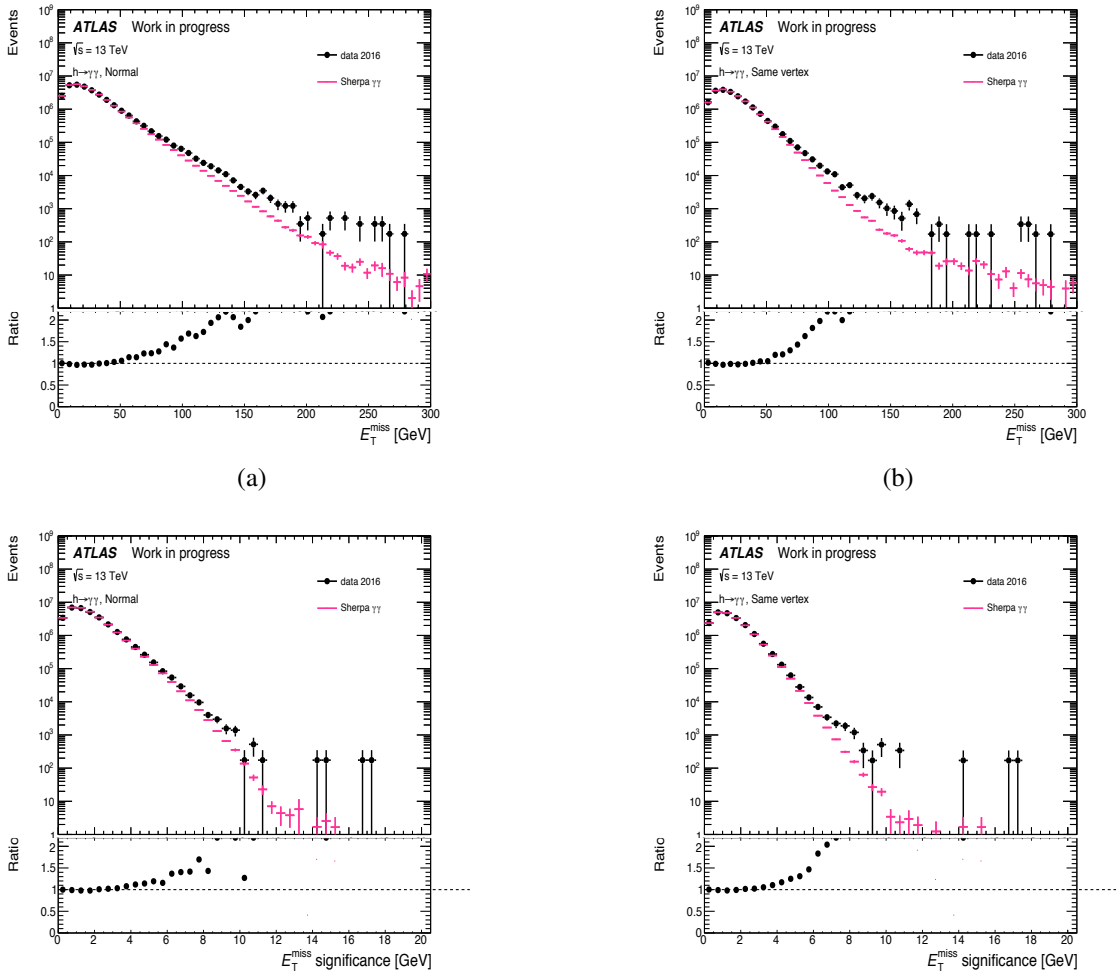


(b)



(c)

Figure 6.15: $E_{\mathrm{T}}^{\mathrm{miss}}$ distributions for the $ggh125$ MC comparing $E_{\mathrm{T}}^{\mathrm{miss}}$ reconstructed using the diphoton vertex with that reconstructed with the hardest vertex. This is for events with 50 GeV < Hardest vertex $E_{\mathrm{T}}^{\mathrm{miss}}$ < 100 GeV. Distributions are as follows: (a) SoftClus term, (b) Softrack term and (c) $\sum E_{\mathrm{T}}$ [5].



(a) (b)

(c) (d)

Figure 6.16: $E_{\mathrm{T}}^{\mathrm{miss}}$ distributions comparing 2015+2016 data corresponding to 24.8 fb^{-1} and Sherpa $\gamma\gamma$, where (a) and (b) are $E_{\mathrm{T}}^{\mathrm{miss}}$ distributions while (c) and (d) are $E_{\mathrm{T}}^{\mathrm{miss}}$ significance distributions. The left shows the nominal case while the right shows the same vertex selection case. The MC have been normalized to the total number of events in the inclusive sample of the data [6].

6.3.5 2016 data versus MC

This section presents the performance of the $E_{\mathrm{T}}^{\mathrm{miss}}$ reconstruction based on pp collision data recorded in 2015 and part of 2016 at $\sqrt{s}$ = 13 TeV and the amount of data corresponds to 24.8 fb^{-1} of integrated luminosity. The data is compared to Sherpa $\gamma\gamma$ MC and the SM ggh MC, respectively, looking at events passing 105 GeV < $m_{\gamma\gamma}$ < 160 GeV. In Figures 6.17 and 6.18, the MC have been normalized to the total number of events in the inclusive sample of the

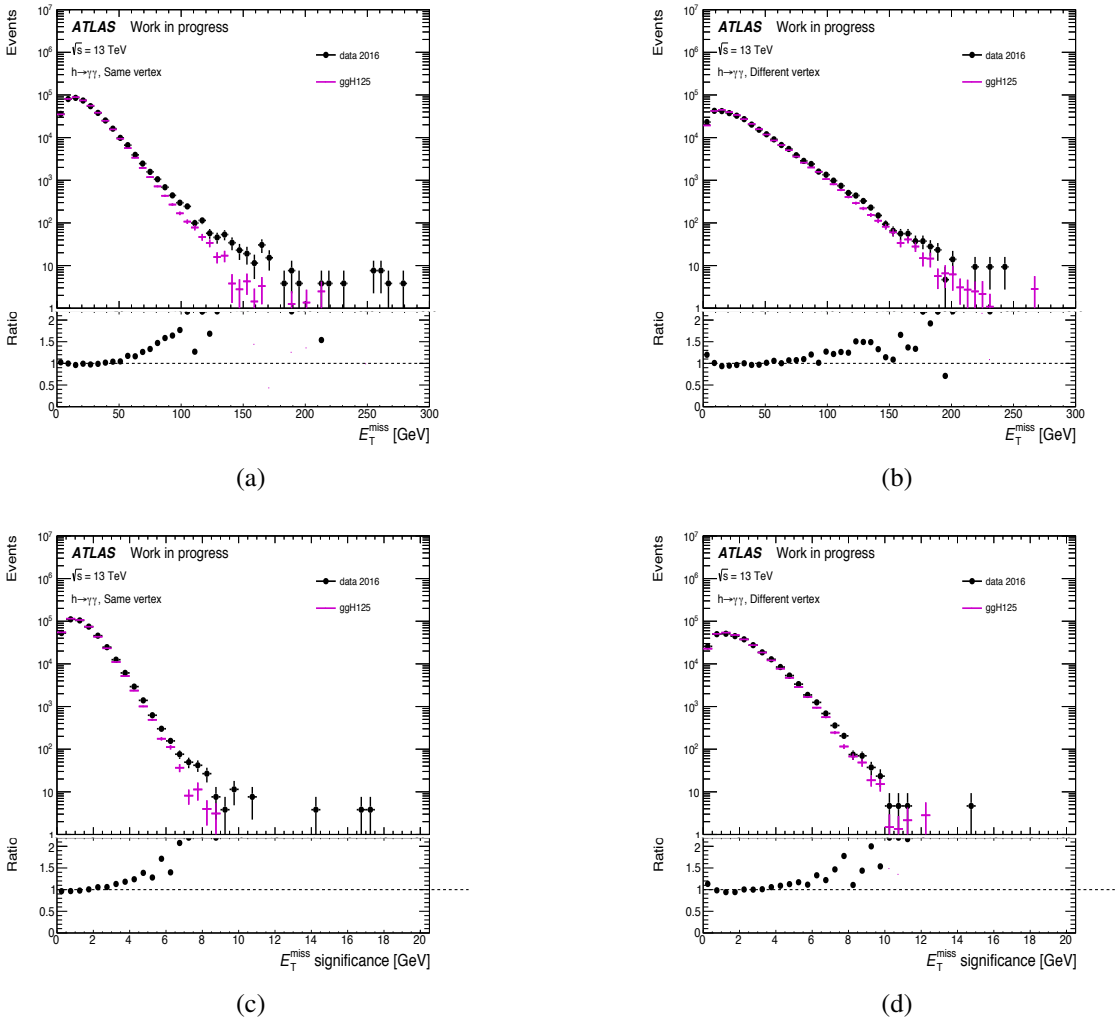


Figure 6.17: $E_{\mathrm{T}}^{\mathrm{miss}}$ distributions comparing 2015+2016 data corresponding to 24.8 fb^{-1} and ggh MC, where (a) and (b) are $E_{\mathrm{T}}^{\mathrm{miss}}$ distributions while (c) and (d) are $E_{\mathrm{T}}^{\mathrm{miss}}$ significance distributions. The left shows the same vertex case while the right shows the different vertex case. The MC have been normalized to the total number of events in the inclusive sample of the data [6].

data set. Distributions are split into the same vertex case as well as the different vertex case. For all the $E_{\mathrm{T}}^{\mathrm{miss}}$ distributions, the MC tends to undershoot the data, more so in the Sherpa $\gamma\gamma$ cases. These discrepancies will be reduced by the addition of more MC such as the γj MC and other processes with real $E_{\mathrm{T}}^{\mathrm{miss}}$ as shown in the next chapters. When making the same vertex selection, that is, requiring the diphoton vertex to be the same as the hardest vertex, slightly better performance is observed than when requiring them to be different. This is observed

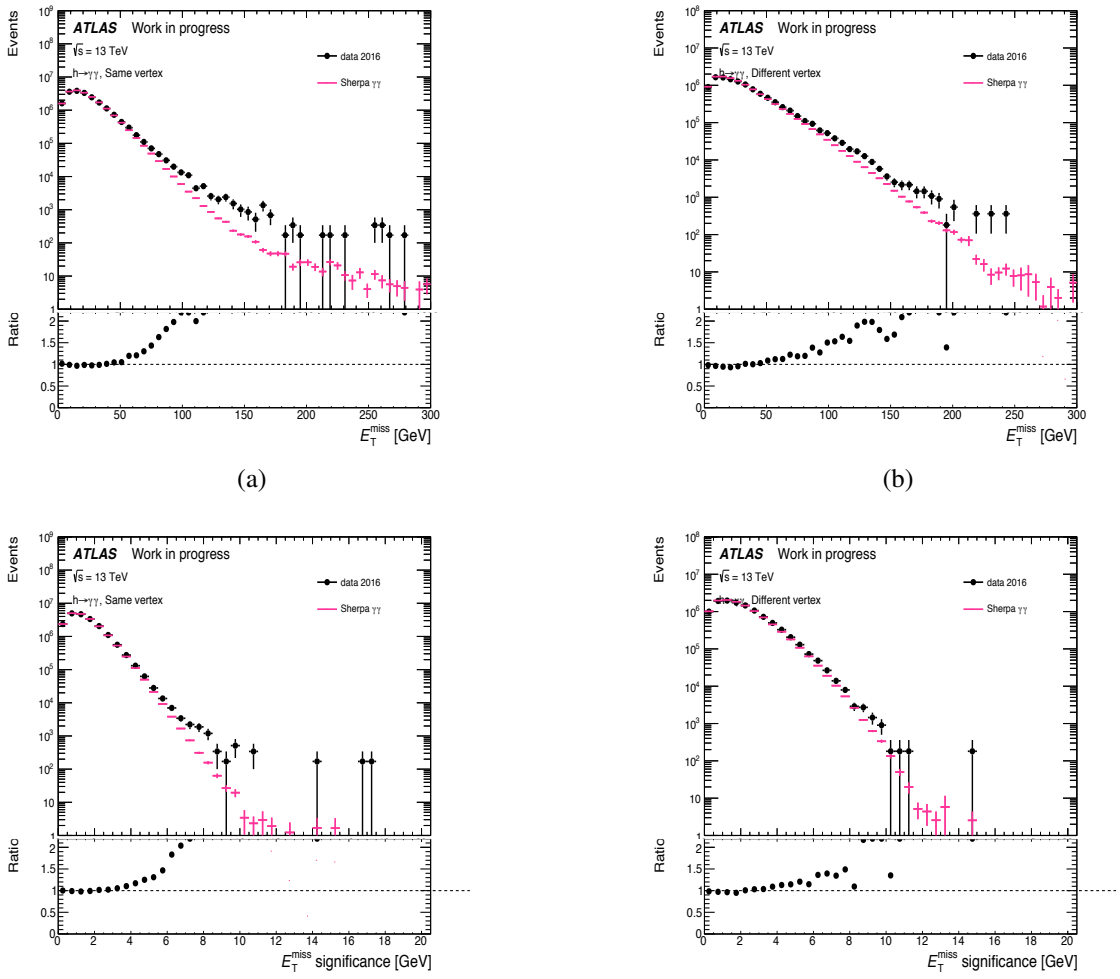
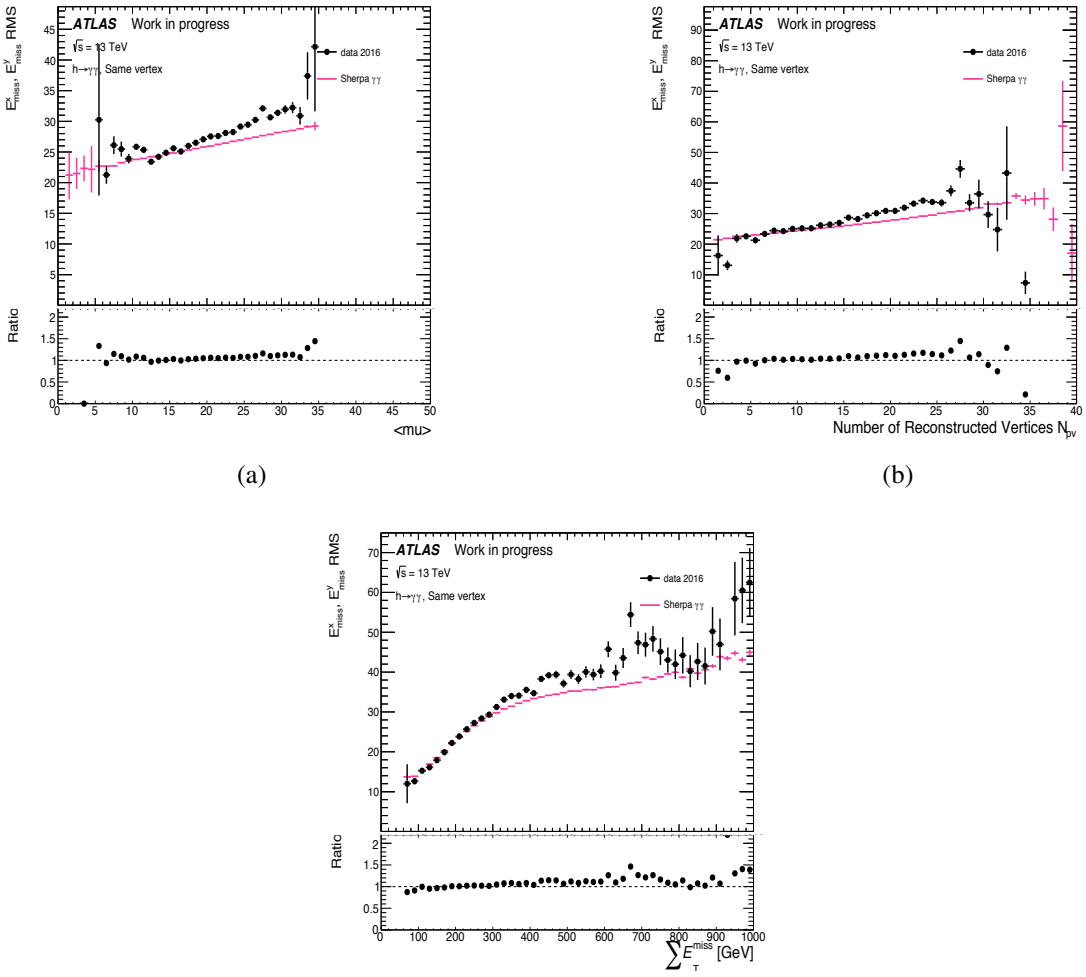


Figure 6.18: $E_{\mathrm{T}}^{\mathrm{miss}}$ distributions comparing 2015+2016 data corresponding to 24.8 fb^{-1} and Sherpa $\gamma\gamma$, where (a) and (b) are $E_{\mathrm{T}}^{\mathrm{miss}}$ distributions while (c) and (d) are $E_{\mathrm{T}}^{\mathrm{miss}}$ significance distributions. The left shows the same vertex case while the right shows the different vertex case. The MC have been normalized to the total number of events in the inclusive sample of the data [6].

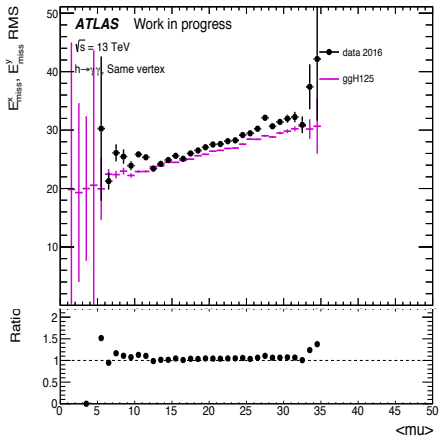
more in the resolution distributions. Commendable agreement is observed in the resolution distributions in Figures 6.19 and 6.20 as a function of μ, $\mathrm{N_{pv}}$ and $\sum E_{\mathrm{T}}$, which are only shown for the same vertex case only. All in all, splitting into same vertex and different cases proves to be more favourable than just the nominal selection.



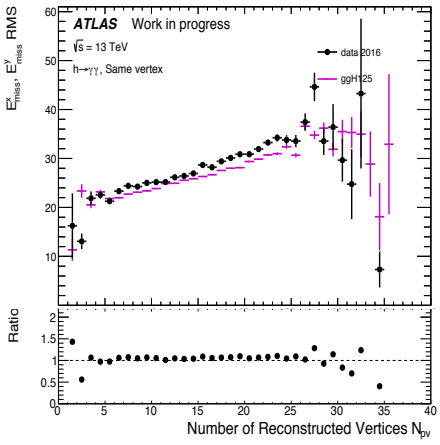
(a) (b)

(c)

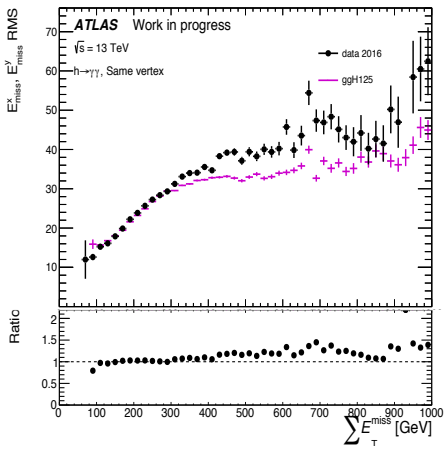
Figure 6.19: $E_{\mathrm{T}}^{\mathrm{miss}}$ resolution distributions showing the x and y components of the $E_{\mathrm{T}}^{\mathrm{miss}}$ as a function of (a) μ, (b) $\mathrm{N_{pv}}$ and (c) $\sum E_{\mathrm{T}}$. The comparisons are between 2015+2016 data corresponding to 24.8 fb^{-1} and Sherpa $\gamma\gamma$ for the same vertex selection case [6].



(a)

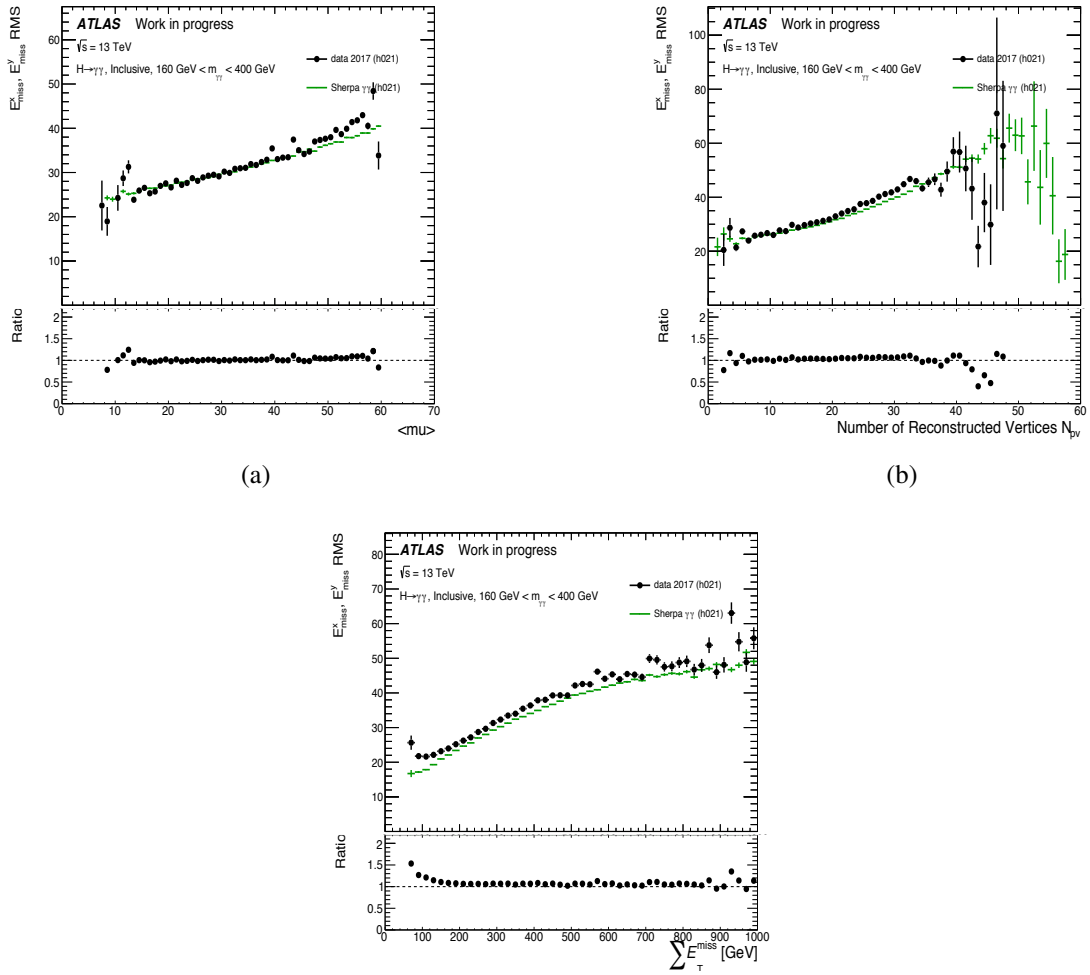


(b)



(c)

Figure 6.20: $E_{\mathrm{T}}^{\mathrm{miss}}$ resolution distributions showing the x and y components of the $E_{\mathrm{T}}^{\mathrm{miss}}$ as a function of (a) μ, (b) $\mathrm{N_{pv}}$ and (c) $\sum E_{\mathrm{T}}$. The comparisons are between 2015+2016 data corresponding to 24.8 fb^{-1} and ggh MC for the same vertex selection case [6].



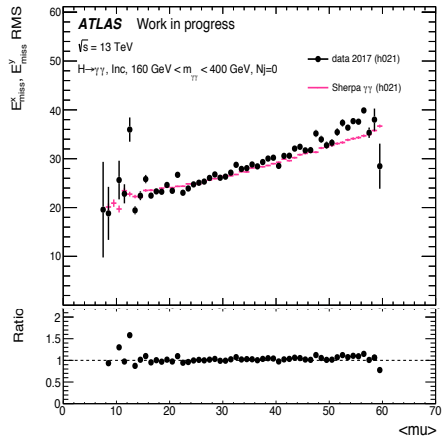
(a) (b)

(c)

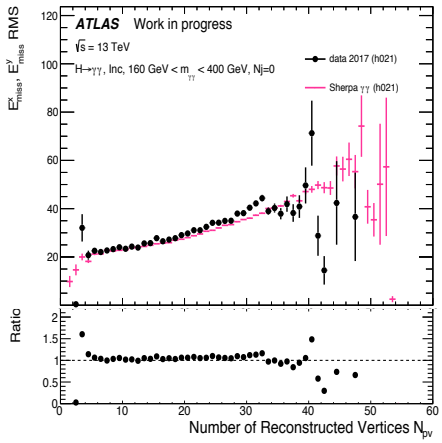
Figure 6.21: $E_{\mathrm{T}}^{\mathrm{miss}}$ resolution distributions showing the x and y components of the $E_{\mathrm{T}}^{\mathrm{miss}}$ as a function of (a) μ, (b) $\mathrm{N_{pv}}$ and (c) $\sum E_{\mathrm{T}}$. The comparisons are between 2017 data corresponding to 43.8 fb^{-1} and Sherpa $\gamma\gamma$ for the inclusive case [16].

6.3.6 2017 data versus MC

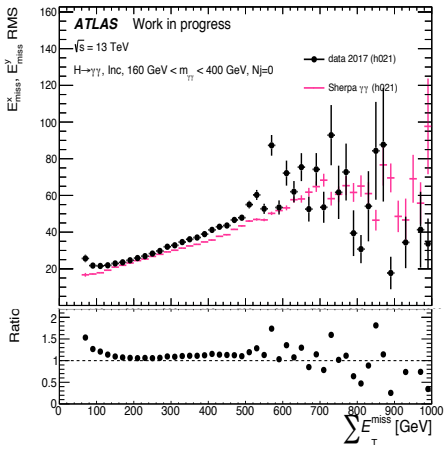
The performance of the $E_{\mathrm{T}}^{\mathrm{miss}}$ reconstruction based on pp collision data recorded in 2015, 2016 and 2017 at $\sqrt{s}$ = 13 TeV and the amount of data corresponds to 43.8 fb^{-1} of integrated luminosity. The data is compared to Sherpa $\gamma\gamma$ MC, looking at events passing 160 GeV < $m_{\gamma\gamma}$ < 400 GeV. Distributions are split into inclusive, 0-jet case, 1-jet case and ≥2-jet case. A majority of pile-up dependence arises from jets, hence the importance of binning in jets. This section only shows $E_{\mathrm{T}}^{\mathrm{miss}}$ resolution distributions showing the x and y components of the $E_{\mathrm{T}}^{\mathrm{miss}}$ as a



(a)



(b)

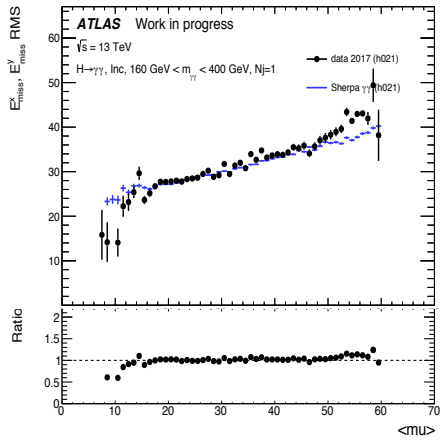


(c)

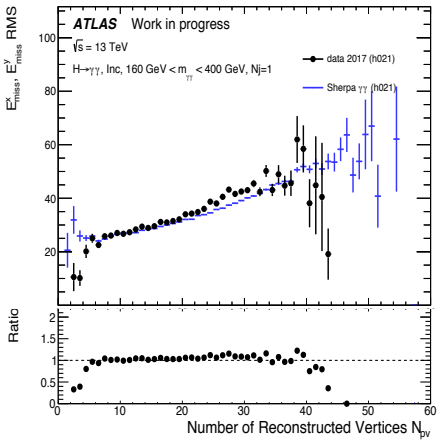
Figure 6.22: $E_{\mathrm{T}}^{\mathrm{miss}}$ resolution distributions showing the x and y components of the $E_{\mathrm{T}}^{\mathrm{miss}}$ as a function of (a) μ, (b) $\mathrm{N_{pv}}$ and (c) $\sum E_{\mathrm{T}}$. The comparisons are between 2017 data corresponding to 43.8 fb^{-1} and Sherpa $\gamma\gamma$ for the Nj=0 case [16]. Additional figures are shown in Appendix B

function of μ, $\mathrm{N_{pv}}$ and $\sum E_{\mathrm{T}}$, the additional figures that supplement this study are shown in Appendix B.

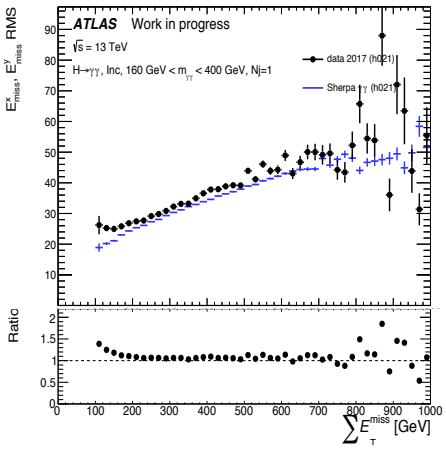
Figure 6.21 shows the inclusive case without any requirement on the number of reconstructed jets. Figure 6.22 shows the 0-jet separately in order to show the difference in $E_{\mathrm{T}}^{\mathrm{miss}}$ performance without the presence of jets. Figures 6.23 and 6.24 show the cases with exactly 1 jet and at least 2 jets, respectively. All resolution distributions show reasonable agreement between data and MC. The most stably performing resolution being that with respect to pile-up



(a)



(b)

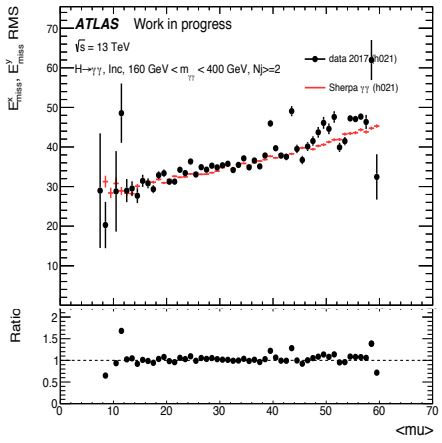


(c)

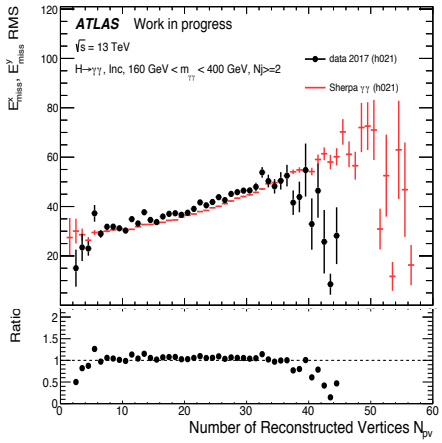
Figure 6.23: $E_{\mathrm{T}}^{\mathrm{miss}}$ resolution distributions showing the x and y components of the $E_{\mathrm{T}}^{\mathrm{miss}}$ as a function of (a) μ, (b) $\mathrm{N_{pv}}$ and (c) $\sum E_{\mathrm{T}}$. The comparisons are between 2017 data corresponding to 43.8 fb^{-1} and Sherpa $\gamma\gamma$ for the Nj=1 case [16]. Additional figures are shown in Appendix B

($\mathrm{N_{pv}}$), having the least slope in comparison to the others in all the jet binning cases. In fact, the resolution as a function of $\mathrm{N_{pv}}$ for the inclusive case has a slightly larger slope than the jet binning cases, indicative of the fact that the slope in this case comes from an increased number of jets at larger $\mathrm{N_{pv}}$.

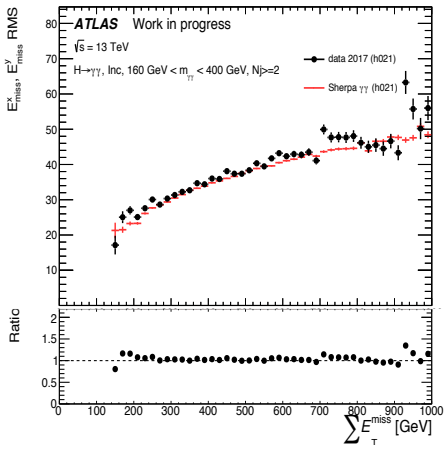
Looking at the 0-jet, 1-jet and ≥2-jet cases it is clear that the degradation is resolution originates mostly from the jet multiplicity and, from the amount of overall activity within the detector.



(a)



(b)

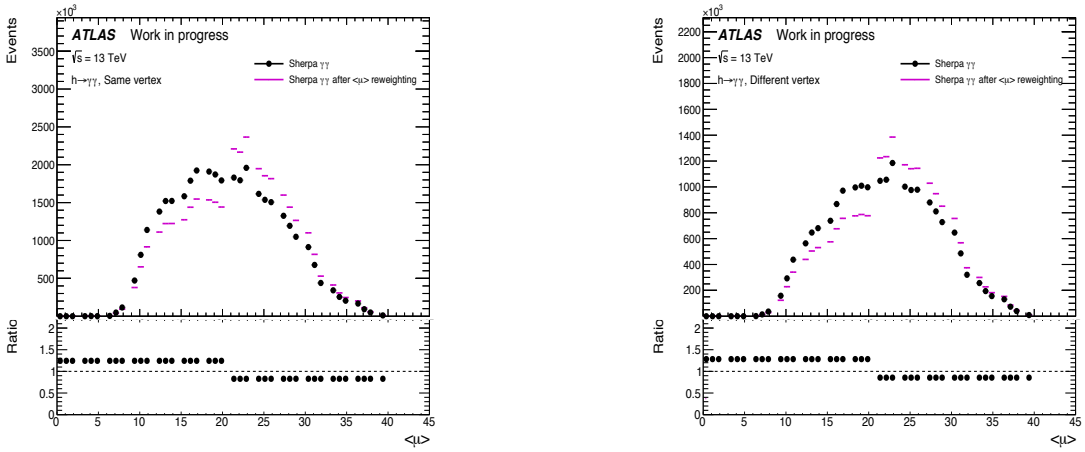


(c)

Figure 6.24: $E_{\mathrm{T}}^{\mathrm{miss}}$ resolution distributions showing the x and y components of the $E_{\mathrm{T}}^{\mathrm{miss}}$ as a function of (a) μ, (b) $\mathrm{N_{pv}}$ and (c) $\sum E_{\mathrm{T}}$. The comparisons are between 2017 data corresponding to 43.8 fb^{-1} and Sherpa $\gamma\gamma$ for the Nj>=2 case [16]. Additional figures are shown in Appendix B

6.3.7 Pile-up dependency validations

This section presents the effects of pile-up on the $E_{\mathrm{T}}^{\mathrm{miss}}$ performance. This is done by re-weighting the average interactions per bunch spacing μ by a factor of 1.5 and observing the effect on the $E_{\mathrm{T}}^{\mathrm{miss}}$ distributions. The re-weighting is done for $\mu > 20$. BSM signal and Sherpa $\gamma\gamma$ MC samples are used in this study, however only the Sherpa MC comparisons are shown since the BSM signal corresponding to the main analyses in this thesis is only introduced in the next chapter. The same vertex and different vertex cases are shown and the events after the μ



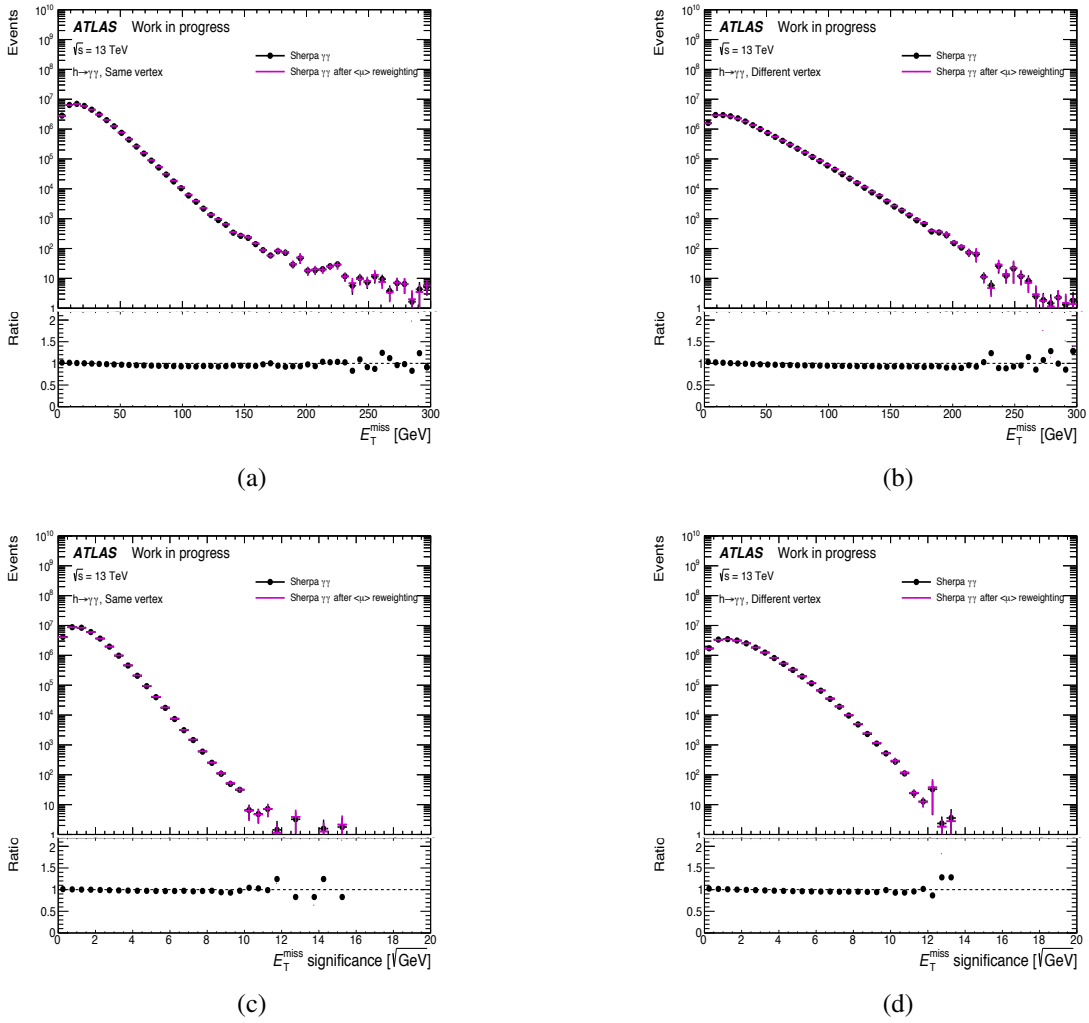
(a) (b)

Figure 6.25: μ distributions comparing Sherpa $\gamma\gamma$ MC before and after re-weighting, where (a) is the same vertex selection case and (b) is the different vertex selection case. The re-weighting of μ is by factor of 1.5. For the same vertex case Δ mean = 1.06 and for the different vertex case Δ mean = 1.00. The events after the μ re-weighting have been normalized to the number of events in the unaltered sample [15].

re-weighting have been normalized to the number of events in the unaltered sample. Figure 6.25 shows the μ distributions comparing the MC before and after the re-weighting process for the two vertex cases. Figure 6.26 shows the effects of this re-weighting on the $E_{\mathrm{T}}^{\mathrm{miss}}$ and $E_{\mathrm{T}}^{\mathrm{miss}}$ significance distributions in the two vertex cases. Very good agreement between both the MC before and after re-weighting for both vertex cases making things look very promising after this pile-up check.

6.4 Conclusions

$E_{\mathrm{T}}^{\mathrm{miss}}$ reconstruction and performance studies have been captured in this section. As mentioned previously, $E_{\mathrm{T}}^{\mathrm{miss}}$ measurements are crucial for several physics analyses at ATLAS such as those that will be discussed in the next chapters. The validation of the photon-pointing method has been presented, accompanied by a pivotal fake $E_{\mathrm{T}}^{\mathrm{miss}}$ suppression method. The same vertex method that we developed allows us to reject fake $E_{\mathrm{T}}^{\mathrm{miss}}$ events by requiring the diphoton vertex to be the same as the hardest vertex. The photon pointing vertex selection in the diphoton



(a) (b)

(c) (d)

Figure 6.26: $E_{\mathrm{T}}^{\mathrm{miss}}$ distributions comparing Sherpa $\gamma\gamma$ MC before and after re-weighting of μ, where (a) and (b) are the $E_{\mathrm{T}}^{\mathrm{miss}}$ distributions and (c) and (d) are the $E_{\mathrm{T}}^{\mathrm{miss}}$ significance distributions. The distributions on the left correspond to the same vertex selection case and those on the right correspond to the different vertex selection case. The re-weighting of μ is by factor of 1.5. For the same vertex case Δ mean = 1.06 for the μ distribution and for the different vertex case Δ mean = 1.00. The events after the μ re-weighting have been normalized to the number of events in the unaltered sample [15].

channel means that there are no hard tracks associated to the physics vertex. As a result, fake $E_{\mathrm{T}}^{\mathrm{miss}}$ events come from the pile-up vertex being harder than the photon pointing one.

$E_{\mathrm{T}}^{\mathrm{miss}}$ validations have also been performed to ensure that 2015 and 2016 data sets do not possess alarming discriminating features. In addition, the impact of the choice of vertex in reconstructing the $E_{\mathrm{T}}^{\mathrm{miss}}$ has been explored. Most importantly, data versus MC $E_{\mathrm{T}}^{\mathrm{miss}}$ performance

checks have been presented based on various datasets which have accumulated over the years. Lastly, essential pile-up checks have been done to ensure stability of $\boldsymbol{E}_{\mathrm{T}}^{\mathrm{miss}}$ performance w.r.t. pile-up interactions. All the paramount $\boldsymbol{E}_{\mathrm{T}}^{\mathrm{miss}}$ validation checks for the diphoton channel have been presented and lay a vital foundation for the consecutive analyses.

CHAPTER 7

SEARCH FOR THE HIGGS BOSON IN ASSOCIATION WITH $E_{\mathrm{T}}^{\mathrm{MISS}}$ IN THE DIPHOTON CHANNEL

This chapter details the search for new physics while searching for the Higgs boson in the diphoton and $E_{\mathrm{T}}^{\mathrm{miss}}$ final state. A final state of this manner can be indicative of phenomena associated with the production of dark matter (DM) candidates. The results of this search are interpreted in terms of a model in which a heavy scalar, denoted 'H', decays into the Higgs boson and DM candidates ($H \to h\chi\chi$). A model which is discussed in detail in Section 1.4 and was formulated based on inconsistencies in the Higgs boson transverse momentum distribution ($p_{T,h}$) measured by ATLAS and CMS as well as other excesses in the data. As explained in Chapter 1, limits were placed on the branching ratio of $H \to h\chi\chi$ using Run II data and the analysis is performed in several categories based on $E_{\mathrm{T}}^{\mathrm{miss}}$ and $E_{\mathrm{T}}^{\mathrm{miss}}$ significance and using the same vertex method which was discussed in Section 6.3.2.

This chapter is organized as follows: Section 7.1 introduces the analysis and Section 7.2 details the data and MC production specific to this analysis. Section 7.3 describes the object and event selection in the diphoton decay channel which is in fact an extension of the content discussed in Chapter 4. The event categorization is documented in Section 7.4 and Section 6.1.2 details the signal and background parameterization. The systematic uncertainties are discussed in Section 7.6 and the results are captured in Section 7.8.

7.1 Introduction

Since its discovery, the Higgs boson has been employed as a tool to explore new physics that can help to unfold the mysteries of the universe [161–163]. In particular, with the consideration that the Higgs boson interacts with DM, the direct detection of DM particles seems feasible. Astrophysicists observe its fingerprint throughout the cosmos [89, 164], however DM particles produced in SM collisions have a very minute interaction probability. As a result, DM searches at the LHC a driven primarily by $E_{\mathrm{T}}^{\mathrm{miss}}$ signatures produced with detectable particles (X+$E_{\mathrm{T}}^{\mathrm{miss}}$). Both ATLAS and CMS have searched for topologies whereby the Standard Model (SM) Higgs boson is expected to be produced from a new interaction between DM and SM particles [165, 165–168]. This study presents an updated search for DM particles (χ) in association with the SM Higgs boson (h) decaying to a pair of photons using data collected at $\sqrt{s}$ = 13 TeV during 2015 and 2016 corresponding to an integrated luminosity of 36.1 fb^{-1}.

Three benchmark models are considered in this DM search [3, 6, 18]. Figure 7.1a describes the Z'_B model [169] model whereby a massive vector mediator emits a Higgs boson and decays into a pair of Dirac fermionic DM candidates. Figure 7.1b describes the Z'-2HDM model [170] whereby Z' is produced resonantly and decays into Higgs boson and an intermediate heavy pseudoscalar A^0 which in turn decays into a pair of Dirac fermionic DM candidates.

Finally, Figure 7.1b describes the heavy-scalar model [3, 6, 18, 67, 171] based on the Madala hypothesis, whereby a heavy-scalar boson (H) is produced primarily via ggF. This model is described in detail in Section 1.4 of this documentation since our Wits Institute for Collider Particle Physics is responsible for its development and thus forms a predominant part of my contribution to this analysis. The heavy-scalar boson or Madala boson is assumed to have a mass in the range $2m_h < m_H < 2m_{top}$, where m_h represents the mass of the SM Higgs boson and m_{top} is the mass of the top quark. The upper bound is set in order to avoid a large branching fraction of $H \to \tau\tau$ which would essentially saturate the width of H leading to a $H \to h\chi\chi$ branching fraction that would be close to zero. On the other hand, the lower bound is set in order to ensure on-shell Higgs boson production. Quartic couplings between H, h and χ which allow for the Higgs boson to be produced in association with $E_{\mathrm{T}}^{\mathrm{miss}}$ are considered, where the DM particle is assumed to be a scalar. For simplicity, the decay branching fraction

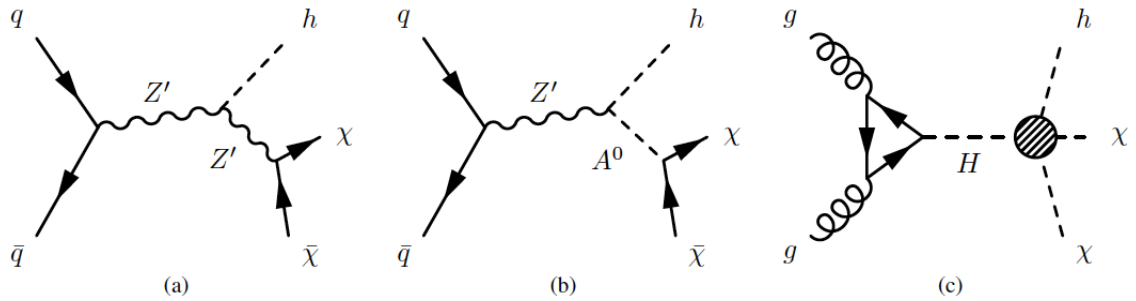


Figure 7.1: Feynman diagrams for the production of DM (χ) in association with a SM Higgs boson (h) arising from three theoretical models considered in this analysis: (a) Z'_B model, (b) Z'-2HDM model, (c) heavy-scalar model.

of $H \to h\chi\chi$ is assumed to be 100% for this model and H can be viewed as being part of a 2HDM+χ structure, where it may be considered as a CP-even heavy-scalar boson [67].

The rest of this chapter will concentrate on the heavy-scalar model based on the Madala hypothesis which is relevant to this thesis and the other introduced models will be referred to when necessary.

7.2 Data and simulation samples

For this analysis data collected in 2015 and 2016 at $\sqrt{s}$ = 13 TeV corresponding to an integrated luminosity of 36.1 fb^{-1} is used. Events that are considered are those recorded under stable beam conditions with the detector functioning efficiently, which is occurring approximately 95% of the time.

7.2.1 Signal samples

The MC signal and background processes are essential for analyses at the LHC as they are used in optimizations, uncertainty estimations and signal and background shape studies. The signal events corresponding to the Z'_B, Z'-2HDM and heavy-scalar models are generated using MadGraph aMC@NLO [146] at LO using the NNPDF3.0LO [172] parton distribution function (PDF) set. The events are then passed to Pythia8 [145] for showering and hadronization

Table 7.1: A summary of all the background processes used in this $h(\rightarrow \gamma\gamma) + E_{\mathrm{T}}^{\mathrm{miss}}$ analysis.

Process	**Generator**	**PDF set**
$\gamma\gamma$ + 3 jets	SHERPA 2.1.1	CT10
γj	Pythia8EvtGen	A14NNPDF23LO
$W\gamma$	SHERPA 2.1.1	CT10
$Z\gamma$	SHERPA 2.1.1	CT10
$W\gamma\gamma$	SHERPA 2.1.1	CT10
$Z\gamma\gamma$	SHERPA 2.1.1	CT10

with the A14 [173] set of tunes parameters using the NNPDF2.3LO PDF set [174].

In the case of the heavy-scalar model, the events are generated with the heavy-scalar mass (m_H) of $260 < m_H < 270$ GeV and $300 < m_H < 350$ GeV in 10 GeV intervals and also $270 < m_H < 300$ GeV in 5 GeV intervals. The mass points $m_\chi = 60$ GeV and $m_H = 275$ GeV are taken as an example of the kinematics that depend on the value of m_H.

7.2.2 Background samples

The dominant background contributions to the $m_{\gamma\gamma}$ spectrum originate from the resonant SM $h \rightarrow \gamma\gamma$ and non-resonant $\gamma\gamma$, γj, $W\gamma$, $Z\gamma$, $W\gamma\gamma$ and $Z\gamma\gamma$ events. The dominant background consists of “reducible" and “irreducible" components. The irreducible component is real (prompt) diphoton events, where a prompt photon originates from the hard scatter vertex.The reducible component includes dijet and γj events, in which jets are misidentified as photons.

The production of the SM $h \rightarrow \gamma\gamma$ samples is summarized in Table 5.1 and that of the prompt diphoton background MC samples is documented in Table 5.2. The remaining backgrounds as well as the specific diphoton background used in this analysis are summarized in Table 7.1.

The heavy-scalar model samples are normalized using the cross section of the SM Higgs boson produced in ggF at the same mass at NNLO+NNLL in QCD. The different pile-up conditions from the same and adjacent bunch crossings as a function of the instantaneous luminosity are simulated by overlaying minimum-bias events generated with PYTHIA8 and EvtGen [175] with the MSTW2008LO PDF set and the A2 [176] tune on the events belonging to all the hard processes. In addition, pile-up weights are applied to the simulated events in

an effort to eradicate discrepancies in the simulated and observed number of interactions per bunch crossing. A fast simulation based on AtlFastII [149] is used to simulate some of the signals and the diphoton continuum background.

7.3 Object and event selection

The object reconstruction and event selection for this analysis inherits from the nominal diphoton selection detailed in Sections 4, 5 and 6. The reconstruction and identification of all the hard physics objects (photons, jets, electrons and muons) used in this analysis is discussed in detail in Section 4. To add on, the reconstruction and performance of $E_{\mathrm{T}}^{\mathrm{miss}}$ are scrutinized in Section 6. The event selection for this $h \to \gamma\gamma$+$E_{\mathrm{T}}^{\mathrm{miss}}$ analysis follows the diphoton selection discussed in Section 5 where the two selected photon candidates are required to satisfy 105 GeV $< m_{\gamma\gamma} <$ 160 GeV and the diphoton mass is calculated with the assumption that the photons originate from the diphoton primary vertex.

7.4 Event categorization

The event categorization in this analysis is influenced by the kinematics of the models described in Section 7.1. In the case of the Z'_B and Z'-2HDM models, the Higgs boson recoils against the pair of DM candidates resulting in large $E_{\mathrm{T}}^{\mathrm{miss}}$ as well as a large diphoton p_T ($p_{\mathrm{T}}^{\gamma\gamma}$). On the contrary, in the case of the heavy-scalar model the $E_{\mathrm{T}}^{\mathrm{miss}}$ and $p_{\mathrm{T}}^{\gamma\gamma}$ spectra are shifted towards smaller values. In order to ensure an increased overall sensitivity of the analysis to these different signal models, the events are classified into categories dependent on $E_{\mathrm{T}}^{\mathrm{miss}}$, $p_{\mathrm{T}}^{\gamma\gamma}$ and other kinematic quantities. As discussed in Section 6.3.2, when the $E_{\mathrm{T}}^{\mathrm{miss}}$ is large, fake $E_{\mathrm{T}}^{\mathrm{miss}}$ events tend to contain large p_{T} pile-up jets inferred by the pile-up vertex being harder than the photon pointing one. The same vertex selection (requiring the diphoton vertex to be the same as the hardest vertex) is therefore implemented in the analysis event categorization in order to reject these fake $E_{\mathrm{T}}^{\mathrm{miss}}$ events. The same vertex selection occurs when the distance between the diphoton vertex and the highest $\sum p_T^2$ vertex in the z direction is less than 0.1 mm.

Table 7.2: A summary of the set categories defined in a sequential manner such that the rows and each category exclude events in the previous one. The 'Rest' category excludes events that are in any of the other categories. The $p_T^{\gamma\gamma} > 15\,\mathrm{GeV}$ requirement in the 'Rest' category is motivated by the fact that the contribution from the SM Higgs boson produced via gluon fusion is very large at low values of $p_T^{\gamma\gamma}$ [18].

Category	Requirements
Mono-Higgs	$S_{E_{\mathrm{T}}^{\mathrm{miss}}} > 7\ \sqrt{\mathrm{GeV}}$, $p_{\mathrm{T}}^{\gamma\gamma} > 90$ GeV, lepton veto
High-$E_{\mathrm{T}}^{\mathrm{miss}}$	$S_{E_{\mathrm{T}}^{\mathrm{miss}}} > 5.5\ \sqrt{\mathrm{GeV}}$, $\mathrm{PV}^{\mathrm{highest}} = \mathrm{PV}^{\gamma\gamma}$
Intermediate-$E_{\mathrm{T}}^{\mathrm{miss}}$	$S_{E_{\mathrm{T}}^{\mathrm{miss}}} > 4\ \sqrt{\mathrm{GeV}}$, $p_{\mathrm{T}}^{\mathrm{hard}} > 40$ GeV, $\mathrm{PV}^{\mathrm{highest}} = \mathrm{PV}^{\gamma\gamma}$
Different vertex	$S_{E_{\mathrm{T}}^{\mathrm{miss}}} > 4\ \sqrt{\mathrm{GeV}}$, $p_{\mathrm{T}}^{\mathrm{hard}} > 40$ GeV, $\mathrm{PV}^{\mathrm{highest}} \neq \mathrm{PV}^{\gamma\gamma}$
Rest	$p_{\mathrm{T}}^{\gamma\gamma} > 15$ GeV

This requirement is made in order to ensure that the diphoton vertex is the same as the highest $\sum p_T^2$ vertex. In addition, the $p_{\mathrm{T}}^{\mathrm{hard}}$ variable defined as the magnitude of the vectorial sum of the transverse momenta of photons and jets in the event. This variable provides further fake $E_{\mathrm{T}}^{\mathrm{miss}}$ suppression in the low-$E_{\mathrm{T}}^{\mathrm{miss}}$ region. Lastly, in order to reject the background events from SM $V\gamma$ and $V\gamma\gamma$ processes (where V stands for W or Z), a lepton veto is applied.

This analysis defines five sequential categories shown in Table 7.2 such that each category excludes the events in the previous row. So the 'Rest' category essentially excludes the events that are in any of all the other categories. The Z'_B and Z'-2HDM signals are used in the optimization and definition of the Mono-Higgs category, providing most of the sensitivity to the corresponding two models. On the other hand, the other four categories provide extra sensitivity to the heavy-scalar model and are optimized using the heavy-scalar samples.

7.4.1 The Madala framework

In order to perform the $h(\rightarrow \gamma\gamma) + E_{\mathrm{T}}^{\mathrm{miss}}$ analysis, a framework is essential to bridge the gap between the nominal HGamAnalysisFramework and this particular final state. The HGamAnalysisFramework is the nominal diphoton analysis framework and is detailed in Section 5.1. The Madala framework was developed to assist the bridging process. This framework was developed by our group and is set up in such a way that it runs over the standard

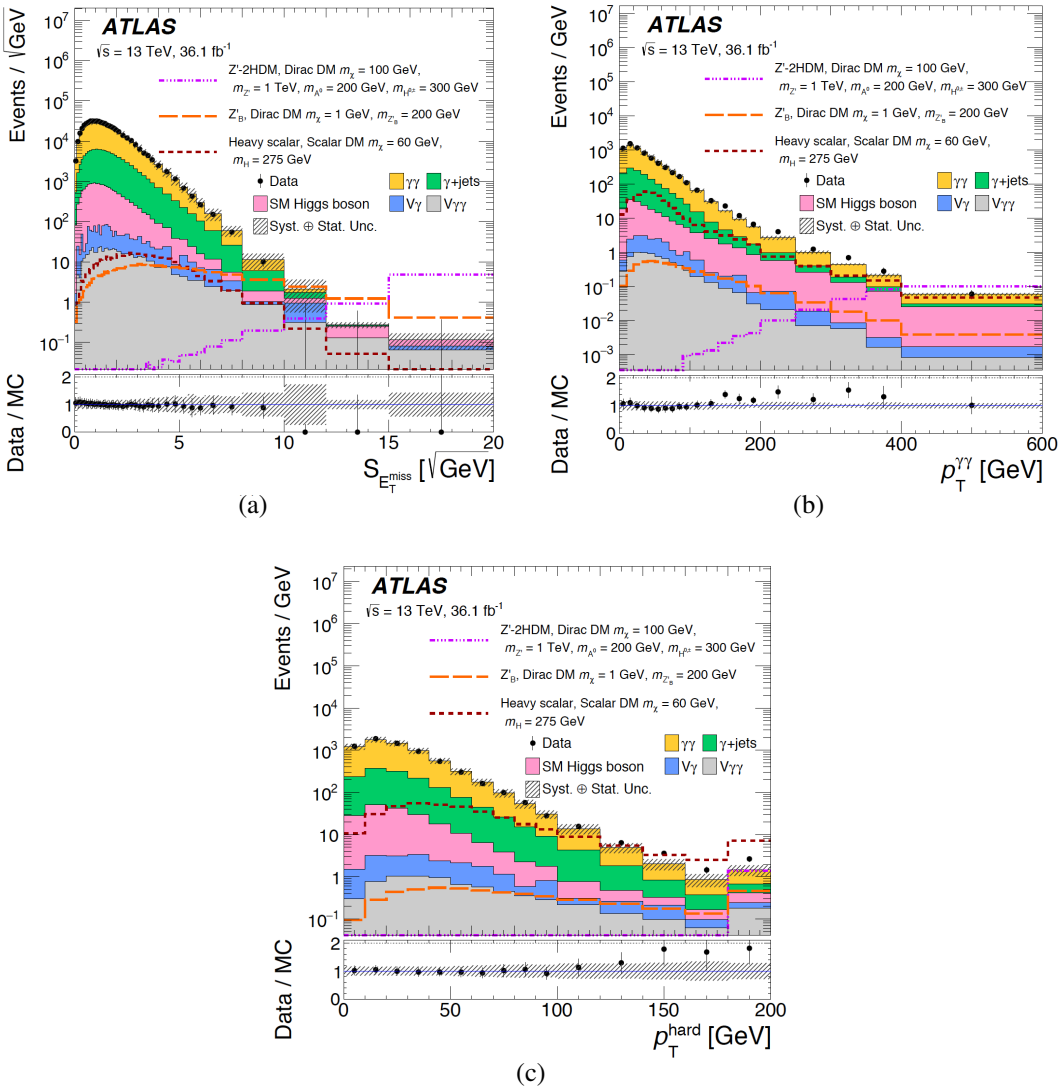
MxAODs produced by the HGamTools package coupled to the HGAMANALYSISFRAMEWORK and produces even smaller files called ntuples in which only information relevant to the $h(\rightarrow \gamma\gamma) + E_{\mathrm{T}}^{\mathrm{miss}}$ analysis is stored and used to produce all the important physics figures and quantitative estimates. The Madala framework is named "Mad2s" and can run over all data and MC in MxAOD format. The upside of running over the centrally produced MxAODs is that they process much faster than DxAODs and any issues with the MxAODs are dealt with quite rapidly by the mainstream $h \rightarrow \gamma\gamma$ analysis team. The output ntuple files produced by the Madala framework are the ones utilized in producing the various physics results that follow.

7.4.2 Categorization results

The events in the ntuples produced by the Madala framework have essentially passed the nominal diphoton selection. As a result, the analysis categorization is performed at the ntuple level. The control distributions in Figure 7.2 correspond to $S_{E_{\mathrm{T}}^{\mathrm{miss}}}$, $p_{\mathrm{T}}^{\gamma\gamma}$ and $p_{\mathrm{T}}^{\mathrm{hard}}$ after selecting photon candidates within $120\,\mathrm{GeV} < m_{\gamma\gamma} < 130\,\mathrm{GeV}$. The $\gamma\gamma$ and γj contributions are normalized to 79% and 19% of the data yield, respectively. These values are estimated from a two-dimensional sideband technique, which involves counting the number of events in which one or both photons pass or fail the identification or isolation requirements. Slight discrepancies are observed in the control distributions, but these do not affect the overall results. The inconsistencies are found mainly in non-resonant backgrounds, which are estimated directly from data. Table 7.3 shows a summary of the expected yields in the $m_{\gamma\gamma}$ range 122 to 128 GeV, where the expectation from MC is normalized with its corresponding cross-section and the data luminosity. The SM Higgs signal comprises all the SM Higgs samples that were summarized in Table 5.1 (ggF, VBF, Wh, Zh and tth). Moreover, the background sample yields correspond to the MC summarized in Table 7.1 of this chapter.

7.5 Signal and background parameterization

The signal and background yields are obtained by fitting analytical functions to the diphoton invariant mass spectrum in each category. The parameters that describe the shape of the signal



(a) (b) (c)

Figure 7.2: The distribution of (a) $S_{E_{\mathrm{T}}^{\mathrm{miss}}}$, (b) $p_{\mathrm{T}}^{\gamma\gamma}$, and (c) $p_{\mathrm{T}}^{\mathrm{hard}}$ after the selection of diphoton candidates in 120 GeV < $m_{\gamma\gamma}$ < 130 GeV and making the SV selection. Expected distributions are shown for data and various MC including signals corresponding to the various models, where for the heavy-scalar model m_H = 275 GeV and scalar DM m_χ = 60 GeV are considered. These signal points that are overlaid represent the model kinematics. The hatched bands represent the quadratic sum of the MC statistical and experimental systematic uncertainties in the total background, while the theoretical uncertainties in the background normalization are not included. The rightmost bin shows the overflow events and the asymmetric error bars on data points come from Poissonian confidence intervals at 68% confidence level [18].

Table 7.3: The event yields in the $m_{\gamma\gamma}$ window 122 GeV to 128 GeV. The expectation from MC is normalized with its corresponding cross-section and to 36.1 fb^{-1} data luminosity.

Cuts	Signal	SM	$V\gamma$	$V\gamma\gamma$	$\gamma\gamma$	γj	Data
$m_{\gamma\gamma}$	587.86	1582.65	97.22	46.40	31276.97	8019.14	41030
Mono-Higgs	18.33	2.25	1.72	1.18	2.36	1.82	7
High-$E_{\mathrm{T}}^{\mathrm{miss}}$	40.44	3.78	3.83	3.20	15.78	7.46	47
Int. $E_{\mathrm{T}}^{\mathrm{miss}}$	74.77	10.17	6.78	3.65	163.14	60.41	269
Diff. vertex	50.80	34.44	4.08	1.91	701.61	283.42	897
Rest	368.12	1227.23	73.95	33.23	22280.03	5665.75	28364

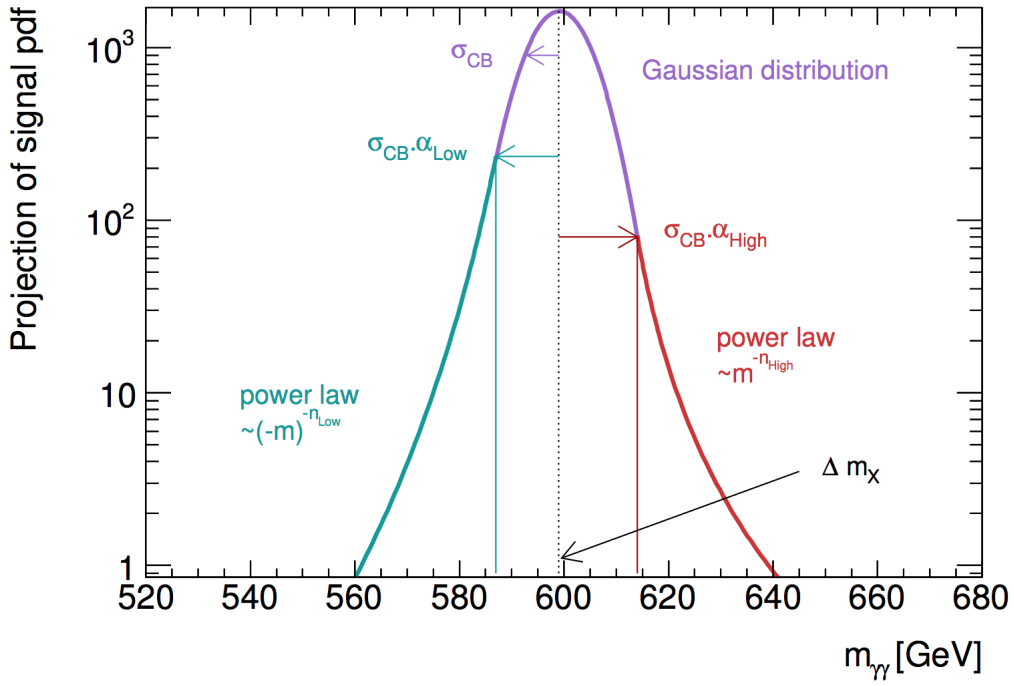


Figure 7.3: An illustration of the double-sided Crystal Ball function and its parameters, for a signal mass m_χ = 600 GeV. The various parameters are elaborated on in the text.

are obtained from simulated signal samples. On the other hand, analytical models used for the background shape are chosen using simulated background samples and the values of their free parameters are determined from fits to data.

7.5.1 Signal modelling

The signal parameterization is performed on a fixed Higgs mass of 125 GeV where the mass distribution for the signal is modelled from MC simulations as the sum of a double-sided Crystal Ball (DSCB) function for the all the categories. Figure 7.3 shows an illustration of the DSCB function and its parameters. The DSCB function modelling method is described in more detail in Reference [128] and is defined as follows:

$$N \cdot \begin{cases} e^{-t^2/2} & \text{if } -\alpha_{Low} \geq t \geq \alpha_{High} \\ \frac{e^{-0.5\alpha_{Low}^2}}{\left[\frac{\alpha_{Low}}{n_{Low}}\left(\frac{n_{Low}}{\alpha_{Low}} - \alpha_{Low} - t\right)\right]^{n_{Low}}} & \text{if } t < -\alpha_{Low} \\ \frac{e^{-0.5\alpha_{High}^2}}{\left[\frac{\alpha_{High}}{n_{High}}\left(\frac{n_{High}}{\alpha_{High}} - \alpha_{High} + t\right)\right]^{n_{High}}} & \text{if } t > \alpha_{High}, \end{cases} \tag{7.1}$$

where the parameter N controls the all-inclusive normalization of the PDF, $t = \Delta m_R/\sigma_{CB}$, $\Delta m_R = m_R - \mu_{CB}$, μ_{CB} is the Gaussian component mean, σ_{CB} is the Gaussian component width, α_{Low} (α_{High}) is the point at which the Gaussian becomes a power law on the low (high) mass side, and n_{Low} (n_{High}) is the exponent of this power law.

Taking into consideration all the SM Higgs and heavy-scalar signal MC at $m_H = 125$ GeV, the signal model that is parametrized as a function on the Higgs boson mass is estimated. Various fits on a signal using 13 TeV MC simulation are shown in Appendix C.

7.5.2 Background modelling

The shape and normalization of the background distribution are attributes that need to be well comprehended in order to accurately measure the number of signal events in data. This is achieved by essentially fitting analytical functions to the background distribution in data. Following this, the selected background model corresponds to the function that introduces the least amount of bias to the signal yield.

The normalization and the shape of the non-resonant background are obtained by fitting the diphoton invariant mass distribution in data for each of the categories. A range of analytic functions are considered for the non-resonant background modelling: exponential functions of different-order polynomials, Bernstein polynomials of different order and an adapted dijet

Table 7.4: The analytic functions used to model the non-resonant $m_{\gamma\gamma}$ distribution, the uncertainty in the signal due to the non-resonant background modelling ($\Delta N_{bkg}^{non-res}$) and the relative uncertainties in the expected non-resonant background and signal for each category. The signal yields used to estimate the relative uncertainty in the signal corresponding to the various categories are calculated in the $120 < m_{\gamma\gamma}$ 130 GeV range. The variable x is defined by $m_{\gamma\gamma}/\sqrt{s}$ and a and b are the background function parameters. In the Rest category case, C_3^j are binomial coefficients while $b_{j,3}$ are Bernstein coefficients [18].

Category	**Function**	$\Delta N_{bkg}^{non-res}$	$\Delta N_{bkg}^{non-res}/N_{bkg}^{non-res}$ [%]	$\Delta N_{bkg}^{non-res}/N_{signal}$ [%]
Mono-Higgs	$exp(a.x)$	1.2	9.8	6.0
High-$E_{\mathrm{T}}^{\mathrm{miss}}$	$(1-x^{1/3})^b.x^a$	2.7	4.0	11.0
Int. $E_{\mathrm{T}}^{\mathrm{miss}}$	$exp(a.x+b.x^2)$	5.8	1.3	14.0
Diff. vertex	$exp(a.x+b.x^2)$	8.4	0.5	26.0
Rest	$\sum_{j=0}^{3} C_3^j x^j (1-x)^{3-j} b_{j,3}$	61	< 0.1	28.0

function [177]. The choice of analytic function to model the background is attached to a potential bias which is referred to as the non-resonant background modelling uncertainty ($\Delta N_{bkg}^{non-res}$). The spurious signal used is equal to the bias on the signal yield caused by the choice of a particular background parametrization. The uncertainty is estimated (for each category) as the signal yield extracted from a signal+background (S+B) maximum likelihood fit to a background-only diphoton invariant mass distribution with small fluctuations.

In this study $\gamma\gamma$, γj, $V\gamma$ and $V\gamma\gamma$ background processes are considered. The $\gamma\gamma$ and γj samples are normalized to the data side bands at the $m_{\gamma\gamma}$ window cut with 79% and 19% of the data yields, respectively. In actual fact, the γj sample is the same as the high statistics $\gamma\gamma$ sample except that it is reweighted to the Anti-ID data $S_{E_{\mathrm{T}}^{\mathrm{miss}}}$ shape and to the γj rate using the purity measurement. The $V\gamma$ and $V\gamma\gamma$ are normalized to their corresponding cross sections. Finally, the samples are all merged and used as inputs to the spurious signal test.

Various functions are tested and for each functional form, several fits are made by varying the position of the signal peak. The criteria for a function to pass a quantity requirement is that the spurious signal value over the fit uncertainty has to be as small as possible ideally. In other words, among the different analytic functions, the parameterization with the smallest $\Delta N_{bkg}^{non-res}$ or that with the least number of free parameters when the same $\Delta N_{bkg}^{non-res}$ values are obtained, is chosen as the nominal background parameterization to describe the non-resonant background shape. In addition to this, a χ^2 test is performed in order to make certain that the selected fit is compatible with data in each category. Table 7.4 shows the selected analytic

functions along with their non-resonant background modelling uncertainties corresponding to each category, whose values are taken as estimates of the systematic uncertainties due to the choice of parameterization. The results of the direct fit method to the various categories are shown in Appendix C.

7.6 Systematic uncertainties

The systematic uncertainties from both experimental and theoretical sources affect the signal efficiency and the SM Higgs background yield estimated from simulated MC samples. The major sources of uncertainties are briefly discussed in this section.

Table 7.5 shows a summary of the experimental and theoretical uncertainties with respect to the yield of the background from SM Higgs boson processes, non-resonant background as well as signal production. Since the parameters of the non-resonant background model are extracted from the fit, the only systematic uncertainty related with the background model is the spurious signal discussed in Section 7.5.2. The nuisance fit parameters are profiled are profiled in the fit, obtaining their values mostly from the side-bands. The uncertainty impacts the sensitivity of the analysis, as expected.

7.6.1 Experimental uncertainties

The uncertainties corresponding to the various objects are calculated by applying the combined performance (CP) group recommendations. The CP group is dedicated to optimizing object identification and selection. The uncertainties are calculated by shifting object values up and down and each shift is compared to the nominal case and the relative shift in the number of selected events is considered. The most important uncertainties in this analysis are those in jet energy scale, resolution and jet vertex tagger which are propagated to the $E_{\mathrm{T}}^{\mathrm{miss}}$ calculation. These need to be taken into account in order to avoid misreconstruction of $E_{\mathrm{T}}^{\mathrm{miss}}$, which can lead to the migration of events among categories. The experimental uncertainties are discussed as follows:

Table 7.5: A breakdown of the dominant systematic uncertainties in the range of 105 GeV < $m_{\gamma\gamma}$ < 160 GeV. The impact of uncertainties on the yield of the SM Higgs boson processes is shown. All production modes of the SM Higgs boson are considered together unless otherwise stated. Representative values for the impact on the four analysis categories are shown, unless a given source has very different impacts on different categories, in which cases the largest and the smallest impacts are shown separately. Values for the impact on all categories are shown and in the cases where the value is substituted by a " – ", the systematic uncertainty is not applicable to the sample [18].

Source	**Signals [%]**	**Backgrounds (SM Higgs) [%]**
Experimental		
Luminosity	3.2	-
Trigger efficiency	0.4	-
Vertex selection	< 0.1	-
Photon energy scale	0.1-2.0	0.1-1.4
Photon energy resolution	0.1-0.2	0.1-1.1
Photon identification efficiency	2.9-4.3	1.9-3.8
Photon isolation efficiency	1.2	0.8-1.6
$E_{\mathrm{T}}^{\mathrm{miss}}$ reconstruction (diphoton vertex)	< 0.1	0.5-1.9
$E_{\mathrm{T}}^{\mathrm{miss}}$ reconstruction (jets, soft term)	1.0-1.4	0.8-23
Diphoton vertex with largest $\sum p_T^2$	< 0.1-1.9	0.1-6.0
Pileup reweighting	0.2-5.6	0.7-11
Non-resonant background modelling	-	0.1-9.8
Theoretical		
Factorization and renormalization scale	0.6-11	2.5-6.0
PDF+α_s	11-25	1.2-2.9
Multiple parton-parton interactions	< 1	0.4-5.8
B($H \to \gamma\gamma$)	1.73	-

- The 3.2% uncertainty in the combined 2015 and 2016 integrated luminosity is derived from a calibration of the luminosity scale using x-y beam separation scans performed in 2015 and 2016 following a method similar to that used in Reference [178].

- The efficiency of the diphoton trigger is evaluated in MC using a trigger matching technique and in data using a bootstrap method [179]. The trigger efficiency uncertainty is found to be 0.4% in the 105 GeV < $m_{\gamma\gamma}$ < 160 GeV diphoton mass window.

- The vertex selection uncertainty is obtained by comparing photon-pointing vertices in $Z \to ee$ events in data and MC simulation, whereby each electron track is discarded

and its corresponding cluster is recalibrated as that belonging to a photon [180]. The efficiency in data agrees with that in the MC within 0.01%.

- Systematic uncertainties due to the photon energy scale and resolution inherit from Run 1 results [128], with slight updates in case of corrections using the Run 2 data. The uncertainty in the energy scale is less than 1% while that in the energy resolution is less than 2%.

- The uncertainty in the photon identification efficiency [181] is obtained from the difference between applying and not applying the corrections to the EM shower shape variables (summarized in Table 4.1) in simulation. The uncertainty is found to be less than 3.8% for SM Higgs background in all categories, 2.9% for simplified model samples, and 4.3% for the heavy-scalar model.

- The uncertainty in the photon calorimeter isolation efficiency is obtained from the efficiency differences between applying and not applying corrections derived from inclusive photon events to the isolation variables in simulation. The use of the inclusive photon events helps to derive the efficiency uncertainty in the photon track isolation uncertainty. This value is found to be less than 1.6% for the SM Higgs background and 1.2% for all signal the samples.

- The systematic uncertainties in the scale and resolution of the $E_{\mathrm{T}}^{\mathrm{miss}}$ soft term are estimated in 2016 data using the method described in Reference [156]. The overall jet and $E_{\mathrm{T}}^{\mathrm{miss}}$ uncertainties in the SM Higgs processes are as follows for the various categories: 6% (Mono-Higgs), 8% (High-$E_{\mathrm{T}}^{\mathrm{miss}}$), 23% (Intermediate-$E_{\mathrm{T}}^{\mathrm{miss}}$), 22% (Different vertex) and 1% (Rest). In the case of the signal processes, the overall jet and $E_{\mathrm{T}}^{\mathrm{miss}}$ uncertainties are between 1.0 to 1.4%.

- The choice of diphoton vertex also has an effect on the reconstruction of $E_{\mathrm{T}}^{\mathrm{miss}}$ as discussed in Chapter 6. This introduces an uncertainty which is derived from data/MC comparisons in $Z \to ee$ events, affecting processes without genuine $E_{\mathrm{T}}^{\mathrm{miss}}$. The uncertainty

is found to be 0.5% in the Mono-Higgs category and up to 1.9% in the other categories (SM Higgs production cases) and also found to be less than 0.1% for signal processes.

- Requiring the diphoton primary vertex to be the vertex with the largest $\sum p_{\mathrm{T}}^2$ in the event introduces a 6% uncertainty in the SM Higgs boson production in both the High-$\boldsymbol{E}_{\mathrm{T}}^{\mathrm{miss}}$ and Intermediate-$\boldsymbol{E}_{\mathrm{T}}^{\mathrm{miss}}$ categories and a 1.8% in the heavy-scalar signals in the same categories.

- The pile-up reweighting uncertainty is given by 0.2-5.6% in the signal event yield and is included by propagating it through the event selection.

As already mentioned, since the non-resonant background contribution is extracted from the data, it is not affected by the same systematic uncertainties that characterize the MC simulation. The potential bias ($\Delta N_{bkg}^{non-res}$) is added as a systematic uncertainty in order to account for the possible impact on the fitted signal yields of non-resonant background mismodelling. In fact, this is the leading systematic uncertainty of the analysis but is only one third as large as the statistical uncertainty. The ratio $\Delta N_{bkg}^{non-res}/N_{bkg}^{non-res}$ in the diphoton mass range 120 GeV $< m_{\gamma\gamma} <$ 130 GeV is given by 9.8% for the Mono-Higgs category, 4.0% for the High-$\boldsymbol{E}_{\mathrm{T}}^{\mathrm{miss}}$, 1.3% for the Intermediate-$\boldsymbol{E}_{\mathrm{T}}^{\mathrm{miss}}$, 0.5% for the Different vertex category and 0.1% for the rest category.

The experimental systematic terms derived from the MxAODs on the heavy-scalar model (corresponding to m_H = 275 GeV and m_χ = 60 GeV) for all the categories are documented in Appendix C of this documentation.

7.6.2 Theoretical uncertainties

The breakdown of the theoretical uncertainties is as follows:

- Uncertainties due to missing higher-order terms in perturbative QCD affect the predicted cross sections of the SM Higgs-boson and signal processes. The uncertainties are estimated by varying the factorization and renormalization scales up and down from their nominal values by a specific factor and in turn recalculating the cross section in each

case, taking the largest fluctuation from the nominal cross section as the systematic uncertainty [182]. The uncertainties obtained are 0.6-11% for signal and 2.5-6.0% for the SM Higgs boson processes.

- The PDF+α_s uncertainties are estimated using the PDF4LHC recommendations [182] and are found to be 11-25% for all the signal processes. The systematic uncertainties introduced by the multiple parton-parton interactions are estimated using PYTHIA8. The uncertainties are found to go up to 1.4% in the Mono-Higgs category, 3.4% in the High-$E_{\mathrm{T}}^{\mathrm{miss}}$, 3.8% in the Intermediate-$E_{\mathrm{T}}^{\mathrm{miss}}$, 5.8% for the Different vertex category and 0.4% for the rest category.

- The uncertainty in the branching fraction of $H \to \gamma\gamma$ is found to be 1.73% [182].

7.7 Statistical analysis

The extended likelihood fits are performed simultaneously on the $m_{\gamma\gamma}$ shape over all the categories using the S+B model which is described by the following formula:

$$\mathscr{L}_c = \mathrm{Pois}(n_c|N_c(\theta)) \cdot \prod_{i=1}^{n_c} f_c(m_{\gamma\gamma}^i, \theta) \cdot G(\theta), \tag{7.2}$$

where the θs are the nuisance parameters representing the systematic uncertainties. $G(\theta)$ represents the Gaussian constrain terms which constrain the systematics. N_c represents the predicted event yields, summing up the BSM signal, the SM Higgs and the background yields in each category as follows:

$$N_c = \mu \cdot N_{\mathrm{BSM},c}(\theta_c^{\mathrm{yield}}, \theta_c^{\mathrm{migr}}) + N_{\mathrm{Higgs},c}(\theta_c^{\mathrm{yield}}, \theta_c^{\mathrm{migr}}) + N_{\mathrm{bkg},c} + N_{\mathrm{spur},c} \cdot \theta_{spur,c}, \tag{7.3}$$

The main function comprises the BSM shape, the SM Higgs shape and the background shape. The BSM and SM Higgs shapes are parametrized by the DSCB function as described in Section 7.5.1. The SM Higgs strength is fixed to its MC prediction while the BSM signal yields are parametrized by μ (measured BSM yields over its prediction). The background function

form is decided as in Table 7.4 and the parameter of the exponential function is restricted to be negative. The Gaussian constrained terms are appended in the main function and the f_c represents the shape of the signal and backgrounds collectively:

$$f_c(m^i_{\gamma\gamma}) = [(\mu \cdot N_{\mathrm{BSM},c} + N_{\mathrm{Higgs},c} + N_{\mathrm{spur},c} \cdot \theta_{spur,c}) \cdot f_{\mathrm{S},c}(m^i_{\gamma\gamma}, \theta^{\mathrm{shape}}_{\mathrm{S},c}) \tag{7.4}$$

$$+ N_{\mathrm{bkg},c} \cdot f_{\mathrm{bkg},c}(m^i_{\gamma\gamma}, \theta^{\mathrm{shape}}_{\mathrm{bkg},c})]/N_c. \tag{7.5}$$

The test statistics are defined as the likelihood ratio:

$$\lambda(\mu) = -2\ln\frac{\mathscr{L}(\mu, \hat{\theta}_\mu)}{\mathscr{L}(\hat{\mu}, \hat{\theta})}, \tag{7.6}$$

Toy experiments are generated in order to calculate limits and quantify a significance due to a lack of statistics [183]. The fit result both individually and simultaneously on each category are shown in Section 7.8. The ATLAS and CMS statistical analysis agreement on how to set limits in Higgs boson searches is detailed in Reference [184].

7.8 Results

As highlighted in Section 7.7, the results for this analysis are derived from a likelihood fit of the $m_{\gamma\gamma}$ distribution in the range $105\,\mathrm{GeV} < m_{\gamma\gamma} < 160\,\mathrm{GeV}$. Figure 7.4 shows the $m_{\gamma\gamma}$ distributions in the five categories as well as the fitted contribution of a heavy-scalar boson. The SM Higgs boson mass is set to 125.09 GeV [185] and the impact due to the SM Higgs mass uncertainty is considered to be negligible. The signal strength, background shape parameters and nuisance parameters representing the systematic uncertainties are set to be free parameters [183]. The uncertainty of each nuisance parameter is obtained by multiplying the likelihood by a Gaussian penalty function centered on the nominal value of this parameter with a width set to its uncertainty. Moreover, the nominal value of each SM Higgs background nuisance parameter is obtained from the simulation that is normalized to the SM theoretical predictions. The results for the Z'_B and Z'-2HDM models are obtained from the Mono-Higgs category alone whilst those for the heavy-scalar are obtained from a simultaneous fit of all the categories at hand.

Table 7.6 shows the event yields in the observed data, expected signal and backgrounds in the five categories within a window of 120 GeV < $m_{\gamma\gamma}$ < 130 GeV. The heavy-scalar signal corresponds to m_H = 275 GeV and m_χ = 60 GeV and the efficiency times acceptance denoted by $A \times \epsilon$ is also shown for this model. The non-resonant background yields are retrieved from a fit to data while those for the SM Higgs boson are estimated from simulation events. The overall uncertainties are obtained from the quadrature sum of the statistical and systematic uncertainties. From the fitted contributions to $m_{\gamma\gamma}$ in Figure 7.4, no significant excess is observed in any category. In the heavy scalar interpretation, the 95% CL upper limits on the $\sigma(pp \rightarrow H) \times \mathrm{B}(H \rightarrow \gamma\gamma\chi\chi)$ as a function of m_H for m_χ = 50 GeV and m_χ = 60 GeV are shown in Figures 7.6 and 7.5 , respectively. A 100% branching fraction is assumed for $H \rightarrow \mathrm{h}\chi\chi$. No significant excess is observed as well. For the scenario with a DM mass of 50 GeV, the 95% CL upper limit is 12.6 fb for m_H = 260 GeV, and 3.3 fb for m_H = 350 GeV as shown in Table 7.7. For m_χ = 60 GeV, the 95% CL upper limit is 15.4 fb for m_H = 260 GeV, and 4.3 fb for m_H = 350 GeV as shown in Table 7.8.

7.9 Conclusions

A search for DM in association with $E_{\mathrm{T}}^{\mathrm{miss}}$ and a Higgs boson decaying to two photons in association with $E_{\mathrm{T}}^{\mathrm{miss}}$ has been presented [3, 6, 18]. This study is based on data corresponding to an integrated luminosity of 36.1 fb^{-1} of pp collisions at the LHC at a center-of-mass energy of 13 TeV. The results of this analysis are interpreted in the context of the heavy-scalar model or Madala hypothesis. For this search a 95% CL upper limit of 10.3 (10.7) fb is set on the production cross section times the branching fraction of $H \rightarrow \mathrm{h}\chi\chi \rightarrow \gamma\gamma\chi\chi$, for m_H = 270 GeV and a DM particle of 50 (60) GeV, where a 100% branching fraction is assumed for $H \rightarrow \mathrm{h}\chi\chi$. No significant excess over the expected background is observed. The heavy-scalar model is excluded for all the benchmark points investigated. However, the benchmark point assumes 100% branching ratio, which is an extreme case, thus we have to look at other decay channels to observe possible excesses. In future, it would also be useful to explore cases where the branching ratio is not 100% with more data.

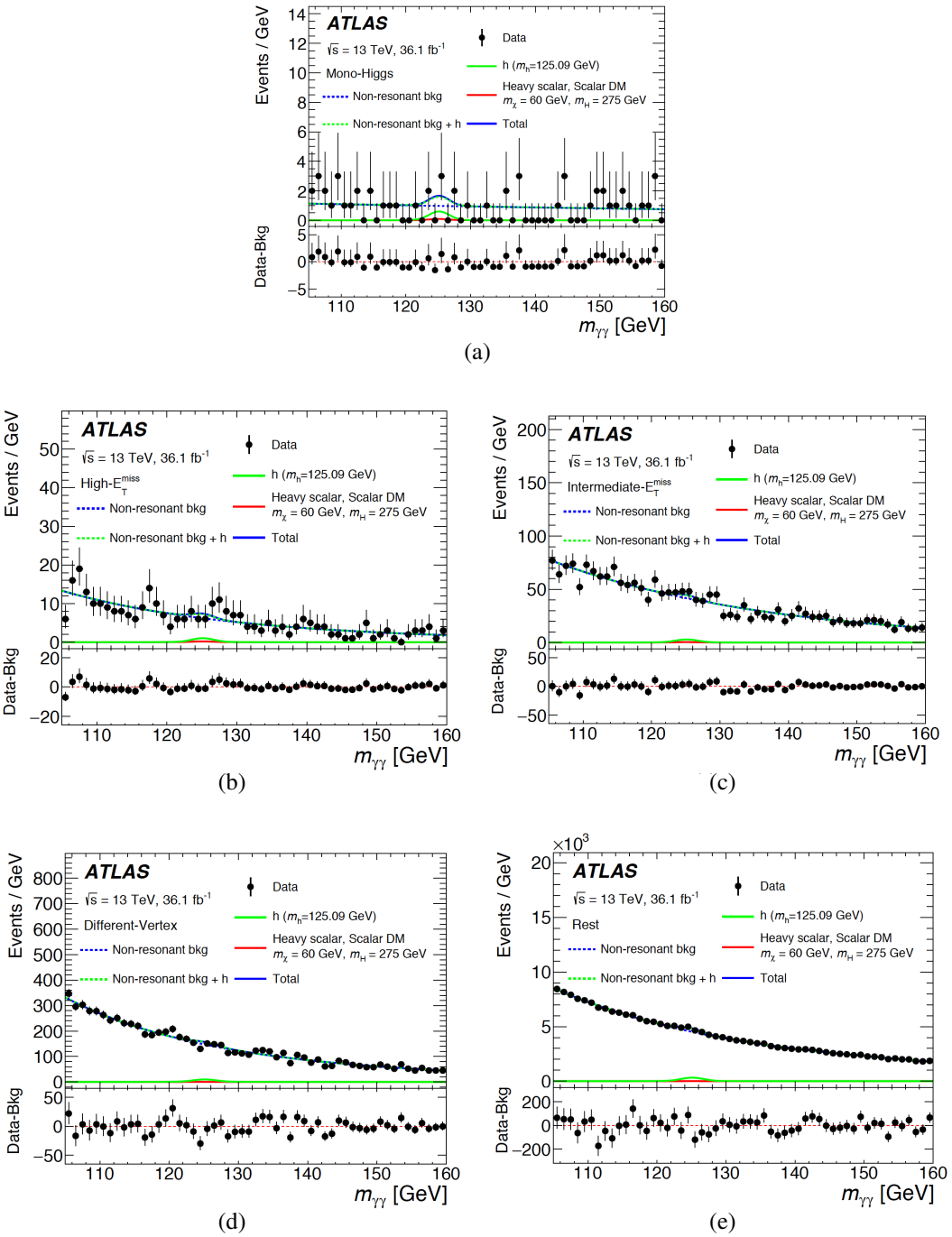


Figure 7.4: The diphoton invariant mass distributions for data and corresponding fitted signal and background in all the five categories, (a) Mono-Higgs category, (b) High-$E_{\mathrm{T}}^{\mathrm{miss}}$ category, (c) Intermediate-$E_{\mathrm{T}}^{\mathrm{miss}}$ category, (d) Different-Vertex category and (e) Rest category. On each distribution, the simultaneous fit result including heavy scalar signal (solid red line), SM Higgs boson (solid green line) and the non-resonant background (dashed blue line) are shown as well as the total of all those contributions (solid blue line). The fitted heavy scalar model signal shown here corresponds to $m_H = 275\,\mathrm{GeV}$ and $m_\chi = 60\,\mathrm{GeV}$ [18].

Table 7.6: Event yields in the range of 120 GeV < $m_{\gamma\gamma}$ < 130 GeV for data, signal models, the SM Higgs boson background and non-Higgs boson backgrounds in each analysis category corresponding to an integrated luminosity of 36.1 fb^{-1}. The signal sample for the heavy scalar model corresponds to m_H = 275 GeV and m_χ = 50 GeV and m_χ = 60 GeV, respectively. The selection efficiency times acceptance denoted as "$A \times \epsilon$" is also shown. The yields for non-resonant background are obtained from a fit to data in the side bands (excluding $m_{\gamma\gamma}$ in the range [120, 130] GeV) while SM Higgs boson events are estimated from simulation. The uncertainties showed corresponds to the total of statistical and systematic uncertainties [6].

Category	**Mono-Higgs**	**High-$E_{\mathrm{T}}^{\mathrm{miss}}$**	**Intermediate-$E_{\mathrm{T}}^{\mathrm{miss}}$**	**Different-Vertex**	**Rest**
Data	9	72	464	1511	46804
Backgrounds					
SM Higgs boson	2.43 ± 0.22	4.2 ± 0.6	11.9 ± 2.7	44 ± 10	1360 ± 110
Non-resonant	9.9 ± 1.9	62 ± 5	418 ± 10	1490 ± 18	45570 ± 110
Total background	12.3 ± 1.9	67 ± 5	430 ± 10	1535 ± 21	46930 ± 170
Heavy scalar, m_H = 275 GeV, m_χ = 50 GeV					
Expected yields	9.9 ± 1.3	32 ± 4	52 ± 6	42 ± 6	198 ± 18
$A \times \epsilon$ (%)	1.11 ± 0.07	3.62 ± 0.13	5.81 ± 0.17	4.73 ± 0.17	22.3 ± 0.4
Heavy scalar, m_H = 275 GeV, m_χ = 60 GeV					
Expected yields	10.9 ± 1.4	23.8 ± 3.2	43 ± 5	33 ± 5	222 ± 20
$A \times \epsilon$ (%)	1.22 ± 0.07	2.67 ± 0.10	4.82 ± 0.14	3.65 ± 0.13	24.9 ± 0.4

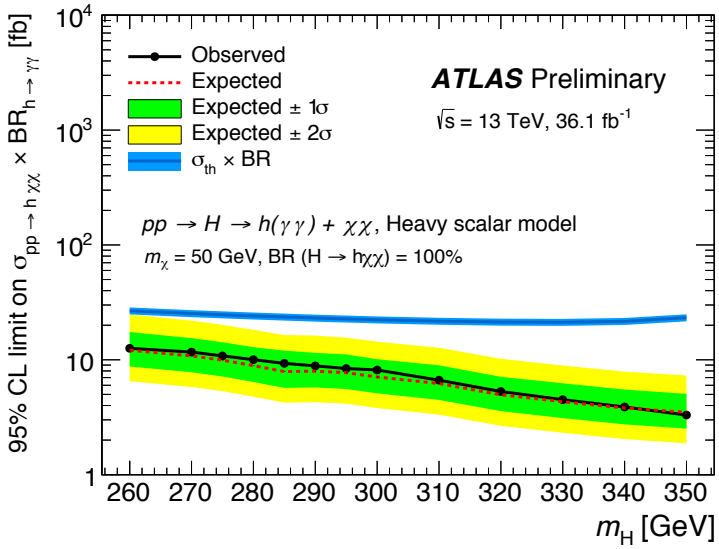


Figure 7.5: The expected and observed 95% CL exclusion upper limits on the heavy-scalar boson H production cross section times the branching ratio BR($H \to h\chi\chi$, $h \to \gamma\gamma$) with a DM candidate of mass 50 GeV as a function of the heavy scalar boson mass in the range [260, 350] GeV. The theoretical prediction for these two models (dark-blue lines with blue bands representing their associated theoretical systematics) are also shown [6].

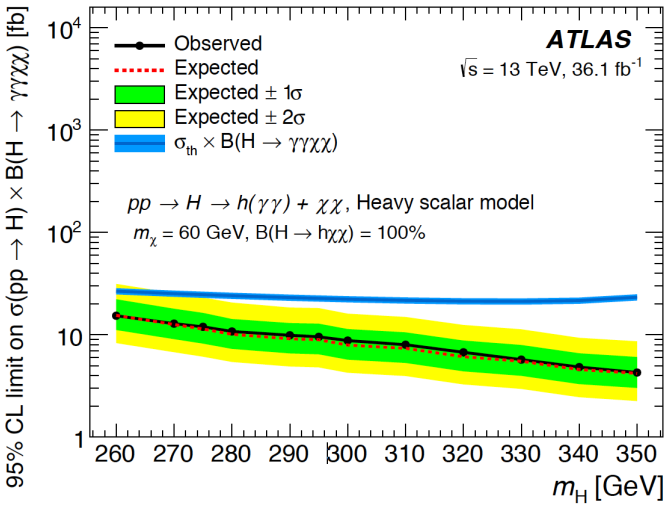


Figure 7.6: The expected and observed 95% CL exclusion upper limits on the heavy-scalar boson H production cross section times the branching ratio BR($H \to h\chi\chi$, $h \to \gamma\gamma$) with a DM candidate of mass 60 GeV as a function of the heavy scalar boson mass in the range [260, 350] GeV. The theoretical prediction for these two models (dark-blue lines with blue bands representing their associated theoretical systematics) are also shown [18].

Table 7.7: The 95% CL observed and expected limits (in fb) on the signal $pp \to h\chi\bar{\chi}$ cross section times BR($h \to \gamma\gamma$) and the associated expected 1 σ deviation limits for the heavy scalar benchmark model for various mediator masses and m_χ = 50 GeV [6].

m_H (GeV)	m_χ (GeV)	Observed	Expected	Expected +1σ	Expected -1 σ
260	50	12.6	12.1	17.5	8.7
270	50	10.7	10.8	15.4	7.7
275	50	10.8	9.9	14.2	7.1
280	50	10.0	8.9	12.9	6.4
285	50	9.3	7.9	12.0	5.7
290	50	8.9	8.0	11.5	5.7
295	50	8.4	7.7	11.1	5.6
300	50	8.2	7.1	10.1	5.1
310	50	6.6	6.2	9.0	4.5
320	50	5.3	5.0	7.1	3.6
330	50	4.5	4.3	6.2	3.1
340	50	3.9	3.8	5.5	2.7
350	50	3.3	3.5	5.0	2.5

Table 7.8: The 95% CL observed and expected limits (in fb) on the signal $pp \to h\chi\bar{\chi}$ cross section times BR($h \to \gamma\gamma$) and the associated expected 1 σ deviation limits for the heavy scalar benchmark model for various mediator masses and m_χ = 60 GeV [6].

m_H (GeV)	m_χ (GeV)	Observed	Expected	Expected +1σ	Expected -1 σ
260	60	15.4	15.5	22.3	11.2
270	60	12.9	12.6	18.0	9.1
275	60	12.0	11.4	16.4	8.2
285	60	10.8	11.1	14.3	7.3
290	60	9.9	9.1	13.0	6.6
295	60	9.6	9.0	12.8	6.5
300	60	8.8	7.9	11.4	5.7
310	60	8.0	7.4	10.6	5.3
320	60	6.8	6.1	8.8	4.4
330	60	5.7	5.5	7.9	4.0
340	60	4.8	4.6	6.6	3.3
350	60	4.3	4.2	6.1	3.0

CHAPTER 8

SEARCH FOR A NEW RESONANCE IN THE DIPHOTON DECAY IN ASSOCIATION WITH $E_{\mathrm{T}}^{\mathrm{MISS}}$ WITH RELEASE 20

In November 2016, an excess was studied with a diphoton invariant mass around 248 GeV associated with moderate $E_{\mathrm{T}}^{\mathrm{miss}}$ with 2015+2016 data [3, 6, 18]. This is statistically consistent with the first assessment of the mass of H, described in Section 1.4. Motivated by this excess, a study was performed with Run 1 data where a similar excess was found. It is of interest to find out whether this excess is real or not with more data. In this effort, an analysis strategy has been put in place. The strategy proposed here is that events be categorized based on 2015+2016 data due to the lack of suitable MC in order to be able to search for the same excess in 2017 data in both diphoton and $Z\gamma$ final states.

This chapter is organized as follows: Section 8.1 introduces the analysis and Section 8.2 details the data and MC production specific to this analysis. Section 8.3 discusses the same vertex tuning method in the context of this analysis. Section 8.4 details the analysis of the excess. Section 8.5 describes the event selection and categorization, which is an extension of the content discussed in Chapter 4. Section 8.6 details the signal and background parameterization and the statistical analysis is discussed in Section 8.7. Finally, the results are captured in Section 8.8 and Section 8.9 summarizes the entire study.

8.1 Introduction

It is clear from this thesis documentation that Higgs boson studies at the LHC have facilitated BSM physics exploration. The search for new physics in association with a $E_{\mathrm{T}}^{\mathrm{miss}}$ signature discussed previously stimulated the development of studies that allow the scrutiny of possible excesses throughout the entire $E_{\mathrm{T}}^{\mathrm{miss}}$ region. Prior to the development of the SV method discussed in Section 6.3.2, it had been particularly intricate to study any excess in the low and intermediate $E_{\mathrm{T}}^{\mathrm{miss}}$ region. Thus, a formulation of this method has allowed us the opportunity to investigate any excesses in this regime. Its ability to suppress fake $E_{\mathrm{T}}^{\mathrm{miss}}$ contamination in this region makes the SV method very valuable.

The excess under scrutiny is mainly observed in the intermediate $E_{\mathrm{T}}^{\mathrm{miss}}$ and two central jets region, with some of it also observed in the zero and one jet regions. The fact that this excess is observed in events with $E_{\mathrm{T}}^{\mathrm{miss}}$ makes it difficult to decide on the $E_{\mathrm{T}}^{\mathrm{miss}}$ selection criteria only. As a result of this dilemma, a scan on both $E_{\mathrm{T}}^{\mathrm{miss}}$ and $E_{\mathrm{T}}^{\mathrm{miss}}$ significance is employed. The final selection is settled based on the position of the largest signal significance. The studies captured in this chapter are done with ATLAS Release 20 (R20) based on 2015+2016 data. In the next chapter, a re-optimization is done using ATLAS Release 21 (R21) based on 2015+2016 data in search for this resonance.

8.2 Data and simulation samples

Data collected in 2015+2016 at $\sqrt{s}$ = 13 TeV is used in this analysis. As already mentioned, the events that are considered are those recorded under stable beam conditions with the detector functioning efficiently. The 2015+2016 data used corresponds to an integrated luminosity of 36.1 fb^{-1}.

8.2.1 Signal samples

In an effort to understand the features in data, a simplified effective approach was implemented whereby a Higgs-like scalar boson H is assumed to produce a diphoton signal through Higgs-

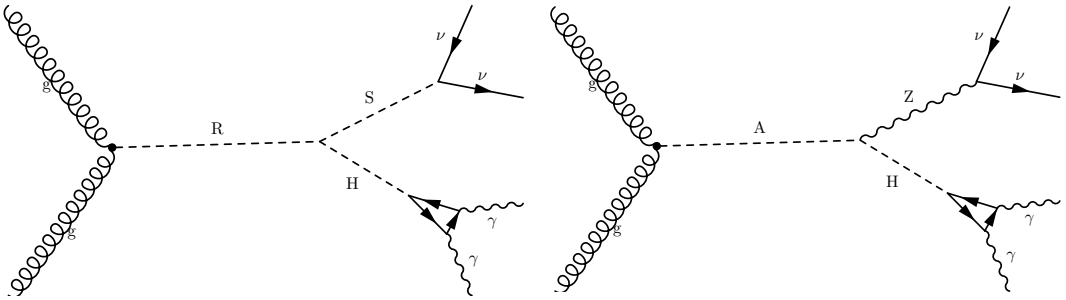


Figure 8.1: Schematic diagrams of the production and decay of the scalars in the simplified (a) RSH model and (b) AZH [15].

like couplings to the weak bosons. In this regard, two different approaches discussed in this section are taken into consideration.

Figure 8.1a shows the RSH model which assumes the production of a heavy scalar R through ggF. This heavy scalar R then decays to the scalar H in association with another CP even scalar S which was introduced in Section 1.4. This H boson then decays to two photons, which is a necessary decay in order to study a diphoton peak around $m_{\gamma\gamma} \approx 250\,\text{GeV}$. Moreover, the S boson can decay either to a pair of jets or neutrinos, allowing us to study the behaviour of diphoton final states in association with $E_{\text{T}}^{\text{miss}}$. In order to ensure that $R \rightarrow SH$ is on-shell, a decision was made to fix m_R =450/420 GeV and m_S = 160 GeV. On the other hand, Figure 8.1b shows the AZH model in which a pseudoscalar A boson decays to ZH. Similarly, the H decays to two photons where the Z can decay either to jets or neutrinos. The mass of the pseudoscalar was considered at m_A = 350/400 GeV, in order to ensure that $A \rightarrow ZH$ is on-shell. The RSH and AZH signals were generated using PYTHIA8 and are summarized in Table 8.1 and all truth level validation distributions can be found in Reference [15].

8.2.2 Background samples

As discussed in Section 7.2.2, the dominant background contributions to the $m_{\gamma\gamma}$ spectrum originate from the SM $h \rightarrow \gamma\gamma$ and $\gamma\gamma$, γj, $W\gamma$, $Z\gamma$, $W\gamma\gamma$ and $Z\gamma\gamma$ events. Table 5.1 summarizes the production of the SM $h \rightarrow \gamma\gamma$ samples and Table 5.2 summarizes that of the prompt diphoton background MC samples. As in the previous analysis case, all the backgrounds used in this

Table 8.1: A list of the signal samples used for $H \to \gamma\gamma$ using the RSH and AZH models [15].

Hard process	Mass point	Decays	Generator setup
$gg \to A \to ZH$	$m_A = 400$ GeV	$Z \to jj$	PYTHIA8, A14, NNPDF23LO
$gg \to A \to ZH$	$m_A = 400$ GeV	$Z \to \nu\nu$	PYTHIA8, A14, NNPDF23LO
$gg \to A \to ZH$	$m_A = 350$ GeV	$Z \to jj$	PYTHIA8, A14, NNPDF23LO
$gg \to A \to ZH$	$m_A = 350$ GeV	$Z \to \nu\nu$	PYTHIA8, A14, NNPDF23LO
$gg \to R \to SH$	$m_A = 450$ GeV	$S \to jj$	PYTHIA8, A14, NNPDF23LO
$gg \to R \to SH$	$m_A = 450$ GeV	$S \to \nu\nu$	PYTHIA8, A14, NNPDF23LO
$gg \to R \to SH$	$m_A = 420$ GeV	$S \to jj$	PYTHIA8, A14, NNPDF23LO
$gg \to R \to SH$	$m_A = 420$ GeV	$S \to \nu\nu$	PYTHIA8, A14, NNPDF23LO

analysis are summarized in Table 7.1.

8.3 The same vertex boundary tuning method

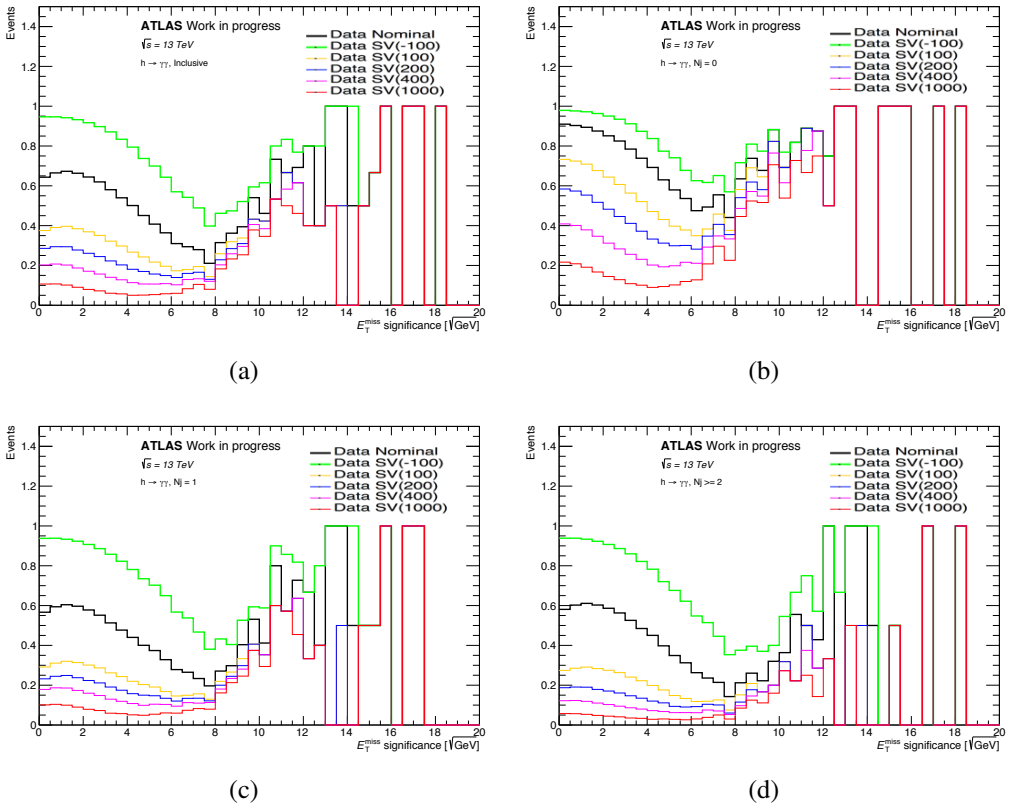
This section presents the performance of the tuning of the SV method selection in the 2015+2016 data conditions corresponding to an integrated luminosity of 36.1 fb^{-1}. As discussed in Section 6.3.2, the SV selection requires the photon pointing vertex to be the same hardest vertex in an event, which implies that the photon pointing $\sum p_T^2$ ought to be larger than any pile-up vertex $\sum p_T^2$. In order to gauge the effects of tuning the SV cut boundary, we observe the effects on $E_{\mathrm{T}}^{\mathrm{miss}}$ and $S_{E_{\mathrm{T}}^{\mathrm{miss}}}$ performance. I performed this study by tuning the SV boundary as follows:

- Selected vertex $\sum p_T^2$ − pile-up vertex $\sum p_T^2 > 0$
- Selected vertex $\sum p_T^2$ − pile-up vertex $\sum p_T^2 >$ -100
- Selected vertex $\sum p_T^2$ − pile-up vertex $\sum p_T^2 > 100$
- Selected vertex $\sum p_T^2$ − pile-up vertex $\sum p_T^2 > 200$
- Selected vertex $\sum p_T^2$ − pile-up vertex $\sum p_T^2 > 400$
- Selected vertex $\sum p_T^2$ − pile-up vertex $\sum p_T^2 > 1000$

Figures 8.2, 8.3, 8.4 and 8.5 show the $S_{E_{\mathrm{T}}^{\mathrm{miss}}}$ distributions for various SV selection cuts and different jet multiplicity bins (0-jet, 1-jet and at least 2-jet cases). The similar distributions

corresponding to $E_{\mathrm{T}}^{\mathrm{miss}}$ can be found in Appendix D. The variations are checked in 2015+2016 data, anti-OneID data, Sherpa $\gamma\gamma$, Vγ, V$\gamma\gamma$, $Wh125$, $Zh125$, $ggZh$, heavy scalar signal and mono-Higgs signals [15]. The anti-OneID data represents the γj sample, which is produced by requiring only one of the two photons in the selection to pass the reverse isolation criteria. For simplicity, this section only shows those corresponding to data, $Wh125$, heavy scalar signal and mono-Higgs signals. Each distribution corresponds to overlaid histograms for the various SV selection cuts for each sample in order to observe the evolution. That is, the idea is to basically observe the effect of tuning the SV selection on the events in each of the samples. In order to remove $Z \rightarrow \ell\ell$,jj events in the signals, I make a cut of $E_{\mathrm{T}}^{\mathrm{miss}}$ truth > 10 GeV.

From the distributions we observe that a substantial amount of the mono-Higgs events survive by simply adjusting the SV selection cut while maintaining background suppression. Also, binning in the number of central jets proves to be useful for the various analyses depending on the $E_{\mathrm{T}}^{\mathrm{miss}}$ or $S_{E_{\mathrm{T}}^{\mathrm{miss}}}$ cut. For all the samples, the SV cut in which the selected vertex $\sum p_T^2$ − pile-up vertex $\sum p_T^2$ > -100 seems to allow for more events to survive than in the other cases, with the events passing the nominal SV selection being the second highest. As a result of this study, one can essentially tune the SV cut to allow for the maximum number of events to survive. In other words, depending on the $E_{\mathrm{T}}^{\mathrm{miss}}$ or $S_{E_{\mathrm{T}}^{\mathrm{miss}}}$ cut, one can fine tune the SV selection boundary to allow for maximum survival of events for various models. This study is of great importance as it can aid in the optimization of the event selection in future alongside the BDT studies documented in Reference [15] which can also improve the analysis by considering more variables. At the moment the nominal selection is used and no tuning is applied to the selection in this analysis as of yet, and this also applies to the results reported in Chapter 9.



(a) (b)

(c) (d)

Figure 8.2: $S_{E_{\mathrm{T}}^{\mathrm{miss}}}$ distributions for 2015+2016 data for different same vertex cuts split into (a) inclusive, (b) 0-jet case, (c) 1-jet case and (d) ≥2-jet case [15].

8.4 Motivation for the resonance search

In this section, I perform an analysis on the excess observed in both Run 1 and Run 2 data, respectively. This study acts as an incentive to pursue the 250 excess and thus motivates this analysis. The model-independent excess check in Run 1 data is performed using 2015 data corresponding to 20.7 fb^{-1} while that in Run 2 is performed using 2015+2016 data corresponding to 36.1 fb^{-1}. This is done by measuring the 250 GeV excess by cutting on $E_{\mathrm{T}}^{\mathrm{miss}}$ and $S_{E_{\mathrm{T}}^{\mathrm{miss}}}$ and splitting into various jet bins.

8.4.1 The excess observed in data at $\sqrt{s}$ = 8 TeV

The excess in Run 1 data is measured by binning in $E_{\mathrm{T}}^{\mathrm{miss}}$ and $S_{E_{\mathrm{T}}^{\mathrm{miss}}}$, splitting into the at least 2-jet case and tuning the boundary using a 2D scan to find the maximum significance. This is

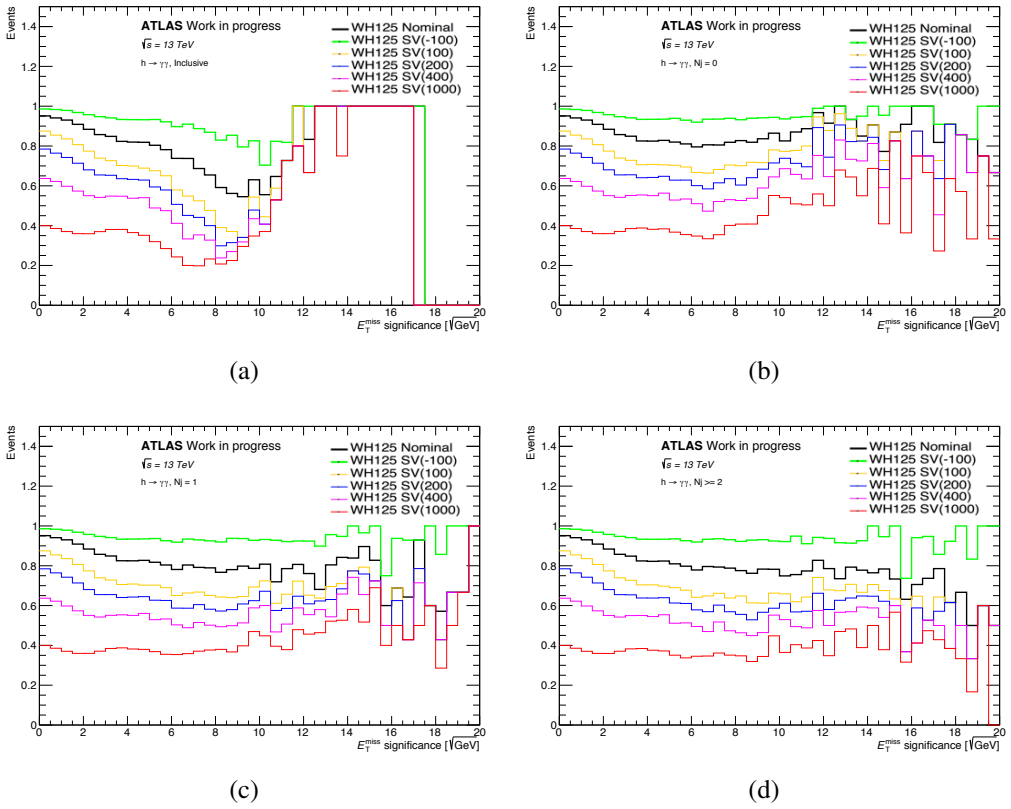


Figure 8.3: $S_{E_{\mathrm{T}}^{\mathrm{miss}}}$ distributions for the Wh sample for different same vertex cuts split into (a) inclusive, (b) 0-jet case, (c) 1-jet case and (d) ≥2-jet case [15].

done for $40 < E_{\mathrm{T}}^{\mathrm{miss}} < 100\,\mathrm{GeV}$ in 10 GeV intervals and $3.0 < S_{E_{\mathrm{T}}^{\mathrm{miss}}} < 5.0\,\sqrt{\mathrm{GeV}}$ in intervals of 0.1. I fit the mass points for the different categories to the $m_{\gamma\gamma}$ spectrum and obtained the significance and yields. Table 8.2 shows the scan results consisting of the significance and corresponding yield values. For all the corresponding fits in Figure 8.6, the mass and width are fixed to 248 GeV and $\sigma = 2.3\,\mathrm{GeV}$, respectively. In the $E_{\mathrm{T}}^{\mathrm{miss}}$ case, the maximum excess occurs at $E_{\mathrm{T}}^{\mathrm{miss}} > 40\,\mathrm{GeV}$ with a significance of $2.4\,\sigma$. In the $S_{E_{\mathrm{T}}^{\mathrm{miss}}}$ case, the maximum excess occurs at $S_{E_{\mathrm{T}}^{\mathrm{miss}}} > 3.7\,\sqrt{\mathrm{GeV}}$ with a significance of $2.6\,\sigma$.

In addition, the excess in the cases where $S_{E_{\mathrm{T}}^{\mathrm{miss}}} > 3.5\,\sqrt{\mathrm{GeV}}$ with a b-tagged jets requirement, a lepton requirement and photon barrel-endcap regions is also studied and are documented in Appendix D.

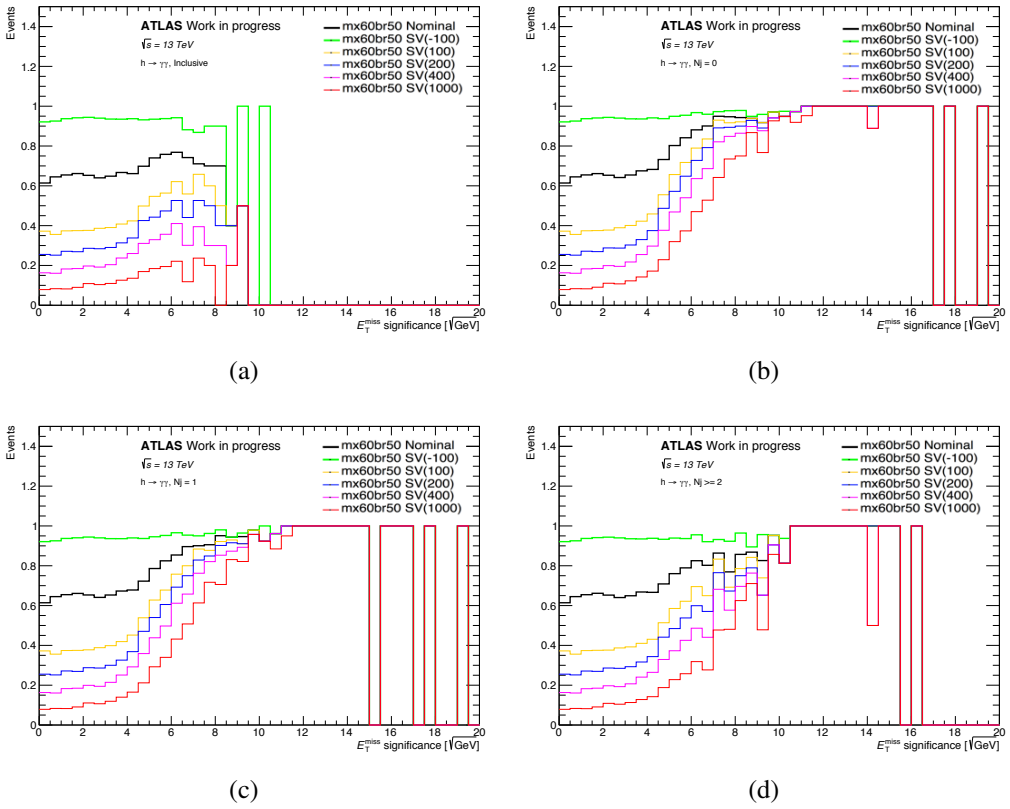


Figure 8.4: $S_{E_{\mathrm{T}}^{\mathrm{miss}}}$ distributions for the heavy-scalar signal sample for different same vertex cuts split into (a) inclusive, (b) 0-jet case, (c) 1-jet case and (d) ≥2-jet cas [15].

8.4.2 The excess observed in data at $\sqrt{s}$ = 13 TeV

In this section, the excess check is performed using 2015+2016 data at $\sqrt{s}$ = 13 TeV. The excess is measured by also cutting on $E_{\mathrm{T}}^{\mathrm{miss}}$ and $S_{E_{\mathrm{T}}^{\mathrm{miss}}}$ with different jet binnings as well as the SV requirement. The jet binning is split into the 0-jet, 1-jet, ≥ 1-jet and ≥ 2-jet cases.

For $E_{\mathrm{T}}^{\mathrm{miss}}$, the scan is done for $50 < E_{\mathrm{T}}^{\mathrm{miss}} < 150$ GeV in 10 GeV intervals and $3.0 < S_{E_{\mathrm{T}}^{\mathrm{miss}}} < 5.0$ $\sqrt{\mathrm{GeV}}$ in intervals of 0.1. The fits require the leading photon to have $p_T > 40$ GeV and the subleading photon to have $p_T > 30$ GeV. For simplicity, and since the ≥ 2-jet case has the maximum significance, Table 8.3 shows scan results highlighting the significance and corresponding yield values for the ≥ 2-jet case. For the fits to the $m_{\gamma\gamma}$ spectrum shown in Figure 8.7, the mass and width are fixed to 248 GeV and σ =2.7 GeV, respectively. In the case of $E_{\mathrm{T}}^{\mathrm{miss}}$, the maximum excess occurs at $E_{\mathrm{T}}^{\mathrm{miss}} > 70$ GeV with a significance of 2.9 σ. In the

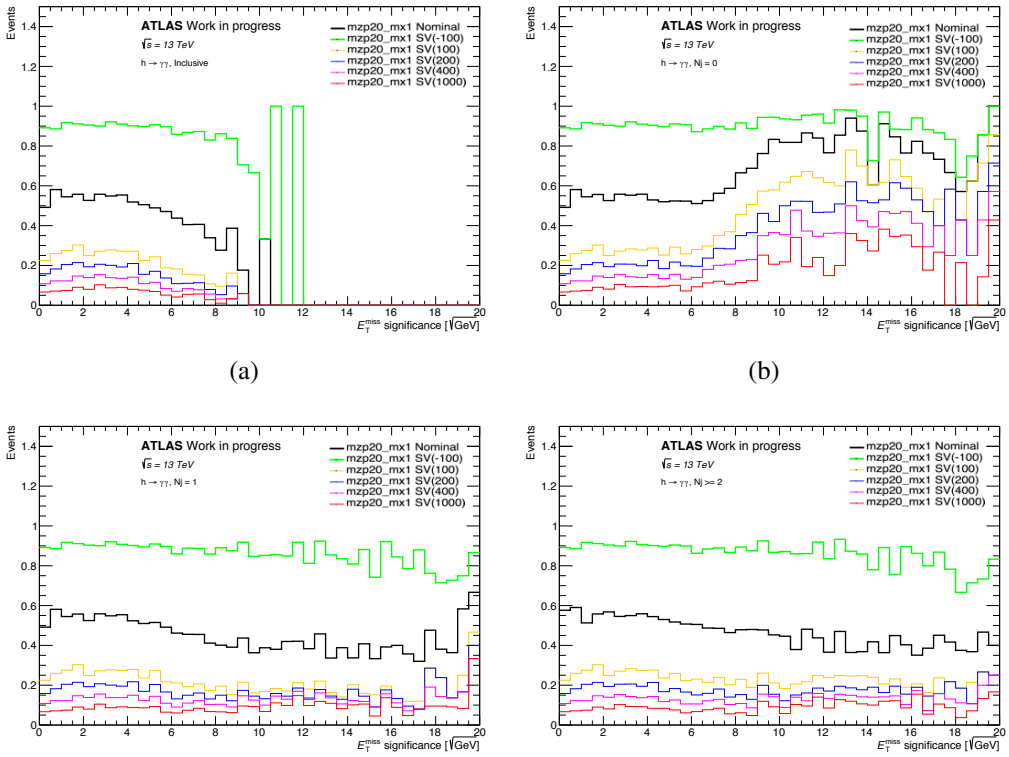
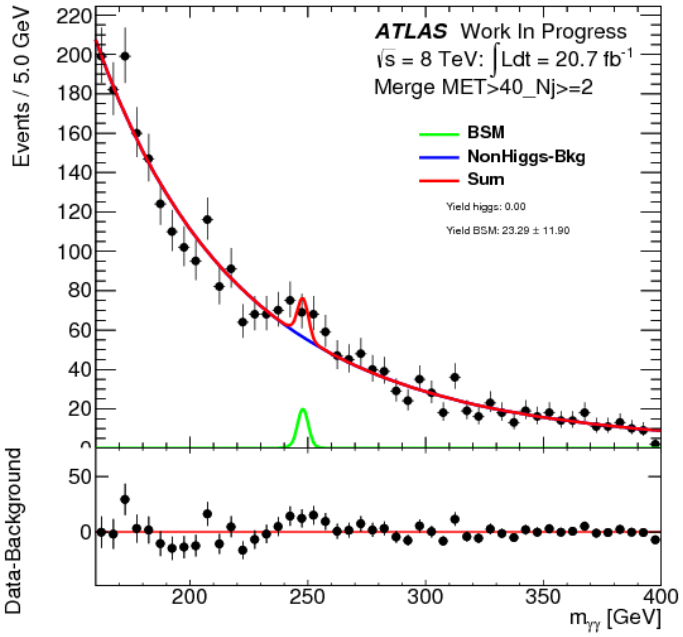


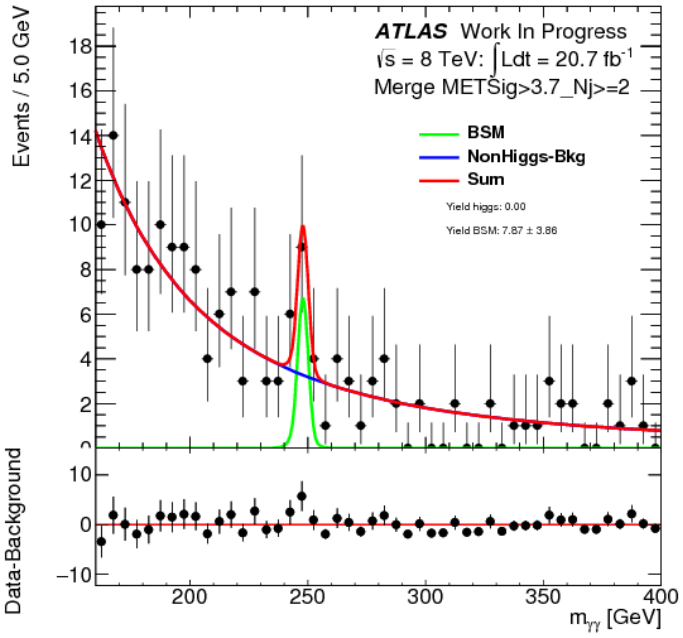
Figure 8.5: $S_{E_{\mathrm{T}}^{\mathrm{miss}}}$ distributions for the mono-Higgs signal sample for different same vertex cuts split into (a) inclusive, (b) 0-jet case, (c) 1-jet case and (d) ≥2-jet case [15].

case of $S_{E_{\mathrm{T}}^{\mathrm{miss}}}$, the maximum excess occurs at $S_{E_{\mathrm{T}}^{\mathrm{miss}}} > 3.2\,\sqrt{\mathrm{GeV}}$ with a significance of $4.0\,\sigma$. The excess is also observed in the 0-jet and 1-jet cases with a higher $S_{E_{\mathrm{T}}^{\mathrm{miss}}}$ cut than $3.2\,\sqrt{\mathrm{GeV}}$, which is not an issue since a cut of $S_{E_{\mathrm{T}}^{\mathrm{miss}}} > 3.2\,\sqrt{\mathrm{GeV}}$ covers most the excess. However, even though the maximum significance occurs at $S_{E_{\mathrm{T}}^{\mathrm{miss}}} > 3.2\,\sqrt{\mathrm{GeV}}$, due to pile-up sensitivity, we set a cut of $S_{E_{\mathrm{T}}^{\mathrm{miss}}} > 3.5\,\sqrt{\mathrm{GeV}}$, which fortunately still has a good significance.

The excess in the cases where $S_{E_{\mathrm{T}}^{\mathrm{miss}}} > 3.5\,\sqrt{\mathrm{GeV}}$ with b-tagged jets required, leptons required and photon barrel-endcap regions considered are summarized in Table D.1 for the Run 2 data case. Figures 8.8 and 8.9 represent the fit distributions to the $m_{\gamma\gamma}$ spectrum. The scans are done for $S_{E_{\mathrm{T}}^{\mathrm{miss}}} > 3.5\,\sqrt{\mathrm{GeV}}$, SV case and with at least two central jets for: photons in the Barrel-Barrel region (BB), Barrel-EndCap region (BE), EndCap-Barrel region (EB) , EndCap-EndCap region (EE), number of b-tagged jets ≥1, number of b-tagged jets ≥2 and number of leptons ≥1, respectively. The maximum significance is found in the EE region. It is



(a)



(b)

Figure 8.6: Fit distributions corresponding to maximum significance for the case of (a) $E_{\mathrm{T}}^{\mathrm{miss}}$ and (b) $S_{E_{\mathrm{T}}^{\mathrm{miss}}}$. For the $E_{\mathrm{T}}^{\mathrm{miss}}$ case, the maximum excess occurs at $E_{\mathrm{T}}^{\mathrm{miss}} > 40\,\mathrm{GeV}$ with a maximum significance of $2.4\,\sigma$. For the $S_{E_{\mathrm{T}}^{\mathrm{miss}}}$ case, the maximum excess occurs at $S_{E_{\mathrm{T}}^{\mathrm{miss}}} > 3.7\,\sqrt{\mathrm{GeV}}$ with a maximum significance of $2.6\,\sigma$ [15].

Table 8.2: Significance and yield results for $40 < E_{\mathrm{T}}^{\mathrm{miss}} < 100$ GeV in 10 GeV intervals and $3.0 < S_{E_{\mathrm{T}}^{\mathrm{miss}}} < 5.0\ \sqrt{\mathrm{GeV}}$ in intervals of 0.1, split into ≥ 2-jet case. Results are shown for Run 1 data corresponding to 20.7 fb^{-1} of integrated luminosity. The highlighted rows correspond to the maximum significance corresponding to the $E_{\mathrm{T}}^{\mathrm{miss}}$ and $S_{E_{\mathrm{T}}^{\mathrm{miss}}}$ cuts, respectively [15, 16].

Cut	Jet bin	Significance	Yield
$MET > 40$	Nj>=2	2.358	28.5362 ± 12.9309
$MET > 50$	Nj>=2	1.342	10.3909 ± 8.27619
$MET > 60$	Nj>=2	1.794	9.93088 ± 6.19296
$MET > 70$	Nj>=2	1.620	5.78028 ± 4.13127
$MET > 80$	Nj>=2	0.975	2.30379 ± 2.68973
$MET > 90$	Nj>=2	0.425	0.610471 ± 1.60779
$MET > 100$	Nj>=2	0.715	0.888182 ± 1.45896
$METSig > 3.0$	Nj>=2	1.836	10.8556 ± 6.56095
$METSig > 3.1$	Nj>=2	2.431	13.0422 ± 6.1856
$METSig >$	Nj>=2	2.447	12.2796 ± 5.8456
$METSig > 3.3$	Nj>=2	2.173	9.87081 ± 5.26359
$METSig > 3.4$	Nj>=2	1.255	5.14035 ± 4.52972
$METSig > 3.5$	Nj>=2	1.508	5.76767 ± 4.35294
$METSig > 3.6$	Nj>=2	2.380	8.62251 ± 4.4279
$METSig > 3.7$	Nj>=2	2.598	8.36392 ± 4.06258
$METSig > 3.8$	Nj>=2	2.248	6.73313 ± 3.73362
$METSig > 3.9$	Nj>=2	2.371	6.63405 ± 3.56198
$METSig > 4.0$	Nj>=2	1.062	2.46734 ± 2.62864
$METSig > 4.1$	Nj>=2	1.408	3.0751 ± 2.62695
$METSig > 4.2$	Nj>=2	1.811	3.7715 ± 2.64643
$METSig > 4.3$	Nj>=2	1.889	3.9079 ± 2.65345
$METSig > 4.4$	Nj>=2	1.802	3.77862 ± 2.65364
$METSig > 4.5$	Nj>=2	1.446	2.85974 ± 2.43703
$METSig > 4.6$	Nj>=2	0.807	1.35021 ± 1.9454
$METSig > 4.7$	Nj>=2	0.876	1.32996 ± 1.78491
$METSig > 4.8$	Nj>=2	0.990	1.4638 ± 1.77798
$METSig > 4.9$	Nj>=2	1.042	1.5283 ± 1.77911
$METSig > 5.0$	Nj>=2	1.205	1.71418 ± 1.78023

worth noting that the excess observed in the EE region is similar to that in the BB region, but with higher significance.

Figure 8.10 shows the significance as a function of $S_{E_{\mathrm{T}}^{\mathrm{miss}}}$ cut comparing Run 1 and Run 2, where Figure 8.10a is the ≥ 1-jet case and Figure 8.10a is the ≥ 2-jet case. A very similar trend in the evolution of the significance as a function of $S_{E_{\mathrm{T}}^{\mathrm{miss}}}$ cut is observed in the two datasets, which is ideal as this shows consistency in both datasets.

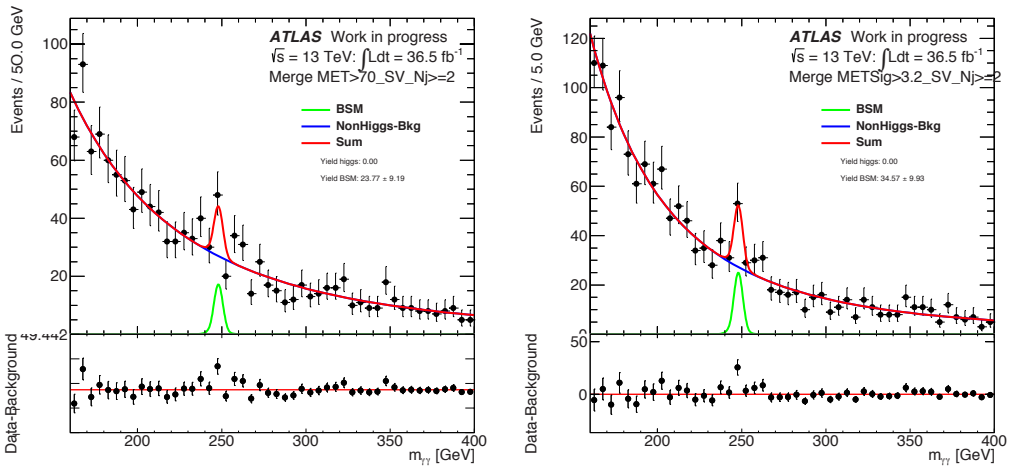
Table 8.3: Significance and yield results for $50 < E_{\mathrm{T}}^{\mathrm{miss}} < 150\,\mathrm{GeV}$ in 10 GeV intervals and $3.0 < S_{E_{\mathrm{T}}^{\mathrm{miss}}} < 5.0\,\sqrt{\mathrm{GeV}}$ in intervals of 0.1, split into the SV case and ≥ 2-jet case. Results are shown for Run 2 data corresponding to 36.1 fb^{-1} of integrated luminosity. The highlighted rows correspond to the maximum significance corresponding to the $E_{\mathrm{T}}^{\mathrm{miss}}$ and $S_{E_{\mathrm{T}}^{\mathrm{miss}}}$ cuts, respectively [15, 16].

Cut	Vertex choice	Jet bin	Significance	Yield
$MET > 50$	SV	Nj>=2	0.877	13.0342 ± 15.1201
$MET > 60$	SV	Nj>=2	0.877	13.0342 ± 15.1201
$MET > 70$	SV	Nj>=2	2.893	23.7735 ± 9.18779
$MET > 80$	SV	Nj>=2	2.779	17.097 ± 7.07701
$MET > 90$	SV	Nj>=2	1.855	8.76925 ± 5.34343
$MET > 100$	SV	Nj>=2	1.532	5.84706 ± 4.3261
$MET > 110$	SV	Nj>=2	1.798	6.03155 ± 3.94548
$MET > 120$	SV	Nj>=2	1.969	5.81573 ± 3.59446
$MET > 130$	SV	Nj>=2	1.161	2.99022 ± 2.98073
$MET > 140$	SV	Nj>=2	0.819	1.85757 ± 2.52533
$MET > 150$	SV	Nj>=2	0.916	1.97783 ± 2.43899
$METSig > 3.0$	SV	Nj>=2	3.565	34.2977 ± 10.8189
$METSig > 3.1$	SV	Nj>=2	3.755	33.9821 ± 10.3033
$METSig > 3.2$	SV	Nj>=2	4.026	34.5717 ± 9.93303
$METSig > 3.3$	SV	Nj>=2	3.335	26.7088 ± 9.12643
$METSig > 3.4$	SV	Nj>=2	3.270	24.7557 ± 8.66963
$METSig > 3.5$	SV	Nj>=2	3.625	25.5593 ± 8.25009
$METSig > 3.6$	SV	Nj>=2	3.238	21.1971 ± 7.62182
$METSig > 3.7$	SV	Nj>=2	3.337	20.6354 ± 7.28872
$METSig > 3.8$	SV	Nj>=2	2.760	15.6949 ± 6.6284
$METSig > 3.9$	SV	Nj>=2	2.582	13.752 ± 6.18765
$METSig > 4.0$	SV	Nj>=2	1.773	8.69624 ± 5.48787
$METSig > 4.1$	SV	Nj>=2	1.739	8.14998 ± 5.28494
$METSig > 4.2$	SV	Nj>=2	1.825	8.20341 ± 5.10299
$METSig > 4.3$	SV	Nj>=2	2.273	9.75719 ± 5.0485
$METSig > 4.4$	SV	Nj>=2	2.383	9.93055 ± 4.95775
$METSig > 4.5$	SV	Nj>=2	1.538	5.91205 ± 4.35318
$METSig > 4.6$	SV	Nj>=2	1.531	5.69982 ± 4.23225
$METSig > 4.7$	SV	Nj>=2	0.402	1.36505 ± 3.5718
$METSig > 4.8$	SV	Nj>=2	0.069	0.235108 ± 3.23268
$METSig > 4.9$	SV	Nj>=2	0.446	1.37301 ± 3.21441
$METSig > 5.0$	SV	Nj>=2	0.138	0.410174 ± 3.01656

8.5 Event selection and categorization

8.5.1 Object and event selection

Object reconstruction and event selection for this analysis also inherits from the diphoton selections discussed in Sections 4, 5 and 6. The hard objects include photons, jets, electrons and muons which are passed to the HGAMANALYSISFRAMEWORK where they are calibrated as per the recommendations. Also, the $E_{\mathrm{T}}^{\mathrm{miss}}$ which is a signature for this analysis is discussed lengthily in Section 6. The Madala framework fetches all the events after the nominal diphoton selection up to before the relative p_T cut in order to allow for flexibility in the adjustment of the $m_{\gamma\gamma}$ window in the analysis. Unlike in the previous analysis, where we looked at events within



(a) (b)

Figure 8.7: Fit distributions corresponding to maximum significance for the case of (a) $E_{\mathrm{T}}^{\mathrm{miss}}$ and (b) $S_{E_{\mathrm{T}}^{\mathrm{miss}}}$. In the case of $E_{\mathrm{T}}^{\mathrm{miss}}$, the maximum excess occurs at $E_{\mathrm{T}}^{\mathrm{miss}} > 70\,\mathrm{GeV}$ with a significance of $2.9\,\sigma$. In the case of $S_{E_{\mathrm{T}}^{\mathrm{miss}}}$, the maximum excess occurs at $S_{E_{\mathrm{T}}^{\mathrm{miss}}} > 3.2\,\sqrt{\mathrm{GeV}}$ with a significance of $4.0\,\sigma$ [15].

$105\,\mathrm{GeV} < m_{\gamma\gamma} < 160\,\mathrm{GeV}$, in this resonance search we are interested in events passing $160\,\mathrm{GeV} < m_{\gamma\gamma} < 400\,\mathrm{GeV}$ to accommodate the excess of interest. All relevant $E_{\mathrm{T}}^{\mathrm{miss}}$ performance studies are documented in Section 6.3.6.

8.5.2 Categorization

In this resonance search, the selected events are divided into categories based on the following variables:

- $S_{E_{\mathrm{T}}^{\mathrm{miss}}} = E_{\mathrm{T}}^{\mathrm{miss}}/\sqrt{\sum E_T}$
- $p_{\mathrm{T}}^{\gamma\gamma}$
- SV = photon pointing vertex $\sum p_T^2$ − pile-up vertex $\sum p_T^2 > 0$
- Number of central jets: 0-jet case, 1-jet case and ≥2-jet case

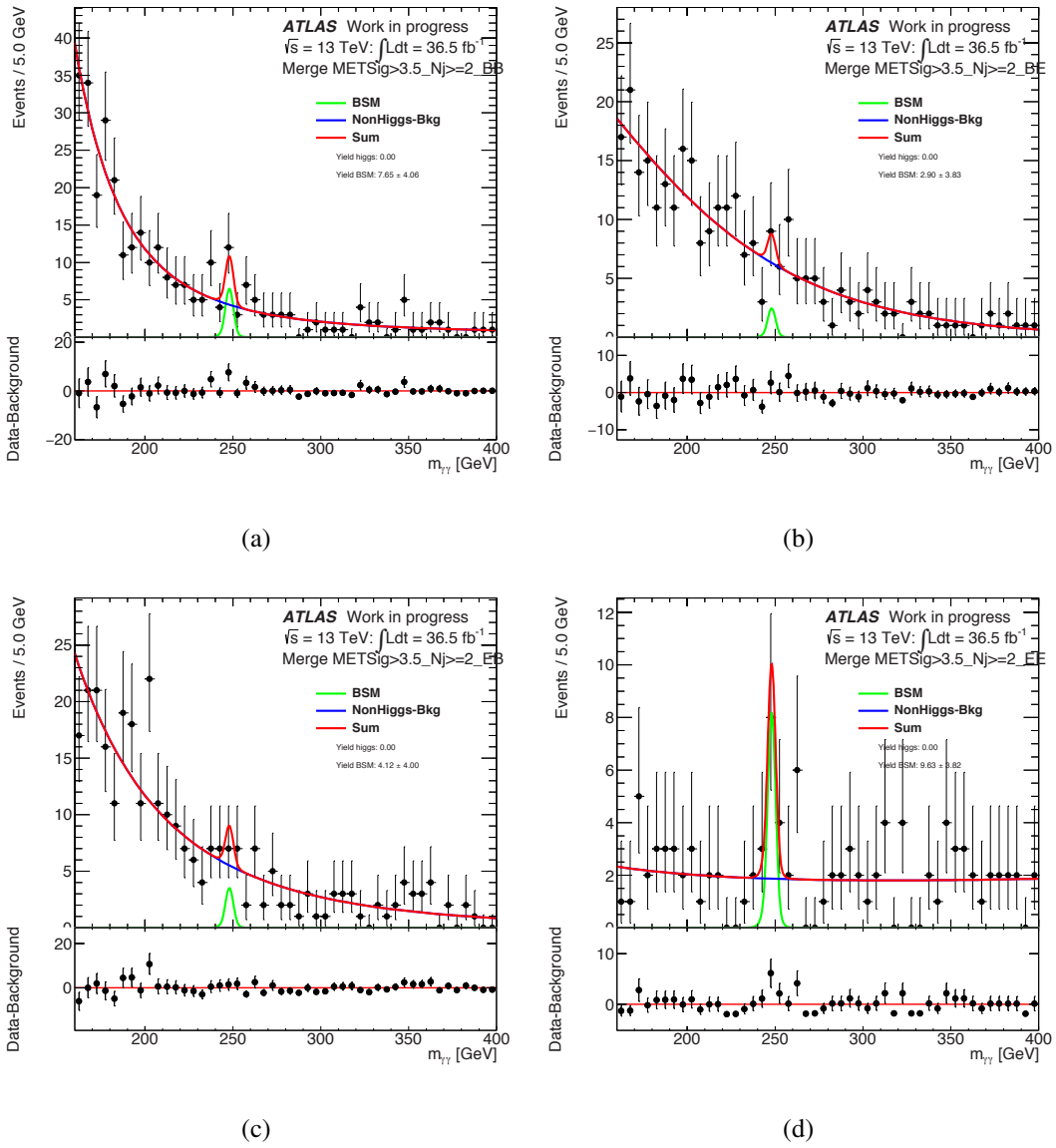
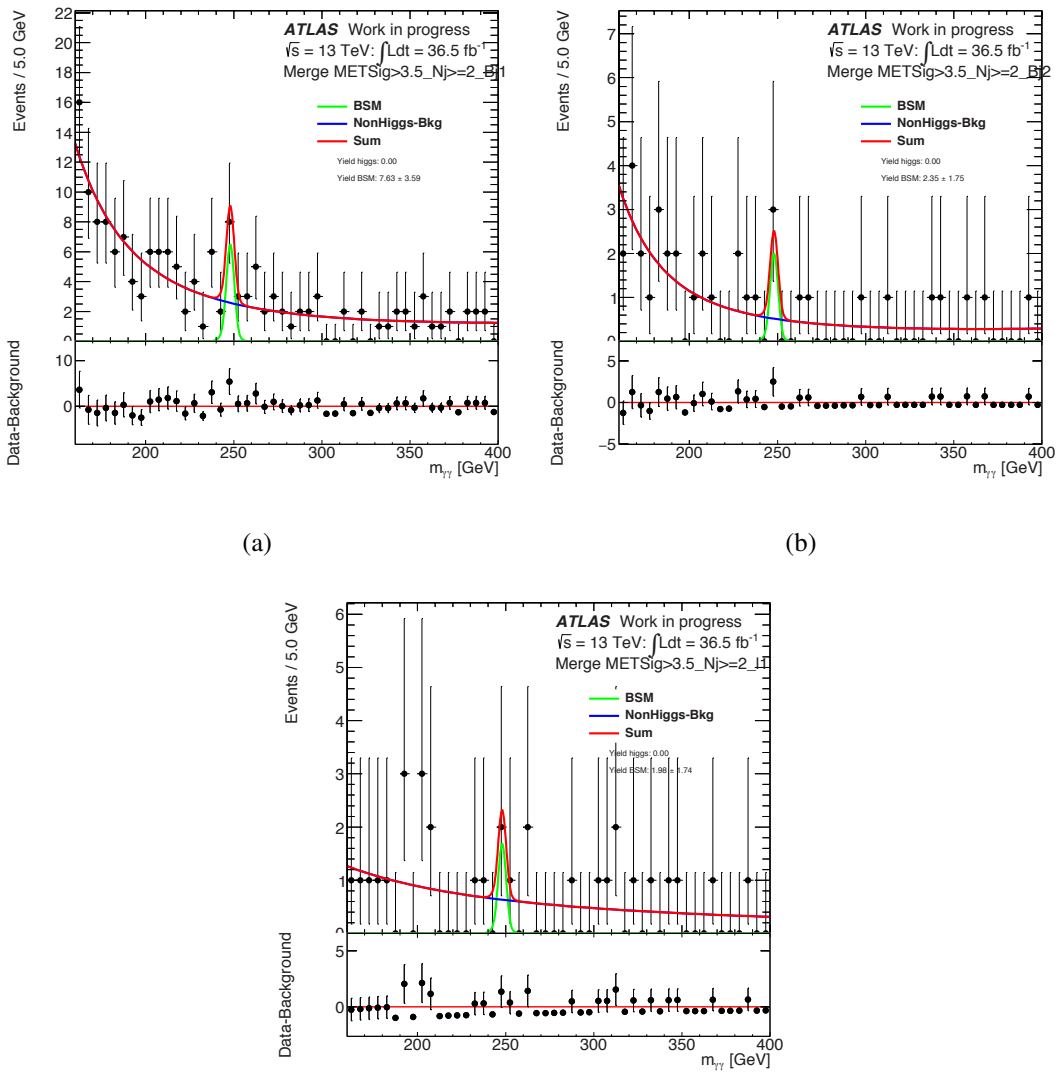


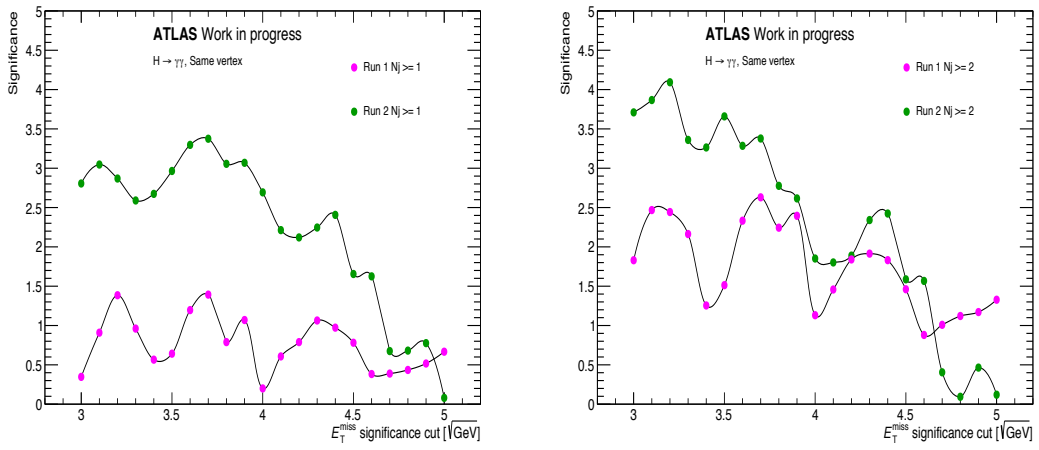
Figure 8.8: Run 2 data $E_{\mathrm{T}}^{\mathrm{miss}}$ fit distributions for $S_{E_{\mathrm{T}}^{\mathrm{miss}}} > 3.5\ \sqrt{\mathrm{GeV}}$, SV case and with at least two central jets for: photons in (a) Barrel-Barrel region (BB), (b) Barrel-EndCap region (BE), (c) EndCap-Barrel region (EB) and (d) EndCap-EndCap region (EE), respectively [15].



(a) (b)

(c)

Figure 8.9: Run 2 data $E_{\mathrm{T}}^{\mathrm{miss}}$ fit distributions for $S_{E_{\mathrm{T}}^{\mathrm{miss}}} > 3.5\ \sqrt{\mathrm{GeV}}$, SV case and with at least two central jets for (a) and (b) number of b-tagged jets ≥2 and (c) number of leptons ≥1 [15].



(a) (b)

Figure 8.10: Distributions showing significance as a function of $S_{E_{\mathrm{T}}^{\mathrm{miss}}}$ cut comparing Run 1 and Run 2 for the (a) ≥ 1-jet and (b) ≥ 2-jet cases [15].

Table 8.4: A summary of the set categories [15].

Category name	**Requirements**
Inclusive	Inclusive
UPMETNj0	$S_{E_{\mathrm{T}}^{\mathrm{miss}}} > 3.5\ \sqrt{\mathrm{GeV}}$, SV, $\mathrm{N_{jets}} = 0$
UPMETNj1	$S_{E_{\mathrm{T}}^{\mathrm{miss}}} > 3.5\ \sqrt{\mathrm{GeV}}$, SV, $\mathrm{N_{jets}} = 1$
UPMETNj2	$S_{E_{\mathrm{T}}^{\mathrm{miss}}} > 3.5\ \sqrt{\mathrm{GeV}}$, SV, $\mathrm{N_{jets}} >= 2$

Table 8.5: The cutflow for data and MC including the statistical uncertainties. Normalized to 36.1 fb^{-1} [15].

Cuts	$V\gamma$	$V\gamma\gamma$	$\gamma\gamma$	γj	**Data**
Inclusive	532.49	324.93	163339.95	39571.40	197857
UPMETNj0	18.57	16.99	567.04	235.23	899
UPMETNj1	27.15	26.65	686.62	241.93	1168
UPMETNj2	32.34	39.40	561.62	181.65	990

The most captivating case is the ≥2-jet case because it possesses the largest observed excess as shown in Section 8.4. The categorization of the events is summarized in Table 8.4 as motivated previously and the corresponding data and MC yields are shown in Table 8.5.

Figures 8.11 and 8.12 show the control distributions corresponding to different variables for

various regions. The data and MC comparisons in the inclusive and ≥2-jet regions are shown in Figure 8.11 and 8.12, respectively, using 36.1 fb^{-1} 2015+2016 data. The background samples used include Sherpa $\gamma\gamma$, Sherpa γj, $V\gamma$ and $V\gamma\gamma$. The SM Higgs signal comprises all the SM Higgs samples: ggF, VBF, Wh, Zh, tth and bbh. Control distributions corresponding to the remaining categories are documented in the supporting note in Reference [15]. There is reasonable agreement between data and MC for all the categories in the various control distributions.

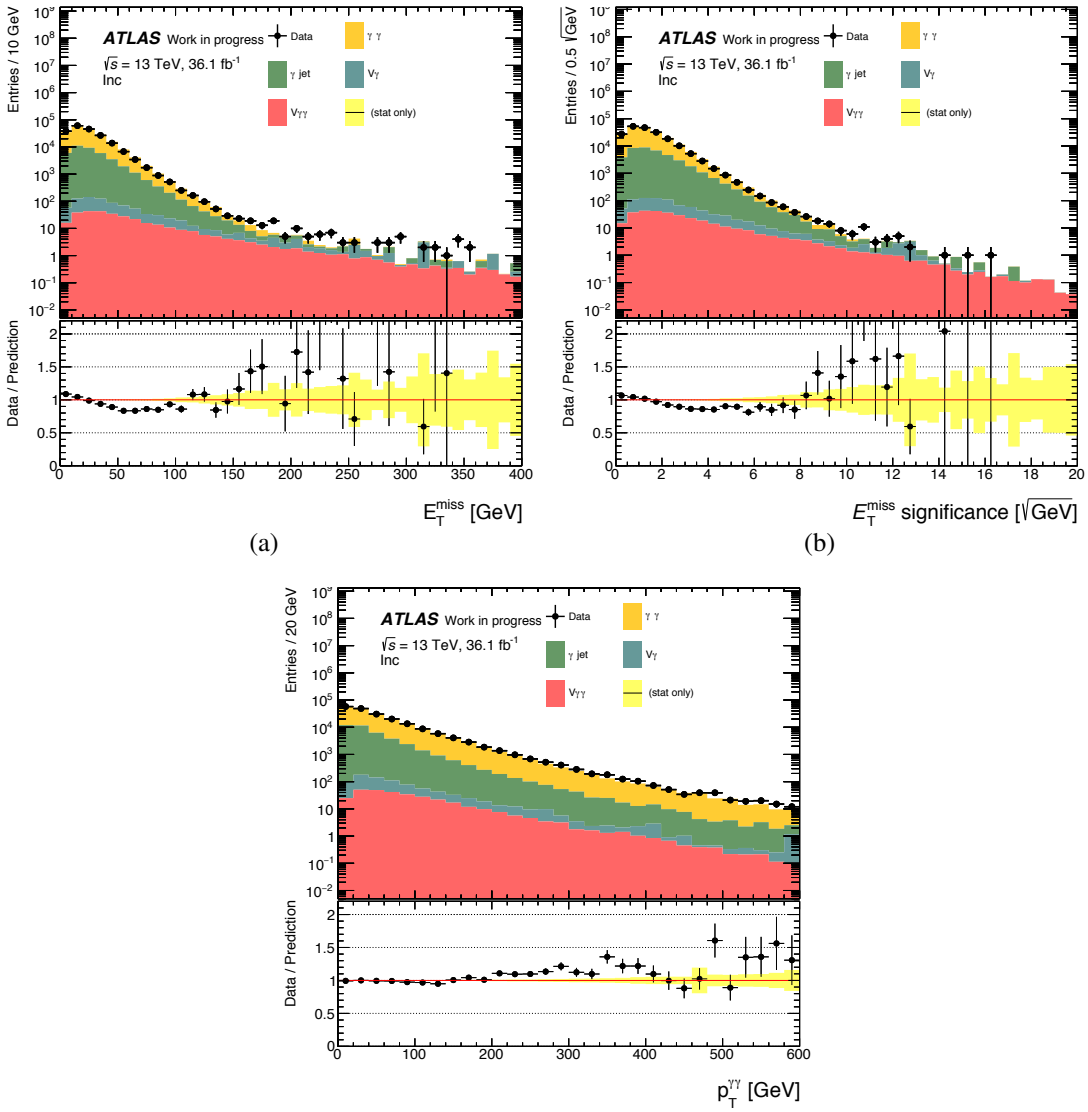
8.6 Signal and background parameterization

The modelling strategy employed here is similar to that of the $h(\rightarrow\gamma\gamma)$+$E_{\mathrm{T}}^{\mathrm{miss}}$ analysis discussed in Section 7.5. As already mentioned, the signal and background yields are obtained by fitting analytical functions to the diphoton invariant mass spectrum in each of the categories.

8.6.1 Signal modelling

The physics model relevant to $H(\rightarrow\gamma\gamma)+E_{\mathrm{T}}^{\mathrm{miss}}$ is lacking in signal MC samples. As a result, in order to gauge the signal shape, a validation is performed between the $\gamma\gamma$ mass spectrum of high-mass $ZX\rightarrow\gamma\gamma+E_{\mathrm{T}}^{\mathrm{miss}}$ and $ggF\rightarrow X$ signal models, under various central jet bins and truth $E_{\mathrm{T}}^{\mathrm{miss}}$ cuts. It is found that the $\gamma\gamma$ mass spectrum is not affected by the different central jet bins and truth $E_{\mathrm{T}}^{\mathrm{miss}}$ cuts. We can therefore directly use $ggF\rightarrow$X high-mass signal MC samples at 150, 200, 250, 300, 350 and 400 GeV, with our set $E_{\mathrm{T}}^{\mathrm{miss}}$ or central jet cuts.

The signal yield is extracted from the $S+B$ fit and the diphoton invariant mass distribution for a resonance of mass m_X is well modelled by the DSCB function which was detailed in Section 7.5.1. Figure 8.13 shows the results of simultaneous fits of DSCB parameters as a function of the invariant mass spectrum in data derived from all full simulation signal samples inclusively. The signal shape at any intermediary mass value that does not correspond to any simulated sample is obtained by assuming that each DSCB parameter has a functional dependence on m_X. In doing so, the parameters of such functions can be determined through a



(a) (b)

(c)

Figure 8.11: The distribution of (a) $E_{\mathrm{T}}^{\mathrm{miss}}$ (b) $S_{E_{\mathrm{T}}^{\mathrm{miss}}}$ and (c) $p_{\mathrm{T}}^{\gamma\gamma}$ after the selection of diphoton candidates in $160\,\mathrm{GeV} < m_{\gamma\gamma} < 400\,\mathrm{GeV}$, cutting on $S_{E_{\mathrm{T}}^{\mathrm{miss}}} > 3.5\,\sqrt{\mathrm{GeV}}$, making the SV selection for the inclusive case. The distributions are done using $36.1\,\mathrm{fb}^{-1}$ corresponding to 2015+2016 data. The expectation from MC is normalized with its corresponding cross-section and the data luminosity and the normalizations of the $\gamma\gamma$ and γj contributions are fixed to 79% and 19% of the data yield [15].

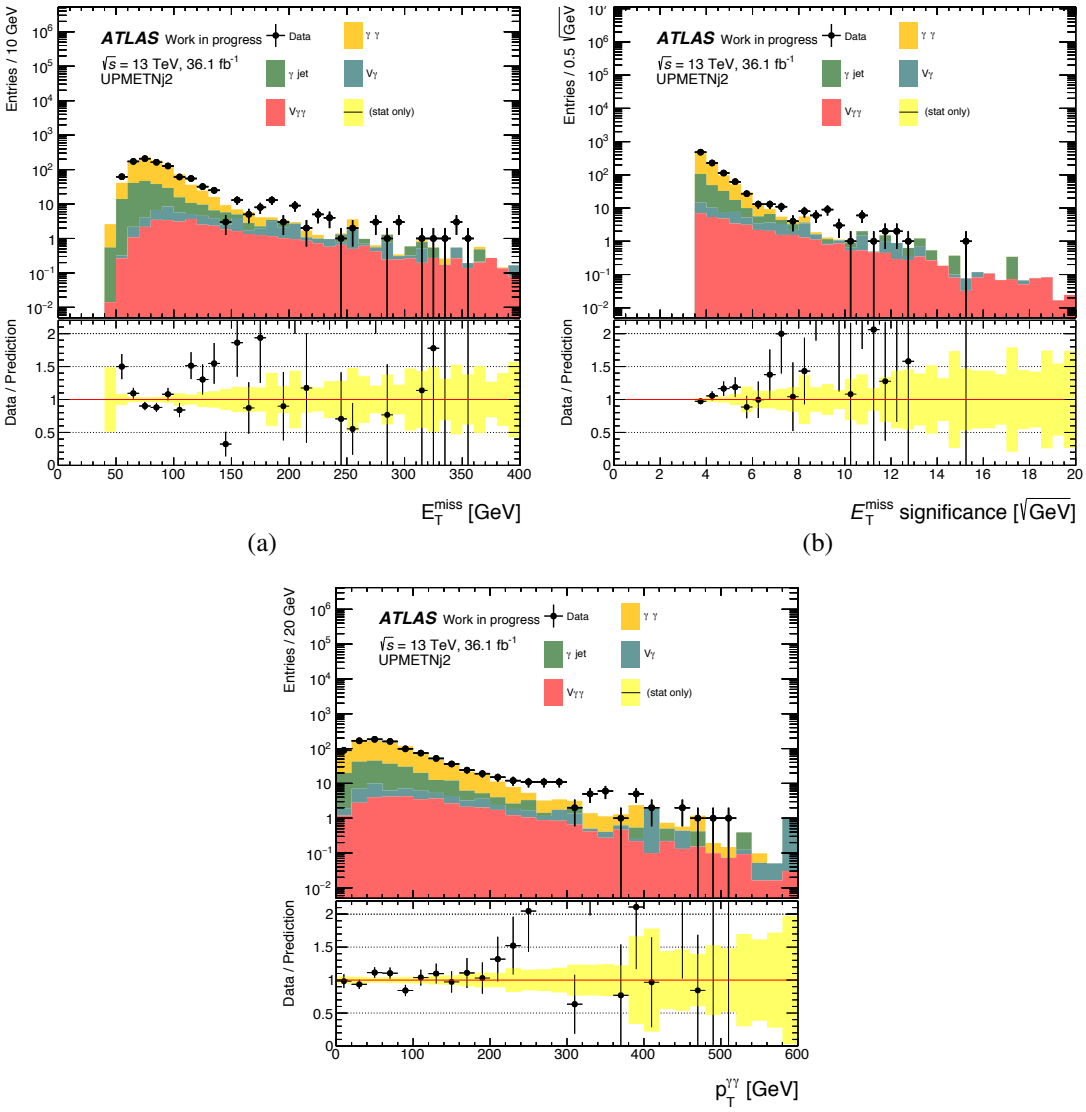


Figure 8.12: The distribution of (a) $E_{\mathrm{T}}^{\mathrm{miss}}$ (b) $S_{E_{\mathrm{T}}^{\mathrm{miss}}}$ and (c) $p_{\mathrm{T}}^{\gamma\gamma}$ after the selection of diphoton candidates in $160\,\mathrm{GeV} < m_{\gamma\gamma} < 400\,\mathrm{GeV}$, cutting on $S_{E_{\mathrm{T}}^{\mathrm{miss}}} > 3.5\,\sqrt{\mathrm{GeV}}$, making the SV selection and splitting into ≥2-jet. The distributions are done using $36.1\,\mathrm{fb}^{-1}$ corresponding to 2015+2016 data. The expectation from MC is normalized with its corresponding cross-section and the data luminosity and the normalizations of the $\gamma\gamma$ and γj contributions are fixed to 79% and 19% of the data yield [15].

simultaneous fit to all the signal samples as represented in Figure 8.13 and the functions used to describe the dependence are summarized in Table 8.6.

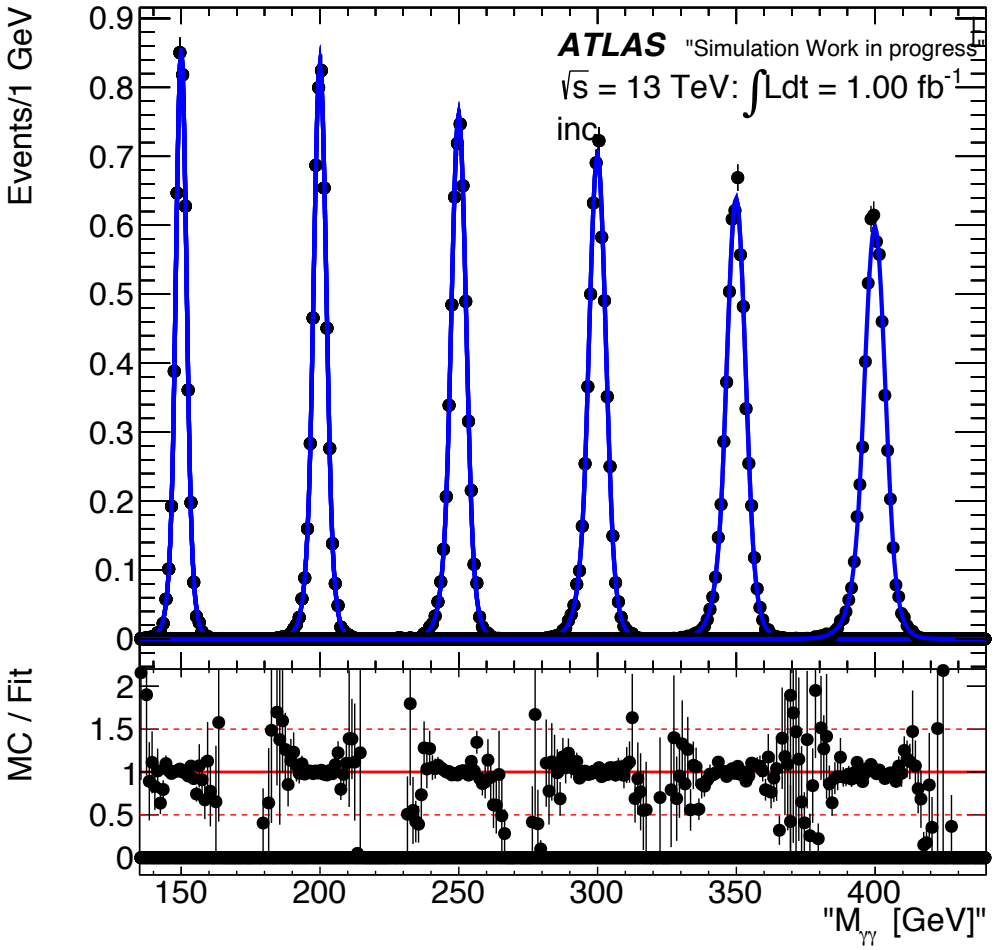


Figure 8.13: The results of simultaneous fits of DCSB parameters as a function of the invariant mass spectrum in data derived from all full simulation signal samples [15].

8.6.2 Spurious signal

The background is parametrized with an analytic function, where the function parameters and the normalization are obtained from fits to the diphoton invariant mass distribution on data. The choice of fit function for each category is made using MC background samples by measuring

Table 8.6: A summary of the parameterization of the fitted parameters from the simultaneous fit, which are described in detail in Section 7.5.1 [15].

Parameter	Fitted function
μ_{CB}	$a_\mu + b_\mu \times x + c_\mu \times x^2 + m_X$
σ_{CB}	$a_\sigma + b_\sigma \times x$
α_{Lo}	$a_{\alpha_{\mathrm{Lo}}} + b_{\alpha_{\mathrm{Lo}}} \times x + c_{\alpha_{\mathrm{Lo}}} \times x^2$
α_{Hi}	$a_{\alpha_{\mathrm{Hi}}} + b_{\alpha_{\mathrm{Hi}}} \times x + c_{\alpha_{\mathrm{Hi}}} \times x^2$
x	$(m_X - 100\mathrm{GeV})/100$ GeV

the bias associated to each function and choosing the function with the smallest number of degrees of freedom that satisfies the bias criteria.

The spurious signal is equal to the bias on the signal yield caused by the choice of a particular background parameterization and it is evaluated [4] by fitting a high statistics background-only sample, scaled to the luminosity of the data, with a signal plus background model. This is done without introducing the corresponding statistical fluctuations.

As mentioned in Section 7.5.2, various functions are tested and for each functional form, several fits are tested by varying the position of the signal peak. In consideration of the narrow width of signal models around $m_{\gamma\gamma}$ = 200 GeV, the binning of background shape is 1 GeV/bin, the S+B fit range is 160-400 GeV and spurious signal scan range is 250-350 GeV. Figure 9.6 shows the maximum ratio of fitted spurious signal yield to its uncertainty, and Table 9.5 also shows the fit property of each tested function. The spurious signal issue was resolved without exceeding the criteria, and we have a very small, less influential spurious signal.

Table 8.7: Fitted spurious signal yield to its uncertainty, spurious signal yield and fit properties of tested functions [15].

Function	max S/δS	max S	Npar	χ^2/ndof	Prob(χ^2)	Fit Range	Status
ExpPoly2	9.5%	-0.53	2	0.17	100%	160-400 GeV	Pass
Bern3	-88%	-6.13	3	34.7	0%	160-400 GeV	Fail
FK0	11.6%	1.11	2	0.12	100%	160-400 GeV	Pass and Selected
FK1	10.7%	1.02	2	0.12	100%	160-400 GeV	Pass
FK2	9.9%	0.94	2	0.12	100%	160-400 GeV	Pass

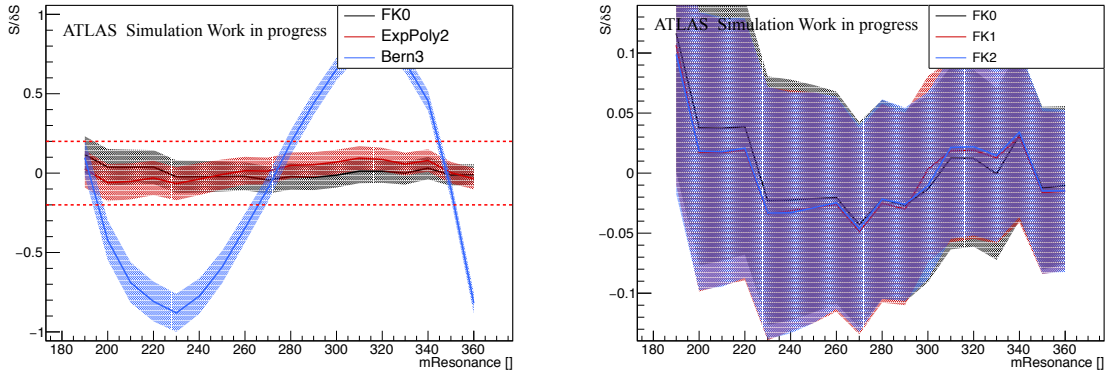


Figure 8.14: Ratio of the fitted spurious signal yield to its uncertainty for the background models of as a function of the resonance mass [15].

8.7 Statistical analysis

The statistical analysis used in this study follows closely to that of the previous $h(\rightarrow \gamma\gamma)+E_{\mathrm{T}}^{\mathrm{miss}}$ study. Maximum-likelihood fits are performed on each $m_{\gamma\gamma}$ distribution for the different categories and various mass hypotheses are tested by varying the resonance mass m_X. The S+B model can be described as:

$$N_{\mathrm{Sig}} \times f_{\mathrm{Sig}}(m_{\gamma\gamma}) + N_{\mathrm{Bkg}} \times f_{\mathrm{Bkg}}(m_{\gamma\gamma}), \tag{8.1}$$

where N_{Sig} is the fitted number of signal events, $f_{\mathrm{Sig}}(m_{\gamma\gamma})$ is the parametrized function which describes the distribution for a given mass hypothesis, N_{Bkg} is the fitted number of background events and $f_{\mathrm{Bkg}}(m_{\gamma\gamma})$ is the parameterized background distribution over the entire diphoton mass window range.

Uncertainties in the model are introduced via nuisance parameters. In the current search, the only nuisance parameter of interest is due to the background modelling in the form of a spurious signal. This uncertainty is constrained using a Gaussian penalty term on the likelihood function and is parametrized according to the mass hypothesis (m_X) being tested.

The local p-value (p_0) for the compatibility with the background-only hypothesis when testing a given signal hypothesis (m_X) is based on a scan given by:

$$q_0(m_X, \alpha) = -2\log\frac{L(N_{\mathrm{Sig}} = 0, m_X, \hat{\hat{\nu}})}{L(\hat{N}_{\mathrm{Sig}}, m_X, \hat{\nu})}, \tag{8.2}$$

where the hat superscript indicates parameters chosen to maximize the likelihood L and double hats are parameters chosen to maximize the likelihood in a background-only fit. The symbol ν represents the nuisance parameters and the local p_0 is calculated using the asymptotic approximation to the test statistics distribution.

The infamous look-elsewhere-effect needs to be accounted for since we are considering a scan over a mass range. This is achieved by computing a global significance by running numerous pseudo-experiments which fit a S+B function to a background only simulated dataset. A scan on the mass is performed for each toy and the largest deviation is selected. The resulting distribution of the test statistic can be integrated from the observed test statistic and above to give the global p_0 value, where the global p_0 value is usually smaller than the local p_0 value.

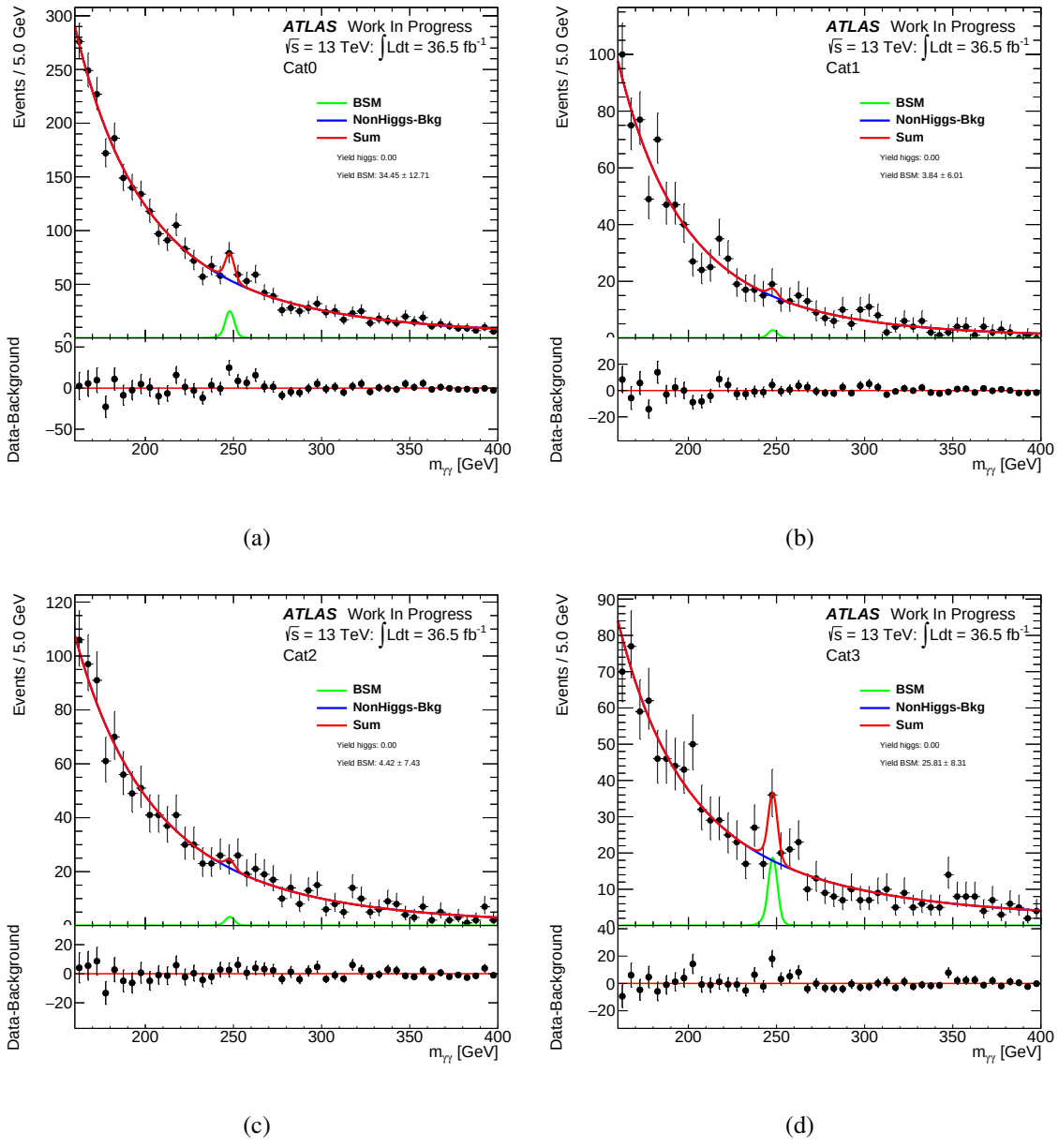
8.8 Results

An unbinned likelihood fit is performed independently in each category. Figure 8.15 shows example fits at the resonant mass of around 248 GeV. Category 0 is the inclusive case, category 1 is the 0-jet case, category 2 is the 1-jet case and category 3 is the ≥2-jet case. The maximum significance is observed in category 3 corresponding to the ≥2-jet case. The resulting p_0 value scans are shown in Figure 8.16 for the category 3 case and those corresponding to the other categories are shown in Appendix D. The category 3 case is of great importance since the largest deviation from the background only hypothesis is observed in this category. Basically, the largest significance occurs at 248 GeV in 2 central jets category. A significance of $3.6\,\sigma$ is observed for $S_{E_{\mathrm{T}}^{\mathrm{miss}}} > 3.5\,\sqrt{\mathrm{GeV}}$ and $4.0\,\sigma$ is observed for $S_{E_{\mathrm{T}}^{\mathrm{miss}}} > 3.2\,\sqrt{\mathrm{GeV}}$. The former case has a global significance of $2.2\,\sigma$ while the latter has a global significance of $2.8\,\sigma$.

In order to gauge how the signal significance is influenced by the luminosity, the S+B fit is done by dividing the 2016 data events into periods and gradually adding them. The resonance parameters and fit function are derived from the signal and background parameterizations.

Figure 8.17 shows the best fit mass, local p-value, and largest signal significance growing with luminosity, under the selections $S_{E_{\mathrm{T}}^{\mathrm{miss}}} > 3.2\,\sqrt{\mathrm{GeV}}$ and $S_{E_{\mathrm{T}}^{\mathrm{miss}}} > 3.5\,\sqrt{\mathrm{GeV}}$, respectively.

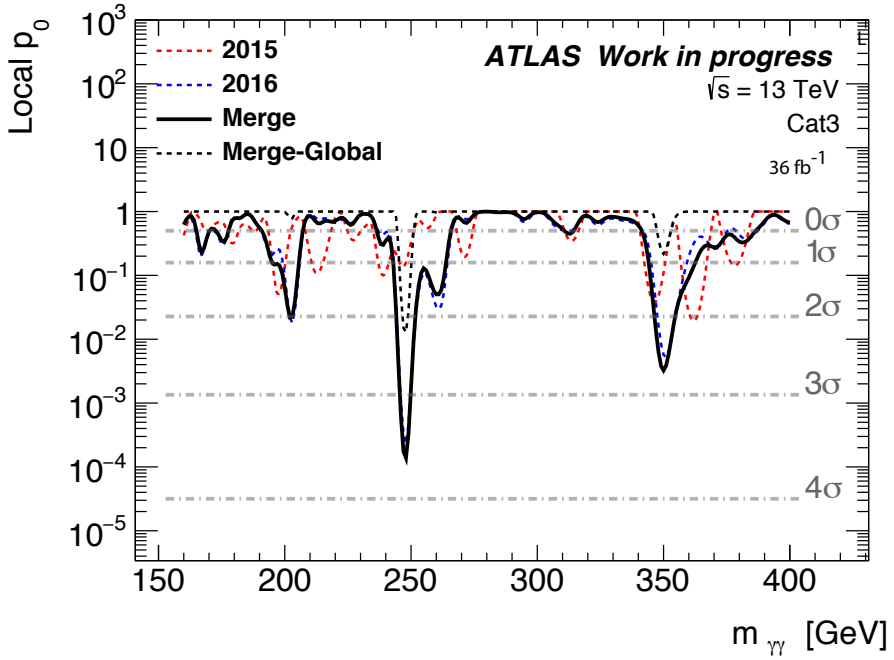
Figure 8.18 shows the largest fitted significance for $S_{E_{\mathrm{T}}^{\mathrm{miss}}} > 3.2\,\sqrt{\mathrm{GeV}}$ and $S_{E_{\mathrm{T}}^{\mathrm{miss}}} >$



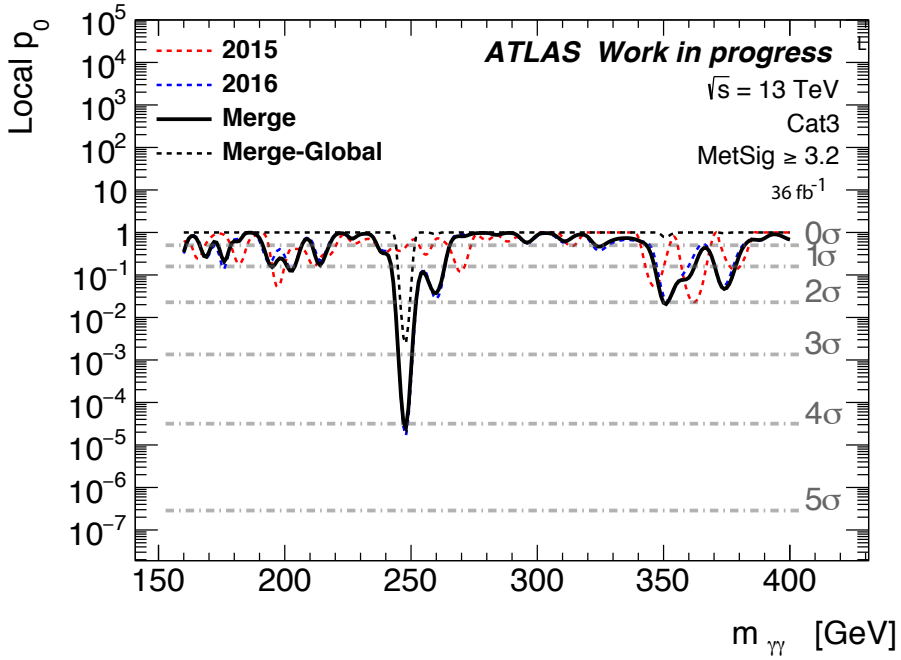
(a) (b)

(c) (d)

Figure 8.15: The individual fits at $m_X = 248$ GeV for each category, where (a) Cat 0 is the inclusive case, (b) Cat 1 is the 0-jet case, (c) Cat 2 is the 1-jet case and (d) Cat 3 is the ≥2-jet case [15].



(a)



(b)

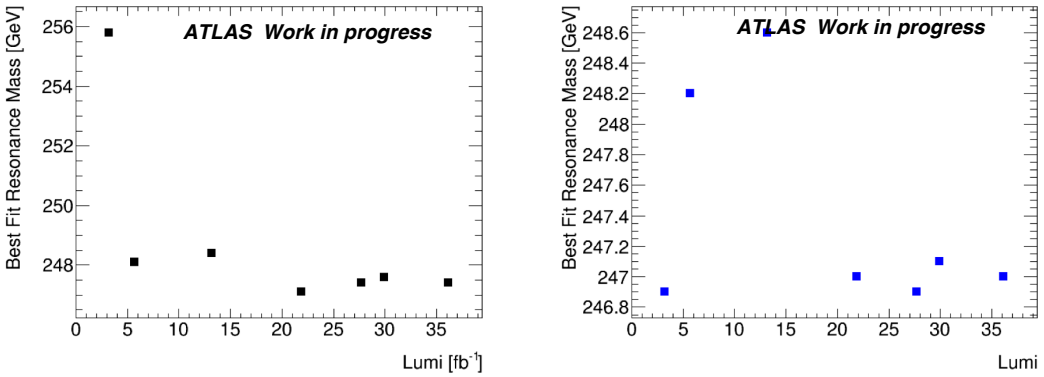
Figure 8.16: Comparison of local p_0 value scans for category 3 with two cuts on the missing energy significance, where (a) has a cut of 3.5 $\sqrt{\text{GeV}}$ and (b) has a cut of 3.2 $\sqrt{\text{GeV}}$. The largest significance from the background only hypothesis occurs at 248 GeV in the category with 2 central jets (category 3) with a slightly lower $S_{E_{\text{T}}^{\text{miss}}}$ and has a value of around 4.0 σ and a corresponding global significance of 2.8 σ [15].

$3.5\sqrt{\mathrm{GeV}}$, respectively, with fixed resonance mass. The distributions for the cases where the resonance mass is made to float are shown in Appendix D.

8.9 Conclusions

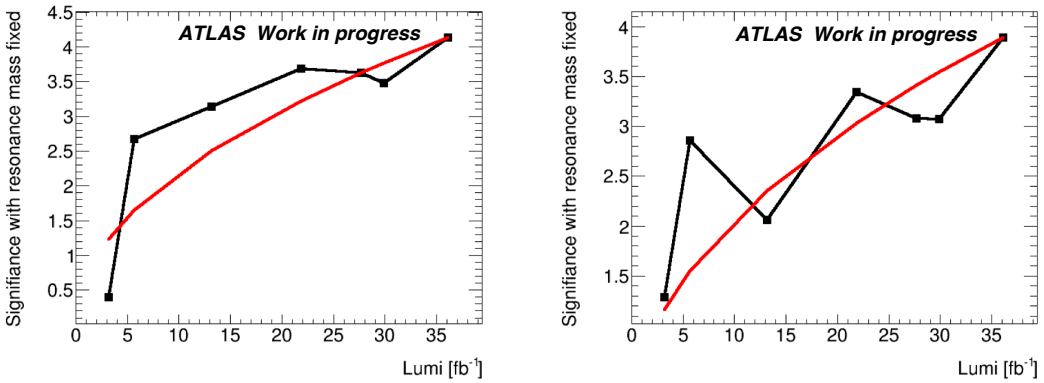
A search for a resonance in the diphoton decay channel in association with $E_{\mathrm{T}}^{\mathrm{miss}}$ has been presented [15]. In 2016, an excess was observed with a diphoton invariant mass around 248 GeV with $E_{\mathrm{T}}^{\mathrm{miss}}$. This excess has been analyzed using Run 1 and Run 2 data, respectively and has essentially motivated the categorization for this resonance search with the ≥2-jet case possessing the largest observed excess as discussed in Section 8.4. The likelihood fits on the diphoton mass distribution for the 248 GeV resonant mass reflect a maximum significance in the 2 central jets category. The fits are done using data so there may be fluctuations, as a result, the current statistics do not allow us to draw any conclusions from the width in the various categories. I added this sentence in the conclusion To add on, in the resulting p_0 value scans, the largest deviation from the background only hypothesis is observed in the at least 2 central jets category. This search has been extrapolated to the $Z\gamma$ channel and the corresponding results are discussed in the next chapter.

An updated study using the latest ATLAS R21 has been done and is documented in the resonance search new supporting note [16]. Additional background suppression variables have been implemented to ensure a clear and maximum significance after categorization. The continuation of this study is documented in Chapter 9.



(a) (b)

Figure 8.17: The fitted resonance mass with largest significance growing with luminosity, with full 2015 and 2016 data for (a) $S_{E_{\mathrm{T}}^{\mathrm{miss}}} > 3.2\ \sqrt{\mathrm{GeV}}$ where the best fit mass is 247 GeV and (b) $S_{E_{\mathrm{T}}^{\mathrm{miss}}} > 3.5\ \sqrt{\mathrm{GeV}}$ where the best fit mass is 247.4 GeV [15].



(a) (b)

Figure 8.18: The largest fitted significance growing with luminosity for (a) $S_{E_{\mathrm{T}}^{\mathrm{miss}}} > 3.2\ \sqrt{\mathrm{GeV}}$ with resonance mass fixed at 247 GeV and (b) $S_{E_{\mathrm{T}}^{\mathrm{miss}}} > 3.5\ \sqrt{\mathrm{GeV}}$ with resonance mass fixed at 247.4 GeV [15].

CHAPTER 9

SEARCH FOR A NEW RESONANCE IN THE DIPHOTON DECAY IN ASSOCIATION WITH $E_{\mathrm{T}}^{\mathrm{MISS}}$ WITH RELEASE 21

The search for an excess with a diphoton invariant mass around 248 GeV associated with $E_{\mathrm{T}}^{\mathrm{miss}}$ is continued. The resonance search detailed in Chapter 8 is redone following the ATLAS calibration changes implemented the latest ATLAS Release 21. A re-optimization is done with R21 using 2015+2016 data and applied to 2017 data. The categories are extrapolated to the $Z\gamma$ search.

This chapter is organized as follows: Section 9.1 introduces the analysis and Section 9.2 touches on the data and MC samples used in this analysis. Section 9.3 recaps the excess considering the end-cap regions with Release 20 and Release 21, respectively. Section 9.4 describes the event optimization. Section 9.5 details the signal and background parameterization and the results are discussed in Section 9.6. Finally, Section 9.7 summarizes the study.

9.1 Introduction

This analysis serves as a continuation of the previous one taking into consideration the software changes between ATLAS R20 and R21. In the newer resonance search supporting notes [15, 16], the excess in 2015+2016 data is re-optimized in order to obtain the best significance considering

these version changes. In addition, the signals observed with the photons in the end-cap regions are now taken into consideration. In fact, a category merging all photon regions will be used in the final fit. The increasing pile-up conditions are a detriment to the analysis such that additional fake $E_{\mathrm{T}}^{\mathrm{miss}}$ suppression techniques have been developed. These methods have been approved by the ATLAS $E_{\mathrm{T}}^{\mathrm{miss}}$ analysis group (JETmiss group) and implemented for even further improvement in this search.

9.2 Data and simulation samples

Data collected in 2015+2016 as well as 2017 at $\sqrt{s}$ = 13 TeV is used in this analysis. The events that are considered are those recorded under stable beam conditions with the detector functioning efficiently. The 2015+2016 data used corresponds to an integrated luminosity of 36.1 fb^{-1} while the 2017 data corresponds to an integrated luminosity of 43.8 fb^{-1}. The MC samples used in this analysis correspond to the ones discussed in Section 8.2.1 in the previous chapter.

9.3 A Recap of analyses of 2015+2016 data in Release 20.7 and Release 21.2

For the two photons in the EEOS and EESS region, the excess is also found to be significant. In the EEOS region the photons are located in the end-caps on opposite sides of the detector, while in the EESS region they are in the end-caps on the same side of the detector. In fact, the EEOS and EESS excess also exists in the 1 central jet bin. Tables 9.1 and 9.2 summarize the signal yields and significance values for the R20 and R21 cases, respectively. In the R21 case, "matched" refers to the same events with the same run number existing in both R20 and R21 after the diphoton selection. When isolating the merged categories, there is a drop from a significance of 4.59 σ to 2.27 σ when moving from R20 to R21. The reason for such a large difference between the two versions can be accounted to the significant change in the calibration of the p_{T} jets in R21. Figure 9.1 shows the corresponding R21 fits with the fit mass fixed at

Table 9.1: The signal yields and the significance in different categories in R20.7. The excess is fit by narrow width assumption. The merged category means merging the EEOS 1 central jet, the EESS 1 central jet and the non-EE 2 central jets categories [16].

Category	Signal Yields	Significance
2 central jets	27.04	3.58
EEOS 1 central jet	20.95	3.62
EESS 1 central jet	4.64	2.36
Non-EE 2 central jets	17.31	2.50
Merge EE and non EE	38.83	4.59

Table 9.2: The signal yields and the significance in different categories in R21.2. The excess is fit by narrow width assumption. The merged category means merging the EEOS 1 central jet, the EESS 1 central jet and the non-EE 2 central jets categories [16].

Category	Signal Yields	Significance
2 central jets	12.99	1.96
EEOS 1 central jets	12.34	1.62
EESS 1 central jets	-0.15	-0.10
Non-EE 2 central jets	9.36	1.53
Merge EE and non EE	15.08	1.99
Merge EE and non EE matched	15.40	2.27

248 GeV which is the best mass point as observed from version R20. Those corresponding to R20 are shown in Appendix D. Peaks are still observed in all cases except in the EESS case where the peak seems to shift slightly. In order to observe a more visible signal in 2017 data, additional $\boldsymbol{E}_{\mathrm{T}}^{\mathrm{miss}}$ suppression methods are necessary.

9.4 Event optimization

The event optimization is performed with 2015+2016 data. Due to the worsening pile-up conditions in 2017, there is a need to introduce some background suppression variables. As a result, the new categories that are set up include the following $\boldsymbol{E}_{\mathrm{T}}^{\mathrm{miss}}$ suppression variables:

- $\Delta\phi_{fjets,\boldsymbol{E}_{\mathrm{T}}^{\mathrm{miss}}}$: the $|\Delta\phi|$ between the vector sum of four momenta of all forward jets and the $\boldsymbol{E}_{\mathrm{T}}^{\mathrm{miss}}$.
  - This selection is motivated by the fact that there is no JVT variable in the forward region and in high pile-up situations having pile-up jets in the forward region is

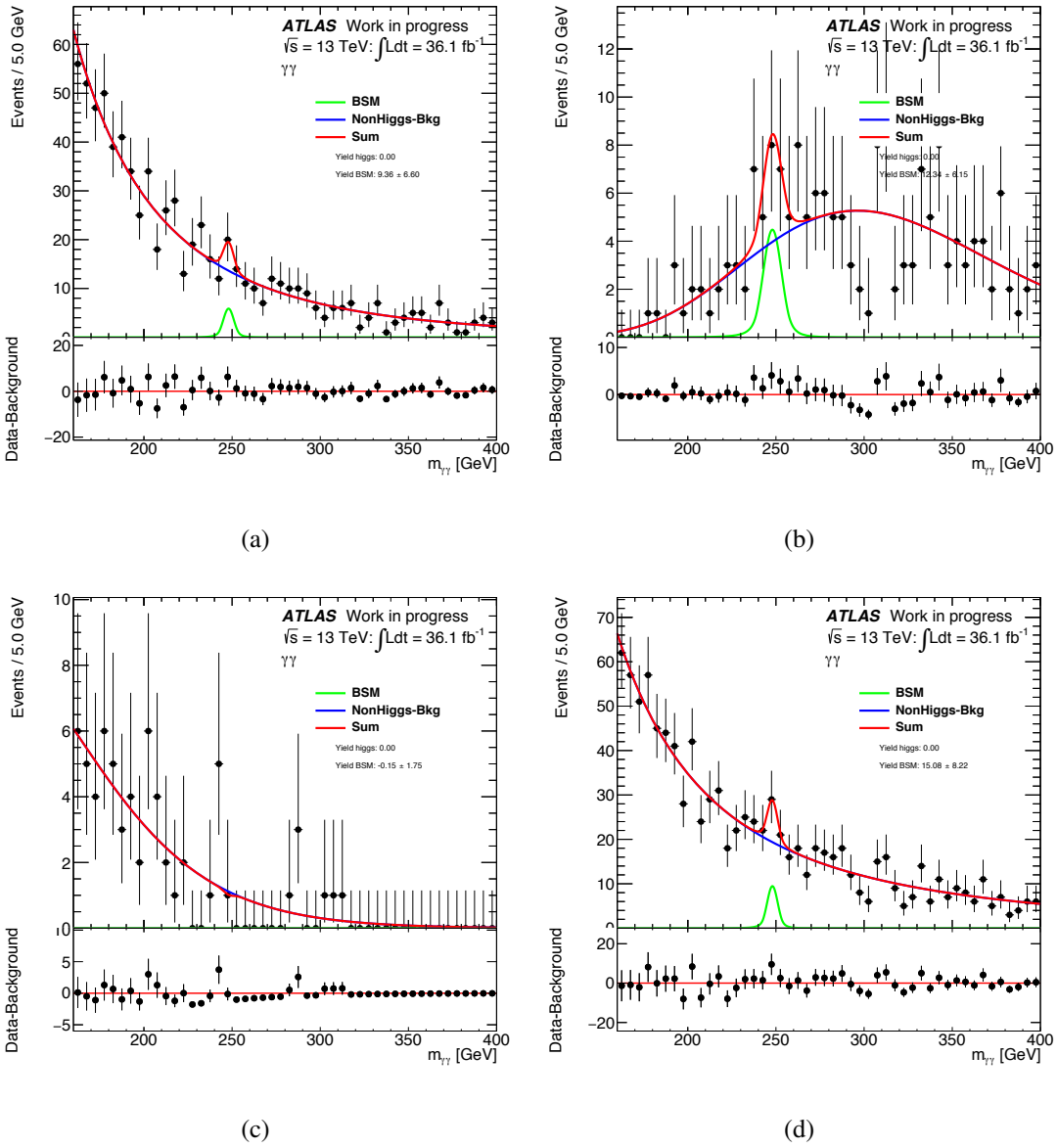


Figure 9.1: The excess in the case of R21 for the (a) non-EE, (b) EEOS, (c) EESS and (d) merge categories. The $m_{\gamma\gamma}$ resolution is set at σ = 3 GeV, 5.2 GeV, 2.75 GeV and 3 GeV, respectively. The fit mass is fixed at 248 GeV and narrow width assumption is considered in all cases. Peaks around 248 GeV are observed in all cases except in the case of the EESS category where the peak seems to have shifted slightly [16].

very likely. These forward jets would contribute to fake $E_{\mathrm{T}}^{\mathrm{miss}}$ as they would not be rejected by the JVT selection.

- $\Delta\phi_{sjets,E_{\mathrm{T}}^{\mathrm{miss}}}$: the $|\Delta\phi|$ between the vector sum of four momenta of all soft jets and the

$E_{\mathrm{T}}^{\mathrm{miss}}$.

  - Contributions to fake $E_{\mathrm{T}}^{\mathrm{miss}}$ from softjets are observed in R20 due to a known jet calibration issue. Even though this issue is fixed in R21, it has a large resolution such that if there are many events containing softjets with overlapping resolution in the same direction, they can result in a relatively large $E_{\mathrm{T}}^{\mathrm{miss}}$. This is not a very strong variable if one cuts at high $E_{\mathrm{T}}^{\mathrm{miss}}$, however, at lower thresholds these softjets can possibly result in fake $E_{\mathrm{T}}^{\mathrm{miss}}$.

- $p_{\mathrm{T}}^{alljets} - p_{\mathrm{T}}^{jj}$: the scalar p_T difference between the vector sum of four momenta of all of the jets above 20 GeV and the leading two central jets.

  - This selection is made to avoid the non-physics jets and all the remaining softjets from being in the same direction in order to prevent resolution overlaps as this can result in fake $E_{\mathrm{T}}^{\mathrm{miss}}$.

- The leading pile-up vertex $\sum p_{\mathrm{T}}^2$: the leading non-physical vertex $\sum p_{\mathrm{T}}^2$, which sums up the p_{T}^2 of all of the tracks for that vertex.

  - In the same vertex method we require the diphoton vertex to be the hardest vertex. It is useful to also check how hard the leading non-physics or pile-up vertex is. If one considers a jet with $p_{\mathrm{T}} > 60$ GeV which cannot be rejected by a JVT selection, then we have fake $E_{\mathrm{T}}^{\mathrm{miss}}$. This hard jet connected to the leading pile-up vertex should have hard tracks which gives a hard $\sum p_{\mathrm{T}}^2$.

In order to decide on the cut position for these four variables, distributions comparing events with fake $E_{\mathrm{T}}^{\mathrm{miss}}$ background to those with truth $E_{\mathrm{T}}^{\mathrm{miss}}$ are essential. Figure 9.2 represents such distributions where the solid lines represent events with fake $E_{\mathrm{T}}^{\mathrm{miss}}$ and the dashed lines represent events with truth $E_{\mathrm{T}}^{\mathrm{miss}}$. Figure 9.2a represents the $\Delta\phi_{fjets,E_{\mathrm{T}}^{\mathrm{miss}}}$ variable which contains a large fraction of background events in the last two bins, thus motivating a cut of < 2.8 rad on this variable. Figure 9.2b represents the $\Delta\phi_{sjets,E_{\mathrm{T}}^{\mathrm{miss}}}$ which proves much weaker than the previous variable, but still shows a few more background events than truth $E_{\mathrm{T}}^{\mathrm{miss}}$ events in the last

Table 9.3: The complete event selection, which includes the discussed fake $E_{\mathrm{T}}^{\mathrm{miss}}$ suppression variables.

Preselection:	At least two well identified, isolated photons (same definition as $h \to \gamma\gamma$) $160 < m_{\gamma\gamma} < 400$, $p_{T,leading\gamma} > 40$ GeV, $p_{T,subleading\gamma} > 30$ GeV Diphoton Vertex is hardest in the event ($\sum p^2_{\mathrm{T}diphoton} > \sum p^2_{\mathrm{T}othervertices}$) $E_{\mathrm{T}}^{\mathrm{miss}}$ cleaning, reject events with bad jets above 20 GeV $S_{E_{\mathrm{T}}^{\mathrm{miss}}} > 3.5\ \sqrt{\mathrm{GeV}}$		
Category:	non-EE	EESS	EEOS
Jet requirements:	≥2 central jets	≥1 central jet	≥1 central jet
$E_{\mathrm{T}}^{\mathrm{miss}}$ suppression:	$\sum p^2_{\mathrm{T}} < 250$ GeV^2 $\Delta\phi_{fjets,E_{\mathrm{T}}^{\mathrm{miss}}} < 2.8$ rad $\Delta\phi_{sjets,E_{\mathrm{T}}^{\mathrm{miss}}} < 2.8$ rad $p_{\mathrm{T}}^{alljets} - p_{\mathrm{T}}^{jj} < 35$ GeV		$\sum p^2_{\mathrm{T}} < 200$ GeV^2
Merge the three categories			

two bins. A cut of $\Delta\phi_{sjets,E_{\mathrm{T}}^{\mathrm{miss}}} < 2.8$ rad is elicited as a result. Figure 9.2c represents the $p_{\mathrm{T}}^{alljets} - p_{\mathrm{T}}^{jj}$ variable in which the fake $E_{\mathrm{T}}^{\mathrm{miss}}$ events have an evidently larger contribution on the right most side of the distribution resulting in a cut of < 35 GeV on this variable. Finally, Figure 9.2d corresponds to the leading pile-up vertex $\sum p^2_{\mathrm{T}}$ variable which shows that the γj events (AntiID17) have a harder leading pile-up vertex $\sum p^2_{\mathrm{T}}$ implying that this cut can essentially kill most of the background events associated with the γj sample. Such a cut is very useful in the EEOS category since after the EEOS selection approximately 50% of the background comes from γj events. Table 9.3 shows the complete events selection which has been optimized for this analysis.

Since there is no suitable signal to predict the number of events in each category, in order to do a simultaneous fit, we merge the three categories. Merging implies simply summing up the previous three regions. The event selections summarized in Table 9.3 are then applied to the R20, R21 and the matched 2015+2016 data. Table 9.4 summarizes the signal yields and the significance in different categories for the different versions. The signal shape is described using a DSCB with a narrow width (fixed at 0) and the mass point is fixed at 248 GeV which is the best fit point obtained from R20. Figure 9.3 shows the R20, R21 and matched 2015+2016 data for the merged case after the fake $E_{\mathrm{T}}^{\mathrm{miss}}$ suppression. When comparing R21 and the matched, the results are quite consistent before and after the fake $E_{\mathrm{T}}^{\mathrm{miss}}$ suppression. There are some discrepancies observed between R20 and R21 especially in the non-EE case after the fake $E_{\mathrm{T}}^{\mathrm{miss}}$

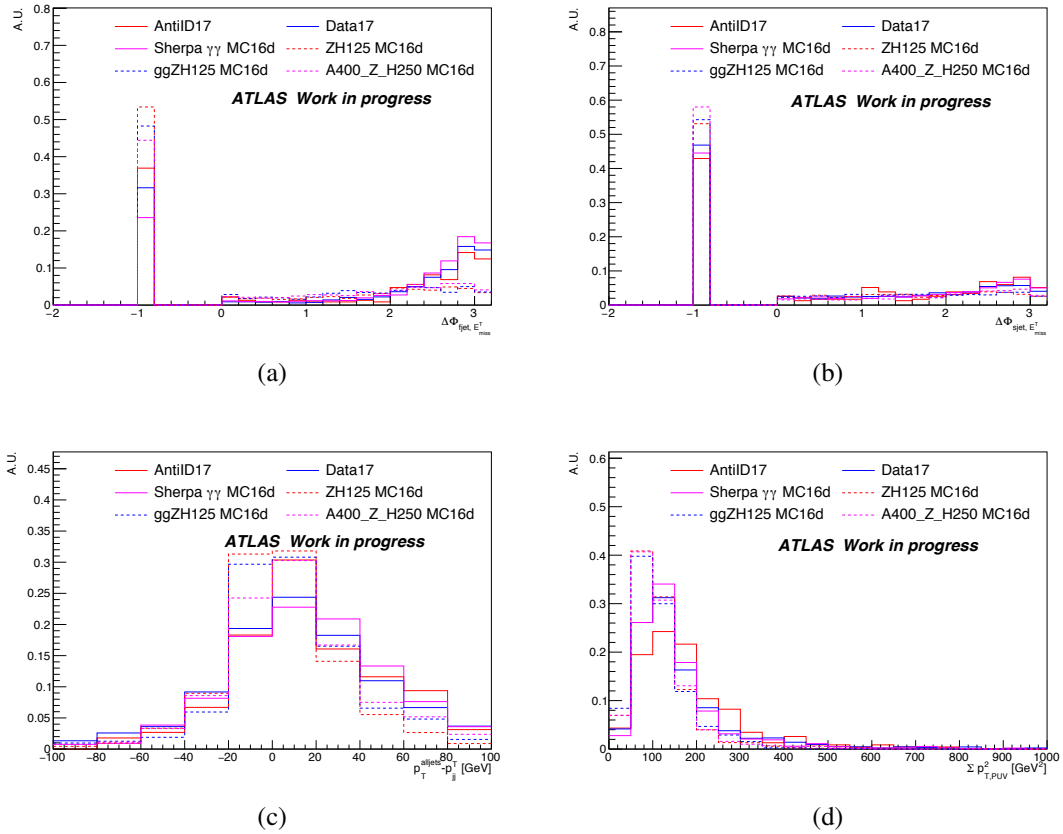


Figure 9.2: The variables used for the suppression of fake $E_{\mathrm{T}}^{\mathrm{miss}}$ in the 2017 pile-up conditions: (a) $\Delta\phi_{fjets,E_{\mathrm{T}}^{\mathrm{miss}}}$, (b) $\Delta\phi_{sjets,E_{\mathrm{T}}^{\mathrm{miss}}}$, (c) $p_{\mathrm{T}}^{alljets} - p_{\mathrm{T}}^{jj}$ and (d) The leading pile-up vertex $\sum p_{\mathrm{T}}^2$. These figures correspond to the 2-jet case with the $S_{E_{\mathrm{T}}^{\mathrm{miss}}}$ cut. The data corresponds to the side-bands of 160-400 GeV, excluding the 240-260 GeV region. The solid lines represent samples with fake $E_{\mathrm{T}}^{\mathrm{miss}}$ while the dashed lines represent those with truth $E_{\mathrm{T}}^{\mathrm{miss}}$ [16].

suppression variables. The overall differences between the R20 and R21 are accounted to fake $E_{\mathrm{T}}^{\mathrm{miss}}$ due to mis-calibration. Even though there is a drop in significance when moving from R20 ($4.59\,\sigma$) for R21 ($2.85\,\sigma$), the significance is still better than in the case where no $E_{\mathrm{T}}^{\mathrm{miss}}$ suppression cuts are applied. The cuts essentially remove half of the background and reduce the fluctuations associated to it while keeping the signal. These cuts are frozen for the analysis and extrapolated to the $Z\gamma$ channel as well.

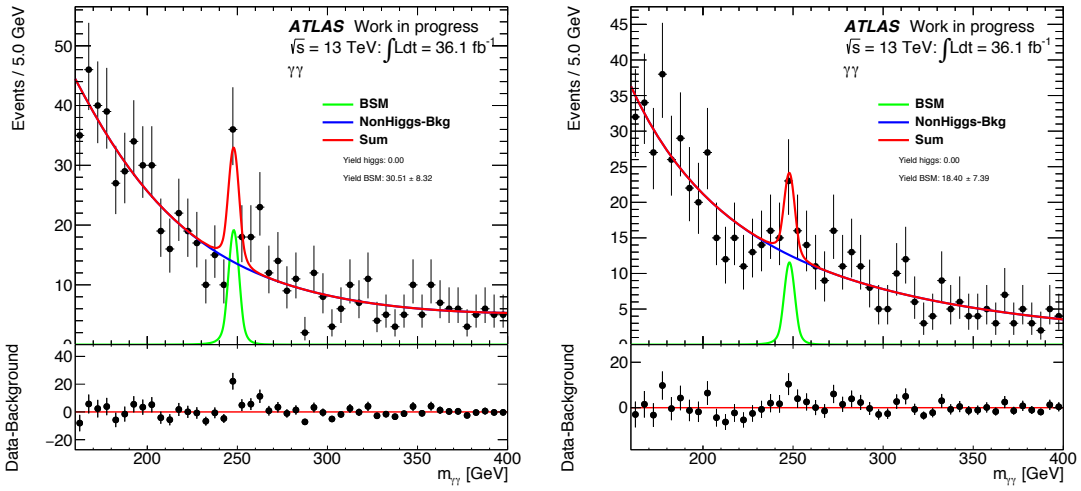
Table 9.4: The signal yields and the significance in different categories in different versions. The mass point is at 248 GeV using narrow width approximation [16].

Category	Signal Yields	Significance
R20.7 EEOS	20.95	3.62
R20.7 EEOS after $E_{\mathrm{T}}^{\mathrm{miss}}$ suppression	20.89	3.86
R20.7 EESS	4.64	2.36
R20.7 EESS after $E_{\mathrm{T}}^{\mathrm{miss}}$ suppression	2.72	1.82
R20.7 non-EE	17.31	2.50
R20.7 non-EE after $E_{\mathrm{T}}^{\mathrm{miss}}$ suppression	9.97	1.95
R20.7 Merge	38.83	4.59
R20.7 Merge after $E_{\mathrm{T}}^{\mathrm{miss}}$ suppression	30.51	4.42
R21.2 EEOS	12.34	1.62
R21.2 EEOS after $E_{\mathrm{T}}^{\mathrm{miss}}$ suppression	13.06	1.85
R21.2 EESS	-0.15	-0.10
R21.2 EESS after $E_{\mathrm{T}}^{\mathrm{miss}}$ suppression	0.28	0.20
R21.2 non-EE	9.36	1.53
R21.2 non-EE after $E_{\mathrm{T}}^{\mathrm{miss}}$ suppression	11.49	2.31
R21.2 Merge	15.08	1.99
R21.2 Merge after $E_{\mathrm{T}}^{\mathrm{miss}}$ suppression	18.40	2.85
R21.2 EEOS matched	10.79	1.57
R21.2 EEOS matched after $E_{\mathrm{T}}^{\mathrm{miss}}$ suppression	9.30	2.23
R21.2 EESS matched	-0.41	-0.22
R21.2 EESS matched after $E_{\mathrm{T}}^{\mathrm{miss}}$ suppression	0.78	0.55
R21.2 non-EE matched	9.59	1.75
R21.2 non-EE matched after $E_{\mathrm{T}}^{\mathrm{miss}}$ suppression	11.57	2.55
R21.2 Merge matched	15.40	2.27
R21.2 Merge matched after $E_{\mathrm{T}}^{\mathrm{miss}}$ suppression	17.49	2.99

9.5 Signal and background parameterization

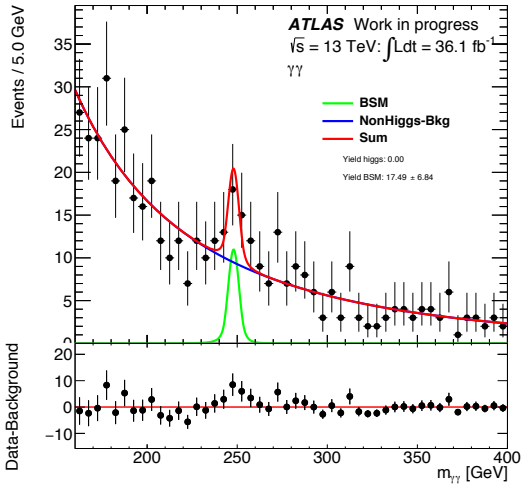
9.5.1 Signal parametrization

The signal parameterization is fairly straight forward in this analysis in that we simply use the A(400)→ZH(250) sample as a template where A is the mass of Axion and the resonance is 250. A DSCB function is used to obtain the shape and the parameters. Figure 9.4 shows the individual fit of DSCB parameters that is performed where the width (CB) of a narrow-width signal from MC shape is 2.74 GeV. This inclusive category shape will be used to do the final fit which will result in a conservative significance. The signal resolution uncertainty is found to be



(a)

(b)



(c)

Figure 9.3: The excess after the full event selection and merging in the case of (a) R20, (b) R21 and (c) matched. The fit mass is fixed at 248 GeV and narrow width assumption is considered in all cases. Peaks around 248 GeV are observed in all cases except in the case of the EESS category where the peak seems to have shifted slightly [16].

approximately 7% while the signal mass scale uncertainty is approximately 0.6% of 250. The uncertainty obtained will essentially be used in the final fit.

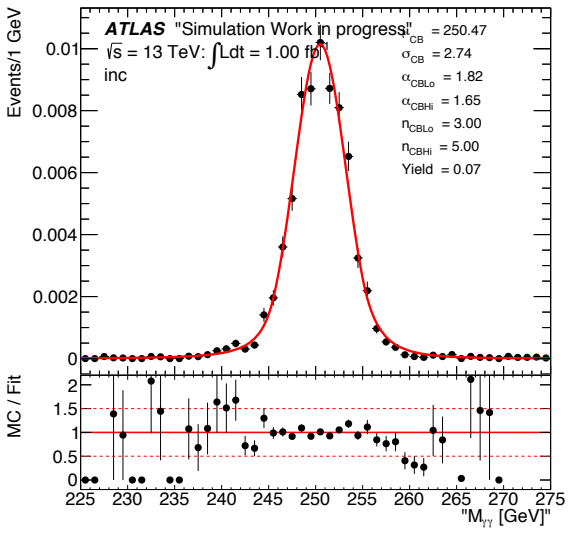


Figure 9.4: Results of individual fit of DCSB parameters, where μ_{CB} can be slightly shifted in the final S+B fit. The MC sample used is A(400)→ZH(250) [16].

9.5.2 Background parametrization

The nominal background shape has three components:

- $\gamma\gamma$
- $V\gamma$ and $V\gamma\gamma$
- jj, γj and jγ

The fraction of $\gamma\gamma$, jj, γj and jγ are obtained from a data driven (2×2D method) using the side-bands of the data not passing the photon ID or isolation. Since we finally report a single fit from a merge of the three categories, each category shape needs to be taken into account. The non-EE and EESS categories have a similar shape which can be perfectly described by the dijet function (FKO function) while that of the EEOS is quite different. A predicament would arise in the case where there is a large fraction of EEOS background which would most likely distort the merged background. A good merge is ensured by employing a re-weighting method. Due to a lack of statistics after the selections, inclusive events without $E_{\mathrm{T}}^{\mathrm{miss}}$ cuts were used. The MC shapes from the three categories were obtained and normalized to the yields in each category

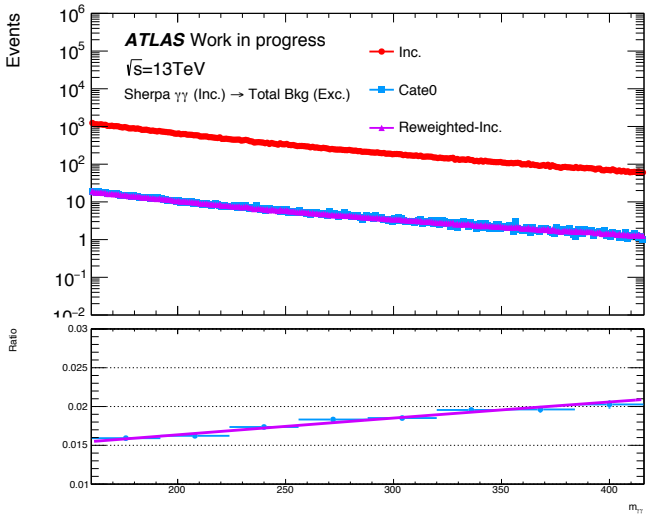


Figure 9.5: Re-weighting strategy from inclusive (nonEE 2 jet + EE 1 jet) Sherpa $\gamma\gamma$ MC events to signal region total background shape. By fitting the ratio between two histograms.

then merged to obtain the final one. In order to gauge the difference between the $m_{\gamma\gamma}$ shape without the cuts and that with cuts, a ratio plot is necessary. Figure 9.5 shows such a ratio plot which reflects the discrepancies and a linear function is used to derive the difference. Finally, the MC shape without the $E_{\mathrm{T}}^{\mathrm{miss}}$ cuts is taken and corrected using the linear function and in turn normalized to the actual number of events in each category then finally merged and input into the spurious signal studies.

As discussed in Section 8.6.2, various function forms are tested as shown in Table 9.5 and it is observed that the regular dijet function (FKO) works well with the merged background. The ratio of the fitted spurious signal yield to its uncertainty for the background models as a function of the resonance mass is shown in Figure 9.6. Several variations done to check the stability of this function choice are documented in the Supporting note in Reference [16]. The conclusion is that the FK0 function is always the best function passing spurious signal criteria with purity, EEOS fraction or signal shape variations. The most important variation is to change the fraction of EEOS events by $\pm$ 15% in the background templates, which introduces a +0.08-1.57 uncertainty on the maximum spurious signal but does not the function decision.

Table 9.5: Fitted spurious signal yield to its uncertainty, spurious signal yield and fit properties of tested functions. The spurious signal yield is normalized to 79.9 fb^{-1}.

Function	**max S/δS**	**max S**	**Npar**	**χ^2/ndof**	**Prob(χ^2)**	**Fit Range**	**Status**
ExpPoly2	-18.3%	-1.59	2	0.69	100%	170-410GeV	Pass
Bern3	52.5%	7.42	3	2.62	0%	170-410GeV	Fail
FK0	-12.6%	-1.10	2	0.55	100%	170-410GeV	Pass and Selected
ExpPoly2	-13.4%	-1.18	2	0.62	100%	180-360GeV	Pass
Bern3	19.6%	2.12	3	0.76	99.3%	180-360GeV	Pass
FK0	-11.0%	1.03	2	0.58	100%	180-360GeV	Pass and Selected

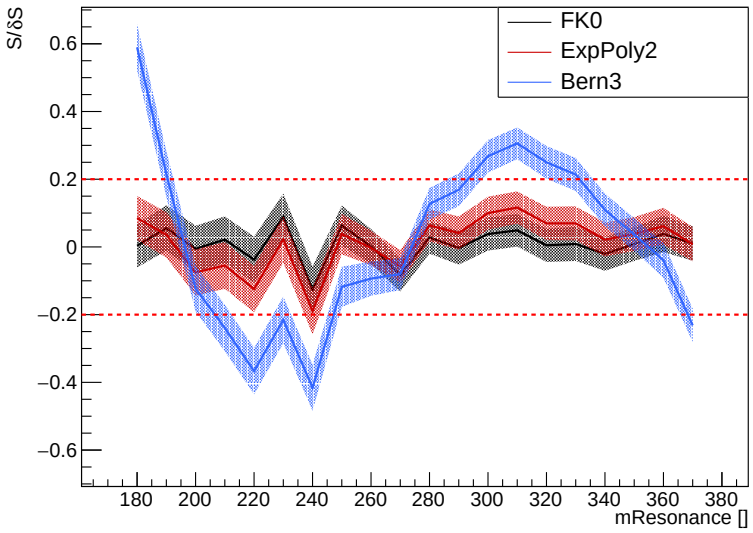


Figure 9.6: Ratio of the fitted spurious signal yield to its uncertainty for the background models as a function of the resonance mass.

9.6 Results

The statistical approach used in this study follows closely to all the previous missing energy studies. The nominal fit is performed at $m_H = 248$ GeV and the default natural width of the signal is set to 0. A signal resolution of 2.75 GeV is used for the merged category, ignoring the mixing of the different resolutions of the categories. The signal resolution is the resolution of the peak at $m_H = 248$ GeV, obtained from the signal parametrization. The resolution and scale uncertainties from the photons are considered, as well as the spurious signal uncertainties from the background. The fit result on the merged category is shown in Figure 9.7 and the

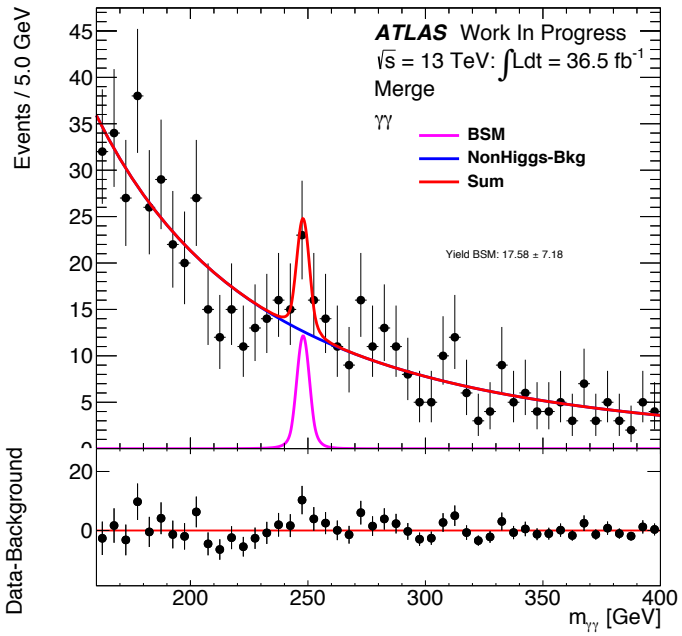


Figure 9.7: Individual fit at $m_X = 248$ GeV for the merged category with 0 width assumption using 2015+2016 data for the $\gamma\gamma + E_{\mathrm{T}}^{\mathrm{miss}}$ [16].

scanned local p-values are shown in Figure 9.8. A toy MC test is performed to obtain the global significance for the 2015+2016 data for each mass point as an example. The global observables are randomized. This is to test the look elsewhere effect due to the scanning mass range and resolution variation with the constraint of nuisance parameter, as shown in Figure 9.9a. The global p-value considering the mass scan only is also shown in Figure 9.9b. The difference between the two figures is due to the look elsewhere effect accounted to the resolution, which gives a degradation of 0.1 σ.

From the previous R20 2015+2016 dataset we are aware that the best mass point is 248 GeV therefore, there is no need to scan the entire mass range. Since we already know that the signal mass point is about 248 GeV, the look-elsewhere-effect is not strong when we look at the 2017 $\gamma\gamma$ data or the $Z\gamma$ data. Only the local and global p-value on the merged category will be reported because there is no suitable model for the simultaneous fit over categories. However, for checking the excess yields distribution, a rough fit on the single categories for a reference are done and the results are shown in the Supporting note in Reference [16]. In addition, due to

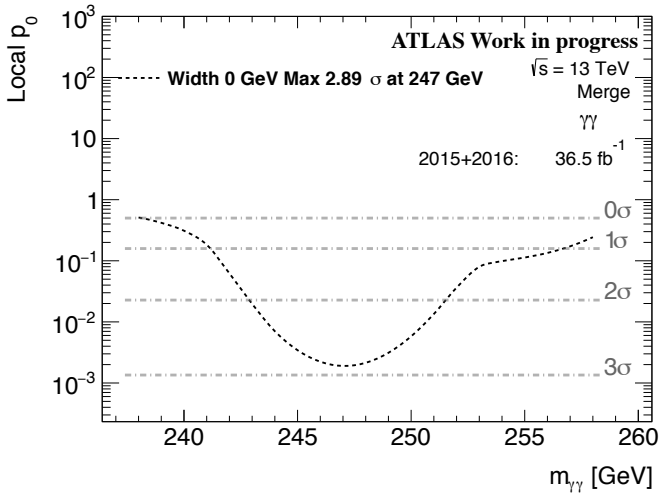
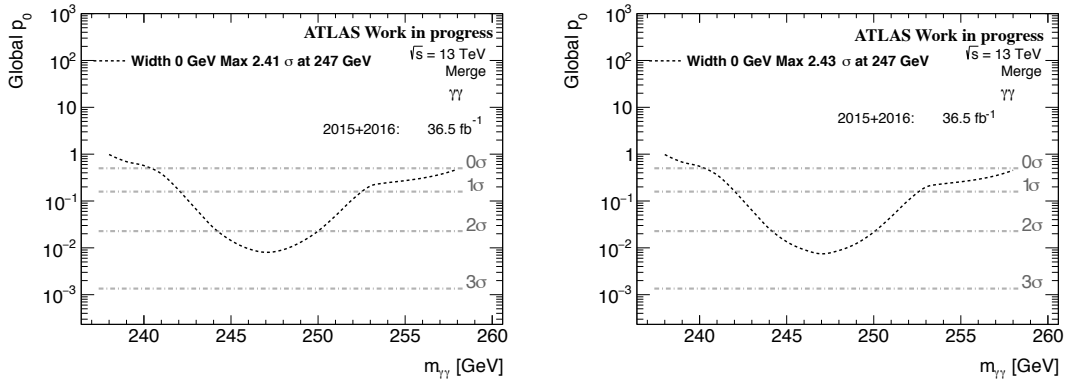


Figure 9.8: Local p_0 value scan as a function of mass for the merged category using 2015+2016 data for the $\gamma\gamma + E_{\mathrm{T}}^{\mathrm{miss}}$, where most of the excess is found around 247 GeV with a maximum local significance of 2.89 σ [16].

the shortage of a suitable branching ratio and model to unify the $\gamma\gamma$ 2015+2016+2017 data and $Z\gamma$ 2015+2016+2017 data, a simultaneous fit cannot be done. Under the circumstances, the local significance corresponding to the two channels are added in quadrature and if any mass point within the 248 ± 10 GeV exceeds the 3 σ local significance, this will yield a publication. In such a publication, only the individual significance corresponding to each analysis would be reported.

For the $\gamma\gamma + E_{\mathrm{T}}^{\mathrm{miss}}$ analysis, the local p_0 value scan as a function of mass for the merged category using 2015+2016 data is shown in Figure 9.8. Most of the excess is found around approximately 247 GeV with a maximum local significance of 2.89 σ. Figure 9.9a shows the global p_0 value scan as a function of mass, considering both mass shift and the resolution variation. A maximum global significance of 2.41 σ is reported. Figure 9.9b shows the global p_0 value scan as a function of mass, considering mass shift only, which yields a maximum global significance of 2.43 σ. The individual fit at $m_X = 248$ GeV for the merged category with 0 width assumption using 2017 data after the unblinding approval is shown in Figure 9.10. The p_0 value scans as a function of mass for the merged category using 2017 data are shown in Figure 9.11. Figure 9.11a shows the local p_0 value scan, where most of the excess is found around 245 GeV with a maximum significance of 1.85 σ. Figure 9.11b shows the global p_0



(a) (b)

Figure 9.9: Global p_0 value scans as a function of mass for the merged category using 2015+2016 data. (a) Considering both mass shift and the resolution variation and (b) mass shift only, for the $\gamma\gamma + \boldsymbol{E}_{\mathrm{T}}^{\mathrm{miss}}$. Most of the excess is found around 247 GeV with a maximum global significance of 2.41 σ and 2.43 σ, respectively [16].

value scan, where most of the excess is found around 245 GeV with a maximum significance of 1.85 σ. The 2015+2016+2017 combination p_0 value scans as a function of mass are shown in Figure 9.12. Figure 9.12a shows the local p_0 value scan, where most of the excess is found around 246 GeV with a maximum significance of 3 σ. Figure 9.12b shows the global p_0 value scan, where most of the excess is found around 246 GeV with a maximum significance of 2.5 σ.

In the case of the $Z\gamma + \boldsymbol{E}_{\mathrm{T}}^{\mathrm{miss}}$ analysis, the fit result on the merged category for 2015+2016+2017 unblinded data is shown in Figure 9.13. Most of the excess is found around approximately 252 GeV with a maximum local significance of 4.14 σ and global significance of 3.41 σ. Figure 9.14 shows the local p-value scans over the years of data taking.

9.7 Conclusions

A search for a resonance in the diphoton decay channel with a $\boldsymbol{E}_{\mathrm{T}}^{\mathrm{miss}}$ signature has been presented [15, 16]. In Section 8.4, the excess with a diphoton invariant mass around 248 GeV was analyzed using Run 1 and Run 2 data using ATLAS R20, and the ≥2-jet case had the largest observed excess. The likelihood fits on the diphoton mass distribution for the 248 GeV resonant mass reflected a maximum significance in the 2 central jets category. To add on, in the

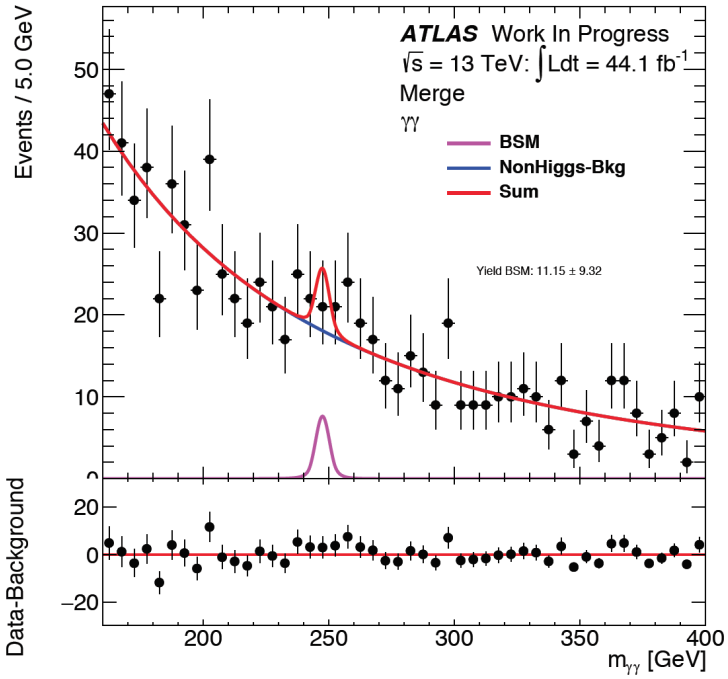
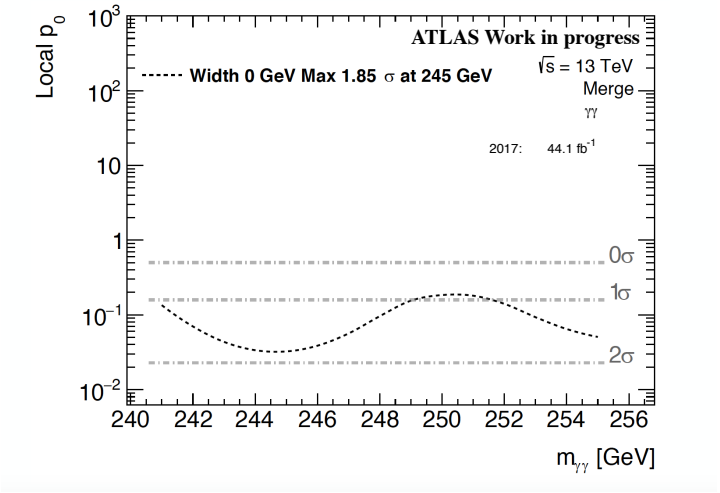


Figure 9.10: The individual fit at $m_X = 248$ GeV for the merged category with 0 width assumption using 2017 data after unblinding approval for the $\gamma\gamma + E_{\mathrm{T}}^{\mathrm{miss}}$ [16].

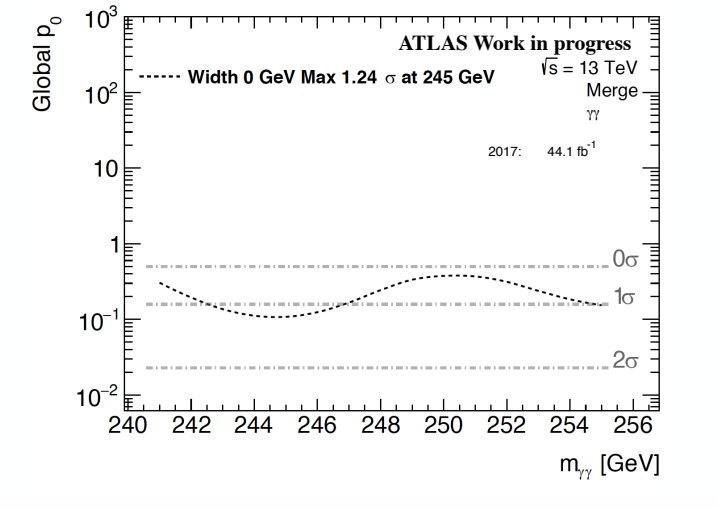
resulting p_0 value scans, the largest deviation from the background only hypothesis is observed in the at least 2 central jets category.

The same analysis was redone using ATLAS R21 and documented in the resonance search new supporting note [16], and summarized in this chapter. The excess checks indicate that categorizing into EEOS and EESS has a notable significance and a migration of signal events to the 1 central jet category is also observed. Additional background suppression variables have been implemented in an effort to suppress fake $E_{\mathrm{T}}^{\mathrm{miss}}$ events to ensure a clear and maximum significance after categorization. These suppression variables were approved by the Jet $E_{\mathrm{T}}^{\mathrm{miss}}$ group. After the full selection, there are discrepancies observed between R20 and R21 which are accounted to fake $E_{\mathrm{T}}^{\mathrm{miss}}$ due to the mis-calibration in R20. These selection cuts were extrapolated to the $Z\gamma + E_{\mathrm{T}}^{\mathrm{miss}}$ analysis.

For the $H(\rightarrow \gamma\gamma) + E_{\mathrm{T}}^{\mathrm{miss}}$ analysis, after unblinding 2017 data and combining 2015, 2016 and 2017 datasets, most of the excess is found around approximately 246 GeV with a maximum



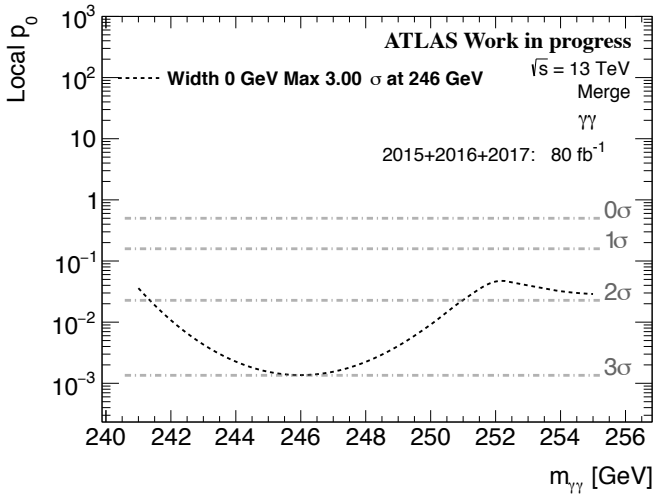
(a)



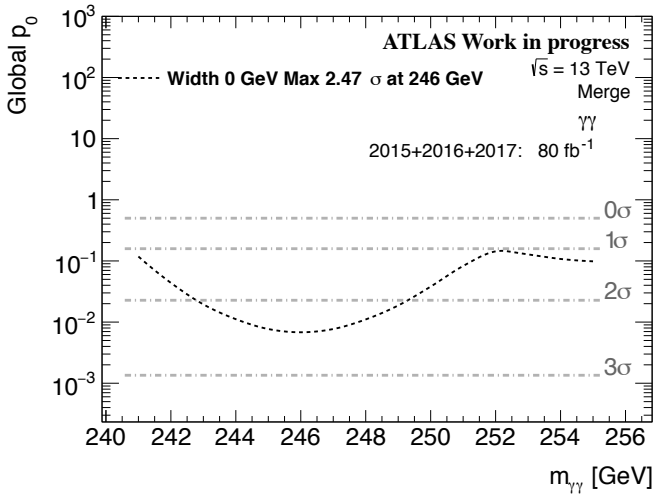
(b)

Figure 9.11: (a) The local p_0 value scans as a function of mass for the merged category using 2017 data and (b) the global p_0 value scans as a function of mass for the merged category using 2017 data for the $\gamma\gamma + \boldsymbol{E}_{\mathrm{T}}^{\mathrm{miss}}$ final state. Most of the excess is found around 245 GeV with a maximum local significance of 1.85 σ and maximum global significance of 1.24 σ, respectively [16].

local significance of 3 σ and a maximum global significance of 2.5 σ. On the other hand, for the $Z\gamma$ case, most of the excess is found around approximately 252 GeV with a maximum local significance of 4.14 σ and global significance of 3.41 σ over the years 2015+2016+2017 of data taking [186].



(a)



(b)

Figure 9.12: (a) The local p_0 value scans as a function of mass for the merged category using 2015+2016+2017 data and (b) the global p_0 value scans as a function of mass for the merged category using 2015+2016+2017 data for the $\gamma\gamma + E_{\mathrm{T}}^{\mathrm{miss}}$ final state. Most of the excess is found around 246 GeV with a maximum local significance of 3 σ and maximum global significance of 2.5 σ, respectively [16].

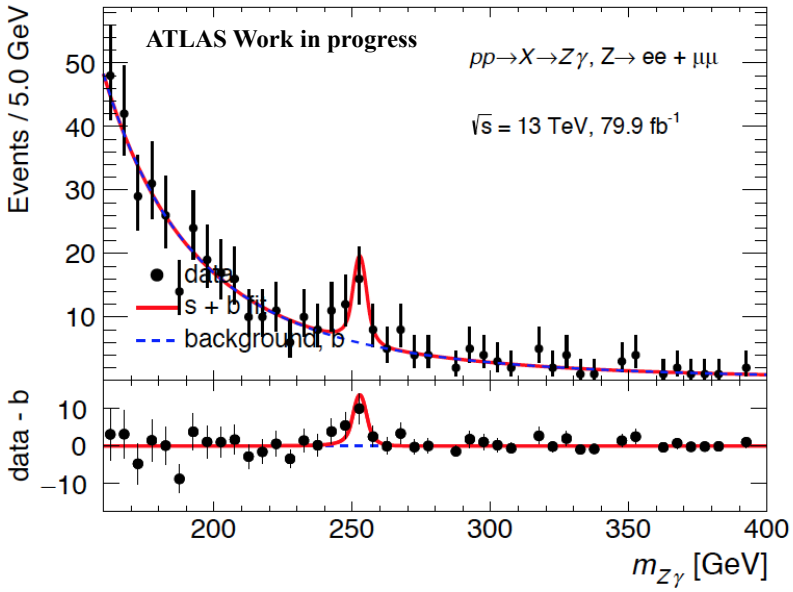


Figure 9.13: The individual fit at $m_X = 248$ GeV for the merged $ee + \mu\mu$ category using 2015+2016+2017 data after unblinding approval for the $Z\gamma + E_{\mathrm{T}}^{\mathrm{miss}}$ analysis. Most of the excess is found around 252 GeV with a maximum local significance of 4.14 σ and a maximum global significance of 3.41 σ [186].

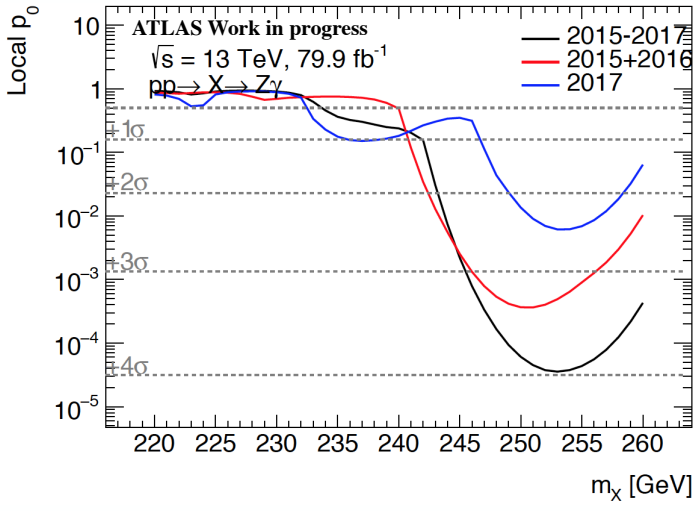


Figure 9.14: The local p_0 value scans as a function of mass for the various years of data taking (2015+2016+2017) for the $Z\gamma + E_{\mathrm{T}}^{\mathrm{miss}}$ analysis. Most of the excess is found around 252 GeV with a maximum local significance of 4.14 σ and a maximum global significance of 3.41 σ [186].

CHAPTER 10

CONCLUSIONS

"I am quite surprised that it happened during my lifetime. It is nice to be right about something sometimes" - Peter Higgs on CERN when scientists detected the Higgs boson particle

The discovery of the Higgs boson by both the ATLAS and CMS experiments back in 2012 provides us with a tool to probe physics beyond the Standard Model. As the last missing piece of the SM of particle physics, the Higgs discovery justified the SM. However, it is clear that the SM is incomplete, as it does not describe a number of phenomena in nature. As discussed in Section 1.1, the SM does not encompass gravity nor account for the DM that constitutes a large fraction of the mass in the universe. With the Higgs mechanism being the attribute that allows us to understand how particles acquire mass as discussed in Section 1.3, a new realm of possibilities was unraveled. This opens up extensions to the SM which could assist us in unveiling answers to the underlying questions we still have about our universe, what is known today as BSM physics. All the research documented in this thesis looks into this realm of BSM physics with the intent to use scientific knowledge and tools to understand our universe further.

This thesis comprises a section on instrumentation and two main analyses, which are centered around the Madala hypothesis that was detailed in Section 1.4. Under instrumentation, a comparative study is done in an effort to assist in the upgrade of the Tile Calorimeter

of the ATLAS detector. With the intention to replace the Tile Calorimeter gap and MBTS scintillators with more radiation resistant ones, several different grades of plastic scintillators were considered for the study. The samples were irradiated with low energy protons and their transmission spectra were analyzed. Among them all, it was found that the EJ 200 polyvinyl toluene (PVT) based polymer provided by ELJEN technologies is the most radiation hard. Light transmission studies showed that following radiation exposure, this sample showed a small decrease in light transmission in comparison to other samples. In addition, this plastic scintillator grade also showed the most annealing after being irradiated using doses closest to those within the ATLAS detector.

The ATLAS physics analyses documented in this thesis involve photons in final states with associated missing transverse energy. These searches for new physics use data collected with the ATLAS detector in 2015, 2016 and 2017. $\boldsymbol{E}_{\mathrm{T}}^{\mathrm{miss}}$ is a key signature for BSM physics emphasizing its importance at the LHC. Numerous $\boldsymbol{E}_{\mathrm{T}}^{\mathrm{miss}}$ reconstruction performance checks have been done in the course of these searches as documented in Chapter 6. Through these important studies, fake $\boldsymbol{E}_{\mathrm{T}}^{\mathrm{miss}}$ suppression methods have been implemented, namely the SV method, which has been approved by ATLAS and is used to improve the quality of the results of our analyses. All the $\boldsymbol{E}_{\mathrm{T}}^{\mathrm{miss}}$ checks ensure the stability of $\boldsymbol{E}_{\mathrm{T}}^{\mathrm{miss}}$ reconstruction at ATLAS, which is useful to not only the analyses in this thesis, but to several other analyses at ATLAS.

A search for a Higgs boson decaying to two photons in association with $\boldsymbol{E}_{\mathrm{T}}^{\mathrm{miss}}$ has been presented in Chapter 7. No significant excess over the expected background is observed for a Madala boson of mass $m_H = 270\,\mathrm{GeV}$ and a DM particle of 50 (60) GeV. With the benchmark assuming 100% branching ratio, other decay channels with leptonic final states are currently being explored by colleagues within the Wits Institute for Collider Particle Physics group. In the process of searching for particles in the context of the Madala hypothesis, an excess with a diphoton invariant mass of approximately 248 GeV was observed. In an effort to explore this excess, Chapters 8 and 9 discuss the direct decay of H to photons in the search for such a resonance in association with $\boldsymbol{E}_{\mathrm{T}}^{\mathrm{miss}}$. Data collected during Run 1 and Run 2 data taking periods was used to analyze this possible excess. The analysis was done using both ATLAS R20 and R21, and the search has been extrapolated to the $Z\gamma$ channel. Corresponding supporting

documents have already been reviewed by the analysis group conveners and the unblinding approval has already been held. The $\gamma\gamma + E_{\mathrm{T}}^{\mathrm{miss}}$ analysis 2017 data was unblinded and the 2015+2016+2017 combination scans show that most of the excess is found around 246 GeV with a maximum local significance of $3\,\sigma$ and a maximum global significance of $2.47\,\sigma$. On the other hand, for the $Z\gamma + E_{\mathrm{T}}^{\mathrm{miss}}$ case, most of the excess is found around approximately 252 GeV with a maximum local significance of $4.14\,\sigma$, which is the result of the local p-value scans over the years 2015+2016+2017 of data taking. The maximum global significance is given by $3.41\,\sigma$ over the years 2015+2016+2017 of data taking.

The future looks promising for the Madala hypothesis, in fact, multi-lepton final states are being explored in this regard. It goes without saying that as we explore further, we get closer and closer to understanding the Madala hypothesis. Run 3 of data taking is anticipated to begin in 2021 with luminosities reaching up to $300\,\mathrm{fb}^{-1}$, which will lead to larger collected data and an enhanced sensitivity to new physics. Run 4 will begin in 2024 and will feature the installation of the High Luminosity LHC (HL-LHC), also enhancing the possibility of new discoveries. It will be interesting to see the evolution of the understanding of the Madala hypothesis with the collection of more data over these years.

APPENDIX A

A COMPARATIVE STUDY OF THE RADIATION HARDNESS OF PLASTIC SCINTILLATORS FOR THE UPGRADE OF THE TILE CALORIMETER AT ATLAS

A.1

In aid of the comparative study of the radiation hardness of plastic scintillators for the upgrade of the Tile Calorimeter at ATLAS Chapter 3. Figure A.1 shows the detailed diagram of the internal components of the Varian Cary 500 spectrophotometer used in the light transmission studies discussed in Section 3.4.2.

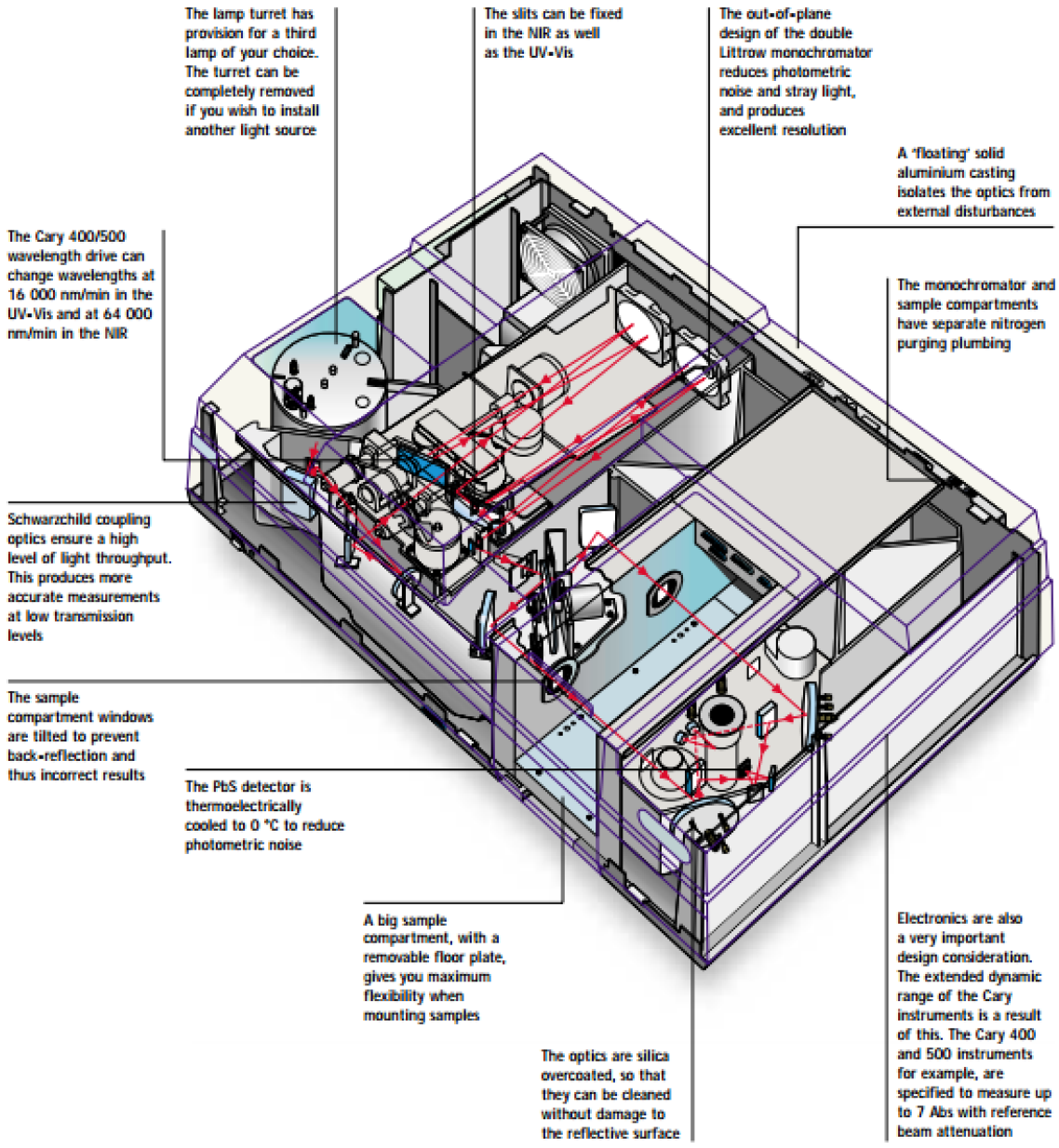


Figure A.1: Detailed diagram of the internal components of the Varian Cary 500 spectrophotometer used for transmission spectroscopy studies.

APPENDIX B

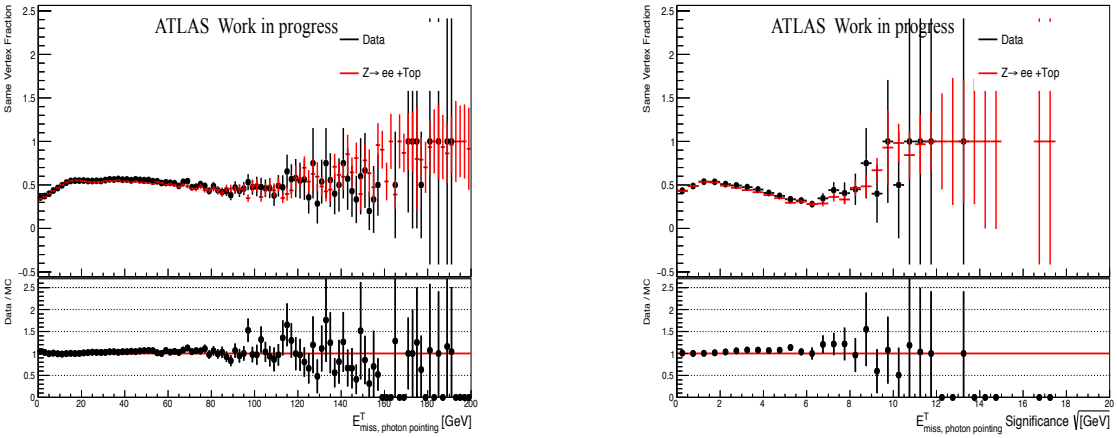
PERFORMANCE OF $E_{\mathrm{T}}^{\mathrm{MISS}}$ RECONSTRUCTION COMPLEMENTARY MATERIAL

B.1

In aid of the $\boldsymbol{E}_{\mathrm{T}}^{\mathrm{miss}}$ validation of the photon pointing method in Section 6.3.1. Figure B.1 shows the comparison of the photon pointing same vertex fraction of $\boldsymbol{E}_{\mathrm{T}}^{\mathrm{miss}}$ between data and MC in the $Z \to e^+e^-$ control region. The distributions correspond to $\boldsymbol{E}_{\mathrm{T}}^{\mathrm{miss}}$ and $\boldsymbol{E}_{\mathrm{T}}^{\mathrm{miss}}$ significance, respectively and good agreement between data and MC is observed.

B.2

In support of the 2017 data and Sherpa $\gamma\gamma$ MC $\boldsymbol{E}_{\mathrm{T}}^{\mathrm{miss}}$ performance studies in Section 6.3.6. Figure B.2 shows the general $\boldsymbol{E}_{\mathrm{T}}^{\mathrm{miss}}$ and $\boldsymbol{E}_{\mathrm{T}}^{\mathrm{miss}}$ significance distributions for events passing $160\,\mathrm{GeV} < m_{\gamma\gamma} < 400\,\mathrm{GeV}$ and split into 0-jet case, 1-jet case and ≥2-jet case.



(a) (b)

Figure B.1: The comparison of the photon pointing same vertex fraction of $E_{\mathrm{T}}^{\mathrm{miss}}$ between data and MC in the $Z \to e^+e^-$ control region. Distributions correspond to (a) $E_{\mathrm{T}}^{\mathrm{miss}}$ and (b) $E_{\mathrm{T}}^{\mathrm{miss}}$ significance. Good agreement between data and MC is observed [6].

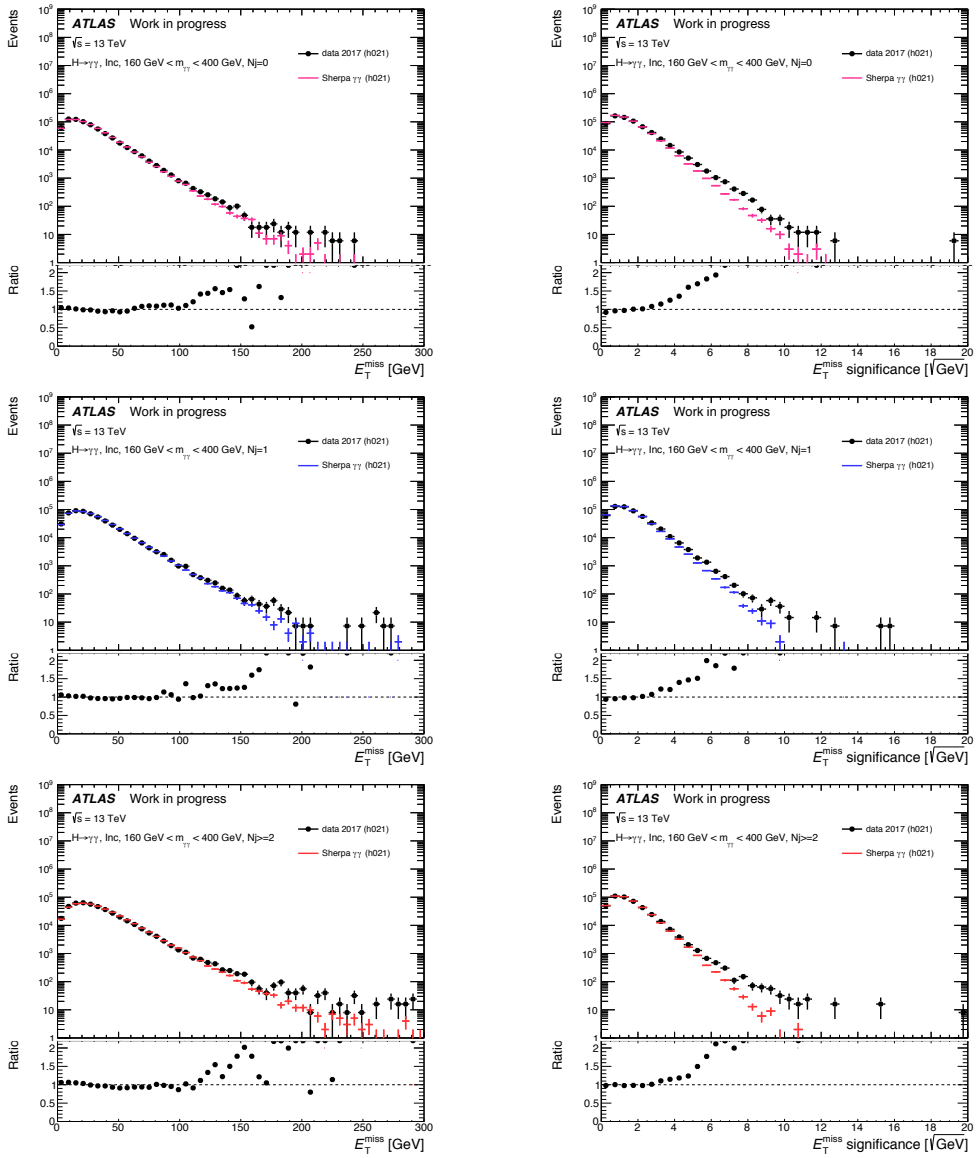


Figure B.2: $E_{\mathrm{T}}^{\mathrm{miss}}$ and $E_{\mathrm{T}}^{\mathrm{miss}}$ significance distributions for 2017 data corresponding to 43.8 fb^{-1} versus Sherpa $\gamma\gamma$, where the top distributions are for the 0-jet case, the middle row corresponds to the 1-jet case and the bottom row corresponds to the ≥2-jet case. These are all inclusive, that is, not split into same vertex or different vertex cases. The MC have been normalized to the total number of events in the inclusive sample of the data [16].

APPENDIX C

SEARCH FOR THE HIGGS BOSON IN ASSOCIATION WITH $E_{\mathrm{T}}^{\mathrm{MISS}}$ IN THE DIPHOTON CHANNEL

C.1

In support of the signal parametrization discussed in Section 7.5.1, Figure C.2 shows the results of a single fit of a DSCB function (lines) for a signal with m_h = 125 GeV where all heavy-scalar processes are summed. The signal mass distribution is modelled from MC simulations as the sum of a DSCB function for the all the categories summarized in Table 7.2.

C.2

In the case of the spurious signal studies, using all the SM Higgs and heavy scalar signal MC at value of m_h = 125 GeV, we estimate a signal model that is parametrized as a function of Higgs mass. The different fits on a signal with m_h = 125 GeV using 13 TeV MC simulation are shown in Figure C.2.

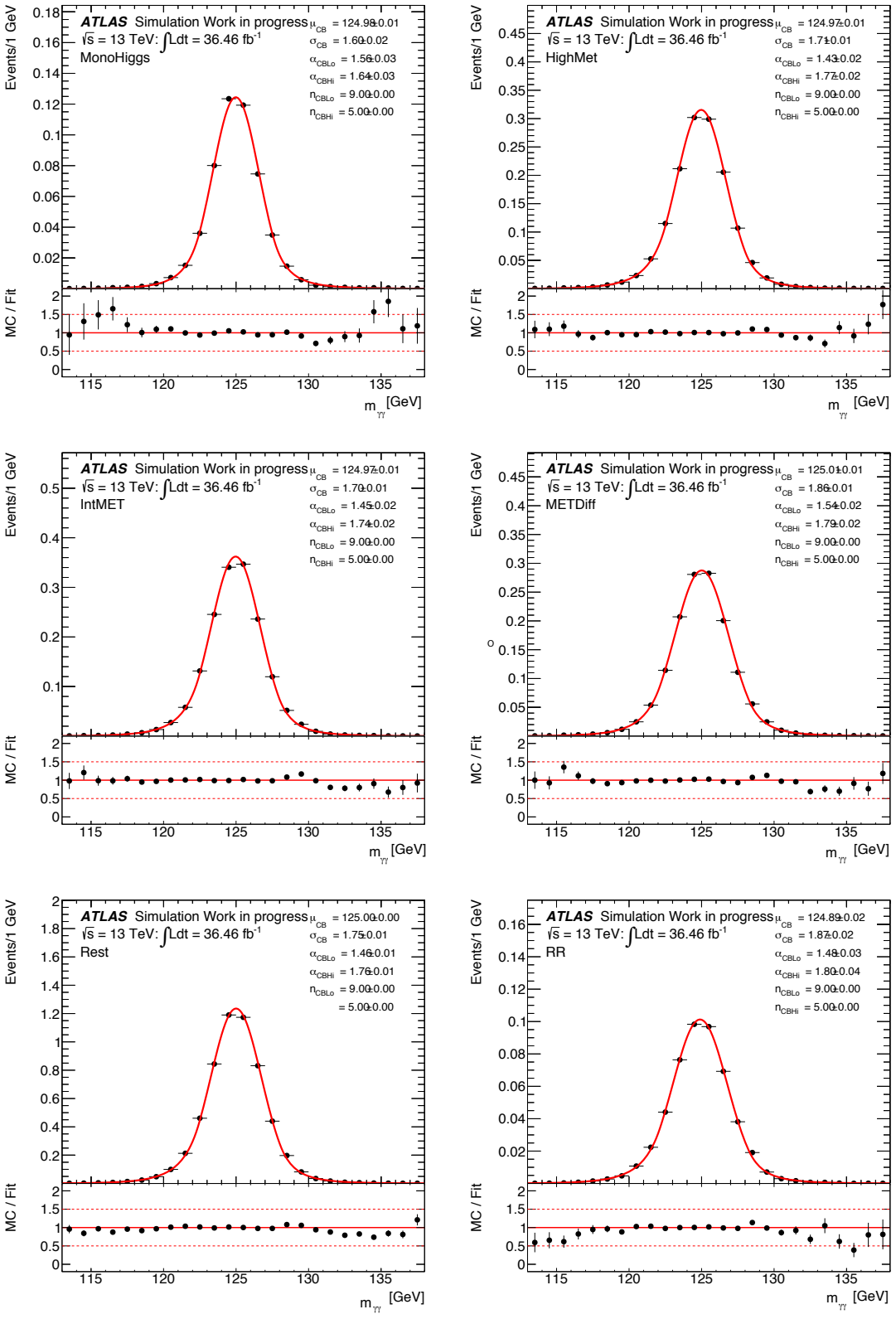


Figure C.1: The results of a single fit of a DSCB function (lines) for a signal with m_h = 125 GeV where all heavy-scalar processes are summed [6].

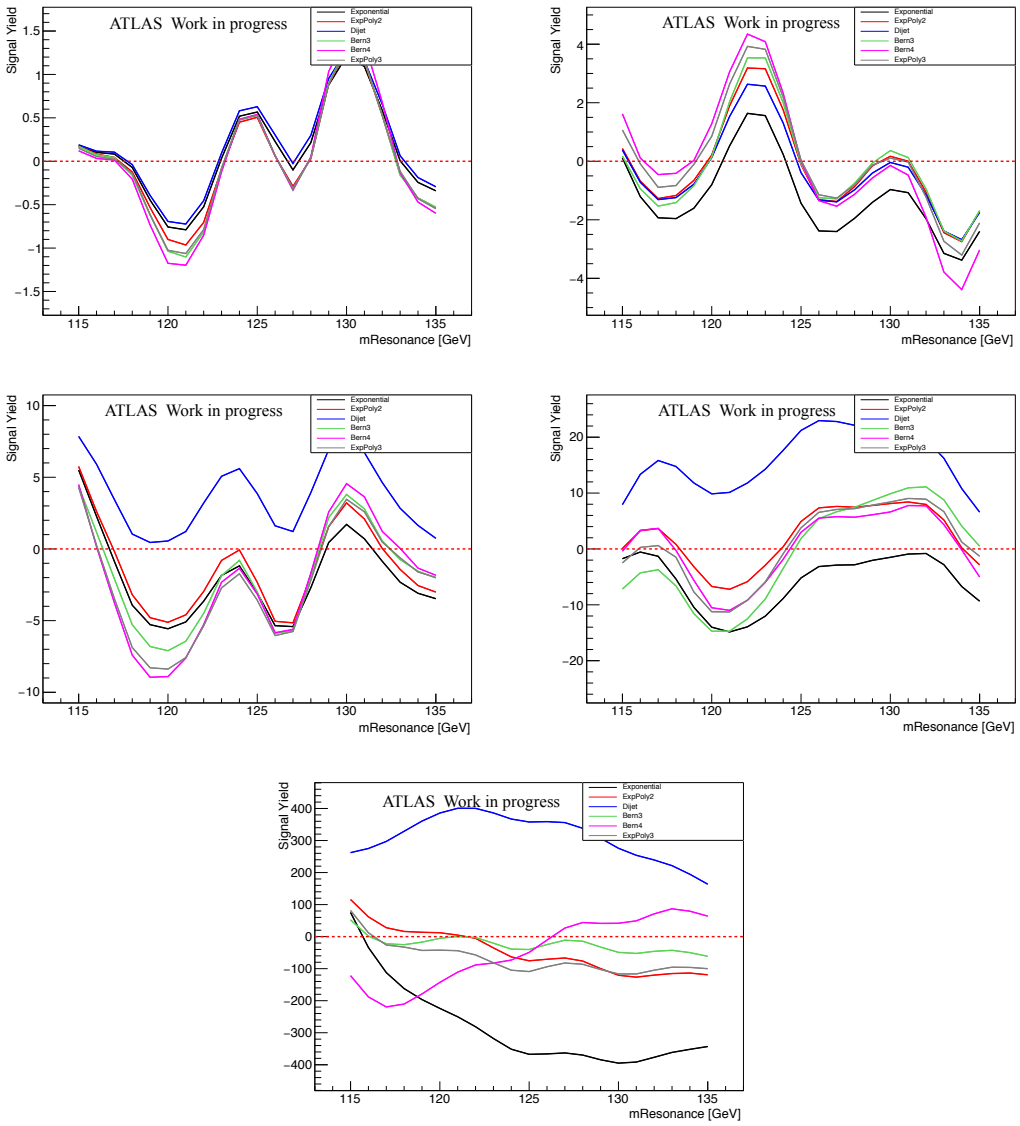


Figure C.2: The spurious signal results of the direct fit method. First row: left corresponds to the mono Higgs category, right, high-$\boldsymbol{E}_{\mathrm{T}}^{\mathrm{miss}}$ category. Second row: left corresponds to the intermediate-$\boldsymbol{E}_{\mathrm{T}}^{\mathrm{miss}}$ category and the right, different vertex category. Third row, rest category [6].

Table C.1: The experimental systematic terms derived from the MxAOD, on the heavy scalar model corresponding to m_H = 275 GeV and m_χ = 60 GeV for the Mono Higgs category [6].

Systematic name	**Magnitude Up (%)**	**Magnitude Down (%)**
EG_RESOLUTION_ALL	+ 0.1	-0.7
EG_SCALE_ALL	+ 1.4	-0.5
JET_BJES_Response	+ 0.0	-0.0
JET_EffectiveNP_1	+ 2.7	-4.4
JET_EffectiveNP_2	+ 1.8	-2.8
JET_EffectiveNP_3	+ 1.2	-1.0
JET_EffectiveNP_4	+ 0.1	-0.1
JET_EffectiveNP_6restTerm	+ 0.1	-0.4
JET_EtaIntercalibration_Modelling	+ 2.0	-2.4
JET_EtaIntercalibration_NonClosure	+ 0.5	-0.2
JET_EtaIntercalibration_TotalStat	+ 0.8	-1.1
JET_Flavor_Composition	+ 2.9	-5.1
JET_Flavor_Response	+ 1.9	-1.1
JET_JER_SINGLE_NP	+ 0.6	-0.6
JET_Pileup_OffsetMu	+ 0.4	-0.3
JET_Pileup_OffsetNPV	+ 0.4	-0.9
JET_Pileup_PtTerm	+ 0.0	-0.4
JET_Pileup_RhoTopology	+ 0.9	-1.4
JET_PunchThrough_MC15	+ 0.0	-0.0
JET_SingleParticle_HighPt	+ 0.0	-0.0
MET_JetTrk_Scale	+ 0.0	-0.0
MET_SoftTrk_ResoPara	+ 0.5	-0.5
MET_SoftTrk_ResoPerp	+ 0.2	-0.2
MET_SoftTrk_Scale	+ 0.2	-0.4
PH_EFF_ID_Uncertainty	+ 4.2	-4.1
PH_EFF_TRKISO_Uncertainty	+ 1.1	-1.1
PH_Iso_DDonoff	+ 0.0	-0.0
PRW_DATASF	+ 2.0	-0.3

Table C.2: The experimental systematic terms derived from the MxAOD, on the heavy scalar model corresponding to $m_H = 275\,\text{GeV}$ and $m_\chi = 60\,\text{GeV}$ for the High-$E_{\text{T}}^{\text{miss}}$ category [6].

Systematic name	**Magnitude Up (%)**	**Magnitude Down (%)**
EG_RESOLUTION_ALL	+ 0.3	-0.3
EG_SCALE_ALL	+ 0.4	-1.1
JET_BJES_Response	+ 0.0	-0.0
JET_EffectiveNP_1	+ 3.1	-3.4
JET_EffectiveNP_2	+ 0.5	-0.1
JET_EffectiveNP_3	+ 0.5	-0.7
JET_EffectiveNP_4	+ 0.3	-0.2
JET_EffectiveNP_6restTerm	+ 0.4	-0.1
JET_EtaIntercalibration_Modelling	+ 2.4	-3.0
JET_EtaIntercalibration_NonClosure	+ 0.0	-0.4
JET_EtaIntercalibration_TotalStat	+ 1.1	-1.4
JET_Flavor_Composition	+ 5.2	-5.0
JET_Flavor_Response	+ 2.6	-2.3
JET_JER_SINGLE_NP	+ 2.7	-2.7
JET_Pileup_OffsetMu	+ 0.8	-2.4
JET_Pileup_OffsetNPV	+ 0.7	-1.8
JET_Pileup_PtTerm	+ 0.2	-0.3
JET_Pileup_RhoTopology	+ 1.4	-1.8
JET_PunchThrough_MC15	+ 0.0	-0.0
JET_SingleParticle_HighPt	+ 0.0	-0.0
MET_JetTrk_Scale	+ 0.0	-0.0
MET_SoftTrk_ResoPara	+ 1.7	-1.7
MET_SoftTrk_ResoPerp	+ 0.2	-0.2
MET_SoftTrk_Scale	+ 0.2	-0.8
PH_EFF_ID_Uncertainty	+ 4.3	-4.2
PH_EFF_TRKISO_Uncertainty	+ 1.2	-1.2
PH_Iso_DDonoff	+ 0.0	-0.0
PRW_DATASF	+ 1.3	-1.5

Table C.3: The experimental systematic terms derived from the MxAOD, on the heavy scalar model corresponding to $m_H = 275\,\mathrm{GeV}$ and $m_\chi = 60\,\mathrm{GeV}$ for the Intermediate-$E_{\mathrm{T}}^{\mathrm{miss}}$ category [6].

Systematic name	**Magnitude Up (%)**	**Magnitude Down (%)**
EG_RESOLUTION_ALL	+ 0.5	-0.2
EG_SCALE_ALL	+ 0.1	-0.9
JET_BJES_Response	+ 0.0	-0.1
JET_EffectiveNP_1	+ 2.4	-3.1
JET_EffectiveNP_2	+ 0.3	-0.4
JET_EffectiveNP_3	+ 0.5	-0.2
JET_EffectiveNP_4	+ 0.1	-0.1
JET_EffectiveNP_6restTerm	+ 0.2	-0.2
JET_EtaIntercalibration_Modelling	+ 1.2	-1.0
JET_EtaIntercalibration_NonClosure	+ 0.1	-0.1
JET_EtaIntercalibration_TotalStat	+ 0.6	-0.2
JET_Flavor_Composition	+ 2.2	-3.0
JET_Flavor_Response	+ 0.1	-0.2
JET_JER_SINGLE_NP	+ 2.5	-2.5
JET_Pileup_OffsetMu	+ 0.6	-0.6
JET_Pileup_OffsetNPV	+ 0.5	-0.0
JET_Pileup_PtTerm	+ 0.1	-0.1
JET_Pileup_RhoTopology	+ 0.4	-0.2
JET_PunchThrough_MC15	+ 0.0	-0.0
JET_SingleParticle_HighPt	+ 0.0	-0.0
MET_JetTrk_Scale	+ 0.0	-0.0
MET_SoftTrk_ResoPara	+ 0.9	-0.9
MET_SoftTrk_ResoPerp	+ 0.7	-0.7
MET_SoftTrk_Scale	+ 1.2	-0.4
PH_EFF_ID_Uncertainty	+ 4.3	-4.2
PH_EFF_TRKISO_Uncertainty	+ 1.2	-1.2
PH_Iso_DDonoff	+ 0.0	-0.0
PRW_DATASF	+ 5.0	-4.2

Table C.4: The experimental systematic terms derived from the MxAOD, on the heavy scalar model corresponding to m_H = 275 GeV and m_χ = 60 GeV for the Different vertex category [6].

Systematic name	**Magnitude Up (%)**	**Magnitude Down (%)**
EG_RESOLUTION_ALL	+ 0.4	-0.2
EG_SCALE_ALL	+ 0.3	-0.7
JET_BJES_Response	+ 0.0	-0.0
JET_EffectiveNP_1	+ 4.0	-3.6
JET_EffectiveNP_2	+ 0.4	-0.6
JET_EffectiveNP_3	+ 0.6	-0.3
JET_EffectiveNP_4	+ 0.2	-0.5
JET_EffectiveNP_6restTerm	+ 0.0	-0.0
JET_EtaIntercalibration_Modelling	+ 2.9	-2.7
JET_EtaIntercalibration_NonClosure	+ 0.0	-0.3
JET_EtaIntercalibration_TotalStat	+ 1.6	-1.4
JET_Flavor_Composition	+ 5.4	-4.6
JET_Flavor_Response	+ 1.9	-2.1
JET_JER_SINGLE_NP	+ 2.0	-2.0
JET_Pileup_OffsetMu	+ 1.4	-1.7
JET_Pileup_OffsetNPV	+ 1.5	-1.1
JET_Pileup_PtTerm	+ 0.5	-0.1
JET_Pileup_RhoTopology	+ 1.5	-1.4
JET_PunchThrough_MC15	+ 0.0	-0.0
JET_SingleParticle_HighPt	+ 0.0	-0.0
MET_JetTrk_Scale	+ 0.0	-0.0
MET_SoftTrk_ResoPara	+ 2.0	-2.0
MET_SoftTrk_ResoPerp	+ 2.6	-2.6
MET_SoftTrk_Scale	+ 2.9	-2.0
PH_EFF_ID_Uncertainty	+ 4.3	-4.2
PH_EFF_TRKISO_Uncertainty	+ 1.3	-1.3
PH_Iso_DDonoff	+ 0.0	-0.0
PRW_DATASF	+ 3.9	-3.6

Table C.5: The experimental systematic terms derived from the MxAOD, on the heavy scalar model corresponding to m_H = 275 GeV and m_χ = 60 GeV for the Rest category [6].

Systematic name	**Magnitude Up (%)**	**Magnitude Down (%)**
EG_RESOLUTION_ALL	+ 0.0	-0.1
EG_SCALE_ALL	+ 0.2	-0.1
JET_BJES_Response	+ 0.0	-0.0
JET_EffectiveNP_1	+ 0.3	-0.5
JET_EffectiveNP_2	+ 0.3	-0.3
JET_EffectiveNP_3	+ 0.4	-0.2
JET_EffectiveNP_4	+ 0.1	-0.1
JET_EffectiveNP_6restTerm	+ 0.1	-0.1
JET_EtaIntercalibration_Modelling	+ 0.6	-0.7
JET_EtaIntercalibration_NonClosure	+ 0.1	-0.0
JET_EtaIntercalibration_TotalStat	+ 0.2	-0.2
JET_Flavor_Composition	+ 0.7	-0.8
JET_Flavor_Response	+ 0.3	-0.3
JET_JER_SINGLE_NP	+ 0.2	-0.2
JET_Pileup_OffsetMu	+ 0.2	-0.2
JET_Pileup_OffsetNPV	+ 0.1	-0.1
JET_Pileup_PtTerm	+ 0.0	-0.0
JET_Pileup_RhoTopology	+ 0.1	-0.1
JET_PunchThrough_MC15	+ 0.0	-0.0
JET_SingleParticle_HighPt	+ 0.0	-0.0
MET_JetTrk_Scale	+ 0.0	-0.0
MET_SoftTrk_ResoPara	+ 0.2	-0.2
MET_SoftTrk_ResoPerp	+ 0.5	-0.5
MET_SoftTrk_Scale	+ 0.7	-0.4
PH_EFF_ID_Uncertainty	+ 4.3	-4.2
PH_EFF_TRKISO_Uncertainty	+ 1.2	-1.2
PH_Iso_DDonoff	+ 0.0	-0.0
PRW_DATASF	+ 0.0	-0.1

APPENDIX D

SEARCH FOR A NEW RESONANCE IN THE DIPHOTON DECAY IN ASSOCIATION WITH $E_{\mathrm{T}}^{\mathrm{MISS}}$ COMPLEMENTARY MATERIAL

D.1

In support of SV tuning method discussed in Section 8.3, Figures D.1, D.2, D.3 and D.4 show the $E_{\mathrm{T}}^{\mathrm{miss}}$ distributions for various SV selection cuts and different jet multiplicity bins (0-jet, 1-jet and at least 2-jet cases) for to 2015+2016 data, $Wh125$, heavy scalar signal and mono-Higgs signals.

D.2

In support of excess checks discussed in Section 8.4, the excess in the cases where $S_{E_{\mathrm{T}}^{\mathrm{miss}}}$ $> 3.5\ \sqrt{\mathrm{GeV}}$ with b-tagged jets requirement, lepton requirement and photon barrel-endcap regions is also studied and are summarized in Table D.1 for the Run 2 data case. For all the fits in Figures D.5 and D.6 corresponding to Run 1 data, the mass and width are fixed to 248 GeV and σ = 2.3 GeV, respectively. In the Run 2 case, the width is fixed to σ = 2.7 GeV, represented by Figures 8.8 and 8.9.

Table D.1: Run 2 data significance and yield results for the scans of $S_{E_{\mathrm{T}}^{\mathrm{miss}}} > 3.5\ \sqrt{\mathrm{GeV}}$, SV case and with at least two central jets for: photons in Barrel-Barrel region (BB), Barrel-EndCap region (BE), EndCap-Barrel region (EB), EndCap-EndCap region (EE), number of b-tagged jets ≥1, number of b-tagged jets ≥2 and number of leptons ≥1, respectively [15].

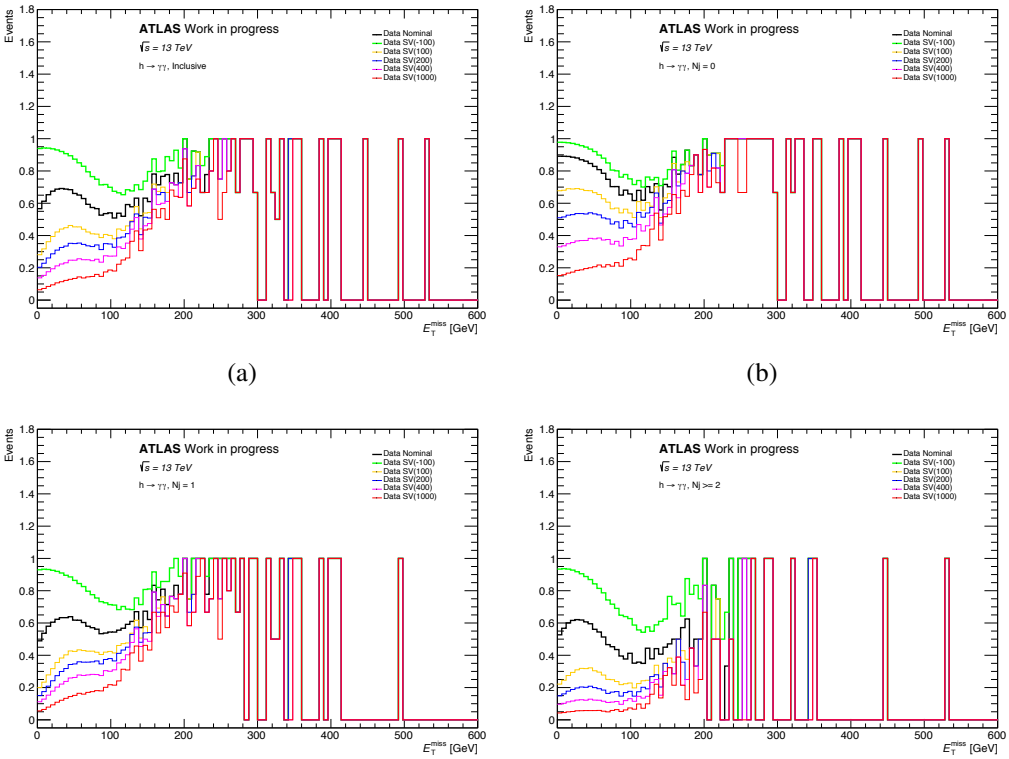
Cut	Vertex choice	Jet bin	Significance	Yield
$METSig > 3.5$	Nj>=2	ll	1.439	1.92233 ± 1.76216
$METSig > 3.5$	Nj>=2	Bj2	1.838	2.25681 ± 1.75662
$METSig > 3.5$	Nj>=2	Bj1	2.727	7.80981 ± 3.71192
$METSig > 3.5$	Nj>=2	BB	2.261	7.94249 ± 4.26112
$METSig > 3.5$	Nj>=2	BE	0.721	2.75997 ± 4.04816
$METSig > 3.5$	Nj>=2	EB	1.191	4.59421 ± 4.24516
$METSig > 3.5$	Nj>=2	EE	3.638	10.3048 ± 3.95841

The scans are done for $S_{E_{\mathrm{T}}^{\mathrm{miss}}} > 3.5\ \sqrt{\mathrm{GeV}}$, SV case and with at least two central jets for: photons in Barrel-Barrel region (BB), Barrel-EndCap region (BE), EndCap-Barrel region (EB), EndCap-EndCap region (EE), number of b-tagged jets ≥1, number of b-tagged jets ≥2 and number of leptons ≥1, respectively.

D.3

To supplement the results in this analysis (Section 8.8), the unbinned likelihood fits performed independently in categories 0, 1, 2 and 3 corresponding to the inclusive, 0-jet case, 1-jet case and ≥2-jet case are shown. Figures D.7 and D.8 the resulting p_0 value scans for all the categories. In addition, Figures D.9 shows the largest fitted significance for $S_{E_{\mathrm{T}}^{\mathrm{miss}}} > 3.2\ \sqrt{\mathrm{GeV}}$ and $S_{E_{\mathrm{T}}^{\mathrm{miss}}} > 3.5\ \sqrt{\mathrm{GeV}}$, respectively, with a floating fixed resonance mass.

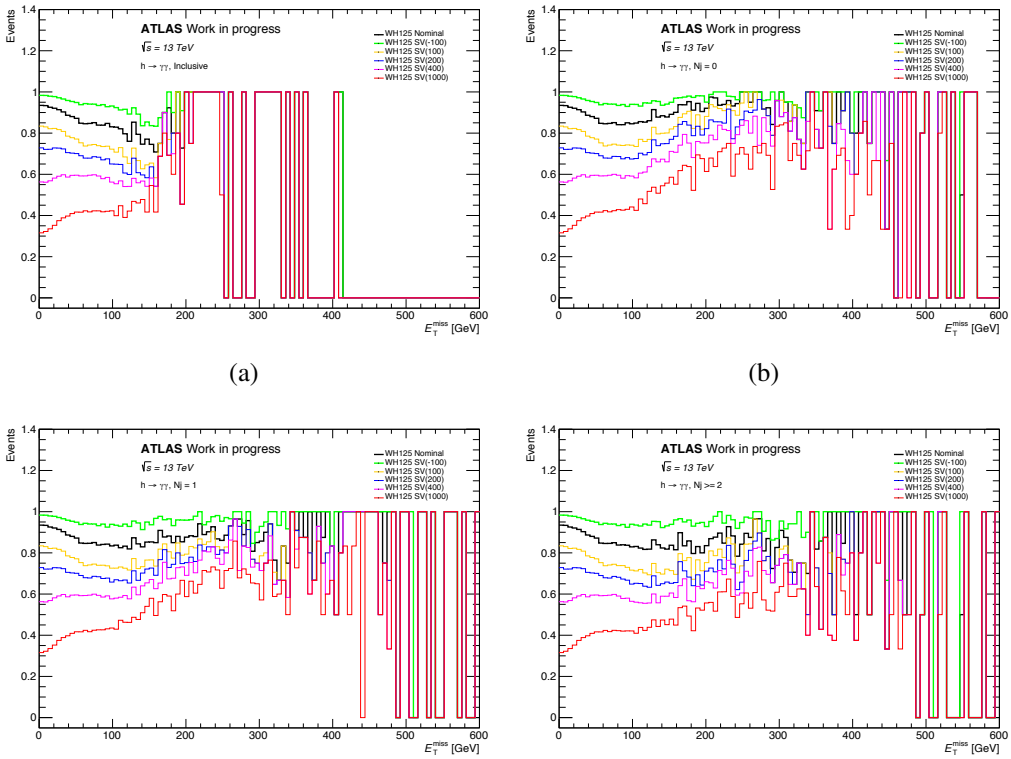
In support of Section 9.3, the excess fits corresponding to R20 are shown in Figure D.10.



(a) (b)

(c) (d)

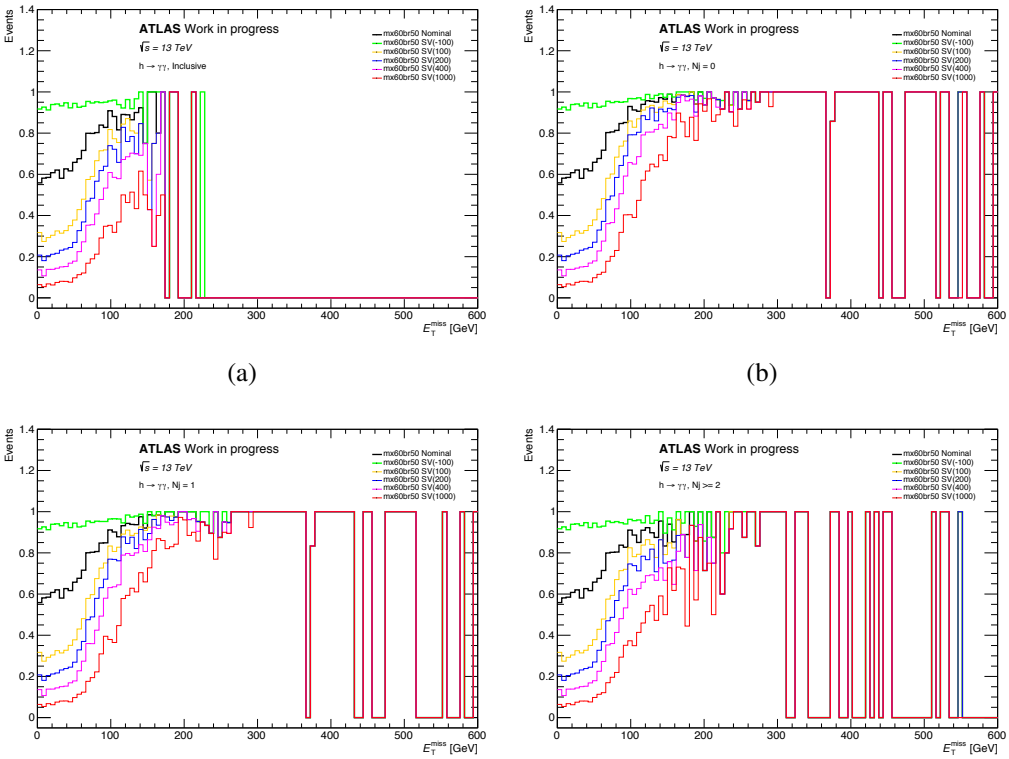
Figure D.1: $\boldsymbol{E}_{\mathrm{T}}^{\mathrm{miss}}$ distributions for 2015+2016 data for different same vertex cuts split into (a) inclusive, (b) 0-jet case, (c) 1-jet case and (d) ≥2-jet case [15].



(a) (b)

(c) (d)

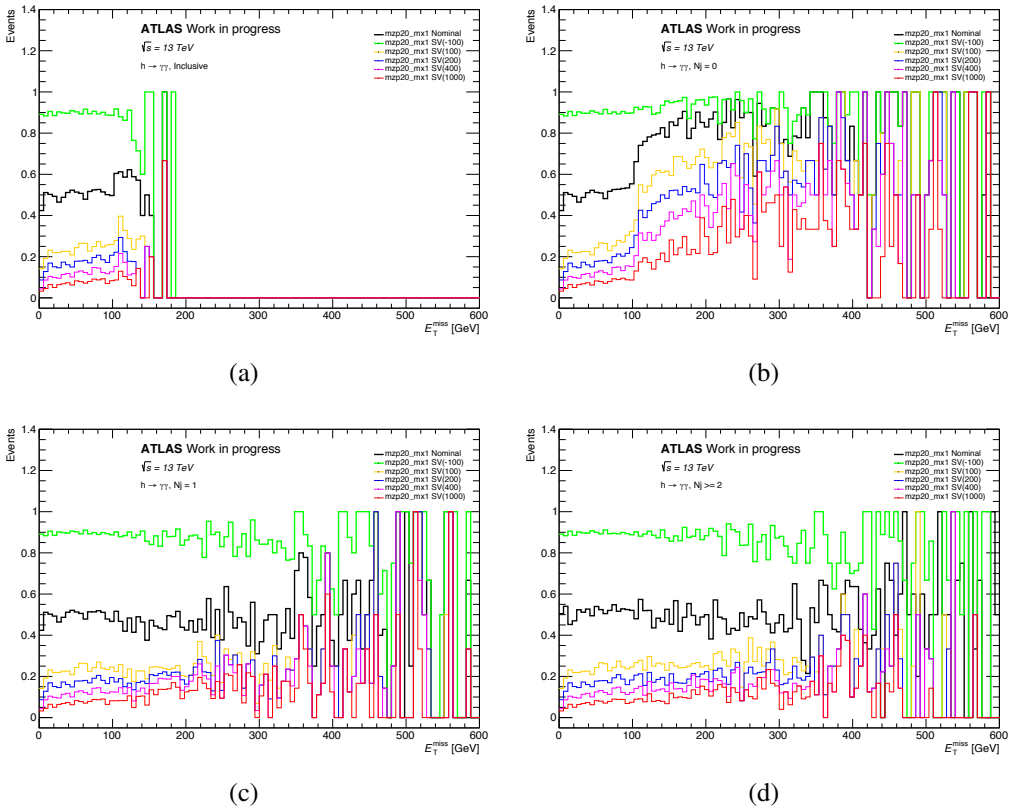
Figure D.2: $E_{\mathrm{T}}^{\mathrm{miss}}$ distributions for the Wh sample for different same vertex cuts split into (a) inclusive, (b) 0-jet case, (c) 1-jet case and (d) ≥2-jet case [15].



(a) (b)

(c) (d)

Figure D.3: $E_{\mathrm{T}}^{\mathrm{miss}}$ distributions for the heavy-scalar signal sample for different same vertex cuts split into (a) inclusive, (b) 0-jet case, (c) 1-jet case and (d) ≥2-jet case [15].



(a) (b)

(c) (d)

Figure D.4: $E_{\mathrm{T}}^{\mathrm{miss}}$ distributions for the mono-Higgs signal sample for different same vertex cuts split into (a) inclusive, (b) 0-jet case, (c) 1-jet case and (d) ≥2-jet case [15].

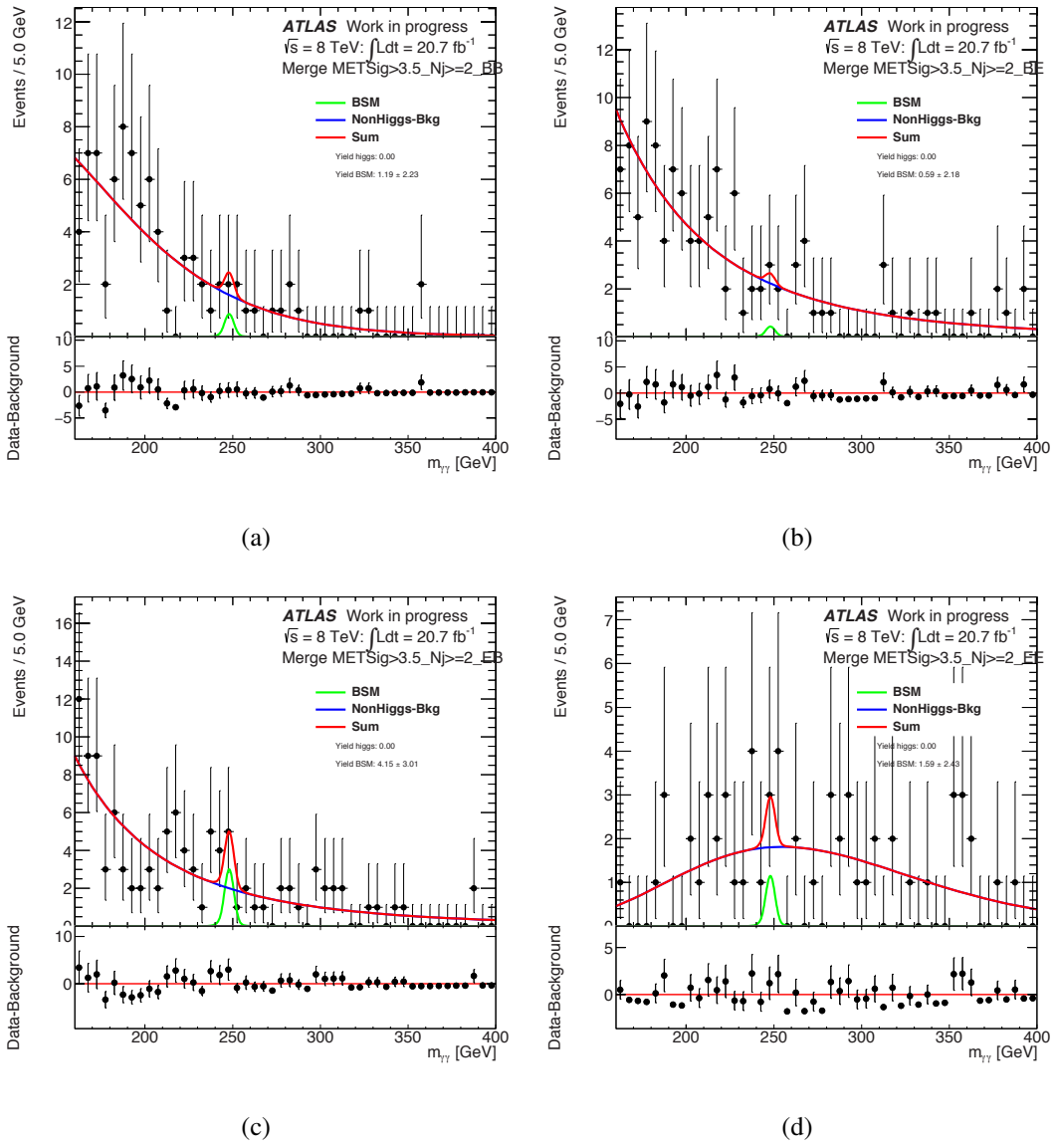
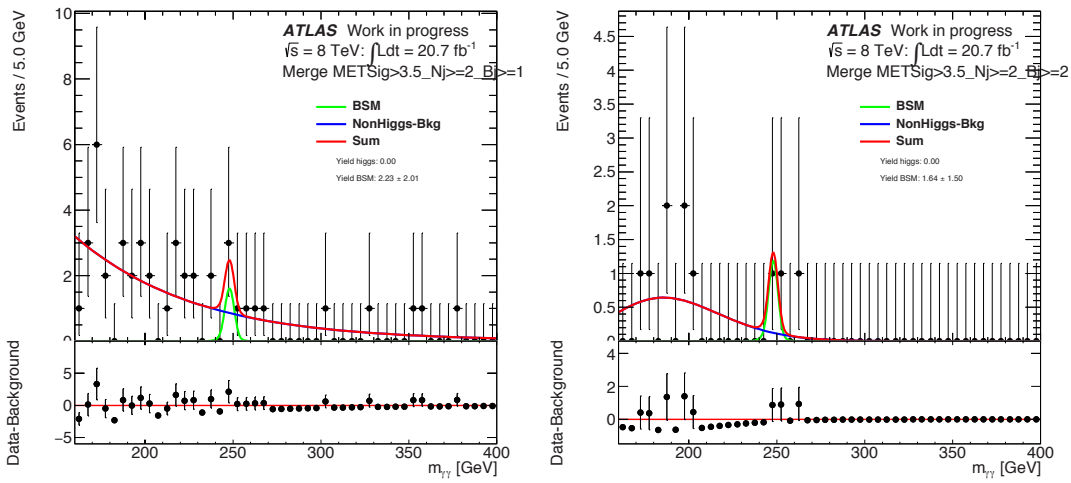
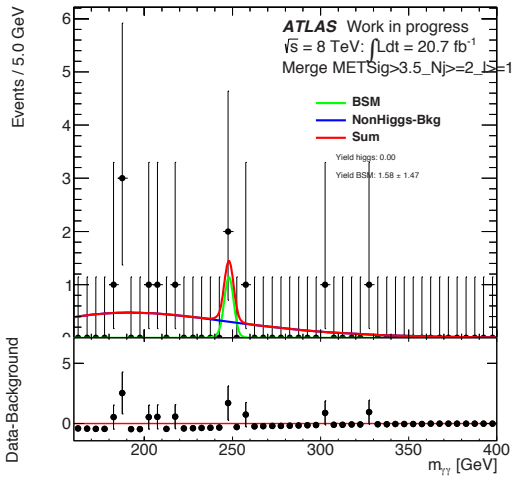


Figure D.5: Run 1 data $E_{\mathrm{T}}^{\mathrm{miss}}$ fit distributions for $S_{E_{\mathrm{T}}^{\mathrm{miss}}} > 3.5\ \sqrt{\mathrm{GeV}}$, SV case and with at least two central jets for: photons in (a) Barrel-Barrel region (BB), (b) Barrel-EndCap region (BE), (c) EndCap-Barrel region (EB) and (d) EndCap-EndCap region (EE), respectively [15].



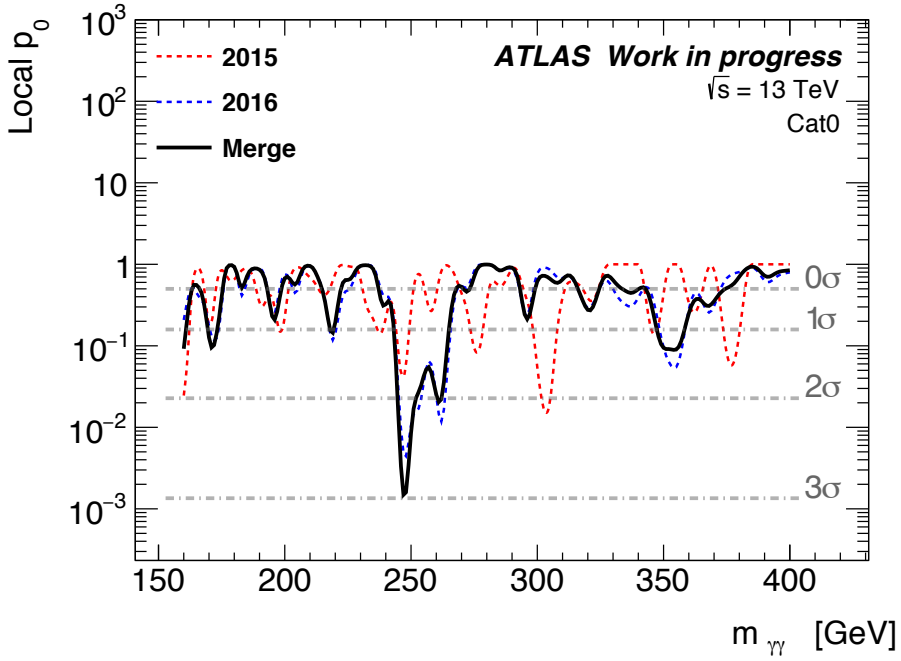
(a)

(b)

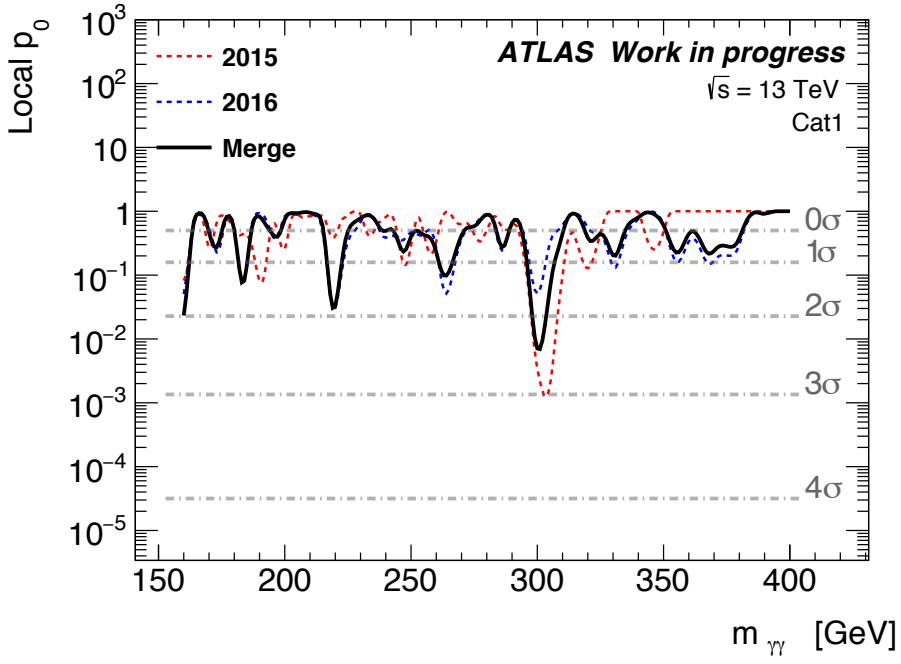


(c)

Figure D.6: Run 1 data $E_{\mathrm{T}}^{\mathrm{miss}}$ fit distributions for $S_{E_{\mathrm{T}}^{\mathrm{miss}}} > 3.5\ \sqrt{\mathrm{GeV}}$, SV case and with at least two central jets for (a) number of b-tagged jets ≥2 and (b) number of leptons ≥1 [15].

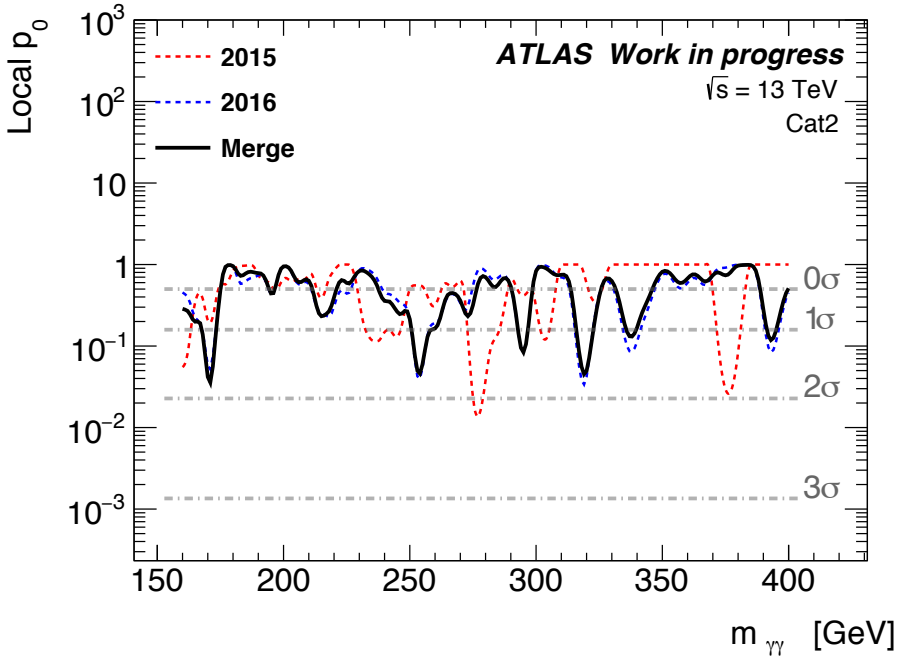


(a)

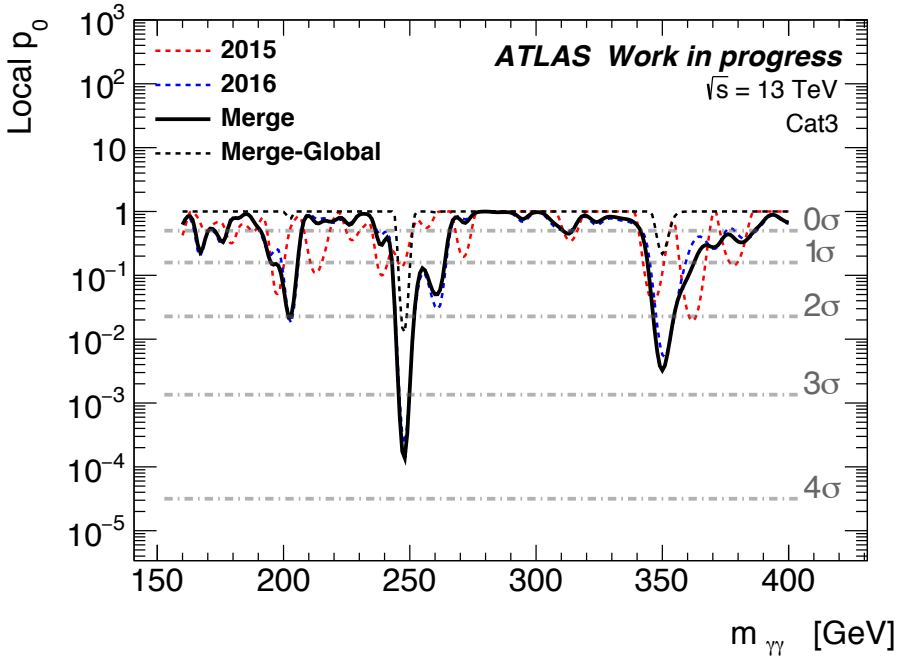


(b)

Figure D.7: Local p_0 value scans as a function of mass for the (a) inclusive category and (b) 1-jet category [15].

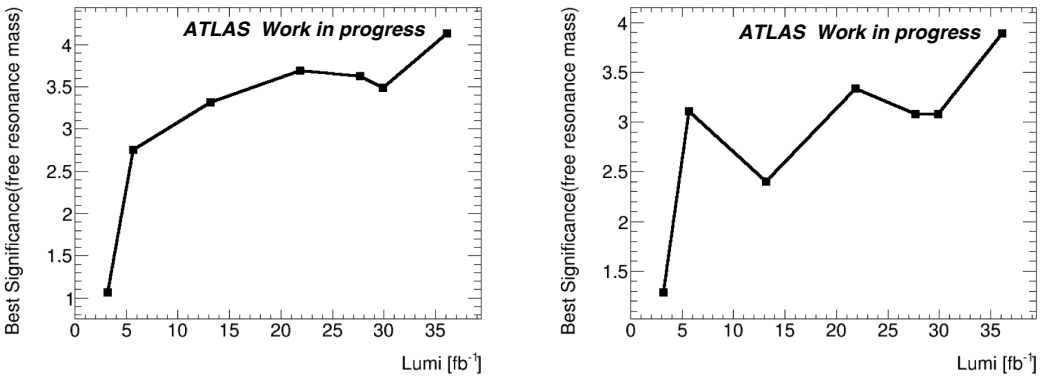


(a)



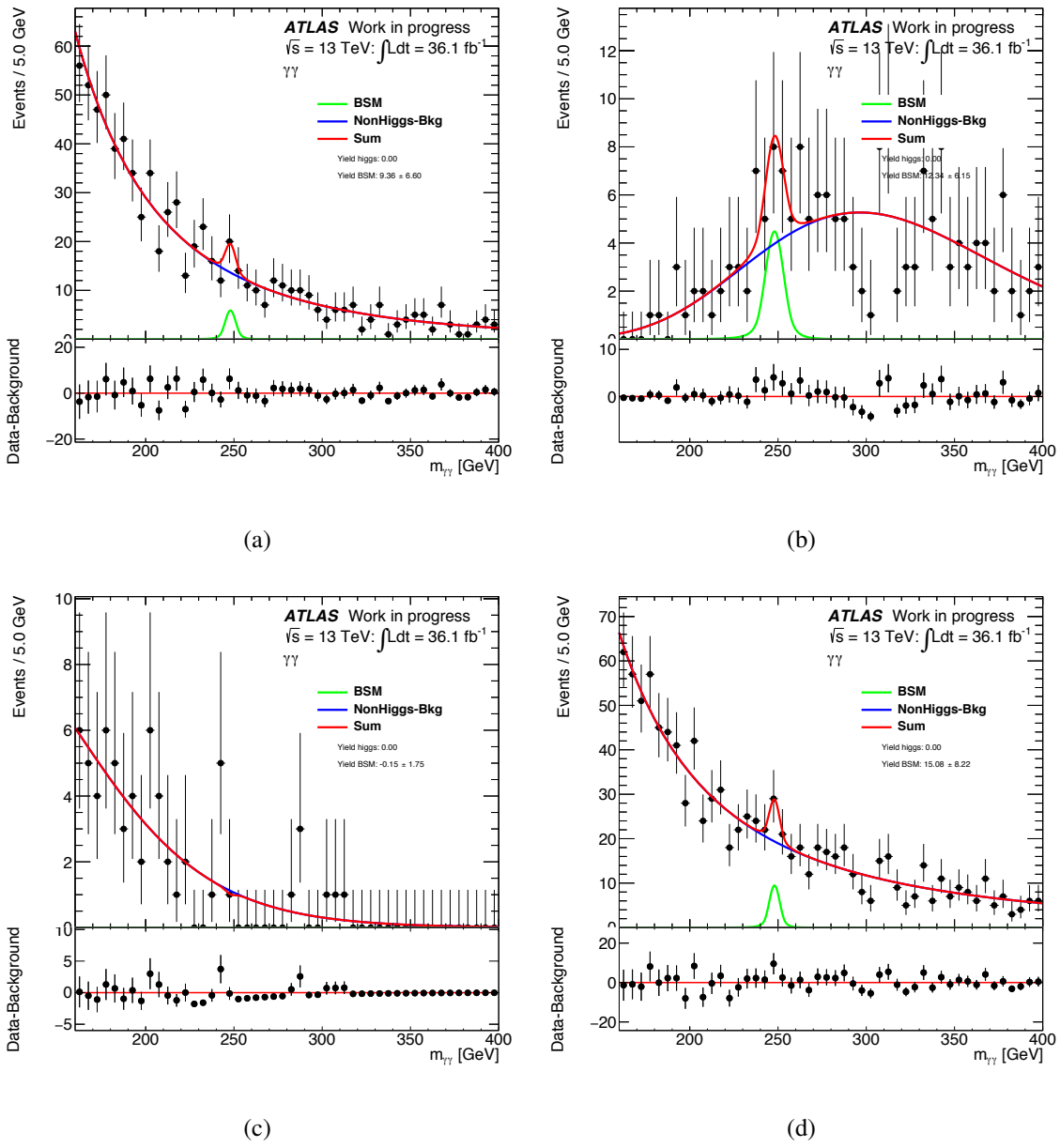
(b)

Figure D.8: Local p_0 value scans as a function of mass for the (a) inclusive category and (b) ≥2-jet case (category 3). The largest significance from the background only hypothesis occurs at 248 GeV in the category with 2 central jets and has a value of around 3.6 σ. This corresponds to a global significance of 2.2 σ [15].



(a) (b)

Figure D.9: The largest fitted significance for (a) $S_{E_{\mathrm{T}}^{\mathrm{miss}}} > 3.2\sqrt{\mathrm{GeV}}$ with and (b) $S_{E_{\mathrm{T}}^{\mathrm{miss}}} > 3.5\sqrt{\mathrm{GeV}}$ with floating resonance mass [15].



(a) (b)

(c) (d)

Figure D.10: The excess in the case of R20 for the (a) non-EE, (b) EEOS, (c) EESS and (d) merge categories. The $m_{\gamma\gamma}$ resolution is set at $\sigma = 3$ GeV, 5.2 GeV, 2.75 GeV and 3 GeV, respectively. The fit mass is fixed at 248 GeV and narrow width assumption is considered in all cases. Peaks around 248 GeV are observed in all cases [16].

BIBLIOGRAPHY

[1] S. Liao et al., *Supporting note: Selection and performance for the $H \to \gamma\gamma$ and $H \to Z\gamma$ analyses*, Tech. Rep. ATL-COM-PHYS-2015-1326, CERN, Geneva, Oct, 2015. https://cds.cern.ch/record/2062580.

[2] S. Liao et al., *Measurement of Higgs Boson fiducial cross-section in the diphoton decay channel in pp collisions at centre-of-mass energy of 13 TeV with the ATLAS detector*, Tech. Rep. ATL-COM-PHYS-2015-1388, CERN, Geneva, Nov, 2015. https://cds.cern.ch/record/2103377.

[3] S. Liao et al., *Search for a Higgs boson with the di-photon decay in association with missing energy in pp collisions at $\sqrt{s}$ =13 TeV with the ATLAS detector*, Tech. Rep. ATL-COM-PHYS-2015-1589, CERN, Geneva, Dec, 2015. https://cds.cern.ch/record/2118127.

[4] S. Liao et al., *Supporting note: Selection and performance for the $H \to \gamma\gamma$ and $H \to Z\gamma$ analyses*, Tech. Rep. ATL-COM-PHYS-2016-109, CERN, Geneva, Feb, 2016. https://cds.cern.ch/record/2130656.

[5] S. Liao et al., *Supporting note: Search for a Higgs boson with the di-photon decay in association with missing energy in pp collisions at $\sqrt{s}$ =13 TeV with the ATLAS detector*, Tech. Rep. ATL-COM-PHYS-2016-473, CERN, Geneva, May, 2016. https://cds.cern.ch/record/2151831.

[6] S. Liao et al., *Supporting note for the Search for a Higgs boson with the di-photon 2 decay in association with missing energy in pp collisions at $\sqrt{s}$ =13 TeV with the ATLAS detector*, Tech. Rep. ATL-COM-PHYS-2016-1732, CERN, Geneva, Nov, 2016.

https://cds.cern.ch/record/2235629.

[7] S. Liao et al., *Supporting note: Search for dark matter in events with missing transverse momentum and a Higgs boson decaying to two photons in pp collisions at $\sqrt{s}$ =13 TeV with the ATLAS detector*, Tech. Rep. ATL-COM-PHYS-2016-708, CERN, Geneva, Jun, 2016.
https://cds.cern.ch/record/2158908.

[8] S. Liao et al., *Supporting note: Selection and performance for the $H \to \gamma\gamma$ and $H \to Z\gamma$ analyses*, Tech. Rep. ATL-COM-PHYS-2016-862, CERN, Geneva, Jul, 2016.
https://cds.cern.ch/record/2196102.

[9] S. Liao et al., *An updated search for new phenomena in events with missing transverse momentum and a Higgs boson decaying to two photons in pp collisions at $\sqrt{s}$ =13 TeV with the ATLAS detector*, Tech. Rep. ATL-COM-PHYS-2016-911, CERN, Geneva, Jul, 2016.
https://cds.cern.ch/record/2199133.

[10] S. Liao et al., *Search for new phenomena in events with missing transverse momentum and a Higgs boson decaying to two photons in pp collisions at $\sqrt{s}$ =13 TeV with the ATLAS detector*, Tech. Rep. ATLAS-COM-CONF-2016-078, CERN, Geneva, Jul, 2016.
https://cds.cern.ch/record/2201588.

[11] S. Liao et al., *Supporting note: Search for dark matter in events with missing transverse momentum and a Higgs boson decaying to two photons in pp collisions at $\sqrt{s}$ =13 TeV with the ATLAS detector using data in full years of 2015 and 2016*, Tech. Rep. ATL-COM-PHYS-2016-1735, CERN, Geneva, Nov, 2016.
https://cds.cern.ch/record/2235659.

[12] ATLAS Collaboration, *Search for new phenomena in events with missing transverse momentum and a Higgs boson decaying to two photons in pp collisions at*

$\sqrt{s}$ =13 TeV with the ATLAS detector, Tech. Rep. ATLAS-CONF-2016-087, CERN, Geneva, Aug, 2016.
http://cds.cern.ch/record/2206281.

[13] ATLAS Collaboration, *Search for new phenomena in events with missing transverse momentum and a Higgs boson decaying to two photons in pp collisions at $\sqrt{s}$ =13 TeV with the ATLAS detector*, Tech. Rep. ATLAS-CONF-2016-011, CERN, Geneva, Mar, 2016.
https://cds.cern.ch/record/2139812.

[14] S. Liao et al., *Supporting note: Selection and performance for the $H \to \gamma\gamma$ and $H \to Z\gamma$ analyses, Spring 2017*, Tech. Rep. ATL-COM-PHYS-2017-357, CERN, Geneva, Apr, 2017.
https://cds.cern.ch/record/2258158.

[15] S. Liao et al., *Search for a resonance in the di-photon decay in association with missing energy in pp collisions at $\sqrt{s}$ =13 TeV with the ATLAS detector*, Tech. Rep. ATL-COM-PHYS-2017-1225, CERN, Geneva, Aug, 2017.
https://cds.cern.ch/record/2280188.

[16] S. Liao et al., *Supporting note: Search for a new resonance in the di-photon decay in association with missing transverse energy in pp collisions at $\sqrt{s}$ =13 TeV with the ATLAS detector*, Tech. Rep. ATL-COM-PHYS-2018-970, CERN, Geneva, Jul, 2018.
https://cds.cern.ch/record/2628349.

[17] S. Liao, *Dark matter search in events with missing transverse energy and a Higgs boson decaying to two photons with the ATLAS detector.*, Tech. Rep. ATL-COM-PHYS-2018-1641, CERN, Geneva, Nov, 2018.
https://cds.cern.ch/record/2648813.

[18] ATLAS Collaboration, *Search for dark matter in association with a Higgs boson decaying to two photons at $\sqrt{s}$ =13 TeV with the ATLAS detector*, Phys. Rev. **D96** no. 11, (2017) 112004, arXiv:1706.03948 [hep-ex].

[19] S. Liao, R. Erasmus, H. Jivan, C. Pelwan, G. Peters, and E. Sideras-Haddad, *A comparative study of the radiation hardness of plastic scintillators for the upgrade of the Tile Calorimeter of the ATLAS detector*, J. Phys. Conf. Ser. **645** no. 1, (2015) 012021.

[20] H. Jivan, E. Sideras-Haddad, R. Erasmus, S. Liao, M. Madhuku, G. Peters, K. Sekonya, and O. Solvyanov, *Radiation hardness of plastic scintillators for the Tile Calorimeter of the ATLAS detector*, J. Phys. Conf. Ser. **645** no. 1, (2015) 012019.

[21] C. Pelwan, H. Jivan, D. Joubert, J. Keartland, S. Liao, G. Peters, and E. Sideras-Haddad, *Characterization of plastic scintillators using magnetic resonance techniques for the upgrade of the Tile Calorimeter in the ATLAS detector*, J. Phys. Conf. Ser. **645** no. 1, (2015) 012023.

[22] J. E. Mdhluli, R. Erasmus, Y. U. Davydov, H. Jivan, S. Liao, C. Pelwan, E. Sideras-Haddad, B. Mellado, G. Peters, and C. Sandrock, *Neutron irradiation and light transmission assessment of plastic scintillators of the TileCal section of the ATLAS detector, in 61st Annual Conference of the South African Institute of Physics (SAIP2016): Johannesburg, South Africa, July 4-8, 2016*, pp. , 128–133.

[23] K. G. Tomiwa, X. Ruan, S. Liao, and B. Mellado, *Reconstruction of missing energy in events with two photons at the ATLAS detector in Large Hadron Collider, in 62 nd Annual Conference of the South African Institute of Physics (SAIP2017), Stellenbosch, South Africa, July 3-7, 2017*, pp. , 176–181.

[24] S. Liao, *Reconstruction and performance of missing transverse energy at the ATLAS detector, to be published in Workshop on High Energy Particle Physics (HEPPW2018) proceedings, STIAS, Stellenbosch Institute for Advanced Study, Stellenbosch , South Africa, January 31-February 2, 2018*,.

[25] A. Salam, *Weak and Electromagnetic Interactions*, Conf. Proc. **C680519** (1968) 367–377.

[26] W. N. Cottingham and D. A. Greenwood, *An introduction to the standard model of particle physics*.
Cambridge University Press, 2007.

[27] S. L. Glashow, *Partial-symmetries of weak interactions*, Nuclear Physics **22** no. 4, (1961) 579 – 588. http://www.sciencedirect.com/science/article/pii/0029558261904692.

[28] S. Weinberg, *A Model of Leptons*, Phys. Rev. Lett. **19** (1967) 1264–1266. https://link.aps.org/doi/10.1103/PhysRevLett.19.1264.

[29] S. Weinberg, *The Quantum theory of fields. Vol. 1: Foundations*.
Cambridge University Press, 2005.

[30] M. E. Peskin and D. V. Schroeder, *An Introduction to quantum field theory*.
Addison-Wesley, Reading, USA, 1995.

[31] D. J. Griffiths, *Introduction to elementary particles; 2nd rev. version*.
Physics textbook. Wiley, New York, NY, 2008.

[32] E. D. Bloom et al., *High-Energy Inelastic $e-p$ Scattering at 6° and 10°*, Phys. Rev. Lett. **23** (1969) 930–934. https://link.aps.org/doi/10.1103/PhysRevLett.23.930.

[33] J. M. Campbell, J. W. Huston, and W. J. Stirling, *Hard Interactions of Quarks and Gluons: A Primer for LHC Physics*, Rept. Prog. Phys. **70** (2007) 89, arXiv:hep-ph/0611148 [hep-ph].

[34] O. W. Greenberg, *Color: From baryon spectroscopy to QCD*, pp. , 130–139. 1992.
arXiv:hep-ph/9301207 [hep-ph].

[35] C. S. Wu, E. Ambler, R. W. Hayward, D. D. Hoppes, and R. P. Hudson, *Experimental Test of Parity Conservation in Beta Decay*, Phys. Rev. **105** (1957) 1413–1414.

[36] Y. Nambu, *Quasi-Particles and Gauge Invariance in the Theory of Superconductivity*, Phys. Rev. **117** (1960) 648–663. https://link.aps.org/doi/10.1103/PhysRev.117.648.

[37] F. Englert and R. Brout, *Broken Symmetry and the Mass of Gauge Vector Mesons*, Phys. Rev. Lett. **13** (1964) 321–323. https://link.aps.org/doi/10.1103/PhysRevLett.13.321.

[38] P. W. Higgs, *Broken Symmetries and the Masses of Gauge Bosons*, Phys. Rev. Lett. **13** (1964) 508–509. https://link.aps.org/doi/10.1103/PhysRevLett.13.508.

[39] T. W. B. Kibble, *Symmetry Breaking in Non-Abelian Gauge Theories*, Phys. Rev. **155** (1967) 1554–1561. https://link.aps.org/doi/10.1103/PhysRev.155.1554.

[40] P. W. Higgs, *Spontaneous Symmetry Breakdown without Massless Bosons*, Phys. Rev. **145** (1966) 1156–1163. https://link.aps.org/doi/10.1103/PhysRev.145.1156.

[41] A. Azatov and J. Galloway, *Electroweak Symmetry Breaking and the Higgs Boson: Confronting Theories At Colliders*, International Journal of Modern Physics A **28** no. 02, (2013) 1330004, arXiv:1212.1380.

[42] The LHC Higgs Cross Section Working Group, *Handbook of LHC Higgs Cross Sections: 2. Differential Distributions*, arXiv:1201.3084 [hep-ph].

[43] C. Anastasiou et al., *Higgs Boson Gluon-Fusion Production in QCD at Three Loops*, Phys. Rev. Lett. **114** (2015) 212001, arXiv:1503.06056 [hep-ph].

[44] C. Anastasiou et al., *High precision determination of the gluon fusion Higgs boson cross-section at the LHC*, JHEP **05** (2016) 058, arXiv:1602.00695 [hep-ph].

[45] S. Actis, G. Passarino, C. Sturm, and S. Uccirati, *NLO Electroweak Corrections to Higgs Boson Production at Hadron Colliders*, Phys. Lett. **B670** (2008) 12–17, arXiv:0809.1301 [hep-ph].

[46] C. Anastasiou, R. Boughezal, and F. Petriello, *Mixed QCD-electroweak corrections to Higgs boson production in gluon fusion*, JHEP **04** (2009) 003, arXiv:0811.3458 [hep-ph].

[47] M. Ciccolini, A. Denner, and S. Dittmaier, *Strong and electroweak corrections to the production of Higgs + 2jets via weak interactions at the LHC*, Phys. Rev. Lett. **99** (2007) 161803, arXiv:0707.0381 [hep-ph].

[48] M. Ciccolini, A. Denner, and S. Dittmaier, *Electroweak and QCD corrections to Higgs production via vector-boson fusion at the LHC*, Phys. Rev. **D77** (2008) 013002, arXiv:0710.4749 [hep-ph].

[49] L. Altenkamp, S. Dittmaier, R. V. Harlander, H. Rzehak, and T. J. E. Zirke, *Gluon-induced Higgs-strahlung at next-to-leading order QCD*, JHEP **02** (2013) 078, arXiv:1211.5015 [hep-ph].

[50] A. Denner, S. Dittmaier, S. Kallweit, and A. Muck, *Electroweak corrections to Higgs-strahlung off W/Z bosons at the Tevatron and the LHC with HAWK*, JHEP **03** (2012) 075, arXiv:1112.5142 [hep-ph].

[51] W. Beenakker, S. Dittmaier, M. Kramer, B. Plumper, M. Spira, and P. M. Zerwas, *NLO QCD corrections to t anti-t H production in hadron collisions*, Nucl. Phys. **B653** (2003) 151–203, arXiv:hep-ph/0211352 [hep-ph].

[52] S. Dawson, C. Jackson, L. H. Orr, L. Reina, and D. Wackeroth, *Associated Higgs production with top quarks at the large hadron collider: NLO QCD corrections*, Phys. Rev. **D68** (2003) 034022, arXiv:hep-ph/0305087 [hep-ph].

[53] Y. Zhang, W.-G. Ma, R.-Y. Zhang, C. Chen, and L. Guo, *QCD NLO and EW NLO corrections to $t\bar{t}H$ production with top quark decays at hadron collider*, Phys. Lett. **B738** (2014) 1–5, arXiv:1407.1110 [hep-ph].

[54] S. Frixione, V. Hirschi, D. Pagani, H. S. Shao, and M. Zaro, *Electroweak and QCD corrections to top-pair hadroproduction in association with heavy bosons*, JHEP **06** (2015) 184, arXiv:1504.03446 [hep-ph].

[55] C. Anastasiou and K. Melnikov, *Higgs boson production at hadron colliders in NNLO QCD*, Nuclear Physics B **646** no. 1, (2002) 220 – 256. http://www.sciencedirect.com/science/article/pii/S0550321302008374.

[56] R. V. Harlander and W. B. Kilgore, *Next-to-next-to-leading order Higgs production at hadron colliders*, Phys. Rev. Lett. **88** (2002) 201801, arXiv:hep-ph/0201206 [hep-ph].

[57] S. Actis, G. Passarino, C. Sturm, and S. Uccirati, *NNLO Computational Techniques: The Cases $H \to \gamma\gamma$ and $H \to gg$*, Nucl. Phys. **B811** (2009) 182–273, arXiv:0809.3667 [hep-ph].

[58] P. Bolzoni, F. Maltoni, S.-O. Moch, and M. Zaro, *Vector boson fusion at NNLO in QCD: SM Higgs and beyond*, Phys. Rev. **D85** (2012) 035002, arXiv:1109.3717 [hep-ph].

[59] P. Bolzoni, F. Maltoni, S.-O. Moch, and M. Zaro, *Higgs production via vector-boson fusion at NNLO in QCD*, Phys. Rev. Lett. **105** (2010) 011801, arXiv:1003.4451 [hep-ph].

[60] O. Brein, A. Djouadi, and R. Harlander, *NNLO QCD corrections to the Higgs-strahlung processes at hadron colliders*, Phys. Lett. **B579** (2004) 149–156, arXiv:hep-ph/0307206 [hep-ph].

[61] LHC Higgs Cross Section Working Group Collaboration, J. R. Andersen et al., *Handbook of LHC Higgs Cross Sections: 3. Higgs Properties*, arXiv:1307.1347 [hep-ph].

[62] A. Denner, S. Heinemeyer, I. Puljak, D. Rebuzzi, and M. Spira, *Standard model Higgs-boson branching ratios with uncertainties*, European Physical Journal C **71** no. 9, (2011) 1–29, arXiv:1107.5909.

[63] CDF, D0 Collaboration, T. N. P. H. W. Group, *Updated Combination of CDF and D0 Searches for Standard Model Higgs Boson Production with up to 10.0 fb^{-1} of Data*, 2012. arXiv:1207.0449 [hep-ex].

[64] ATLAS Collaboration, *Observation of a new particle in the search for the Standard Model Higgs boson with the ATLAS detector at the LHC*, Physics Letters B **716** no. 1, (2012) 1–29, arXiv:1207.7214.

[65] CMS Collaboration, *Observation of a new boson at a mass of 125 GeV with the CMS experiment at the LHC*, Physics Letters B **716** no. 1, (2012) 30–61, arXiv:1207.7235.

[66] S. von Buddenbrock, N. Chakrabarty, A. S. Cornell, D. Kar, M. Kumar, T. Mandal, B. Mellado, B. Mukhopadhyaya, and R. G. Reed, *The compatibility of LHC Run 1 data with a heavy scalar of mass around 270 GeV*, arXiv:1506.00612 [hep-ph].

[67] S. von Buddenbrock, N. Chakrabarty, A. S. Cornell, D. Kar, M. Kumar, T. Mandal, B. Mellado, B. Mukhopadhyaya, R. G. Reed, and X. Ruan, *Phenomenological signatures of additional scalar bosons at the LHC*, Eur. Phys. J. **C76** no. 10, (2016) 580, arXiv:1606.01674 [hep-ph].

[68] ATLAS Collaboration, *Measurements of fiducial and differential cross sections for Higgs boson production in the diphoton decay channel at $\sqrt{s}$ =8 TeV TeV with ATLAS*, JHEP **09** (2014) 112, arXiv:1407.4222 [hep-ex].

[69] ATLAS Collaboration, *Fiducial and differential cross sections of Higgs boson production measured in the four-lepton decay channel in pp collisions at $\sqrt{s}$ =8 TeV with the ATLAS detector*, Phys. Lett. **B738** (2014) 234–253, arXiv:1408.3226 [hep-ex].

[70] CMS Collaboration, *Measurement of differential cross sections for Higgs boson production in the diphoton decay channel in pp collisions at $\sqrt{s}$ =8 TeV*, Eur. Phys. J. **C76** no. 1, (2016) 13, arXiv:1508.07819 [hep-ex].

[71] CMS Collaboration, *Measurement of differential and integrated fiducial cross sections for Higgs boson production in the four-lepton decay channel in pp collisions at $\sqrt{s}$ =7 and 8 TeV* , JHEP **04** (2016) 005, arXiv:1512.08377 [hep-ex].

[72] ATLAS Collaboration, *Searches for Higgs boson pair production in the $hh \to bb\tau\tau, \gamma\gamma WW^*, \gamma\gamma bb, bbbb$ channels with the ATLAS detector*, Phys. Rev. **D92** (2015) 092004, arXiv:1509.04670 [hep-ex].

[73] CMS Collaboration, *Search for two Higgs bosons in final states containing two photons and two bottom quarks in proton-proton collisions at 8 TeV*, Phys. Rev. **D94** no. 5, (2016) 052012, arXiv:1603.06896 [hep-ex].

[74] CMS Collaboration, *Searches for a heavy scalar boson H decaying to a pair of 125 GeV Higgs bosons hh or for a heavy pseudoscalar boson A decaying to Zh, in the final states with $h \to \tau\tau$*, Phys. Lett. **B755** (2016) 217–244, arXiv:1510.01181 [hep-ex].

[75] CMS Collaboration, *Searches for heavy Higgs bosons in two-Higgs-doublet models and for $t \to ch$ decay using multilepton and diphoton final states in pp collisions at 8 TeV*, Phys. Rev. D **90** (2014) 112013. https://link.aps.org/doi/10.1103/PhysRevD.90.112013.

[76] ATLAS Collaboration, *Search for $H \to \gamma\gamma$ produced in association with top quarks and constraints on the Yukawa coupling between the top quark and the Higgs boson*

using data taken at 7 TeV and 8 TeV with the ATLAS detector, Phys. Lett. **B740** (2015) 222–242, arXiv:1409.3122 [hep-ex].

[77] ATLAS Collaboration, *Search for the associated production of the Higgs boson with a top quark pair in multilepton final states with the ATLAS detector*, Phys. Lett. **B749** (2015) 519–541, arXiv:1506.05988 [hep-ex].

[78] ATLAS Collaboration, *Search for the Standard Model Higgs boson produced in association with top quarks and decaying into $b\bar{b}$ in pp collisions at $\sqrt{s}$ =8 TeV with the ATLAS detector*, Eur. Phys. J. **C75** no. 7, (2015) 349, arXiv:1503.05066 [hep-ex].

[79] CMS Collaboration, *Search for the associated production of the Higgs boson with a top-quark pair*, JHEP **09** (2014) 087, arXiv:1408.1682 [hep-ex].

[80] ATLAS Collaboration, *Search for a high-mass Higgs boson decaying to a W boson pair in pp collisions at $\sqrt{s}$ =8 TeV with the ATLAS detector*, JHEP **01** (2016) 032, arXiv:1509.00389 [hep-ex].

[81] ATLAS Collaboration, *Search for an additional, heavy Higgs boson in the $H \to ZZ$ decay channel at $\sqrt{s}$ =8 TeV in pp collision data with the ATLAS detector*, Eur. Phys. J. **C76** no. 1, (2016) 45, arXiv:1507.05930 [hep-ex].

[82] CMS Collaboration, *Search for a Higgs boson in the mass range from 145 to 1000 GeV decaying to a pair of W or Z bosons*, JHEP **10** (2015) 144, arXiv:1504.00936 [hep-ex].

[83] S. von Buddenbrock, *Exploring LHC Run 1 and 2 data using the Madala hypothesis*, J. Phys. Conf. Ser. **878** no. 1, (2017) 012030, arXiv:1706.02477 [hep-ph].

[84] S. von Buddenbrock, A. S. Cornell, Y. Fang, A. Fadol Mohammed, M. Kumar, B. Mellado, and K. G. Tomiwa, *The emergence of multi-lepton anomalies at the LHC and their compatibility with new physics at the EW scale*, arXiv:1901.05300 [hep-ph].

[85] CMS Collaboration, *Measurement of inclusive and differential fiducial cross sections for Higgs boson production in the H-to-4l decay channel in p-p collisions at 7 TeV and 8 TeV*, arXiv:1512.08377 [hep-ex].

[86] M. Kumar, S. von Buddenbrock, N. Chakrabarty, A. S. Cornell, D. Kar, T. Mandal, B. Mellado, B. Mukhopadhyaya, and R. G. Reed, *The impact of additional scalar bosons at the LHC*, J. Phys. Conf. Ser. **802** no. 1, (2017) 012007, arXiv:1603.01208 [hep-ph].

[87] S. von Buddenbrock, A. S. Cornell, E. D. R. Iarilala, M. Kumar, B. Mellado, X. Ruan, and E. M. Shrif, *Constraints on a 2HDM with a singlet scalar and implications in the search for heavy bosons at the LHC*, arXiv:1809.06344 [hep-ph].

[88] S. von Buddenbrock, A. S. Cornell, A. Fadol, M. Kumar, B. Mellado, and X. Ruan, *Multi-lepton signatures of additional scalar bosons beyond the Standard Model at the LHC*, J. Phys. **G45** no. 11, (2018) 115003, arXiv:1711.07874 [hep-ph].

[89] G. Bertone, D. Hooper, and J. Silk, *Particle dark matter: Evidence, candidates and constraints*, Phys. Rept. **405** (2005) 279–390, arXiv:hep-ph/0404175 [hep-ph].

[90] L. Evans and P. Bryant, *LHC Machine*, Journal of Instrumentation **3** no. 08, (2008) S08001. http://stacks.iop.org/1748-0221/3/i=08/a=S08001.

[91] O. S. Brüning, P. Collier, P. Lebrun, S. Myers, R. Ostojic, J. Poole, and P. Proudlock, *LHC Design Report*.
CERN Yellow Reports: Monographs. CERN, Geneva, 2004.
https://cds.cern.ch/record/782076.

[92] O. S. Brüning, P. Collier, P. Lebrun, S. Myers, R. Ostojic, J. Poole, and P. Proudlock, *LHC Design Report*.
CERN Yellow Reports: Monographs. CERN, Geneva, 2004.
https://cds.cern.ch/record/815187.

[93] ATLAS Collaboration, *The ATLAS Experiment at the CERN Large Hadron Collider*, JINST **3** (2008) S08003.

[94] CMS Collaboration, *The CMS Experiment at the CERN LHC*, JINST **3** (2008) S08004.

[95] ALICE Collaboration, *The ALICE experiment at the CERN LHC*, JINST **3** (2008) S08002.

[96] LHCb Collaboration, *LHCb Detector Performance*, Int. J. Mod. Phys. A **30** no. LHCB-DP-2014-002. CERN-PH-EP-2014-290. LHCB-DP-2014-002. CERN-LHCB-DP-2014-002, (2014) 1530022. 73 p. https://cds.cern.ch/record/1978280.

[97] ATLAS Collaboration Collaboration, *ATLAS inner detector: Technical Design Report, 1*. Technical Design Report ATLAS. CERN, Geneva, 1997. https://cds.cern.ch/record/331063.

[98] S. Haywood, L. Rossi, R. Nickerson, and A. Romaniouk, *ATLAS inner detector: Technical Design Report, 2*. Technical Design Report ATLAS. CERN, Geneva, 1997. https://cds.cern.ch/record/331064.

[99] ATLAS Collaboration, *The ATLAS Inner Detector commissioning and calibration*, Eur. Phys. J. **C70** (2010) 787–821, arXiv:1004.5293 [physics.ins-det].

[100] ATLAS Collaboration, *ATLAS calorimeter performance: Technical Design Report*. Technical Design Report ATLAS. CERN, Geneva, 1996. https://cds.cern.ch/record/331059.

[101] F. Bauer et al., *Construction and Test of MDT Chambers for the ATLAS Muon Spectrometer*, Nucl. Instrum. Meth. **A461** (2001) 17–20, arXiv:1604.02000 [physics.ins-det].

[102] ATLAS Collaboration, *ATLAS muon spectrometer: Technical Design Report*.

Technical Design Report ATLAS. CERN, Geneva, 1997.
https://cds.cern.ch/record/331068.

[103] ATLAS Collaboration, *ATLAS magnet system: Technical Design Report, 1*.
Technical Design Report ATLAS. CERN, Geneva, 1997.
https://cds.cern.ch/record/338080.

[104] ATLAS Collaboration, *Track Reconstruction Performance of the ATLAS Inner Detector at* $\sqrt{s} = 13$ *TeV*, Tech. Rep. ATL-PHYS-PUB-2015-018, CERN, Geneva, Jul, 2015.
https://cds.cern.ch/record/2037683.

[105] "ATLAS experiment public images.".
http://atlasexperiment.org/photos/calorimeters.html.

[106] ATLAS Collaboration, *ATLAS liquid-argon calorimeter: Technical Design Report*.
Technical Design Report ATLAS. CERN, Geneva, 1996.
https://cds.cern.ch/record/331061.

[107] ATLAS Collaboration, *ATLAS tile calorimeter: Technical Design Report*.
Technical Design Report ATLAS. CERN, Geneva, 1996.
https://cds.cern.ch/record/331062.

[108] ATLAS Collaboration, *Readiness of the ATLAS Tile Calorimeter for LHC collisions*, Eur. Phys. J. **C70** (2010) 1193–1236, arXiv:1007.5423 [physics.ins-det].

[109] A. Artamonov et al., *The ATLAS forward calorimeters*, JINST **3** (2008) P02010.

[110] T. Argyropoulos et al., *Cathode strip chambers in ATLAS: Installation, commissioning and in situ performance*, IEEE Trans. Nucl. Sci. **56** (2009) 1568–1574.

[111] P. Jenni, M. Nessi, M. Nordberg, and K. Smith, *ATLAS high-level trigger, data-acquisition and controls: Technical Design Report*.
Technical Design Report ATLAS. CERN, Geneva, 2003.
https://cds.cern.ch/record/616089.

[112] G. Barrand et al., *A software architecture and framework for building HEP data processing applications*, Computer Physics Communications **140** no. 1, (2001) 45 – 55.

[113] P. Bruza, S. L. Gollub, J. M. Andreozzi, I. I. Tendler, B. B. Williams, L. A. Jarvis, D. J. Gladstone, and B. W. Pogue, *Time-gated scintillator imaging for real-time optical surface dosimetry in total skin electron therapy*, Physics in Medicine & Biology **63** no. 9, (2018) 095009. https://doi.org/10.1088%2F1361-6560%2Faaba19.

[114] CMS HCAL Collaboration, *Brightness and uniformity measurements of plastic scintillator tiles at the CERN H2 test beam*, JINST **13** no. 01, (2018) P01002, arXiv:1709.08672 [physics.ins-det].

[115] S. Baccaro, A. Cemmi, I. Di Sarcina, B. Esposito, G. Ferrara, A. Grossi, M. Montecchi, S. Podda, F. Pompili, L. Quintieri, and M. Riva, *Radiation Damage Tests on Diamond and Scintillation Detector Components for the ITER Radial Neutron Camera*, IEEE Transactions on Nuclear Science **PP** (2018) 1–1.

[116] M. P. Taggart, C. Payne, and P. J. Sellin, *Investigation into neutron damage of EJ-299 and EJ-200 plastic scintillators*, pp. , 1–4.
Oct, 2016.

[117] F. Ozok, T. Yetkin, E. A. Yetkin, E. Iren, and M. N. Erduran, *Geant4 simulation of a conceptual calorimeter based on secondary electron emission*, Journal of Instrumentation **12** (2017) P07014.

[118] F. Porter, M. Freedman, F. Wagner, and I. Sherman, *Response of NaI, anthracene and plastic scintillators to electrons and the problems of detecting low energy electrons with scintillation counters*, Nuclear Instruments and Methods **39** (1966) 35–44.

[119] K. D. Rakes, *Evaluating the response of polyvinyl toluene scintillators used in portal detectors*, tech. rep., AIR FORCE INST OF TECH WRIGHT-PATTERSON AFB OH GRADUATE SCHOOL OF ENGINEERING AND MANAGEMENT, 2008.

[120] A. Kastalsky, S. Luryi, and B. Spivak, *Semiconductor high-energy radiation scintillation detector*, Nucl. Instrum. Meth. **A565** (2006) 650–656, arXiv:physics/0608248 [physics.ins-det].

[121] C. Zorn, *A pedestrian's guide to radiation damage in plastic scintillators*, Nucl. Phys. Proc. Suppl. **32** (1993) 377–383. [,377(1992)].

[122] L. Torrisi, *Radiation damage in polyvinyltoluene (PVT)*, Radiation Physics and Chemistry - RADIAT PHYS CHEM **63** (2002) 89–92.

[123] ATLAS Collaboration, *Performance of the ATLAS Inner Detector Track and Vertex Reconstruction in the High Pile-Up LHC Environment*, arXiv:1704.07983 [hep-ex].

[124] T. Cornelissen, M. Elsing, S. Fleischmann, W. Liebig, E. Moyse, and A. Salzburger, *Concepts, Design and Implementation of the ATLAS New Tracking (NEWT)*. No. ATL-SOFT-PUB-2007-007. ATL-COM-SOFT-2007-002. Geneva, Mar, 2007. https://cds.cern.ch/record/1020106.

[125] G. Welch and G. Bishop, *An Introduction to the Kalman Filter*, University of North Carolina at Chapel Hill, Chapel Hill, NC (1995).

[126] ATLAS Collaboration Collaboration, *Performance of primary vertex reconstruction in proton-proton collisions at $\sqrt{s}$ =7 TeV in the ATLAS experiment*, Tech. Rep. ATLAS-CONF-2010-069, CERN, Geneva, Jul, 2010. https://cds.cern.ch/record/1281344.

[127] ATLAS Collaboration, *Reconstruction of primary vertices at the ATLAS experiment in Run 1 proton-proton collisions at the LHC*, Eur. Phys. J. **C77** no. 5, (2017) 332, arXiv:1611.10235 [physics.ins-det].

[128] ATLAS Collaboration, *Measurement of Higgs boson production in the diphoton decay channel in pp collisions at center-of-mass energies of 7 and 8 TeV with the ATLAS*

detector, Phys. Rev. **D90** no. 11, (2014) 112015, arXiv:1408.7084 [hep-ex].

[129] ATLAS Collaboration, *Electron and Photon Reconstruction with the ATLAS Detector*, Nucl. Part. Phys. Proc. **273-275** (2016) 2539–2541.

[130] ATLAS Collaboration, *Electron and photon energy calibration with the ATLAS detector using LHC Run 1 data*, Eur. Phys. J. **C74** no. 10, (2014) 3071, arXiv:1407.5063 [hep-ex].

[131] ATLAS Collaboration, *Electron and photon energy calibration with the ATLAS detector using data collected in 2015 at $\sqrt{s}$ =13 TeV*, Tech. Rep. ATL-PHYS-PUB-2016-015, CERN, Geneva, Aug, 2016. https://cds.cern.ch/record/2203514.

[132] ATLAS Collaboration, *Electron efficiency measurements with the ATLAS detector using 2012 LHC proton-proton collision data*, Eur. Phys. J. **C77** no. 3, (2017) 195, arXiv:1612.01456 [hep-ex].

[133] W. Lampl, S. Laplace, D. Lelas, P. Loch, H. Ma, S. Menke, S. Rajagopalan, D. Rousseau, S. Snyder, and G. Unal, *Calorimeter Clustering Algorithms: Description and Performance*, Tech. Rep. ATL-LARG-PUB-2008-002. ATL-COM-LARG-2008-003, CERN, Geneva, Apr, 2008. https://cds.cern.ch/record/1099735.

[134] ATLAS Collaboration Collaboration, *Electron efficiency measurements with the ATLAS detector using the 2015 LHC proton-proton collision data*, Tech. Rep. ATLAS-CONF-2016-024, CERN, Geneva, Jun, 2016. https://cds.cern.ch/record/2157687.

[135] ATLAS Collaboration, *Tagging and suppression of pileup jets with the ATLAS detector*, Tech. Rep. ATLAS-CONF-2014-018, CERN, Geneva, May, 2014. https://cds.cern.ch/record/1700870.

[136] ATLAS Collaboration, *Jet energy measurement with the ATLAS detector in proton-proton collisions at $\sqrt{s}$ =7 TeV*, Eur. Phys. J. **C73** no. 3, (2013) 2304, arXiv:1112.6426 [hep-ex].

[137] M. Cacciari, G. P. Salam, and G. Soyez, *The Anti-k(t) jet clustering algorithm*, JHEP **04** (2008) 063, arXiv:0802.1189 [hep-ph].

[138] ATLAS Collaboration, *Jet energy measurement and its systematic uncertainty in proton-proton collisions at $\sqrt{s}$ =7 TeV with the ATLAS detector*, Eur. Phys. J. **C75** (2015) 17, arXiv:1406.0076 [hep-ex].

[139] ATLAS Collaboration, *Tagging and suppression of pileup jets with the ATLAS detector*, Tech. Rep. ATLAS-CONF-2014-018, CERN, Geneva, May, 2014. https://cds.cern.ch/record/1700870.

[140] ATLAS Collaboration, *Measurements of Higgs boson properties in the diphoton decay channel with 36 fb^{-1} of pp collision data at $\sqrt{s}$ = 13 TeV with the ATLAS detector*, Phys. Rev. **D98** (2018) 052005, arXiv:1802.04146 [hep-ex].

[141] G. Barrand et al., *GAUDI - A software architecture and framework for building HEP data processing applications*, Comput. Phys. Commun. **140** (2001) 45–55.

[142] R. Brun and F. Rademakers, *ROOT: An object oriented data analysis framework*, Nucl. Instrum. Meth. **A389** (1997) 81–86.

[143] S. Alioli, P. Nason, C. Oleari, and E. Re, *NLO Higgs boson production via gluon fusion matched with shower in POWHEG*, JHEP **04** (2009) 002, arXiv:0812.0578 [hep-ph].

[144] P. Nason and C. Oleari, *NLO Higgs boson production via vector-boson fusion matched with shower in POWHEG*, JHEP **02** (2010) 037, arXiv:0911.5299 [hep-ph].

[145] T. Sjostrand, S. Mrenna, and P. Z. Skands, *A Brief Introduction to PYTHIA 8.1*, Comput. Phys. Commun. **178** (2008) 852–867, arXiv:0710.3820 [hep-ph].

[146] J. Alwall, R. Frederix, S. Frixione, V. Hirschi, F. Maltoni, O. Mattelaer, H. S. Shao, T. Stelzer, P. Torrielli, and M. Zaro, *The automated computation of tree-level and next-to-leading order differential cross sections, and their matching to parton shower simulations*, JHEP **07** (2014) 079, arXiv:1405.0301 [hep-ph].

[147] S. Agostinelli et al., *GEANT4: A Simulation toolkit*, Nucl. Instrum. Meth. **506** no. 3, (2003) 250 – 303. http://www.sciencedirect.com/science/article/pii/S0168900203013688.

[148] J. Allison et al., *Geant4 developments and applications*, IEEE Trans. Nucl. Sci. **53** (2006) 270.

[149] ATLAS Collaboration, *The ATLAS Simulation Infrastructure*, Eur. Phys. J. **C70** (2010) 823–874, arXiv:1005.4568 [physics.ins-det].

[150] T. Gleisberg, S. Hoeche, F. Krauss, M. Schonherr, S. Schumann, F. Siegert, and J. Winter, *Event generation with SHERPA 1.1*, JHEP **02** (2009) 007, arXiv:0811.4622 [hep-ph].

[151] B. Lenzi and D. Delgove, *Selection of the diphoton production vertex using multivariate techniques for $H \to \gamma\gamma$ and other analyses*, Tech. Rep. ATL-COM-PHYS-2015-1321, CERN, Geneva, Oct, 2015. https://cds.cern.ch/record/2062239.

[152] ATLAS Collaboration, *Search for supersymmetry in final states with missing transverse momentum and multiple b-jets in proton-proton collisions at $\sqrt{s} = 13$ TeV with the ATLAS detector*, JHEP **06** (2018) 107, arXiv:1711.01901 [hep-ex].

[153] ATLAS Collaboration, *Search for supersymmetry in final states with charm jets and missing transverse momentum in 13 TeV pp collisions with the ATLAS detector*, JHEP **09** (2018) 050, arXiv:1805.01649 [hep-ex].

[154] ATLAS Collaboration, *Search for dark matter in events with missing transverse momentum and a Higgs boson decaying to two photons in pp collisions at*

$\sqrt{s}$ =8 TeV with the ATLAS detector, Phys. Rev. Lett. **115** no. 13, (2015) 131801, arXiv:1506.01081 [hep-ex].

[155] ATLAS Collaboration, *Search for dark matter at $\sqrt{s}$ = 13 TeV in final states containing an energetic photon and large missing transverse momentum with the ATLAS detector*, Eur. Phys. J. **C77** no. 6, (2017) 393, arXiv:1704.03848 [hep-ex].

[156] ATLAS Collaboration, *Expected performance of missing transverse momentum reconstruction for the ATLAS detector at $\sqrt{s}$ =13 TeV*, Tech. Rep. ATL-PHYS-PUB-2015-023, CERN, Geneva, Jul, 2015. https://cds.cern.ch/record/2037700.

[157] ATLAS Collaboration, *Performance of missing transverse momentum reconstruction for the ATLAS detector in the first proton-proton collisions at at $\sqrt{s}$ =13 TeV*, Tech. Rep. ATL-PHYS-PUB-2015-027, CERN, Geneva, Jul, 2015. https://cds.cern.ch/record/2037904.

[158] ATLAS Collaboration, *Pile-up Suppression in Missing Transverse Momentum Reconstruction in the ATLAS Experiment in Proton-Proton Collisions at $\sqrt{s}$ =8 TeV*, Tech. Rep. ATLAS-CONF-2014-019, CERN, Geneva, May, 2014. https://cds.cern.ch/record/1702055.

[159] M. Cacciari and G. P. Salam, *Pileup subtraction using jet areas*, Phys. Lett. **B659** (2008) 119–126, arXiv:0707.1378 [hep-ph].

[160] M. Cacciari, G. P. Salam, and G. Soyez, *The Catchment Area of Jets*, JHEP **04** (2008) 005, arXiv:0802.1188 [hep-ph].

[161] G. Arcadi, A. Djouadi, and M. Raidal, *Dark Matter through the Higgs portal*, arXiv:1903.03616 [hep-ph].

[162] K. Peters, *Prospects for beyond Standard Model Higgs boson searches at future LHC runs and other machines*, PoS **CHARGED2016** (2017) 028, arXiv:1701.05124 [hep-ex].

[163] J. Erler and M. Schott, *Electroweak Precision Tests of the Standard Model after the Discovery of the Higgs Boson*, Prog. Part. Nucl. Phys. **106** (2019) 68–119, arXiv:1902.05142 [hep-ph].

[164] Particle Data Group Collaboration, C. Patrignani et al., *Review of Particle Physics*, Chin. Phys. **C40** no. 10, (2016) 100001.

[165] CMS Collaboration, *Search for associated production of dark matter with a Higgs boson decaying to* $\mathrm{b\bar{b}}$ *or* $\gamma\gamma$ *at* $\sqrt{s}$ *=13 TeV*, JHEP **10** (2017) 180, arXiv:1703.05236 [hep-ex].

[166] ATLAS Collaboration, *Search for dark matter produced in association with a Higgs boson decaying to two bottom quarks in pp collisions at* $\sqrt{s}$ *=8 TeV with the ATLAS detector*, Phys. Rev. **D93** no. 7, (2016) 072007, arXiv:1510.06218 [hep-ex].

[167] ATLAS Collaboration, *Search for dark matter in association with a Higgs boson decaying to b-quarks in pp collisions at* $\sqrt{s}$ *=13 TeV with the ATLAS detector*, Phys. Lett. **B765** (2017) 11–31, arXiv:1609.04572 [hep-ex].

[168] ATLAS Collaboration, *Search for Dark Matter Produced in Association with a Higgs Boson Decaying to* $b\bar{b}$ *using 36* fb^{-1} *of pp collisions at* $\sqrt{s}$ *=13 TeV with the ATLAS Detector*, Phys. Rev. Lett. **119** no. 18, (2017) 181804, arXiv:1707.01302 [hep-ex].

[169] D. Abercrombie et al., *Dark Matter Benchmark Models for Early LHC Run-2 Searches: Report of the ATLAS/CMS Dark Matter Forum*, arXiv:1507.00966 [hep-ex].

[170] A. Berlin, T. Lin, and L.-T. Wang, *Mono-Higgs Detection of Dark Matter at the LHC*, JHEP **06** (2014) 078, arXiv:1402.7074 [hep-ph].

[171] ATLAS Collaboration, *Search for new phenomena in events with missing transverse momentum and a Higgs boson decaying to two photons in pp collisions at*

$\sqrt{s}$ *=13 TeV with the ATLAS detector*, Tech. Rep. ATLAS-CONF-2016-087, CERN, Geneva, Aug, 2016.
https://cds.cern.ch/record/2206281.

[172] NNPDF Collaboration, *Parton distributions for the LHC Run II*, JHEP **04** (2015) 040, arXiv:1410.8849 [hep-ph].

[173] ATLAS Collaboration, *ATLAS Run 1 Pythia8 tunes*, Tech. Rep. ATL-PHYS-PUB-2014-021, CERN, Geneva, Nov, 2014.
https://cds.cern.ch/record/1966419.

[174] R. D. Ball et al., *Parton distributions with LHC data*, Nucl. Phys. **B867** (2013) 244–289, arXiv:1207.1303 [hep-ph].

[175] D. J. Lange, *The EvtGen particle decay simulation package*, Nuclear Instruments and Methods in Physics Research Section A: Accelerators, Spectrometers, Detectors and Associated Equipment **462** no. 1, (2001) 152 – 155. http://www.sciencedirect.com/science/article/pii/S0168900201000894. BEAUTY2000, Proceedings of the 7th Int. Conf. on B-Physics at Hadron Machines.

[176] ATLAS Collaboration, *Summary of ATLAS Pythia 8 tunes*, Tech. Rep. ATL-PHYS-PUB-2012-003, CERN, Geneva, Aug, 2012.
https://cds.cern.ch/record/1474107.

[177] CDF Collaboration, *Search for new particles decaying into dijets in proton-antiproton collisions at s**(1/2) = 1.96-TeV*, Phys. Rev. **D79** (2009) 112002, arXiv:0812.4036 [hep-ex].

[178] ATLAS Collaboration, *Luminosity determination in pp collisions at* $\sqrt{s}$ *=8 TeV using the ATLAS detector at the LHC*, Eur. Phys. J. **C76** no. 12, (2016) 653, arXiv:1608.03953 [hep-ex].

[179] ATLAS Collaboration, *Performance of the ATLAS Trigger System in 2015*, Eur. Phys. J. **C77** no. 5, (2017) 317, arXiv:1611.09661 [hep-ex].

[180] ATLAS Collaboration, *Search for resonances in diphoton events at $\sqrt{s}$ =13 TeV with the ATLAS detector*, JHEP **09** (2016) 001, arXiv:1606.03833 [hep-ex].

[181] ATLAS Collaboration, *Photon identification in 2015 ATLAS data*, Tech. Rep. ATL-PHYS-PUB-2016-014, CERN, Geneva, Aug, 2016. https://cds.cern.ch/record/2203125.

[182] LHC Higgs Cross Section Working Group Collaboration, D. de Florian et al., *Handbook of LHC Higgs Cross Sections: 4. Deciphering the Nature of the Higgs Sector*, arXiv:1610.07922 [hep-ph].

[183] G. Cowan, K. Cranmer, E. Gross, and O. Vitells, *Asymptotic formulae for likelihood-based tests of new physics*, Eur. Phys. J. **C71** (2011) 1554, arXiv:1007.1727 [physics.data-an].

[184] B. Mistlberger and F. Dulat, *Limit setting procedures and theoretical uncertainties in Higgs boson searches*, arXiv:1204.3851 [hep-ph].

[185] ATLAS, CMS Collaboration, *Combined measurement of the Higgs boson mass in pp collisions at $\sqrt{s}$ =7 and 8 TeV with the ATLAS and CMS experiments*, Phys. Rev. Lett. **114** (2015) 191803, arXiv:1503.07589 [hep-ex].

[186] X. Ruan et al., *Supporting Note: Searching for heavy resonance decaying into Zγ with missing transverse energy in pp collisions at $\sqrt{s}$ =13 TeV with the ATLAS detector*, Tech. Rep. ATL-COM-PHYS-2018-953, CERN, Geneva, Jun, 2018. https://cds.cern.ch/record/2627618.